Doctoral Dissertation
博士論文

Study of diagnostic methods of nodal line semimetals and an intrinsic link to topological crystalline insulators
(ノーダルライン半金属の判別手法と トポロジカル結晶絶縁体への接続に関する研究)

Department of Physics, Graduate School of Science,
The University of Tokyo
東京大学大学院理学系研究科
物理学専攻

Ikuma Tateishi
立石　幾真

Abstract

In this thesis, we enhance the diagnostic method for nodal line semimetals in the case where spin-orbit coupling is negligible. We also show that the nodal line semimetals diagnosed by the present enhanced method ("δ indices") are linked to topological crystalline insulators when the spin-orbit coupling is introduced. This link reveals a clear difference between the topological crystalline insulator classes that have not been distinguished by the previous methods. Our result suggests that the obtained link can lead to the enhancement of the diagnostic methods for topological insulators and topological crystalline insulators.

In the derivation of the δ indices, we assume not only time-reversal and space inversion symmetries, which guarantee the stability of nodal lines, but also a four-fold rotation or four-fold screw symmetry. The δ indices are derived by considering a subgroup reduction of space groups and by applying the "symmetry-based indicator" defined in the space group with lower symmetry. With this approach, we give calculation formulas of the δ indices based on symmetry eigenvalues for each of the five Bravais lattices with a four-fold rotation or screw symmetry (i) primitive tetragonal lattice, (ii) body-centered tetragonal lattice, (iii) primitive cubic lattice, (iv) face-centered cubic lattice, and (v) body-centered cubic lattice. By using the δ indices, we give three kinds of nodal line semimetals that are newly diagnosed by the δ indices: (a) face-centered cubic lattice (Ca, Ba, and SnSe), (b) body-centered square lattice (Ca_2As), and (c) nonsymmorphic tetragonal lattice (tight-binding model in the space group 127).

Based on the above examples of nodal line semimetals, we discuss to what kind of topological insulator class these nodal line semimetals are linked when spin-orbit coupling is introduced. By using $\boldsymbol{k}\cdot\boldsymbol{p}$ perturbation models, we show that these nodal line semimetals are linked to topological crystalline insulators by introducing spin-orbit coupling. In the examples (a) and (b), we show that a nontrivial mirror Chern number emerges on the mirror-invariant plane that is penetrated by the nodal lines before introducing spin-orbit coupling. It is also proved that the value of mirror Chern number corresponds to how many times the mirror-invariant plane is penetrated by the nodal lines. In particular, in the example (a), two types of nodal line configurations are realized depending on a parameter. We show that, by checking the differences in the nodal line configurations, it is possible to diagnose two different topological crystalline insulators classes that have not been diagnosed by the previous methods. This link between the nodal lines and the mirror Chern numbers is also confirmed in real materials, by comparing the results of first-principles calculations for Ca and Ba. In the example (c), on the other hand, we show that a characteristic configuration of nodal lines (concentric intersecting coplanar ellipses, CICE nodal lines), which appear due to the nature of the nonsymmorphic space

group, is linked to a glide-protected topological crystalline insulator. In this case, we show that the CICE nodal lines correspond to the nontrivial glide topological invariants. This result suggests that by finding a nodal line semimetal with CICE nodal lines, we can find a topological crystalline insulator protected by the glide symmetry, which has not been diagnosed by the previous methods.

These results introduce a nwe perspective of using the intrinsic link and hypothetical SOC-neglecting first-principles calculations to enhance the diagnostic methods of topological insulators with SOC. Since the link is expected to be generally extended, the perspective should be useful from now on in many aspects including diagnostic methods and materials design.

Contents

Chapter 1

Introduction

Topological materials science has been one of the most actively studied areas in the field of condensed matter physics in recent years. One of the earliest proposed topological phenomena is the quantum Hall effect [1, 2]. The Hall conductivity of a quantum Hall system, which is a two-dimensional insulator, is quantized with an integer called the Chern number, hence the quantum Hall system is also called a Chern insulator [3, 4, 5]. Quantized to integer values such as the Chern number, the properties of the topological systems are robust against continuous (or "adiabatic") perturbations of parameters. This robustness is a key feature of topological materials.

Starting with the Chern insulator, various classes of topological insulators (TI) have been proposed [6, 7]. Among them, the proposal of time-reversal (TR) protected topological insulators has attracted plenty of attention [8, 9, 10]. These materials are characterized by gapless (metallic) surface states while the inside of the crystal (bulk) is insulating [Fig. 1.1]. This class of topological insulators can be realized in three-dimensional crystals [11, 12, 13, 14, 15, 16, 17, 18, 19] and are of interest for experimental as well as theoretical studies. Subsequently, topological crystal insulators (TCI) [20, 21, 22], which are protected by crystal symmetry such as mirror, rotation, or glide, have been proposed. These insulators also have characteristic surface states on the surfaces where the crystal symmetry is protected.

The topological insulators listed above are materials having three-dimensional insulating bulk states and two-dimensional gapless surface states. Recently, a new class of topological insulators with three-dimensional insulating bulk states and one-dimensional gapless hinge states has been proposed. These materials are called higher-order topological insulators (HOTI) [23, 24, 25, 26, 27].

Not only the topological insulators but also materials called topological semimetals have been the subject of research in this field [28, 29, 30]. Topological semimetals consist of valence and conduction bands that are degenerate at a point or a line in momentum space and have a linear dispersion around them. This degenerate point (degenerate line) is called a "node point" ("nodal line"). The stability of these nodes is protected by the symmetry of the crystal. A typical topological semimetal is graphene [31]. Graphene is known to have Dirac-cone-shaped band dispersions at high symmetry points in momentum space. A material with similar characteristics — a node point and linear dispersion around it — can be realized in 3D systems and is called a Dirac semimetal [Fig. 1.2]
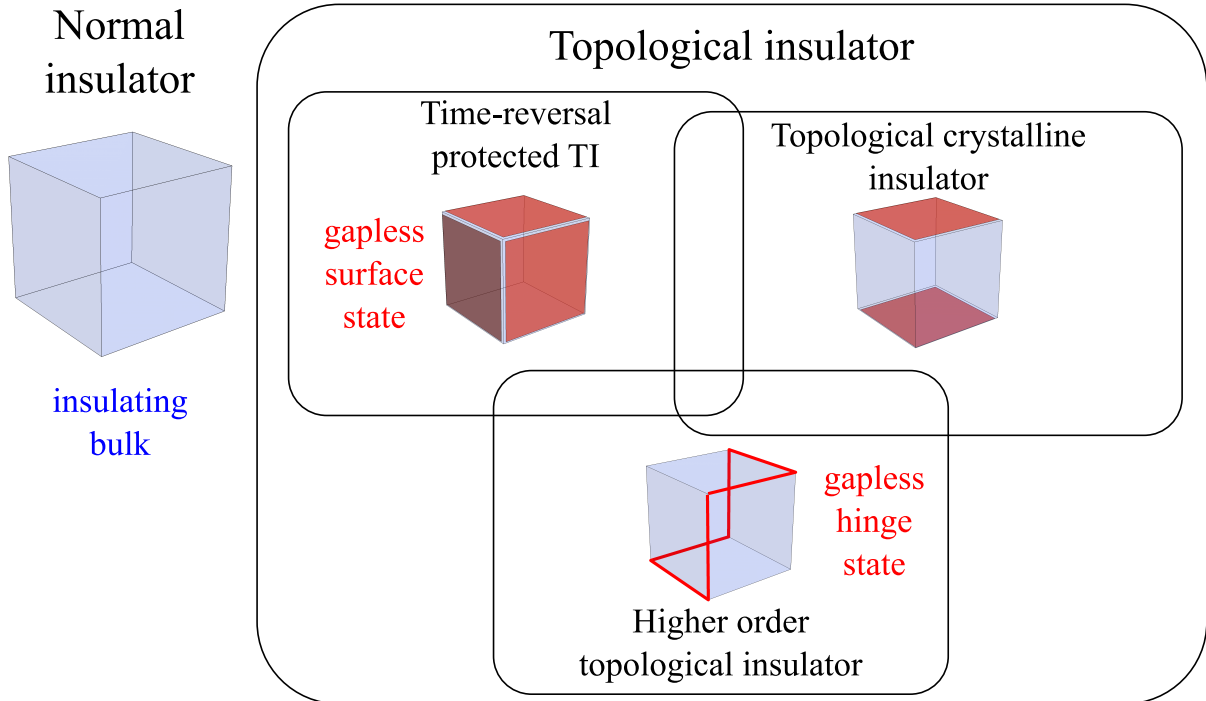
Figure 1.1. Various topological insulators and their surface (hinge) states. Blue cubes represent insulating bulks and red planes represent gapless surface states. For a higher-order topological insulator, a gapless hinge state is shown as a red line.

[32, 33, 34, 35]. In Dirac semimetals, each band of the linear dispersion is doubly degenerate with respect to the spin degree of freedom, just as in graphene. There are also materials with the same point nodes, but without spin degeneracy, called Weyl semimetals [36, 37, 38, 39, 40]. In contrast to Dirac and Weyl semimetals that have point nodes, there are materials with line nodes, which are called nodal line semimetals [41, 30, 42, 43]. The line nodes of most nodal line semimetals have spin degeneracy and are sometimes called Dirac nodal line semimetals.

As summarized above, there are a great variety of topological materials, each with different properties. To be of interest to experimental and applied studies, explicit material examples should be proposed. Then, given a material example or a certain band dispersion, how can we diagnose whether it is a topological material or not? Furthermore, if it is a topological material, how can we diagnose its topological class in more detail? The first possibility is to calculate the topological invariants that characterize each topological material class, such as the Chern number. However, in general, topological invariants are given as integrals of wavefunctions in the whole Brillouin zone, and their numerical evaluations can be time-consuming. Considering the need to scan material databases to find topological materials with desired properties, a method with less calculation cost is preferable. Therefore, the development of a classification theory of topological materials and a simple diagnostic method has been an important topic of research in this field [44, 45, 46, 47, 48, 49, 50, 43, 30].
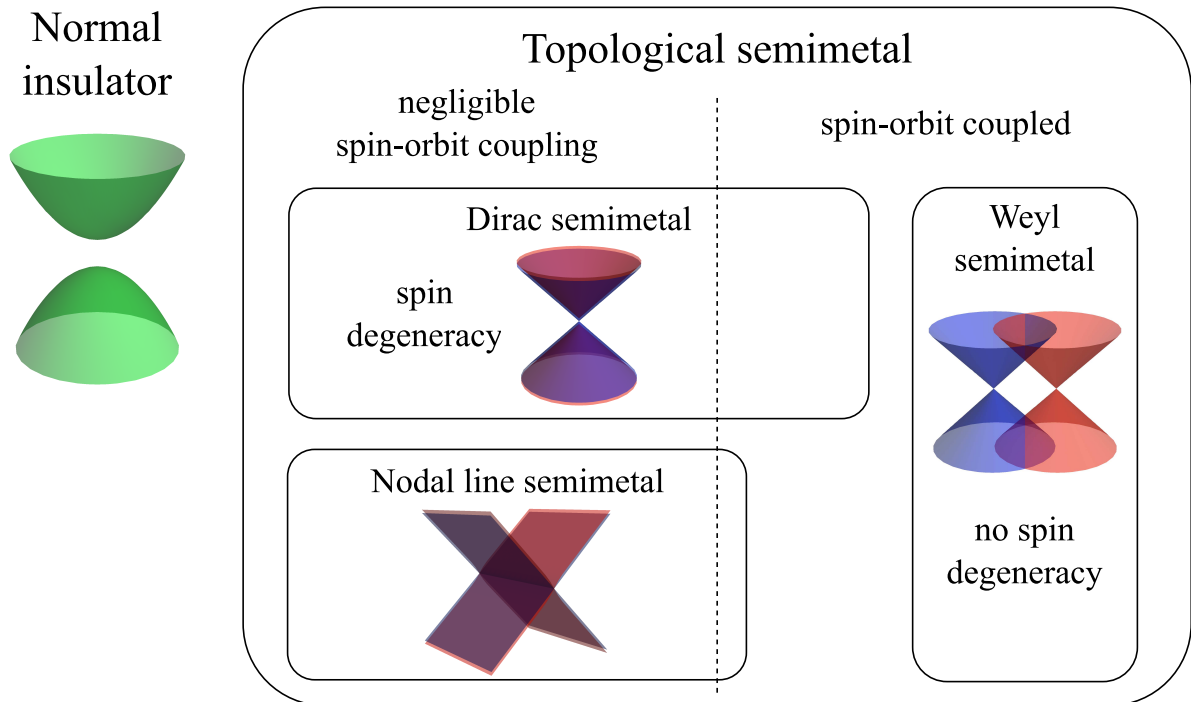
Figure 1.2. Various topological semimetals and their band dispersions. Red and blue bands correspond to the spin degree of freedom.

In this dissertation, we focus on the fact that some topological semimetals can not be diagnosed by previous methods. Then, we propose a new method to diagnose them. Therefore, in this introduction chapter, we briefly summarize the diagnostic methods proposed so far. In particular, a method called "symmetry-based indicator" and diagnostic methods of nodal line semimetals is reviewed in detail since they play an important role in the following chapters. In chapter 2, we clarify two problems that need to be solved in this dissertation. In chapter 3, as a solution to one of the problems, we define a new diagnostic method for nodal line semimetals. In chapter 4, to solve the other problem, we discuss an "intrinsic link" between nodal line semimetals that are newly diagnosed and topological crystalline insulators.

1.1 Definition of topological classes

Before going to the diagnostic methods of topological classes, we define what "identical topological classes" and "distinct topological classes" mean in topological materials. Given materials, models, or phases A and B, a statement "A and B are topologically identical" is defined as follows [6, 47].

> **topologically identical**
>
> "A and B are topologically identical" means that A and B are connected by continuous parameter variation with keeping:
>
> - "gapped" energy spectrum (band dispersion)
>
> - symmetry of the system

"Topologically distinct" is defined as a complement of this statement. To be more specific, topologically distinct materials (models or phases) cannot be continuously connected without closing the gap or breaking the symmetry of the system.

In the above statement, we quote "gapped" because the word "gapped" can have different meanings depending on the topological materials we focus on. For topological insulators, this "gapped" truly means a gapped energy spectrum. In a band dispersion picture in the momentum space, it is written as

$$\forall \boldsymbol{k} \in \mathrm{BZ}, \quad E_{j+1}(\boldsymbol{k}) - E_j(\boldsymbol{k}) > 0 \tag{1.1}$$

for a certain band index $j \in \mathbb{N}$, where BZ is Brillouin zone and $E_j(\boldsymbol{k})$ is the band dispersion of the j-th band. Note that the Fermi energy E_f is not involved in the above definition (see Fig. 1.3, top right). Furthermore, E_j and E_{j+1} can be dispersive near the Fermi energy, and the material can be metallic (see Fig. 1.3, bottom left). When we really try to use a materials as a topological "insulator", we need to find a material in which Fermi energy is locating between E_j and E_{j+1} (see Fig. 1.3, top left).

On the other hand, in the definition of classes of topological semimetals, we cannot use the definition (1.1) since topological semimetals are gapless by their definition. Therefore, for topological semimetals, we focus on some specific points in momentum space, and the word "gapped" in the topological semimetals means

$$\forall \boldsymbol{k} \in \{\boldsymbol{k}_1, \boldsymbol{k}_2 \dots\}, \quad E_{j+1}(\boldsymbol{k}) - E_j(\boldsymbol{k}) > 0. \tag{1.2}$$

How to choose the points $\{\boldsymbol{k}_1, \boldsymbol{k}_2, \dots\}$ is explained in Section 1.3.

In the field of topological material science, the word "topologically trivial" and "topologically nontrivial" are often used. This "trivial" means "identical to a material that everyone believes is not a topological insulator (semimetal)". In this dissertation, the word "normal (trivial) insulator" is used for an insulator that gapped energy spectrum in the bulk, surfaces, hinges, and corners[1], as commonly used in the field of topological material science.

---

[1]in all momentum in the bulk, surface, and hinge momentum space
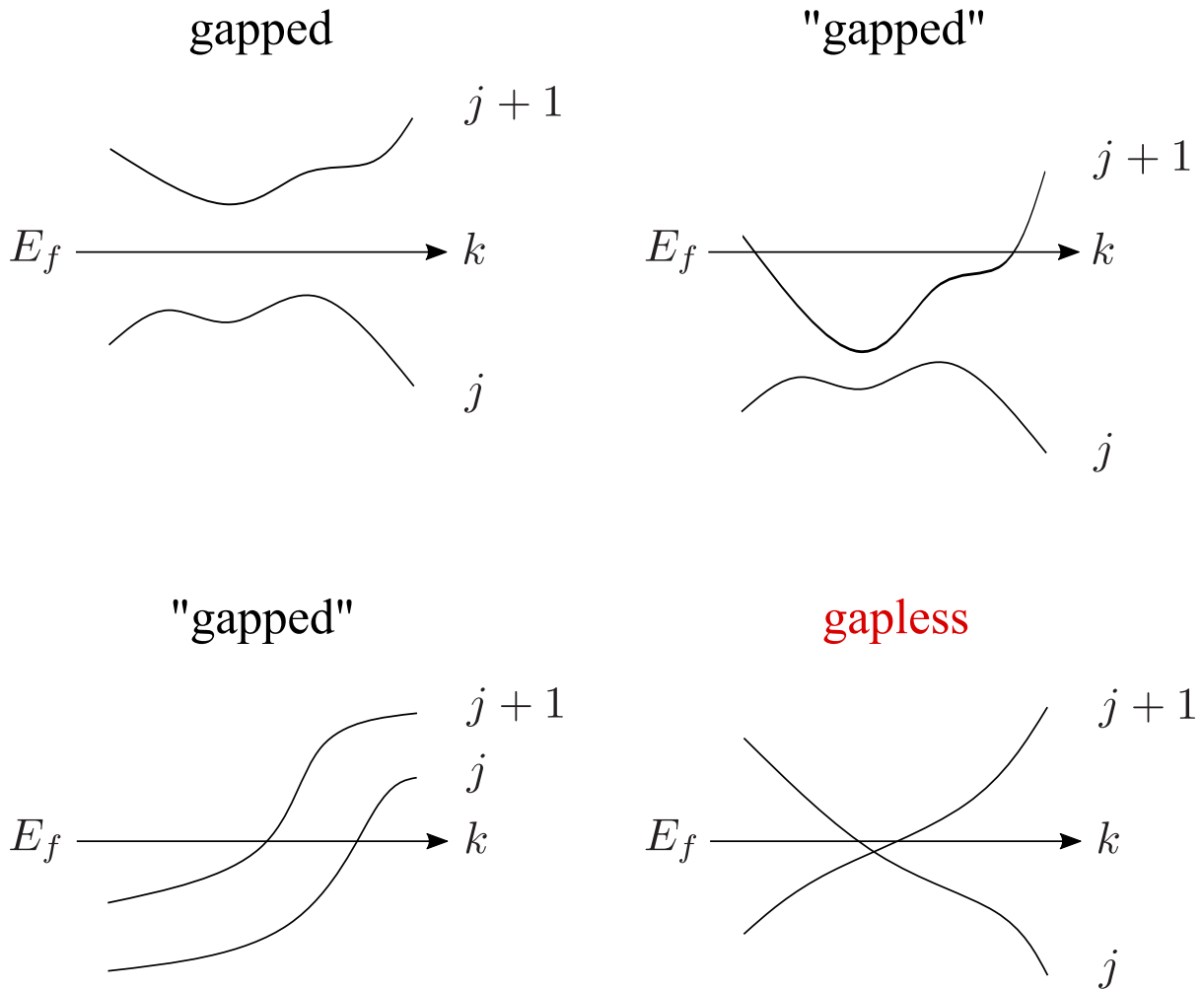
Figure 1.3. Examples of gapped and gapless band dispersions between the j-th and $(j+1)$-th bands. E_f is the Fermi energy. Only the bottom right one is a gapless case. The other three are "gapped" in our definition. However, in terms of real material properties, only the top left is an insulator.

1.1.1 Classification theories and diagnostic methods

Based on the above definition of topological classes, classification theories have been actively studied. One of the most famous classifications is the Altland-Zirnbauer's (AZ) symmetry class [51] and its periodic table of topological invariants. Further, recent studies based on the K-theory [52] have revealed topological properties of cases where crystalline symmetries are added to the AZ symmetry classes. Although these classification theories play a crucial role in the field of topological material science, they can give only a "framework" of topological classes. For example, it is shown that the AII class in the AZ symmetry class is classified by $\mathbb{Z}_2$-valued invariants, but the classification theory does not tell us how to calculate the invariants, i.e., the Fu-Kane formula (see section 1.2) is not given. To realize high-throughput materials search, explicit methods to calculate the invariants (diagnostic methods)[2] are desired. In the following sections, we review those diagnostic methods. The detailed relation between classification theories and reviewed diagnostic methods is discussed in Appendix B.

---

[2]Note that this differentiation of the words "classification theory" and "diagnostic method" is not necessarily common. It is a local rule in this dissertation.

1.2 Diagnostic methods for topological insulators

In this section, we review diagnostic methods for topological insulators. First, we introduce diagnostic methods for inversion symmetric systems. These methods use almost the same formulas and applicable from one-dimensional (1D) systems to three-dimensional (3D) systems [53]. In 3D systems, the formula is known as Fu-Kane formula, which is also well-known as "$\mathbb{Z}_2$ index". After reviewing these inversion based indices, we introduce the symmetry-based indicator. The symmetry-based indicator is applicable for all kinds of crystalline symmetric cases and thus diagnoses a wider variety of topological insulators.

1.2.1 Inversion based indices

First, we briefly review diagnostic methods based on the inversion symmetry. We review topological properties of a 1D chain model (the Su-Schrieffer-Heeger model), the quantum Hall system (the Chern insulator), the 2D Time-reversal protected topological insulator, and the 3D Time-reversal protected topological insulator. While topological properties of these cases are not protected by the inversion symmetry, easy diagnostic methods have been given when the inversion symmetry is additionally assumed. Since these methods are well known today, we only exhibit the conclusions here (See Appendix A.3 for the derivation and details).

1D chain model (Su-Schrieffer-Heeger model)

The 1D spinless fermion chain model called the Su-Schrieffer-Heeger model (SSH model) [54, 55] consists of two sites A and B in a unit cell and alternative hoppings between them t_1 and t_2 [Fig. 1.4]. When a finite length of the chain is considered, the model can have end states, and the presence or absence of the end states is diagnosed by the Berry phase θ.
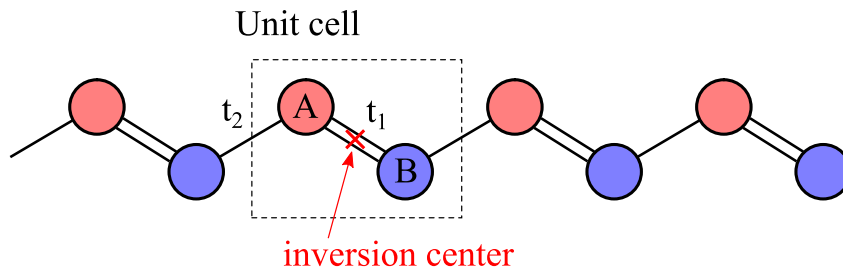
Figure 1.4. Su-Schrieffer-Heeger model.

When the system additionally has the inversion symmetry, the Berry phase calculation is simplified. Generally, in the 1D momentum space, there are two inversion-invariant points, $k = 0$ and $k = \pi$. The Berry phase θ is written with the inversion eigenvalues of

Table 1.1: Diagnostic method of the SSH model.

t_1 and t_2	Berry phase	inversion eigenvalue	end state
$t_1 > t_2$	$\theta = 0$	$\chi_{k=0}\chi_{k=\pi} = 1$	No
$t_1 < t_2$	$\theta = \pi$	$\chi_{k=0}\chi_{k=\pi} = -1$	Yes

the occupied band in these points $(\chi_{k=0}, \chi_{k=\pi})$ as

$$e^{i\theta} = \chi_{k=0}\chi_{k=\pi}. \tag{1.3}$$

Therefore, the product of the inversion eigenvalues works as a diagnostic method of the topological class of the SSH model [Table 1.1]. (The detailed derivation and some point to be noted are given in Appendix A.3.1.)

2D quantum Hall system (Chern insulator)

The Chern insulator is a quantum Hall system and the Hall conductivity is given as $\frac{-e^2}{h}\mathcal{C}$, where $\mathcal{C} \in \mathbb{Z}$ is the Chern number [2]. When the Chern insulator has the inversion symmetry, the parity of the Chern number is diagnosed by calculating the product of the inversion eigenvalues. In a 2D system, there are four inversion-invariant points. These points are called "Time-Reversal Invariant Momenta (TRIM)" since TR and inversion work on a momentum $\boldsymbol{k}$ in the same way. The Chern number $\mathcal{C}$ is written with the inversion eigenvalues as

$$e^{i\pi\mathcal{C}} = \prod_{n:\text{occupied}} \prod_{\boldsymbol{k}:4\text{TRIM}} \chi_n(\boldsymbol{k}), \tag{1.4}$$

where n is the band index and $\chi_n(\boldsymbol{k})$ is the inversion eigenvalue of the n-th band in $\boldsymbol{k}$. The diagnostic method of the Chern insulator is summarized in Fig. 1.5 and Table 1.2. (The detailed derivation is given in Appendix A.3.2.)

Table 1.2: Diagnostic method of the Chern insulator.

Chern number	Hall conductivity	Chiral edge state	inversion eigenvalue
$\mathcal{C} = 0 \pmod 2$	$\frac{-e^2}{h}2\mathbb{Z}$	Indeterminate	$\prod \chi_n(\boldsymbol{k}) = 1$
$\mathcal{C} = 1 \pmod 2$	$\frac{-e^2}{h}(1 + 2\mathbb{Z})$ (nonzero)	Yes	$\prod \chi_n(\boldsymbol{k}) = -1$
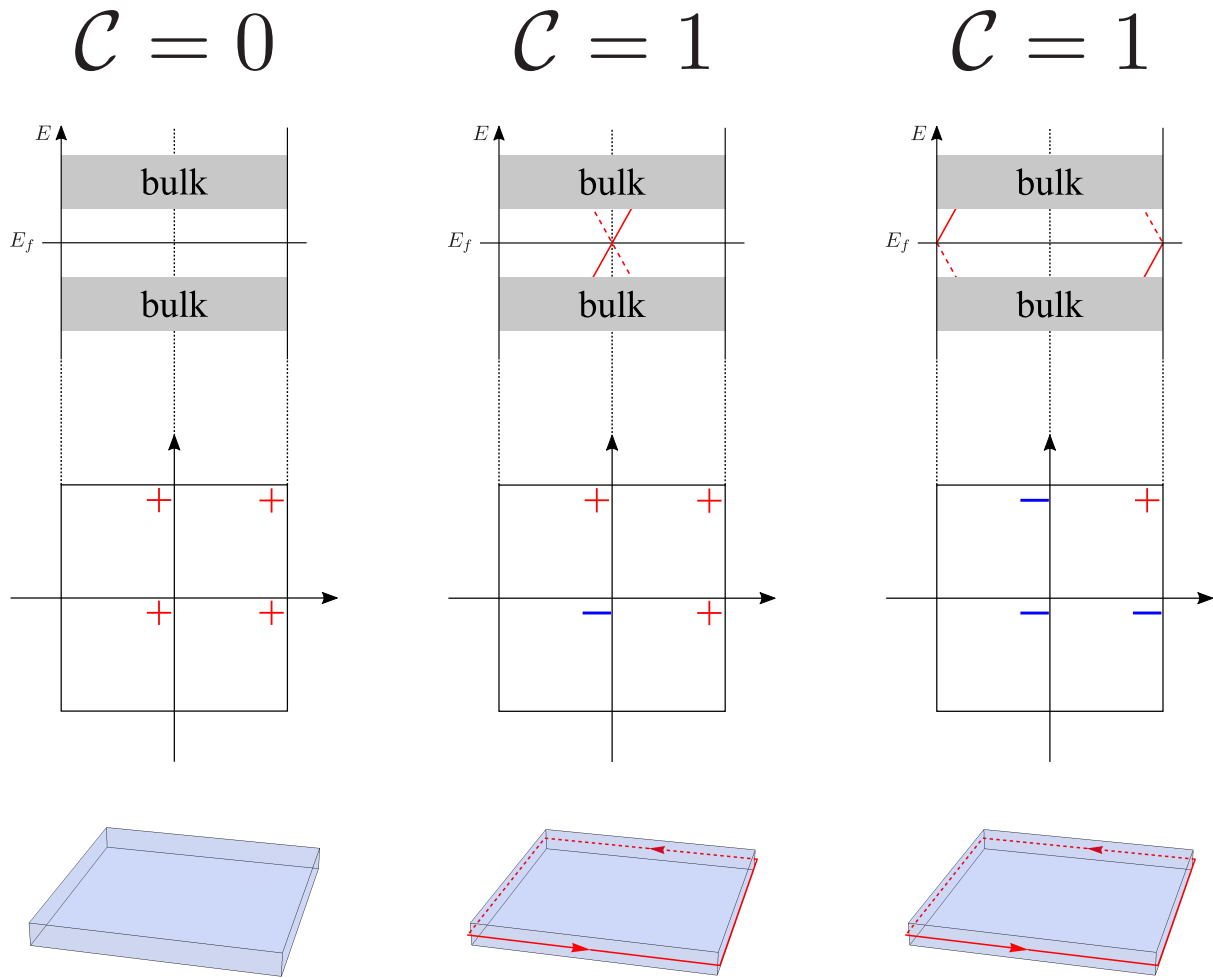
Figure 1.5. Chern number, edge band dispersion, bulk inversion eigenvalues, and chiral edge state. In the edge band dispersion, the chiral edge states appear around the momentum where the projected bulk momentum line includes the flip of the inversion eigenvalue. The chiral edge state drawn with a solid line (dashed line) is on the front side (backside) of the finite 2D system.

2D topological insulator (TR protected TI)

For the cases of the SSH model and the Chern insulator, we have reviewed spinless or spin undegenerate systems. We next review the 2D TR protected topological insulators [8, 9, 10]. To get a nontrivial insulator in TR symmetric system, significant (unignorable) spin-orbit coupling (SOC) is generally required[3]. Hence, in the following discussion, the existence of significant SOC is assumed.

The topological property of the TR protected topological insulator is characterized by a topological invariant $\nu = 0, 1$. When the system has also the inversion symmetry, the ν is diagnosed by using the inversion eigenvalues. Since the system has both TR and inversion symmetries, all bands appear as doubly degenerate pairs in TRIM. The topological invariant ν is written with the inversion eigenvalues defined in each pair as

$$(-1)^\nu = \prod_{n:\text{occupied}} \prod_{\boldsymbol{k}:\text{4TRIM}} \chi_{2n}(\boldsymbol{k}), \tag{1.5}$$

where n is the band index. Because we need to see one band of a paired bands, only $\chi_{2n}(\boldsymbol{k})$ is taken into account and $\chi_{2n-1}(\boldsymbol{k})$ is not[4].

Now $\chi = \pm 1$, and thus it can also be written by counting the -1 inversion eigenvalues as

$$\nu = \sum_{\boldsymbol{k}:\text{4TRIM}} n^-(\boldsymbol{k}) \pmod 2, \tag{1.6}$$

where $n^-(\boldsymbol{k})$ is the number of occupied band pair with -1 inversion eigenvalues.

The diagnostic method is summarized in Fig. 1.6 and Table 1.3. (The detailed derivation is given in Appendix A.3.3.)

Table 1.3: Diagnostic method of the 2D TR protected topological insulator

ν	Helical edge state	$\prod \chi$
0	No[5]	1
1	Yes	-1

---

[3]Here, "significant" means "nonzero". In principle, even really small SOC can give a nontrivial topological insulator. However, from a practical point of view, a system with a too small gap is not a good example. If the bandgap is too small (compared to the interested energy scale), the system can be approximately recognized as another class of topological material.

[4]Generally, $\chi_{2n-1}(\boldsymbol{k}) = \chi_{2n}(\boldsymbol{k})$

[5]if exists, not protected generally

$$\nu = 0 \qquad\qquad \nu = 1 \qquad\qquad \nu = 1$$
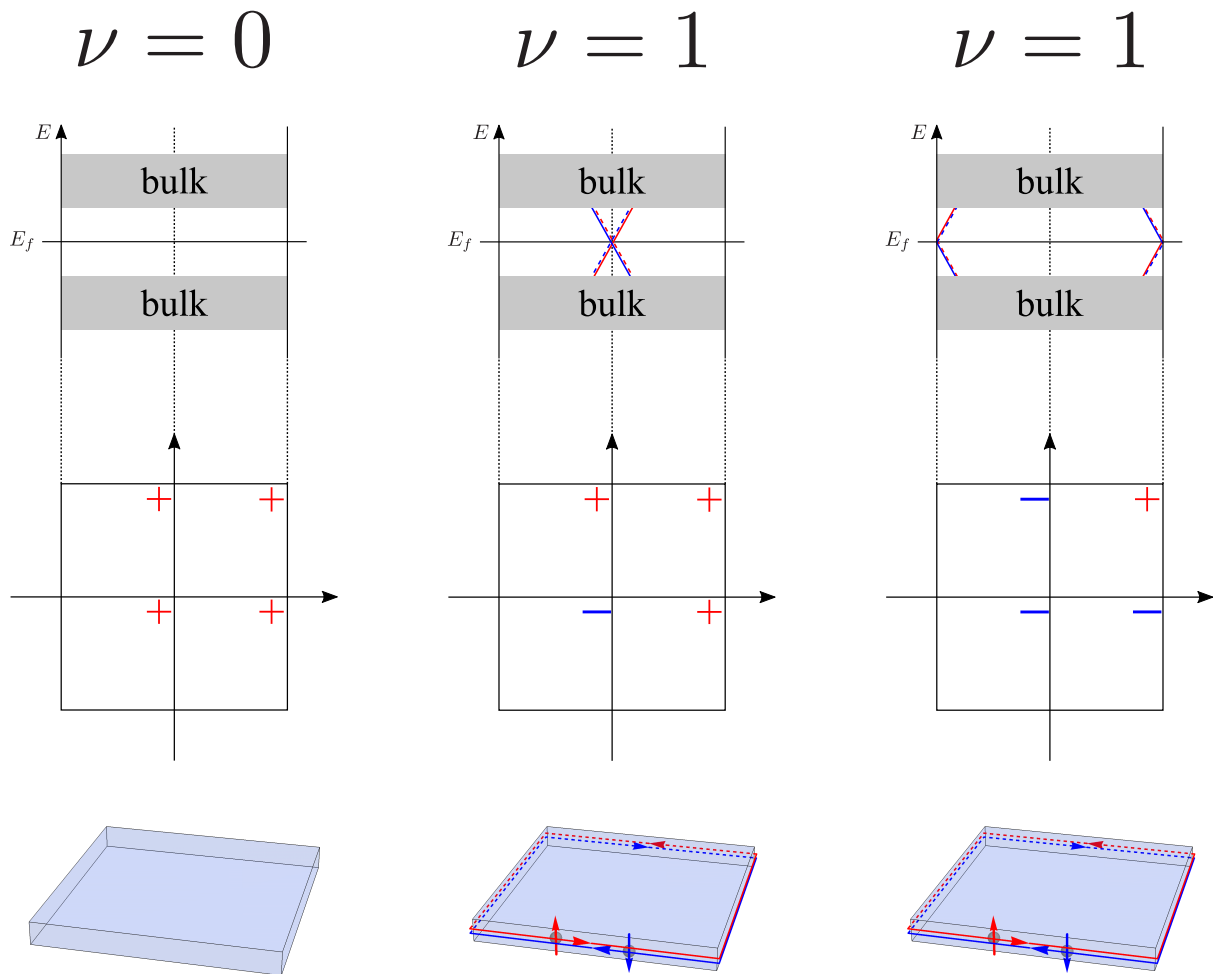
Figure 1.6. Topological invariant ν, edge band dispersion, bulk inversion eigenvalues $\prod_n \chi_{2n}(\boldsymbol{k})$, and helical edge state. In the edge band dispersion, the helical edge states appear around the momentum where the projected bulk momentum line includes the flip of the inversion eigenvalue. The helical edge state drawn with a solid line (dashed line) is on the front side (backside) of the finite 2D system. The red and blue lines correspond to the spin index 1 and 2.

3D topological insulator (TR protected TI)

The 3D TR protected TI [11, 12, 13] is mostly understood as an extension of the 2D case. The only, but crucial difference is the existence of the "strong invariant ν_0". The strong invariant characterizes "strong topological insulators", which are robust against perturbations. On the other hand, there are "weak invariants ν_1, ν_2, ν_3" and they characterize "weak topological insulators". The weak topological insulators are not necessarily robust against perturbations, such as a super-cell periodic perturbation. These invariants are conventionally written in $(\nu_0; \nu_1 \nu_2 \nu_3)$.

When the system has the inversion symmetry, the topological invariants are written with inversion eigenvalues as

$$
\begin{aligned}
\nu_0 &= \sum_{\substack{\boldsymbol{k}:8\mathrm{TRIM}}} n^-(\boldsymbol{k}) \pmod 2, \\
\nu_1 &= \sum_{\substack{\boldsymbol{k}:4\mathrm{TRIM} \\ m_1=1}} n^-(\boldsymbol{k}) \pmod 2, \\
\nu_2 &= \sum_{\substack{\boldsymbol{k}:4\mathrm{TRIM} \\ m_2=1}} n^-(\boldsymbol{k}) \pmod 2, \\
\nu_3 &= \sum_{\substack{\boldsymbol{k}:4\mathrm{TRIM} \\ m_3=1}} n^-(\boldsymbol{k}) \pmod 2.
\end{aligned}
\tag{1.7}
$$

where the TRIM are represented by $m_1, m_2, m_3 = 0, 1$ and reciprocal lattice vestors $\boldsymbol{b}_1, \boldsymbol{b}_2, \boldsymbol{b}_3$ as $\boldsymbol{k} = \frac{1}{2}(m_1 \boldsymbol{b}_1 + m_2 \boldsymbol{b}_2 + m_3 \boldsymbol{b}_3)$. For example, in a primitive orthorhombic case, the ν_1 is calculated with the four TRIM on $k_x = \pi$. Some examples of the invariants and corresponding topological classes are shown in Fig. 1.7 (with surface Fermi arcs), 1.8 (with helical edge states). The diagnostic method is summarized in Table 1.4. (The detailed derivation is given in Appendix A.3.4.)

Today this diagnostic method of the 3D TR protected topological insulator is widely known as the "Fu-Kane formula" after the name of proposers [44]. It is also well known as "$\mathbb{Z}_2$ index" due to its algebraic structure.

This method just requires to examine only eight momenta in the momentum space and evaluate the inversion eigenvalues of wavefunctions. This process is relatively easy and less time-consuming compared to examining the whole BZ. By this simplicity, this formula has contributed greatly to find an explicit material example of 3D topological insulators.

Table 1.4: Diagnostic method of the 3D TR protected topological insulator

ν_0	$\nu_{1,2,3}$	Helical edge state	$\prod_{8\mathrm{TRIM}}\chi$	$\prod_{4\mathrm{TRIM}}\chi$	class
0	0	No	1	1	trivial
0	1	Some surfaces	1	−1	weak
1	0	All surfaces	−1	1	strong
1	1	All surfaces	−1	−1	strong
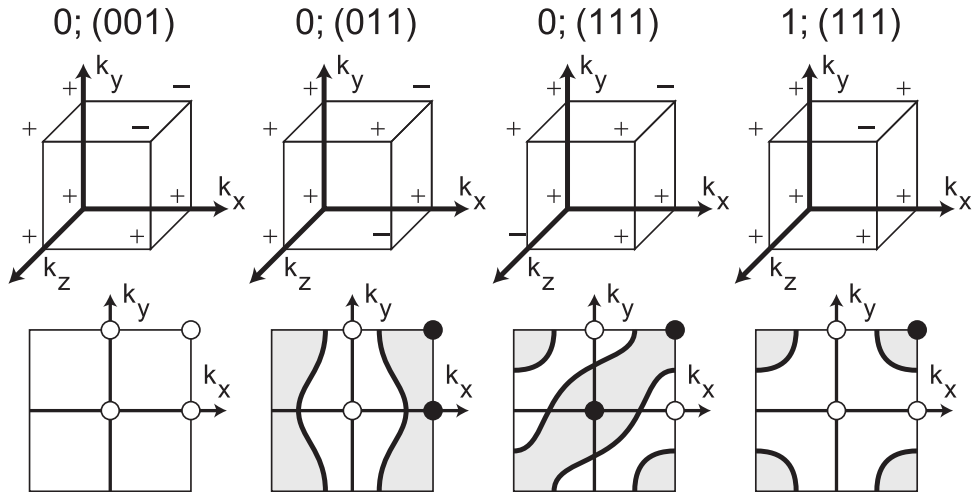
Figure 1.7. Inversion eigenvalues and surface Fermi arc adopted from L. Fu, and C. L. Kane, Physical Review B, **76**, 045302 (2007). In the bottom panels, the solid and open circle represents the eigenvalue product −1 and 1 that is calculated with two points listed in the (001) direction. The thick line in the surface BZ is a possible Fermi arc.

$(\nu_0; \nu_1\nu_2\nu_3) = (0; 000)$

$(\nu_0; \nu_1\nu_2\nu_3) = (1; 000)$

$(\nu_0; \nu_1\nu_2\nu_3) = (0; 001)$

$(\nu_0; \nu_1\nu_2\nu_3) = (0; 100)$
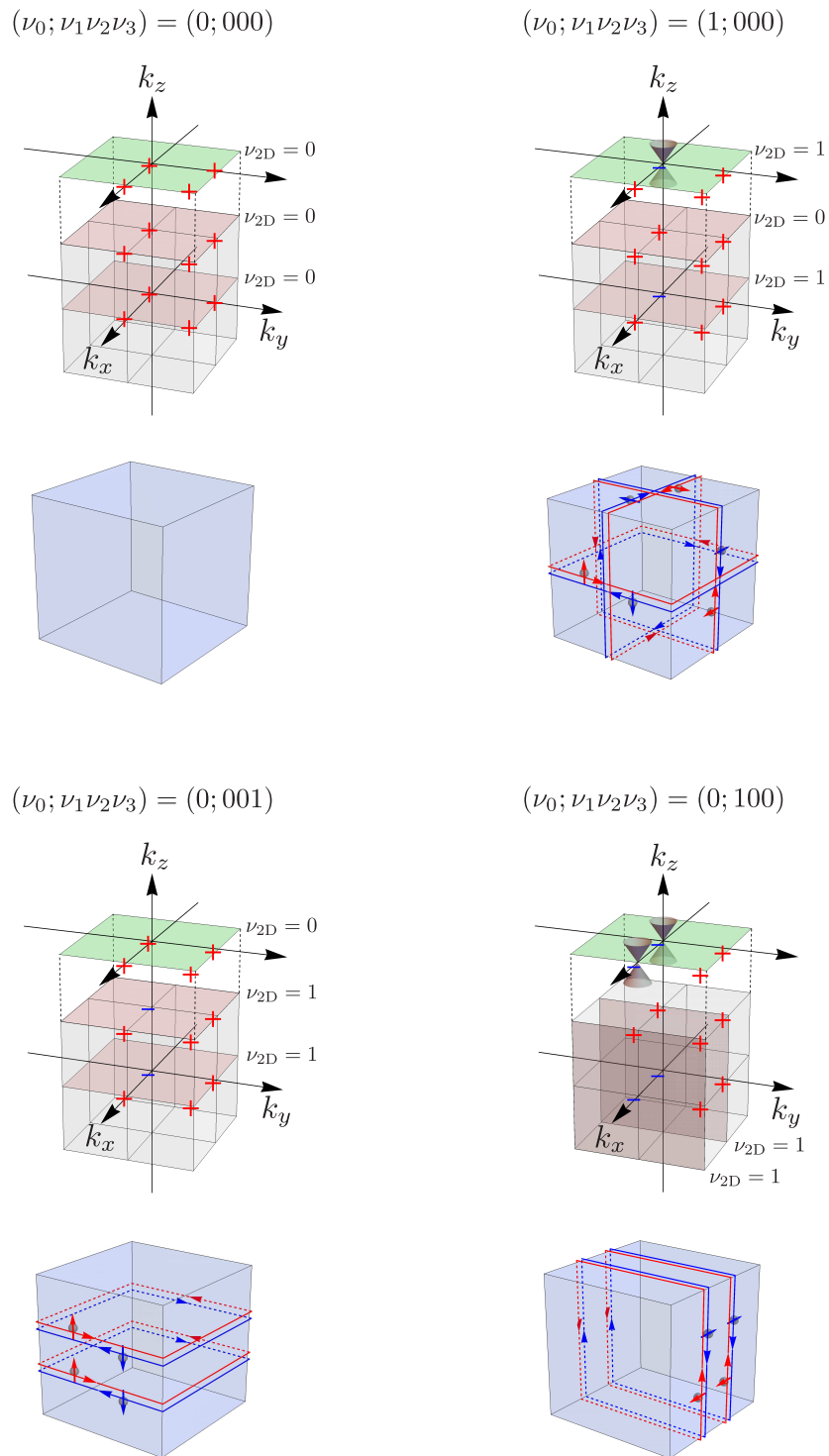
Figure 1.8. 3D TR protected topological insulators and helical edge states. In a strong topological insulator ($\nu_0 = 1$), helical edge states appear on all surfaces. On the other hand, in a weak topological insulator, helical edge states appear on some of the surfaces.

1.2.2 Symmetry-based indicator

In this subsection, we review a recently proposed diagnostic method called "symmetry-based indicator" [47, 48] (It is also called "symmetry indicator", or sometimes just "indicator"). Since the method plays a crucial role in this dissertation, we review this method rather in detail.

In the previous subsection 1.2.1, we have focused on the cases with inversion symmetry and explained the diagnostic methods using the inversion eigenvalue. Then, as a natural conjecture, we expect to be able to examine other crystalline symmetry eigenvalues, such as rotations, mirrors, and so on, to give a more detailed and versatile diagnostic method. The symmetry-based indicator is based on this idea. First, we review in what system the symmetry-based indicator can be defined and how it is given in the system. After that, we summarize how to use it practically. Previous diagnostic methods have been obtained by showing that the topological invariants, which had already been known, can be written using inversion eigenvalues. To derive the symmetry-based indicator, on the other hand, we assume that the combination of the crystalline eigenvalues of the occupied band classifies the topological class of the system. Hence, it is not immediately clear what specific topological invariants and what topological properties each given class has. However, subsequent studies [49, 50] have mapped from the indicators to specific topological invariants, and today the explicit properties of each class are somewhat known.

Note that in this section, we also consider systems with significant SOC.

Idea of the symmetry-based indicator

The idea of the symmetry-based indicator is as follows. Firstly, we choose a space group. Then, we define the set of band structures {BS} and the set of atomic insulators {AI} in that space group. A schematic picture is shown in Fig. 1.9. {AI} is a subgroup of {BS}, as explained later. The topological classes classified by the symmetry-based indicator are given as a quotient group of them as

$$\{\mathrm{BS}\} \, / \, \{\mathrm{AI}\}, \tag{1.8}$$

which means

- If an element of {BS} is included in {AI}, it is trivial.

- All other elements are nontrivial.

- For two nontrivial elements of {BS}, we check the difference between them. Then, if the difference is written with an element of {AI}, the two nontrivial elements of {BS} are defined to be in the same topological class.

Some detailed notes are given in Appendix A.4.
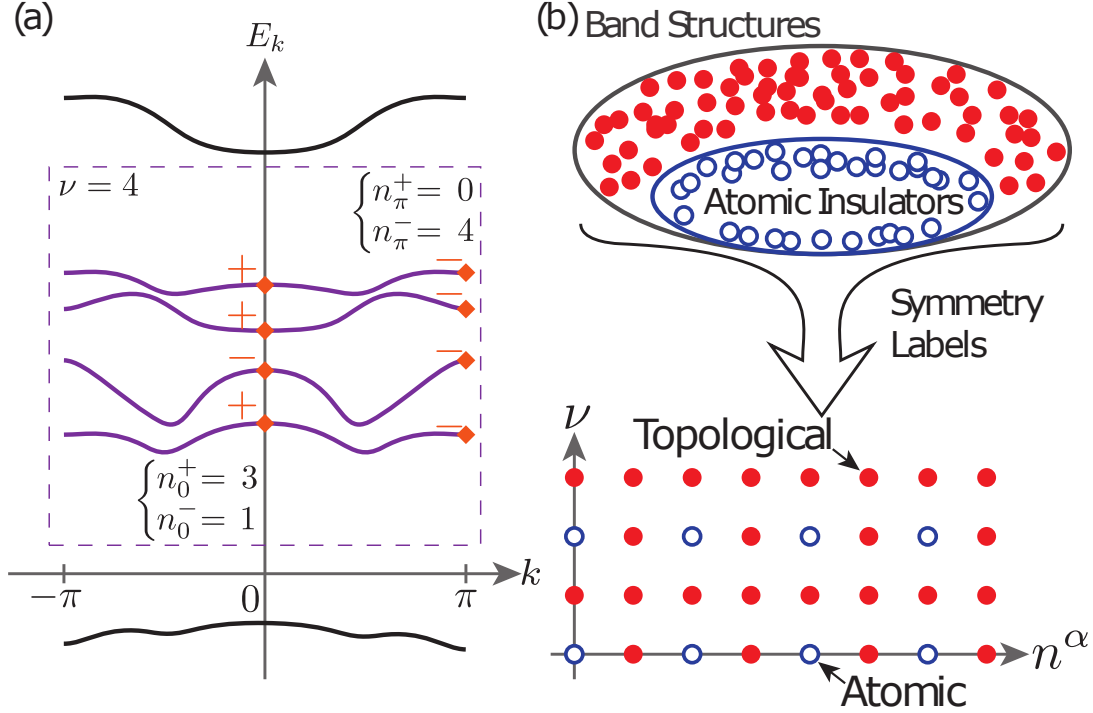
Figure 1.9. Figure adopted from H. C. Po, *et. al.*, Nature communications **8**, 50 (2017). (a) shows how to convert a band dispersion into the symmetry label. (b) is a schematic picture to show the algebraic structure of the derivation of the indicator.

Definition of {BS}

A set "band structures ({BS})" (of some space group) is defined as a set of all the possible occupied bands[6] that satisfy the following "compatibility condition". The number of the occupied bands can be different for each element. The compatibility condition means

$$\forall \boldsymbol{k} \in \{\text{All high symmetry points, lines, and planes in BZ}\}, \quad E_{j+1}(\boldsymbol{k}) > E_j(\boldsymbol{k}), \quad (1.9)$$

where the l-th band ($l \leq j$) is occupied, and the l'-th band ($l' > j$) is unoccupied. Note that this condition does not strictly require the system to be insulator as explained in section 1.1. But for convenience, we refer to the lower j bands as "occupied bands" in this dissertation.

The word "compatibility condition" is originally a rule for connecting bands in momentum space [56]. Since an energy band is continuous while the symmetry eigenvalues are discrete, the connected bands must have the same symmetry eigenvalue from one end to the other end of a high symmetry line or a high symmetry plane. For example, let us assume two high symmetry points Γ and X, and a C_2 rotation[7] high symmetry line

---

[6]The elements of {BS} are not restricted by a realistic material properties. For example, it includes the case where a p orbital is occupied but no s orbital is occupied.

[7]The C_2 rotation means a π rotation. The definitions of the symmetry operations are given in Appendix A.1

(a)

Compativility
condition
satisfied

(b)

Compativility
condition
satisfied

(c)

Compativility
condition
violated
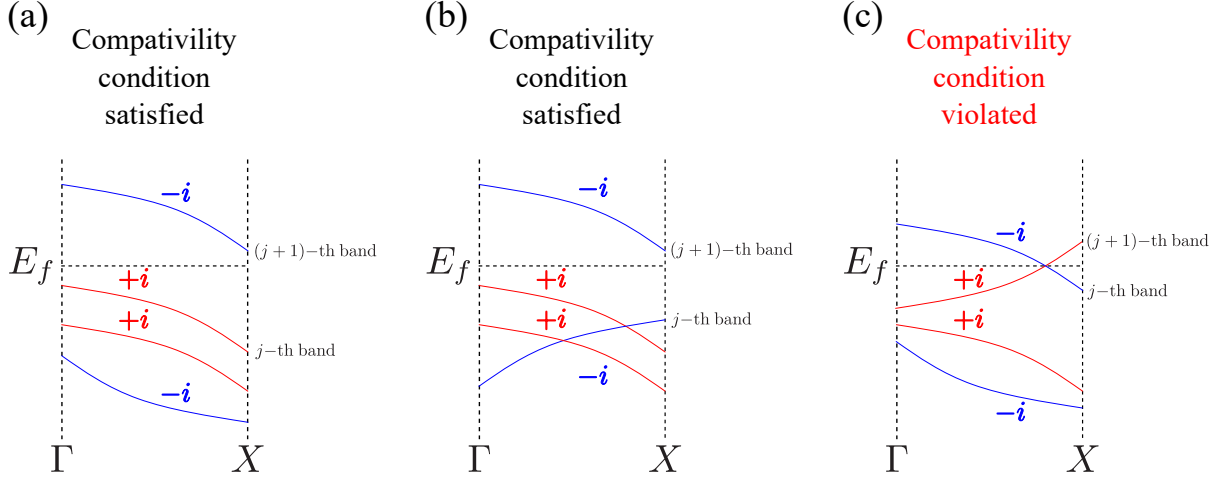
Figure 1.10. Compatibility condition in C_2 rotation invariant line. Here $\pm i$ is the C_2 eigenvalue for the wavefunction of the corresponding band. (a)(b) Due to the compatibility condition, the number of bands with $+i$ $(-i)$ is constant. (c) When the compatibility condition is violated, the system is gapless.

Γ-X [Fig. 1.10]. In a spinful system, a C_2 eigenvalue[8] is $\pm i$. In the cases of Fig. 1.10 (a) and (b), the compatibility condition is satisfied, while in the case of Fig. 1.10 (c), it is not satisfied. Due to this compatibility condition, the number of bands with $+i$ $(-i)$ is constant at the Γ point, X point, and on the Γ-X line. In the following, we do not consider the case of Fig. 1.10 (c).

Note that this definition focuses only on the high symmetry points, lines, and planes in the momentum space. Therefore, gapless points in generic $\boldsymbol{k}$ are neglected. For example, the Weyl semimetal, whose gapless Weyl nodes generally appear in generic $\boldsymbol{k}$, is defined as "gapped" in this definition.

In order to consider the quotient group Eq. (1.8), an element of {BS}, i.e., a set occupied bands, need to be represented in such a way that the addition and subtraction of them are well defined. Therefore, we focus on the symmetry eigenvalues and represent the elements of {BS} as a vector, which is called "symmetry label". In general, space groups have multiple crystalline symmetry operations, so we use the irreducible representations (irreps) instead of the symmetry eigenvalues. The irreps are understood as a generalized conception of the symmetry eigenvalues (See Appendix A.2 for the detail).

Given a set of occupied bands, we check their irreps at each high symmetry point, line, and plane. By counting how many times an irrep appears and listing the result for each irrep, the symmetry label is obtained.

For example, let us see the case of the space group 2, which has only the inversion symmetry. In this case, there are eight high symmetry points (TRIM), and no high symmetry line and plane. We name the TRIM as Γ, X, Y, Z, T, U, V, and R [Fig. 1.11] (the standard name of the high symmetry points is found in [57]). In all points, two irreps are defined, one with a $+1$ inversion eigenvalue and the other with a -1 inversion

---

[8]Since the spin part is transformed by a representation of $SU(2)$, a 2π rotation gives -1 to the spin part $(C_2{}^2 = -1)$. This is originated from the algebraic structure $SU(2)/SO(3) = \mathbb{Z}_2$. In a spinless system, on the other hand, $C_2{}^2 = 1$ and thus a C_2 eigenvalue is ± 1.
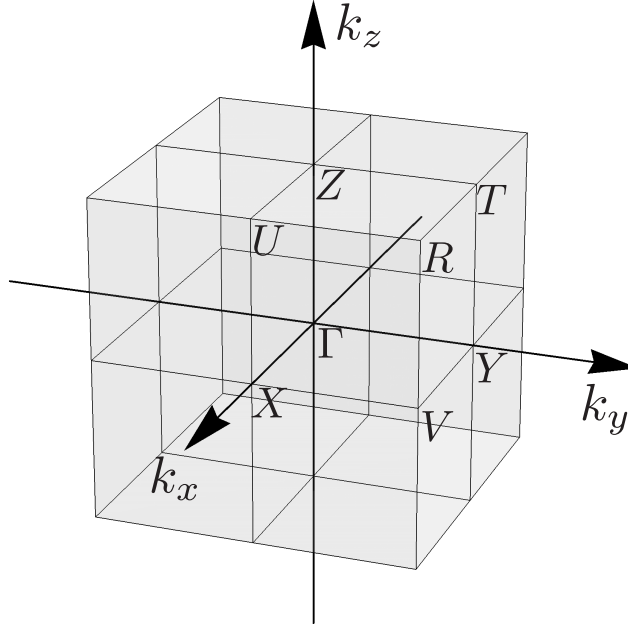
Figure 1.11. 8 TRIM in the BZ of the space group 2.

eigenvalue. For a set of occupied bands, let n_Γ^+ (n_Γ^-) be the number of bands with $+1$ (-1) eigenvalue at the Γ point. By applying the same definition to the other points, the result is summarized as

$$\left(n_\Gamma^+, n_\Gamma^-, n_X^+, n_X^-, n_Y^+, n_Y^-, n_Z^+, n_Z^-, n_T^+, n_T^-, n_U^+, n_U^-, n_V^+, n_V^-, n_R^+, n_R^-\right). \qquad (1.10)$$

The length is 16. However, when the number of occupied bands is j, $n_\Gamma^+ + n_\Gamma^- = j$ must be satisfied, and so on. Consequently, the set of occupied bands, which is an element of {BS}, is represented by a symmetry label

$$\left(j, n_\Gamma^+, n_X^+, n_Y^+, n_Z^+, n_T^+, n_U^+, n_V^+, n_R^+\right). \qquad (1.11)$$

In general space groups, the compatibility condition (eigenvalue connectivity) restricts the independent components. Using this representation, {BS} is extended to a linear space. (This extension involves some complicated problems and they are discussed in Appendix A.4.2.)

Note that topologically identical occupied bands as defined in section 1.1 are represented by the same symmetry label. For example, the symmetry label does not depend on the energy sequence within the occupied bands, which has nothing to do with the topological classification.

Definition of {AI}

Next, we define the set of {AI} in a specified space group. The idea of {AI} is that if an element of {BS} is topologically identical with an element of {AI}, we will say the

element of {BS} is trivial. For this purpose, the elements of {AI} should be "clearly trivial band structures". Therefore, we choose an element of {AI} as a set of occupied bands that are flat since they are originate from isolated orbitals (This is why it is called "atomic insulators"). {AI} is also represented by the symmetry label.

A systematical process exists for enumerating the elements of {AI}, and it can be completed in a finite number of trials (See Appendix A.4.2 for the detail). The explicit {AI} for each space group is available in the website Ref. [57].

Explicit symmetry-based indicators and calculation formulas

The elements of the quotient group {BS} / {AI} have periodic structures. In mathematically, it is written as

$$\forall b \in \{\mathrm{BS}\} / \{\mathrm{AI}\}, \ \exists n \in \mathbb{Z}, \ \mathrm{s. \ t.} \ nb \in \{\mathrm{AI}\}, \tag{1.12}$$

where nb is defined as $nb = \sum_{j=1}^{n} b$. The symmetry-based indicator is given as a $\mathbb{Z}_n$-valued index from this periodic structure. In general space groups, the periodic structure can exist in two or more dimensions. The symmetry-based indicators of each space group are summarized in Table 1.5.

The Fu-Kane's $\mathbb{Z}_2$ indices are included in the symmetry-based indicator. The Fu-Kane formula is valid in a system with TR and inversion symmetries. It corresponds to the space group 2, and the symmetry-based indicator in the space group 2 is given as $\mathbb{Z}_2 \times \mathbb{Z}_2 \times \mathbb{Z}_2 \times \mathbb{Z}_4$ in Table 1.5. The former three $\mathbb{Z}_2$ are weak indices, and the $\mathbb{Z}_4$ includes the strong index. The symmetry-based indicator has shown that there are subdividing topological classes beyond the Fu-Kane's strong index in TR and inversion symmetric systems.

The calculation formula of the indicators are given in Ref. [49] (The tables are also given in Appendix A.4.3). All of the indicators in Table 1.5 are calculated by checking only the high symmetry points in the BZ. As explained before, the symmetry-based indicator cannot predict specific topological invariants on its own but the Ref. [49] have mapped the indicators into explicit topological invariants such as strong index, weak index, mirror Chern number, and so on. Hence, today by calculating the symmetry-based indicator we can diagnose the topological properties of a system. The explicit workflow is detailed in the next section. Since the symmetry-based indicator can be calculated by checking only the high-symmetry points in the BZ, it has allowed high-throughput materials search [58, 59, 60, 61].

Note that although the symmetry-based indicator is comprehensive and diagnoses a wide range of topological classes, it is not the perfect diagnostic method. For example, as we can see in the Ref. [49], some systems with a nontrivial mirror Chern number are diagnosed as trivial by the symmetry-based indicator. Not only that, a topological class characterized by the indicator can have two or more possible combinations of topological invariants. If we need to distinguish them, a diagnostic method beyond the symmetry-based indicator is required. This is one of the purposes of this dissertation.

Table 1.5: Symmetry-based indicators of band topology for systems with time-reversal symmetry and significant SOC adopted from H. C. Po, *et. al.*, Nature communications **8**, 50 (2017).

X_{BS}	Space groups
$\mathbb{Z}_2$	81, 82, 111, 112, 113, 114, 115, 116, 117, 118
	119, 120, 121, 122, 215, 216, 217, 218, 219, 220
$\mathbb{Z}_3$	188, 190
$\mathbb{Z}_4$	52, 56, 58, 60, 61, 62, 70, 88, 126, 130
	133, 135, 136, 137, 138, 141, 142, 163, 165
	167, 202, 203, 205, 222, 223, 227, 228, 230
$\mathbb{Z}_8$	128, 225, 226
$\mathbb{Z}_{12}$	176, 192, 193, 194
$\mathbb{Z}_2 \times \mathbb{Z}_4$	14, 15, 48, 50, 53, 54, 55, 57, 59, 63, 64, 66
	68, 71, 72, 73, 74, 84, 85, 86, 125, 129, 131, 132
	134, 147, 148, 162, 164, 166, 200, 201, 204, 206, 224
$\mathbb{Z}_2 \times \mathbb{Z}_8$	87, 124, 139, 140, 229
$\mathbb{Z}_3 \times \mathbb{Z}_3$	174, 187, 189
$\mathbb{Z}_4 \times \mathbb{Z}_8$	127, 221
$\mathbb{Z}_6 \times \mathbb{Z}_{12}$	175, 191
$\mathbb{Z}_2 \times \mathbb{Z}_2 \times \mathbb{Z}_4$	11, 12, 13, 49, 51, 65, 67, 69
$\mathbb{Z}_2 \times \mathbb{Z}_4 \times \mathbb{Z}_8$	83, 123
$\mathbb{Z}_2 \times \mathbb{Z}_2 \times \mathbb{Z}_2 \times \mathbb{Z}_4$	2, 10, 47

X_{BS}: the quotient group between the group of band structures and atomic insulators.

Diagnosis workflow

Finally, we show a practical way to use the symmetry-based indicator. Although the derivation of the symmetry-based indicator is too complicated, we can skip it in practice by using some tables given by previous studies. Now we discuss a case of a 3D system with TR symmetry and SOC.

Suppose a band dispersion and wavefunctions of a system are given. Mainly the case given by the first-principles calculation is assumed, but it works in cases such as a tight-binding model too. The workflow is given as following.

1. Identify the space group of the system.

2. Decide which bands to calculate.

3. Confirm that the bands satisfy the compatibility condition.

4. Check the irreps of the bands at high symmetry points.

5. Check and calculate the indicator with the Supplementary Table 1, 2, and 3 in Ref. [49].

6. Find the obtained class in the Supplementary Table 7 in Ref. [49] and check the topological invariants.

Let us describe each step in more detail.

Step 1 We have to know what space group the target system belongs to since the symmetry-based indicator is individually defined in each space group. For most cases, previous studies have given a space group. Or, VESTA [62] supports to find it.

Step 2 We decide on which bands we calculate the indicator. Usually, occupied bands are chosen. Even if the system is not an insulator, we can take lower j bands to calculate. We can neglect core electron bands in the low energy area because they have nothing to do with the topological properties unless it is a very insane system.

Step 3 In principle, we need to confirm the chosen bands satisfy the compatibility condition. However, in practice, we do not need to seriously check the compatibility condition. If the system violates the compatibility condition, the resulting indicator will be an unreasonable value, such as fractions or prohibited values[9]. Therefore, we can skip this step, and if we get something wrong we can come back here[10].

---

[9]For example, in the space group 225, the indicator $\mathbb{Z}_8$ is defined but odd numbers are prohibited. If we have $\mathbb{Z}_8 = 1$, we cannot find the corresponding class in the step 6 and we can realize something is wrong.

[10]If we try to check the compatibility condition, it can be relatively easily done by first-principles calculations. A band dispersion is usually plotted along high symmetry lines, and thus a gapless point is often found easily if exists.

Step 4 We list the irreps of the chosen bands for all high symmetry points. Since the formula to calculate the indicator is written only with irreps of high symmetry points, we need not check high symmetry lines and planes. An irrep analysis option is implemented in QUANTUM ESPRESSO [63], and other program packages also support to list irreps (see Appendix A.6).

Step 5 We first see the Supplementary Table 3 in Ref. [49] (or Table A.3) to know the indicator defined in the space group of the target system. If the space group is not listed in the Supplementary Table 3 in Ref. [49], it means that there is no topological band dispersion in the space group. If the space group is listed with an indicator, we can find the explicit calculation formula in the Supplementary Table 1 and 2 in Ref. [49] (or Table A.4 and A.5). Using these tables, we can obtain the symmetry-based indicator of the target system.

Step 6 We identify the topological invariants from the obtained indicator. In the Supplementary Table 7 in Ref. [49], the indicators of each space group are mapped to topological invariants. By referring to the part of the target space group, we can know what kind of topological invariants can be nontrivial. Note that the topological invariants are not necessarily identified uniquely. Generally, for a single value of the symmetry-based indicator, there are several candidates of topological invariants. Those candidates are not distinguished within the symmetry-based indicator. If we need a more detailed diagnosis, a more detailed analysis is required.

Finally, note that we can access a material database [64] that provide the symmetry-based indicator. The accuracy is not necessarily guaranteed, but this database is often useful for checking quickly.

1.3 Diagnostic methods for topological semimetals

In section 1.2, we have reviewed the diagnostic methods of topological insulators. Among them, the Fu-Kane formula and the symmetry-based indicator have been given in systems with TR symmetry and significant SOC. In this section, we next review diagnostic methods in systems with TR symmetry and negligible SOC. In those systems, diagnostic methods mainly work to diagnose nodal line semimetals. To stabilize such nodal lines, inversion symmetry is additionally required [41, 65]. Therefore, the diagnostic methods we review in this section are given for systems with TR and inversion symmetries, and negligible SOC.

First, we review a diagnostic method that is given by applying the symmetry-based indicator [47]. However, only limited nodal line semimetals are diagnosed by this method [Fig. 1.12]. Materials that have been proposed or have been experimentally studied cannot be diagnosed by this method. Hence, some expanded methods have been proposed and we review them next [43, 66].
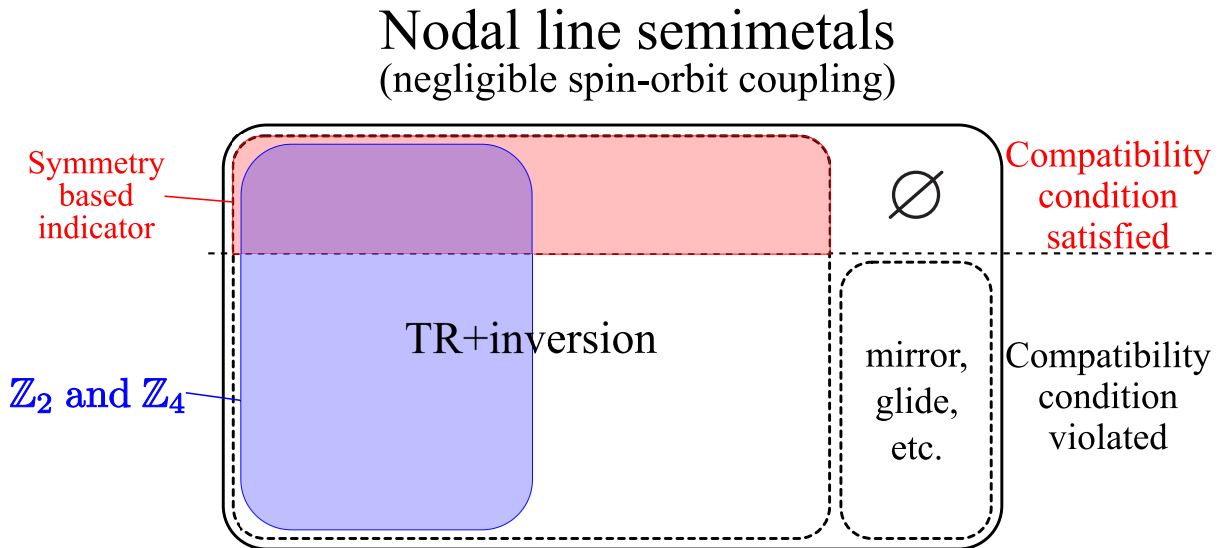
Figure 1.12. Variety of nodal line semimetals in systems with negligible SOC.

1.3.1 Symmetry-based indicator for nodal line semimetals

We can apply the symmetry-based indicator to diagnose nodal line semimetals [47]. The derivation is simple: just redo the derivation of the symmetry-based indicator in the case where SOC is negligible. Here in the systems with negligible SOC, we neglect the spin degree of freedom.

Looking back at the derivation process of the symmetry-based indicator, the compatibility condition is required. Since nodal line semimetals have gapless points by definition, the compatibility condition (Eq. (1.9)) is rewritten as

- At all high symmetry points, lines, and planes, there is no gapless point between E_{j+1} and E_j with different irreps.

Due to this condition, the system mostly need to be gapped at the high symmetry points, lines, and planes, but a gapless point between two bands with the same irreps is allowed as an exception. Such a gapless point can appear on a high symmetry plane. Note that the exception does not break the uniqueness of the symmetry label. All other parts of the derivation are the same as the case with significant SOC. Because of this condition, nodal line semimetals diagnosed by this method inevitably has a nodal line at generic points of the momentum space[11].

The symmetry-based indicator in systems with TR and negligible SOC is given in Table 1.6.

Table 1.6: Symmetry-based indicators of band topology for systems with time-reversal symmetry and negligible SOC adopted from H. C. Po, *et. al.*, Nature communications **8**, 50 (2017).

X_{BS}	Space groups
$\mathbb{Z}_2$	3, 11, 14, 27, 37, 48, 49, 50, 52, 53, 54
	56, 58, 60, 66, 68, 70, 75, 77, 82, 85
	86, 88, 103, 124, 128, 130, 162, 163, 164, 165
	166, 167, 168, 171, 172, 176, 184, 192, 201, 203
$\mathbb{Z}_2 \times \mathbb{Z}_2$	12, 13, 15, 81, 84, 87
$\mathbb{Z}_2 \times \mathbb{Z}_4$	147, 148
$\mathbb{Z}_2 \times \mathbb{Z}_2 \times \mathbb{Z}_2$	10, 83, 175
$\mathbb{Z}_2 \times \mathbb{Z}_2 \times \mathbb{Z}_2 \times \mathbb{Z}_4$	2

X_{BS}: the quotient group between the group of band structures and atomic insulators.

Since the inversion symmetry is required to stabilize nodal lines, all nontrivial indicators are defined in space groups with the inversion symmetry. As was the case with significant SOC, the specific nodal line configuration (or shape) of each class is not immediately known. The mapping form indicators to nodal line configurations are given in a subsequent study Ref. [50]. After we get a specific value of the indicator, we can check Table III in Ref. [50] to find a nodal line configuration of the system.

The indicator in systems with negligible SOC is generally quite different from those in systems with significant SOC. It is because the spin degree of freedom changes the

---

[11]The nodal line can penetrate a high symmetry plane but it is not fixed on the plane by the symmetry. Such case is exactly the case where the system has gapless point on a high symmetry plane within the compatibility condition.

gauge group, and thus SOC is strongly related to the availability of hybridization between bands [56]. Consequently, the presence or absence of SOC affects whether the compatibility condition is satisfied or not. A system with (weak) SOC that satisfies the compatibility condition can become, in infinitely small SOC limit, a system that violates the compatibility condition. Although some examples are reviewed in section 1.4, the link between topological classes of systems with significant and negligible SOC has not discussed enough, and to reveal the link is one of the purposes of this dissertation.

As mentioned at the beginning of section 1.3, nodal line semimetals diagnosed by this method is only a limited part of nodal line semimetals. Rather, the majority of nodal line semimetals are of the kind that cannot be diagnosed by this method. For example, ZrSiSe [67, 68, 69], CaAgAs [70, 71, 72], and CaP$_3$ [73, 74], which are widely studied both theoretically and experimentally, do not satisfy the compatibility condition. These nodal line semimetals have been proposed without using diagnostic methods. They have gapless points on high symmetry lines or planes and it is relatively easy to find with the first-principles calculation, where a band dispersion is usually plotted along high symmetry lines. On the other hand, nodal lines at generic points are not easily captured by the first-principles calculation. Therefore, the symmetry-based indicator is a really useful diagnostic method for them, even if they are not the majority.

Although nodal line semimetals that violate the compatibility condition are relatively easy to find with the first-principles calculation, diagnostic methods for them are desired for efficient exploration. In section 1.3.2, we review diagnostic methods for them.

The symmetry based indicator in the space group 83

Before going to the diagnostic methods for nodal line semimetals that violate the compatibility condition, we clarify the indicator of the space group 83 that plays an important role in this dissertation. The space group 83 belongs to the primitive tetragonal crystal and its generators are C_4 rotation, inversion (I), and lattice translations. In Ref. [50], the indicator of the space group 83 is given as three $\mathbb{Z}_2$-valued indices,

$$\delta_2^{+,\pi}, \delta_2^{-,\pi}, \delta_2'. \tag{1.13}$$

The definitions of them are

$$
\begin{aligned}
\delta_2' &= \delta_2^{+,0} - \delta_2^{+,\pi} = \delta_2^{-,0} - \delta_2^{-,\pi} \quad (\text{mod } 2), \\
\delta_2^{+,0} &= n_{\xi=-1}^+(\Gamma) + n_{\xi=-1}^+(M) + n_{\zeta=-1}^+(X) \quad (\text{mod } 2), \\
\delta_2^{-,0} &= n_{\xi=-1}^-(\Gamma) + n_{\xi=-1}^-(M) + n_{\zeta=-1}^-(X) \quad (\text{mod } 2), \\
\delta_2^{+,\pi} &= n_{\xi=-1}^+(Z) + n_{\xi=-1}^+(A) + n_{\zeta=-1}^+(R) \quad (\text{mod } 2), \\
\delta_2^{-,\pi} &= n_{\xi=-1}^-(Z) + n_{\xi=-1}^-(A) + n_{\zeta=-1}^-(R) \quad (\text{mod } 2).
\end{aligned}
\tag{1.14}
$$

Here, $n_{\xi=-1}^+(\Gamma)$ is the number of occupied bands with the C_4 eigenvalue $\xi = -1$ and the mirror eigenvalue $\sigma = +1$ at the Γ point, $n_{\zeta=-1}^+(X)$ is the number of occupied bands with
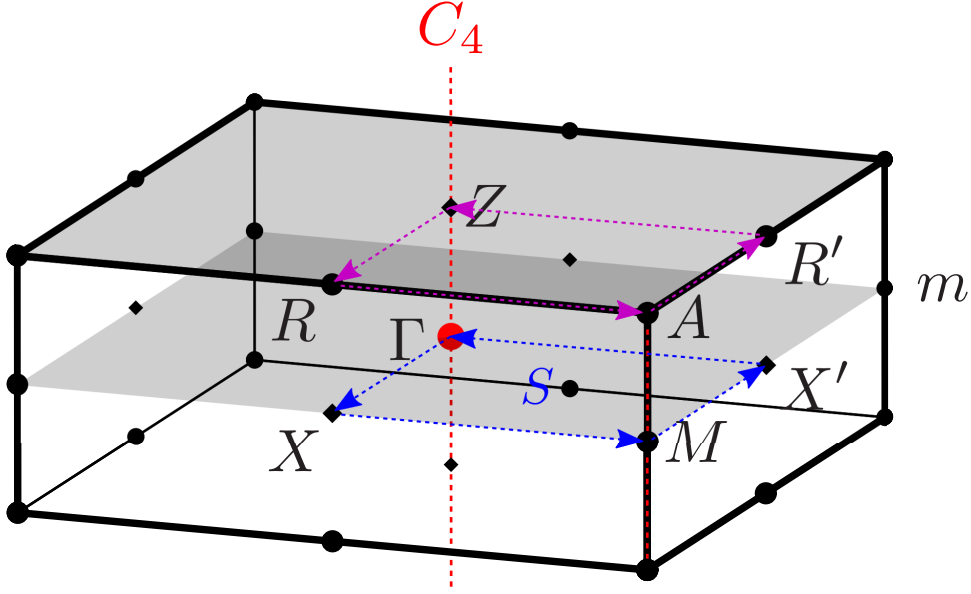
Figure 1.13. Brillouin Zone of the space group 83.

the C_2 eigenvalue $\zeta = -1$ and the mirror eigenvalue $\sigma = +1$ at the X point, and so on [Fig. 1.13].

These indices are interpreted as Berry phases. Generally, a nodal line in a system with negligible SOC is characterized by a π Berry phase [30]. The Berry phase is calculated along a closed loop taken in momentum space. Because a nodal line is interpreted as a π flux of Berry curvature, the Berry phase along the loop is π (mod 2π) when an odd number of nodal lines penetrate the loop. In the space group 83, when $\delta_2^{\pm,0} = 1$, an odd number of nodal lines penetrate the ΓXMX'Γ loop in the $\sigma = \pm 1$ sector, respectively[12] Similarly, $\delta_2^{\pm,\pi}$ is related to the number of nodal lines of the mirror ± 1 sector in the loop ZRAR'Z [Fig. 1.13] (see Appendix A.7.1 for details).

Although four indices are given, the compatibility condition restricts $\delta_2^{+,0} - \delta_2^{+,\pi} = \delta_2^{-,0} - \delta_2^{-,\pi}$ (mod 2). Therefore, there are three independent indices as given in Eq. (1.13).

---

[12]Nodal lines between two bands with different mirror eigenvalues violate the compatibility condition.

1.3.2　Extended methods

In this section, we review diagnostic methods for nodal line semimetals that violate the compatibility condition. The systems with TR and inversion symmetries and negligible SOC are still assumed. In these systems, it is proved that the Fu-Kane formula Eq. (1.7) is used as a diagnostic method [43].

$\mathbb{Z}_2$ index

A condition is required to use the Fu-Kane formula ($\mathbb{Z}_2$ index) in this case instead of the compatibility condition. The condition to use the formula for the lower j bands (occupied bands) is written as

$$\forall \boldsymbol{k} \in \{8 \text{ TRIM}\}, \quad E_{j+1}(\boldsymbol{k}) > E_j(\boldsymbol{k}). \tag{1.15}$$

This condition requires only that the number of occupied bands in the eight TRIM be the same.

As we have reviewed in section 1.3.1, here we use the Berry phase to diagnose nodal line semimetals. As explained in Section 1.2.1, when a loop is taken through four TRIM, the Berry phase along the path can be calculated by the product of the inversion eigenvalues. Note that in this case, the (relevant part of) loop must be inversion-invariant[13]. When the product of inversion eigenvalues of occupied bands in the four TRIM is -1, the loop that goes through the four TRIM is penetrated by an odd number of nodal lines. The independent values of the products of inversion eigenvalue in four TRIM are given almost in the same way as the Fu-Kane formula with 8 TRIM $\boldsymbol{k} = \frac{1}{2}(m_1\boldsymbol{b}_1 + m_2\boldsymbol{b}_2 + m_3\boldsymbol{b}_3)$, $m_{1,2,3} = 0, 1$,

$$
\begin{aligned}
\nu_0 &= \sum_{\boldsymbol{k}:8\text{TRIM}} n^-(\boldsymbol{k}) \pmod 2, \\
\nu_1 &= \sum_{\substack{\boldsymbol{k}:4\text{TRIM} \\ m_1=1}} n^-(\boldsymbol{k}) \pmod 2, \\
\nu_2 &= \sum_{\substack{\boldsymbol{k}:4\text{TRIM} \\ m_2=1}} n^-(\boldsymbol{k}) \pmod 2, \\
\nu_3 &= \sum_{\substack{\boldsymbol{k}:4\text{TRIM} \\ m_3=1}} n^-(\boldsymbol{k}) \pmod 2,
\end{aligned}
\tag{1.16}
$$

where $n^-(\boldsymbol{k})$ is the number of occupied bands with -1 inversion eigenvalues in $\boldsymbol{k}$ [14]. If any one of the $(\nu_0; \nu_1\nu_2\nu_3)$ is 1, the system is a nodal line semimetal. However, even if all of them are 0, the system can be a nodal line semiemtal with an even number of nodal lines. The nodal line configuration in the BZ corresponds to which index is 1. For example, a system with a nodal line like Fig. 1.14 has $(\nu_0; \nu_1\nu_2\nu_3) = (1; 110)$ (see Appendix A.7.2 for details). In Ref. [43], Cu_3NZn and Cu_3NPd have been given as material examples of nodal line semimetals with nontrivial $\mathbb{Z}_2$ indices [Figs. 1.15,1.16].

---

[13]The inversion symmetry is used to transform $\int_{-\pi}^{\pi} dk$ into $\int_0^{\pi} dk$.

[14]Note that $n^-(\boldsymbol{k})$ is NOT "the number of pairs of bands" because the spin degree of freedom is neglected. This is the only difference from the original Fu-Kane formula.
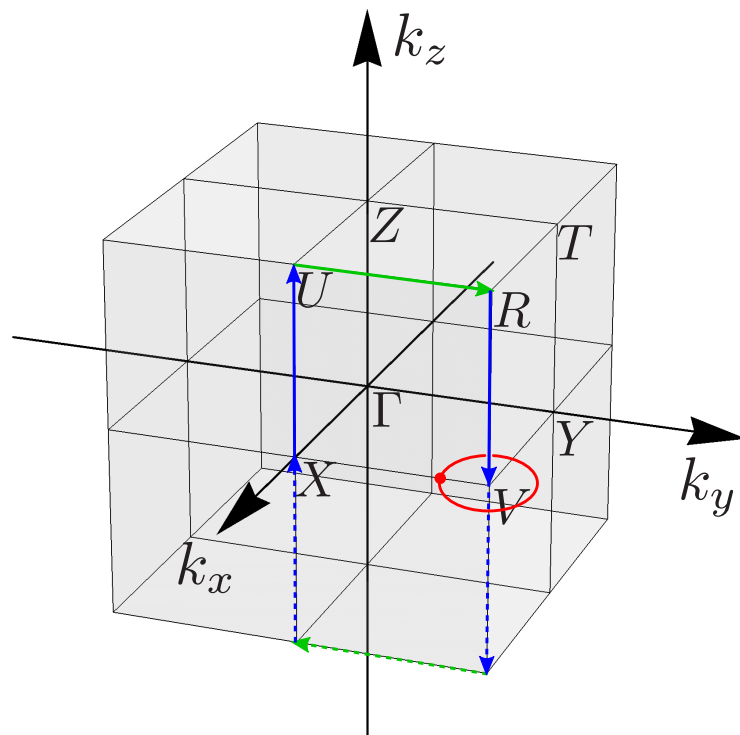
Figure 1.14. Nodal line semimetal with $(\nu_0; \nu_1\nu_2\nu_3) = (1; 110)$. The TR-invariant path through $XURV$ correpdonds to ν_1.
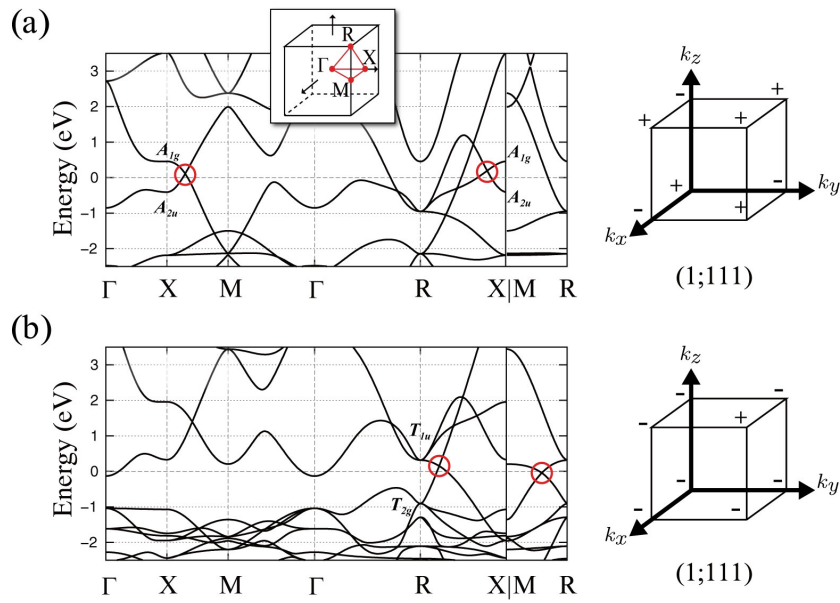
Figure 1.15. Band dispersions and $\mathbb{Z}_2$ indices of nodal line semimetals (a) Cu_3NZn and (b) Cu_3NPd adopted from Y. Kim, *et. al.*, Physical Review Letters **115**, 036806 (2015).
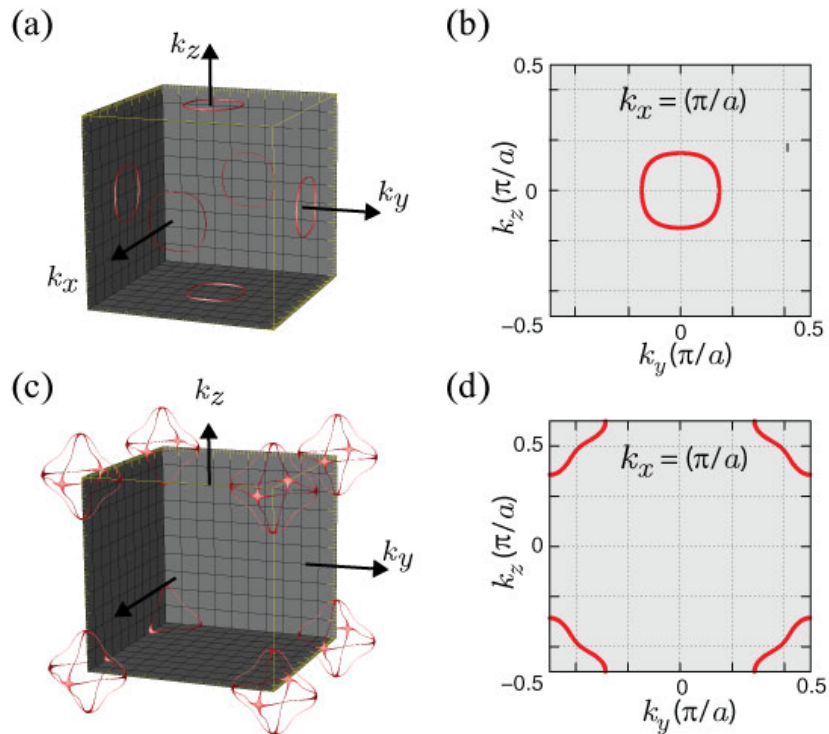
Figure 1.16. BZ and nodal lines in (a)(b) Cu_3NZn and (c)(d) Cu_3NPd adopted from Y. Kim, *et. al.*, Physical Review Letters **115**, 036806 (2015).

$\mathbb{Z}_4$ index

In terms of symmetry of the space group of the system, the Fu-Kane formula requires only the inversion symmetry. The most simple space group with the inversion symmetry is space group 2. Looking at the symmetry-based indicator in Table 1.6, $\mathbb{Z}_2 \times \mathbb{Z}_2 \times \mathbb{Z}_2 \times \mathbb{Z}_4$ is defined in the space group 2. Although this is the case where the compatibility condition is satisfied, it is suggested that the strong index ν_0 for nodal line semimetals can be extended[15] to $\mathbb{Z}_4$. Based on this idea, a subsequent study [66] has succeeded in extending to $\mathbb{Z}_4$.

The $\mathbb{Z}_4$ index is defined as

$$\mathbb{Z}_4 = \sum_{\boldsymbol{k}:8\mathrm{TRIM}} n^-(\boldsymbol{k}) \pmod 4. \tag{1.17}$$

From the definition, $\nu_0 \equiv \mathbb{Z}_4 \pmod 2$. Therefore, $\mathbb{Z}_4 = 1, 3$ are nodal line semimetals with $\nu_0 = 1$, and there is a newly defined topologically nontrivial class $\mathbb{Z}_4 = 2$. The Ref. [66] has shown that the $\mathbb{Z}_4 = 2$ systems are nodal line semimetals with monopole charged[16] nodal lines [30] when $\nu_1 = \nu_2 = \nu_3 = 0$[17]. Since a nodal line in a system with $\mathbb{Z}_4 = 1, 3$ has no monopole charge, an inherently different type of nodal line semimetal is diagnosed by $\mathbb{Z}_4 = 2$. In Ref. [66], $MoTe_2$ have been given as a material example with $\mathbb{Z}_4 = 2$ [Fig. 1.17].

Since $\mathbb{Z}_4$ includes ν_0, the diagnostic method of inversion symmetric systems is summarized in $(\mathbb{Z}_4; \nu_1 \nu_2 \nu_3)$. These four indices are equivalent to the symmetry-based indicator in the space group 2 without SOC [Table 1.6]. The Refs. [43, 66] have shown that these indices can be used for all space groups with the inversion symmetry.

$\mathbb{Z}_4$	Nodal line seimmetal
0	Indeterminate
1	Nodal line semimetal without monopole charge
2	Nodal line semimetal with monopole charge
3	Nodal line semimetal without monopole charge

Table 1.7: $\mathbb{Z}_4$ index and corresponding nodal line semimetals.

---

[15]$\nu_{1,2,3}$ are equivalent. If only one is extended, it should be ν_0.

[16]This "monopole charge" is $\mathbb{Z}_2$-valued but different from the Berry phase. The Berry phase is defined as an integral on a loop in the momentum space (a 1D topological invariant). On the other hand, the monople charge is defined on a closed surface in the momentum space (a 2D topological invariant).

[17]When $\nu_1 = \nu_2 = \nu_3 = 0$, the $\mathbb{Z}_4 = 2$ originates from a double band inversion at a single TRIM.
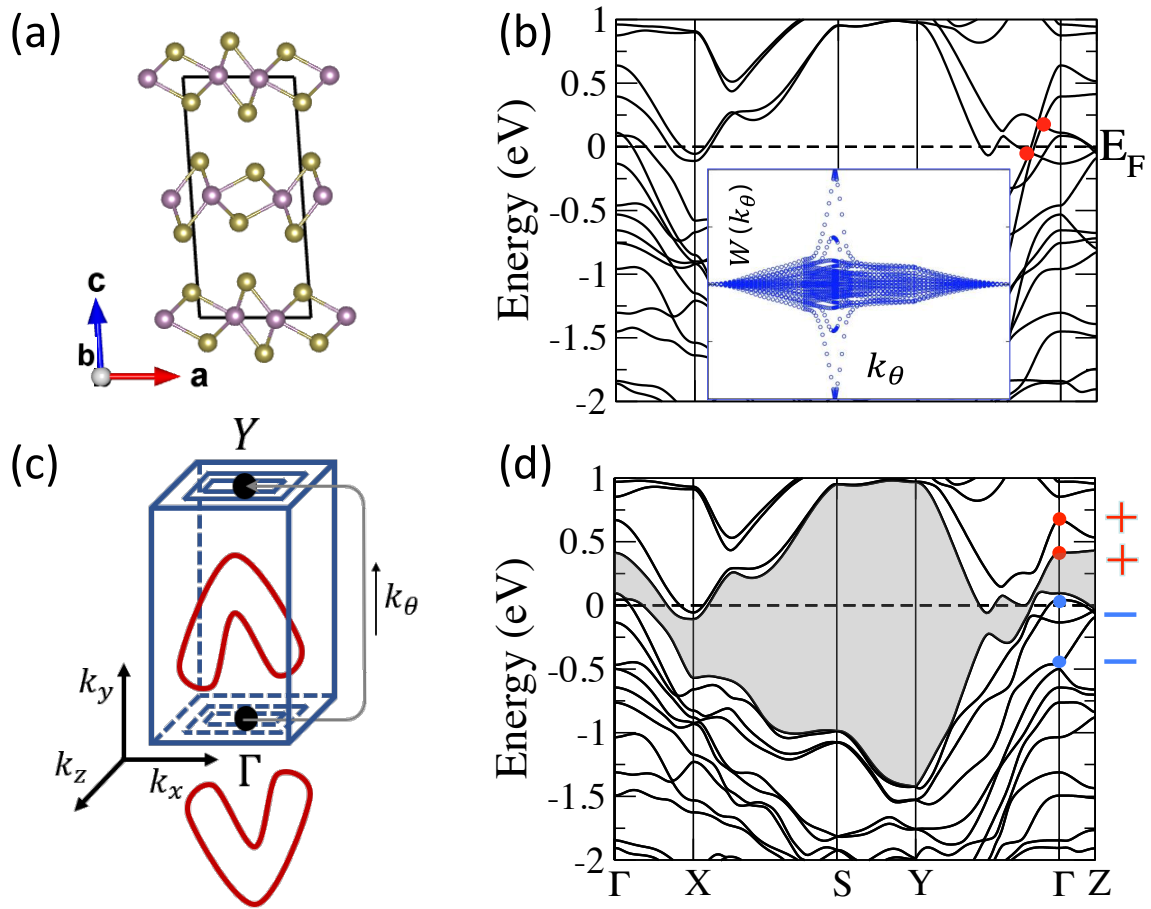
Figure 1.17. Band dispersion and monopole charged nodal lines in MoTe$_2$ as an example of the system with $\mathbb{Z}_4 = 2$ adopted from Z. Wang, *et. al.*, Physical Review Letters **123**, 186401 (2019). (b)(d) A double band inversion occurs at the Γ point and (c) monopole charged nodal lines appear around the Γ point (red lines).

As a summary, the $\mathbb{Z}_4$ index and corresponding nodal line semimetals are listed in Table 1.7 ($\nu_1 = \nu_2 = \nu_3 = 0$ is assumed).

1.4   Intrinsic link between topological insulators and semimetals

In section 1.2 and 1.3, we have reviewed the diagnostic methods of topological insulators and nodal line semimetals independently. The former is discussed in systems with significant SOC, while the latter is in systems with negligible SOC.

Some previous studies have proved that, in some examples, a topological semimetal turns to a topological insulator when SOC is introduced. One of the typical example is graphene [75, 76]. Graphene has Dirac-cone-like point nodes at the high symmetry points when SOC is negligible. When SOC is introduced in graphene, the point nodes get gapped and the system becomes a topological insulator[18].

A similar link can be found between diagnostic methods of topological insulators and nodal line semimetals. As we can see the $\mathbb{Z}_2$ index for TR protected 3D topological insulator (Eq. (1.7)) and the $\mathbb{Z}_2$ index for nodal line semimetals (Eq. (1.16)) are defined almost identically, there is an intrinsic link between topological insulators and nodal line semimetals in inversion symmetric systems. Since the inversion operation does not affect the spin (or pseudospin) part of wavefunctions, the inversion eigenvalue comes from the orbital (or sublattice) part of wavefunctions (Eq. (1.18)).

$$
\begin{aligned}
I\psi = \chi\psi \ &\Rightarrow\ I\psi\alpha = \chi\psi I\alpha = \chi\psi\alpha \\
\psi\alpha \quad &: \quad \text{wavefunction} \\
\psi \quad &: \quad \text{orbital/sublattice part} \\
\alpha \quad &: \quad \text{spin part} \\
\chi \quad &: \quad \text{inversion eigenvalue of orbital part}
\end{aligned}
\tag{1.18}
$$

Therefore, when (weak[19]) SOC is introduced, the inversion eigenvalues of occupied bands are the same as that of when SOC is neglected. Additionally, a nodal line protected by TR and inversion symmetry is generally get gapped when SOC is introduced. From these facts, it can be said that a nodal line semimetal with nontrivial $\mathbb{Z}_2$ index turns into a (TR protected) topological insulator with the same nontrivial $\mathbb{Z}_2$ index [Fig. 1.19].

Not only the Fu-Kane index $(\nu_0; \nu_1\nu_2\nu_3)$, $\mathbb{Z}_4 = 2$ class has a similar link. When SOC is negligible, the $\mathbb{Z}_4 = 2$ class is a monopole charged nodal line semimetal. Looking at the space group 2 with significant SOC in Table 1.5, $\mathbb{Z}_4$ is defined and the $\mathbb{Z}_4 = 2$ class is found to be a higher-order topological insulator protected by the inversion symmetry [77]. From these facts, a monopole charged nodal line semimetal with $\mathbb{Z}_4 = 2$ is expected to be linked to a higher-order topological insulator with $\mathbb{Z}_4 = 2$, and the correctness of this speculation has been demonstrated in MoTe$_2$ [66].

---

[18]Experimentally, the introduction of SOC is realized by decorating Bi$_2$Te$_3$ nanoparticles on graphene [76]

[19]Grnerally, SOC brings about an energy shift in each band. Due to the energy shift, a band inversion can occur between occupied bands and unoccupied bands. Such band inversion generally changes the inversion eigenvalues of occupied bands. However, such a band inversion never occurs in a weak SOC limit since there is a finite gap between occupied bands and unoccupied bands in the zero SOC case.
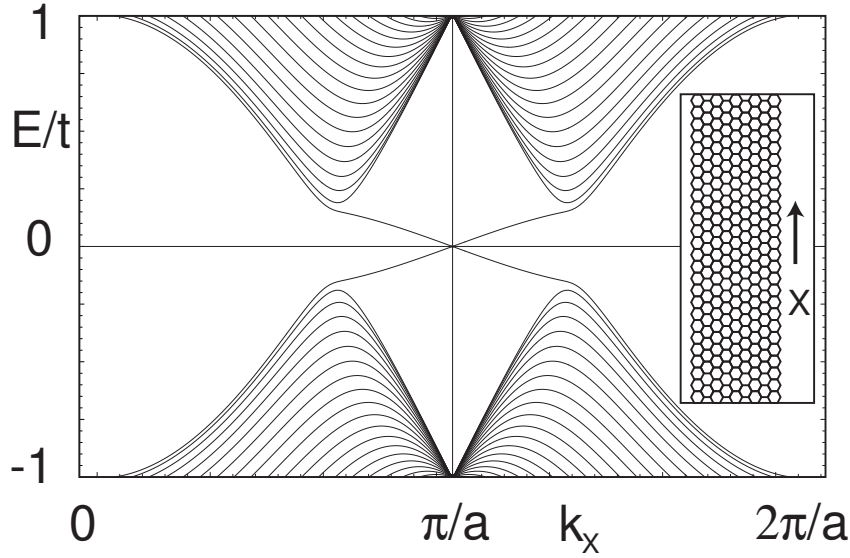
Figure 1.18. Bnad dispersion and edge states in a graphene ribbon with SOC adopted from C. L. Kane, and E. J. Mele, Physical Review Letters **95**, 226801 (2005).

As a summary, it is known that there is an intrinsic link between a nodal line semimetal and a (higher-order) topological insulator characterized by $(\mathbb{Z}_4; \nu_1\nu_2\nu_3)$ [Fig. 1.19].

For the symmetry-based indicator in systems with significant and negligible SOC, the intrinsic link has not been comprehensively discussed. It is because, as is explained, the symmetry-based indicator is independently defined in both cases, and thus the equivalence of the indicators is not as clear as the $\mathbb{Z}_2$ and $\mathbb{Z}_4$. Some case studies are given in Ref. [50], and we can see a nodal line semimetal with a nontrivial indicator is linked to a topological insulator with some nontrivial indicator at least within the case studies.

This means that the band inversion is an amplitude-dependent phenomenon and we can neglect it within the discussion of the link between topological classes.

$\mathbb{Z}_4$	0	1	2	3
ν_0	0	1	0	1

Real space

Significant spin-orbit coupling

TI   HOTI   TI

spin-orbit coupling ON

spin-orbit coupling OFF

Momentum space

Negligible spin-orbit coupling

Nodal line semimetal

Monopole charged nodal line semimetal

Nodal line semimetal
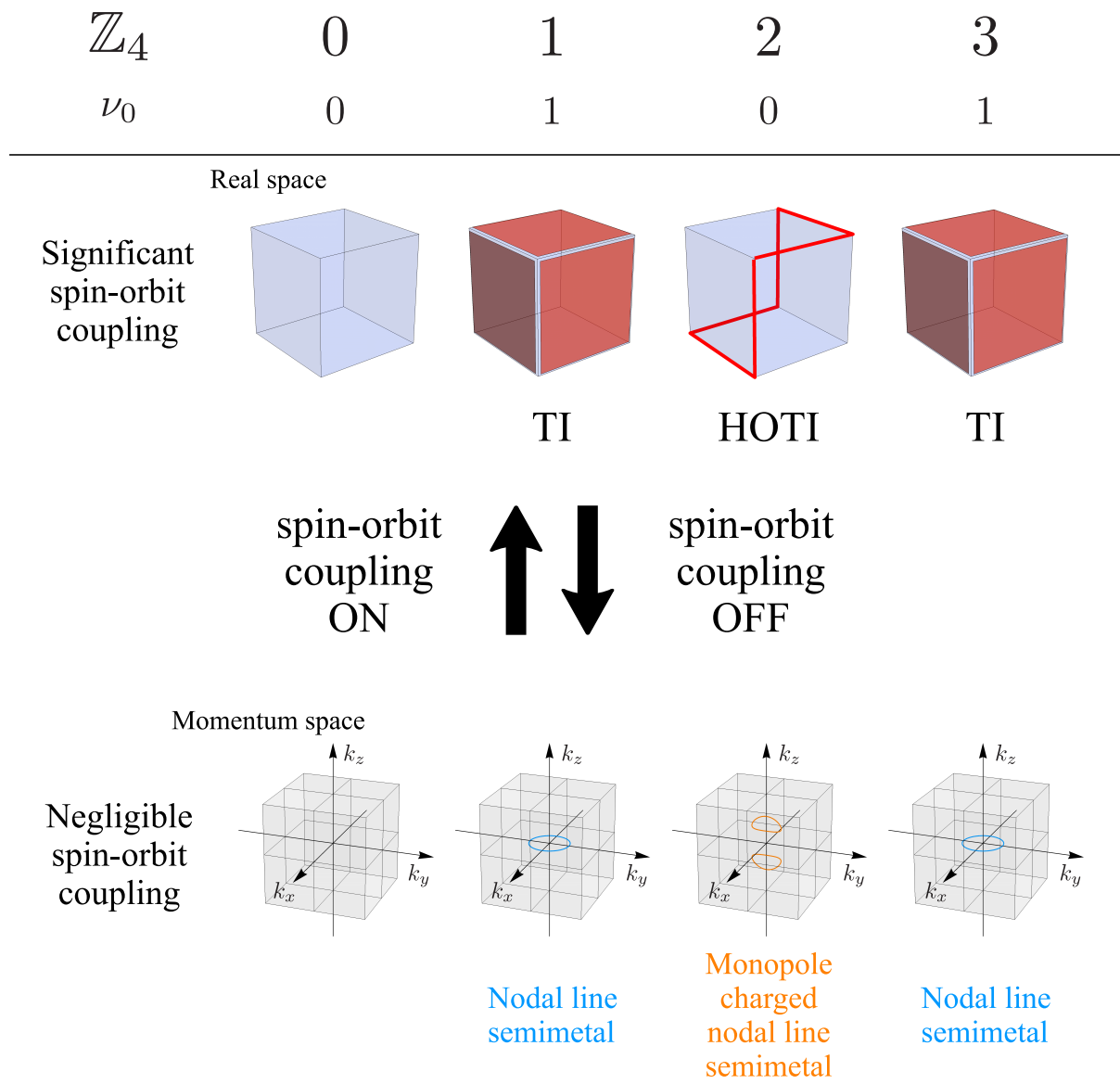
Figure 1.19. Intrinsic link between $\mathbb{Z}_4$ characterized topological insulators and nodal line semimetals.

Chapter 2

Motivation of this dissertation

The diagnostic methods given in previous studies are not a complete method, and there is room for improvement. For example, in the diagnostic methods for topological insulators, the $\mathbb{Z}_8 = 0$ class (considered to be "trivial") in the space group 225 (face centered cubic, FCC) contains a topological crystalline insulator[1] [Table 2.1]. This means some topological crystalline insulators are overlooked in the previous methods. Likewise, two topological crystalline insulators with different topological invariants are classified in the same class $\mathbb{Z}_8 = 4$. This difference results in different physical properties that are important when considering applications. The surface state emerges only on a particular surface in topological crystalline insulators, and the surface is determined by which mirror Chern number is nontrivial. Therefore, topological crystalline insulators with different mirror Chern numbers have different properties, such as compatibility with the symmetry of a substrate. To realize a more detailed and useful materials search, diagnostic methods to distinguish those topological classes easily are desired.

Space group #225 : $Fm\bar{3}m$			
$\mathbb{Z}_8$	weak	$n_{\mathcal{M}_{(001)}}$	$n_{\mathcal{M}_{(110)}}$
0	000	0	0
0	000	4	2
4	000	0	2
4	000	4	0

Table 2.1: Possible topological invariant combinations for $\mathbb{Z}_8 = 0, 4$ classes in the space group 225 with significant SOC excerpted from Supplementary Table 7 in Ref. [49].

Similar examples are also known in the diagnostic methods of nodal line semimetals, i.e., there are nodal line semimetals that are not found by the previous diagnostic meth-

---

[1]The candidates listed in Table 2.1 are "basic set" of candidates. Since we can add or subtract the indicator and invariants, we can get another candidate with larger mirror Chern numbers.
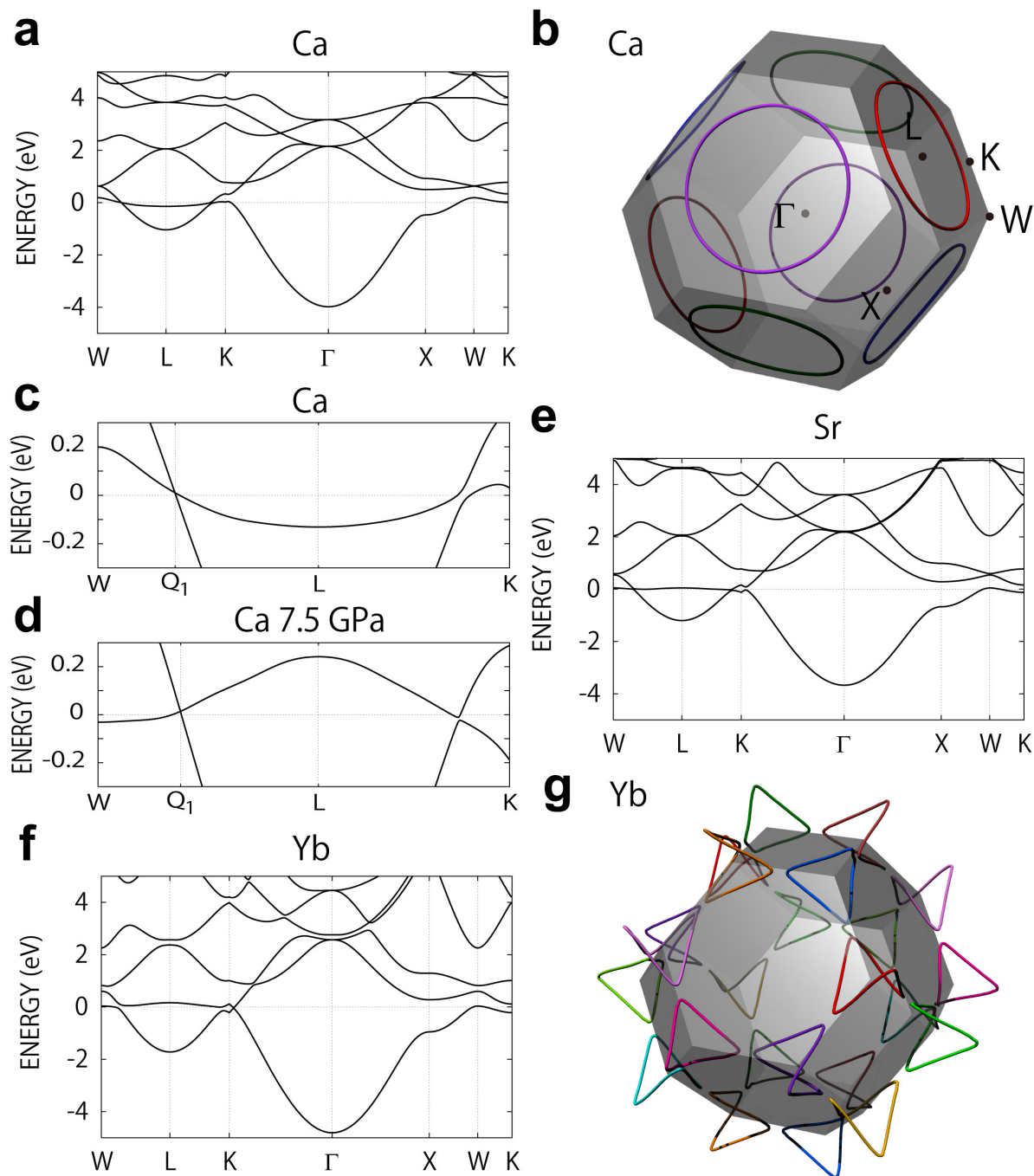
Figure 2.1. Band dispersions and nodal lines in Ca, Sr, and Yb adopted from M. Hirayama, *et. al.*, Nature communications **8**, 14022 (2017). (a) Band dispersion of Ca. (b) Nodal lines and BZ of Ca. The equivalent nodal lines (modulo reciprocal lattice vectors) are shown in the same color. (c)(d) Magnified band dispersions of Ca at ambient pressure and 7.5 GPa, respectively. (e)(f) Band dispersions of Sr and Yb, respectively. (g) Nodal line of Yb. The nodal line in Yb has a completely different shape from that of Ca although that of Sr looks almost the same as that of Ca.
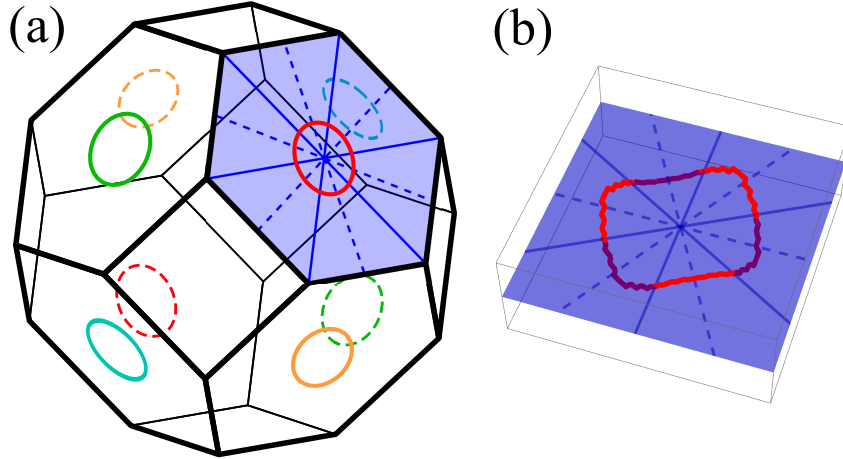
Figure 2.2. Nodal line in FCC SnSe. adopted from I. Tateishi, and H. Matsuura, Journal of the Physical Society of Japan, **87**, 073702 (2018). (a) BZ and nodal lines (red, green, orange, and light blue circles) in SnSe. A dashed line is equivalent (modulo reciprocal lattice vectors) to a solid one with the same color. There are four non-equivalent nodal lines per BZ. (b) Details of the shape of the nodal line. The blue plane represents the hexagonal surface of BZ. The red line is the nodal line. The perpendicular to the surface has been magnified 10 fold. It penetrates the surface of the BZ right on the center-corner line (solid line) and does not touch the center-edge line (dashed line).

ods. Not only suggested by the definition of the previous diagnostic methods, but some material examples have been proposed. Previous studies have shown that FCC alkaline earth metals (Ca, Sr, and Yb) [78] and FCC SnSe [79] have nodal lines around the Fermi level. Looking back section 1.3, the diagnosis by the symmetry-based indicator and $\mathbb{Z}_4$ is considered. However, the space group 225 (FCC) is not included in Table 1.6. It means that there is no nodal line semimetal class that satisfies the compatibility relation. The $\mathbb{Z}_4$ index can be calculated but it results in $\mathbb{Z}_4 = 0$ in all of Ca, Sr, Yb, and SnSe. So these materials are nodal line semimetals that cannot be found by previous diagnostic methods.

As referred to in section 1.4, it is known that a nodal line semimetal is intrinsically linked to a topological insulator. However, since the materials listed above have $\mathbb{Z}_4 = 0$, they are not linked to a TR protected topological insulator nor inversion protected a higher-order topological insulator. A question then naturally presents itself: to what kind of topological (crystalline) insulator class these nodal line semimetals are linked? [Fig. 2.3]

Based on the above, we focus on the following two points that should be clarified in this dissertation.

- To propose a new diagnostic method for the nodal line semimetals that has been overlooked in previous methods

- To clarify to what kind of topological insulator class those nodal line semiemtals are linked

Nodal line semimetals
(negligible spin-orbit coupling)
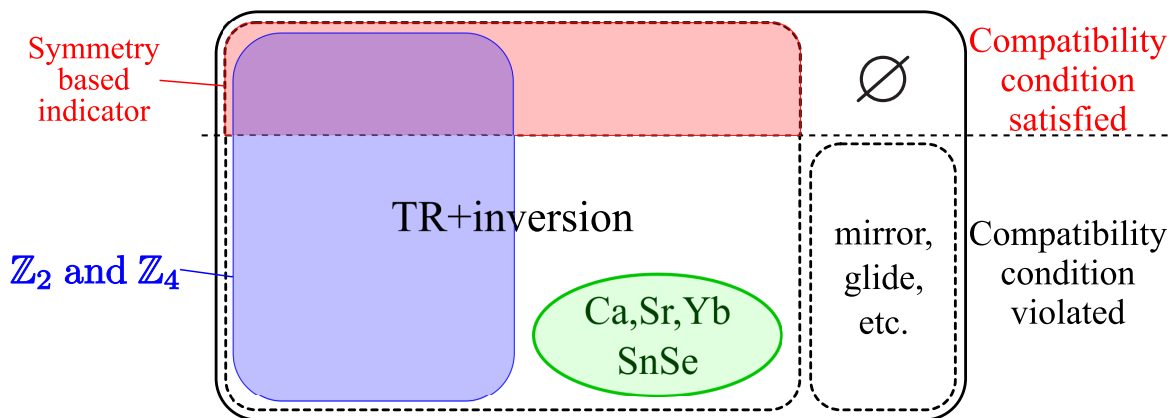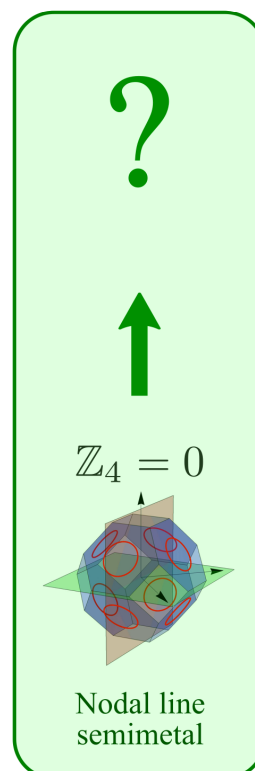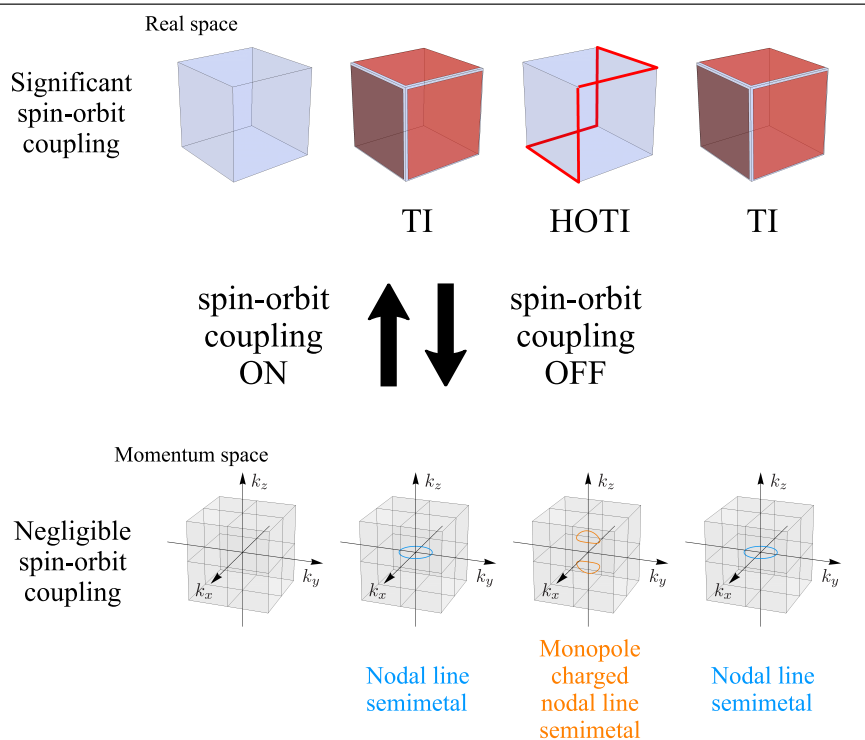
Figure 2.3. Points that should be clarified in this dissertation (shown in green letters and areas).

Chapter 3

δ indices

In this chapter, we derive a new index for diagnosing nodal line semimetals that could not be found by previous methods.

3.1 Applicable systems

To stabilize nodal lines, we assume a system with TR and inversion symmetries and negligible spin-orbit coupling. In this dissertation, we additionally assume C_4 rotation (or screw) symmetry. This assumption is based on a fact that a method used in this dissertation is effective mainly in those systems. The space groups with inversion and C_4 rotation symmetries are summarized in Table 3.1.

Since our purpose is to diagnose nodal line semimetals that violate the compatibility condition, we do not assume the compatibility condition. In other words, we allow for gapless points in high symmetry lines and planes. However, it is assumed that the number of occupied bands is the same at all high symmetry points.

Bravais lattice		Space groups	C_2'
Crystal family	Lattice system		
Tetragonal	Primitive	83-86	No
		123-138	Yes
	Body centered	87,88	No
		139-142	Yes
Cubic	Primitive	221-224	Yes
	Face centered	225-228	
	Body centered	229,230	

Table 3.1: Space groups with inversion and C_4 rotation symmetries. The presence or absence of C_2' is also exhibited. Here, C_2' is two-fold rotation symmetry whose axis is perpendicular to the C_4 axis.

3.2   Method : subgroup reduction

We derive a new diagnostic method by applying the symmetry-based indicator defined in a subgroup of the space group [80].

Suppose there is a nodal line semimetal that violates the compatibility condition. By definition, the nodal line semimetal has a gapless point in a high symmetry line or plane. Consider the subgroup of the space group of the nodal line semimetal. Considering a subgroup is equivalent to neglecting a certain symmetry operation. If we neglect the symmetry operation corresponding to the line or plane where the gapless point exists, the line or plane will become generic points and thus the nodal line semimetal will satisfy the compatibility condition. Since the system satisfies the compatibility condition, we can use the symmetry-based indicator defined in the subgroup to diagnose nodal line semimetals. By rewriting the symmetry-based indicator of the subgroup using the symmetry of the original space group, a new index is obtained.

Let us see an example in space group 255 (FCC). The space group 225 has no indicator as shown in Table 1.6. Let us neglect $C_{3(111)}$ symmetry, and then we obtain the space group 139. However, the space group has no indicator too. Then we next neglect C_{2x} symmetry and obtain the space group 87. The space group 87 has two indicators and they can be used as a diagnostic method. But in fact, further subduction up to the space group 83 gives four indicators and it is shown that the two in the space group 87 is effectively included in the four. If there is still a gapless point on a high symmetry line, for example, the C_4-invariant line, we need to subduce up to the space group 2. In the space group 2, the indicator is exactly $(\mathbb{Z}_4; \nu_1\nu_2\nu_3)$, which has already been known as explained in section 1.3. In summary, the four indicators in the space group 83 works as a new diagnostic method of nodal line semimetal in the space group 225.

We consider the subgroup reduction from general space groups with TR and inversion and C_4 symmetries. To preserve the stability of nodal lines, we do not consider a subgroup reduction that neglects the inversion symmetry. If we keep C_4, the space groups with nontrivial indicators that we can reach are the space group 83-88, 124, 128, and 130 [Fig. 3.2]. The indicators of the space group 84-87, 124, 128, and 130 can be written by the indicators of the space group 83 [Table 3.2]. The space group 88 is an exception, whose indicator z_2' is written with $\mathbb{Z}_4$. If we need to consider further subgroup reductions, we finally arrive at the space group 2 and get indicators $(\mathbb{Z}_4; \nu_1\nu_2\nu_3)$. Using the fact that the indicators in the space groups without C_4 are always given as a part of $(\mathbb{Z}_4; \nu_1\nu_2\nu_3)$ [50], it is proved that $(\mathbb{Z}_4; \nu_1\nu_2\nu_3)$ and $(\delta_2^{+,0}, \delta_2^{-,0}, \delta_2^{+,\pi}, \delta_2^{-,\pi})$ give a sufficient diagnostic method.

Note that this is a "sufficient" diagnostic method and some of them may be always 0 in the symmetry of the original space group. For example, in the space group 255, $\nu_1 = \nu_2 = \nu_3 = 0$.

(a)

(b)

$Fm\bar{3}m$ (#225)

$\{C_{4z}, C_{2x}, C_{3(111)}, I\}$

neglect $C_{3(111)}$

$I4/mmm$ (#139)

$\{C_{4z}, C_{2x}, I\}$

neglect C_{2x}

$I4/m$ (#87)

$\{C_{4z}, I\}$

neglect "Body-centered"

$P4/m$ (#83)

$\{C_{4z}, I\}$

#221 $Pm\bar{3}m$

[4] [2] [2] [4] [2]

#225 $Fm\bar{3}m$ $Im\bar{3}m$ #229

#139 $Fm\bar{3}c$

[3] [3] [3] [3]

#139 $I4/mmm$ [9, 5, 7, 3]

[2] [2]

$P4/mmm$ [2, 5, 7, 3, 9]

#123

[2] #140 $I4/mcm$ [3, 7, 5, 9]

[2] [2] [2] [2]

[2] [2] #127

$P4/mcc$ [2, 7, 5, 3, 9] $P4/mbm$ [9, 5, 7, 3, 2]

#124

[2] [2] [2] [2]

$P4/mnc$ [7, 3, 5, 9] [2] [2] [2]

#128

[2]

$P4/m$ [3, 7, 5, 2, 9]

#83

[2] [2] #87

$I4/m$ [9, 7, 3, 5]
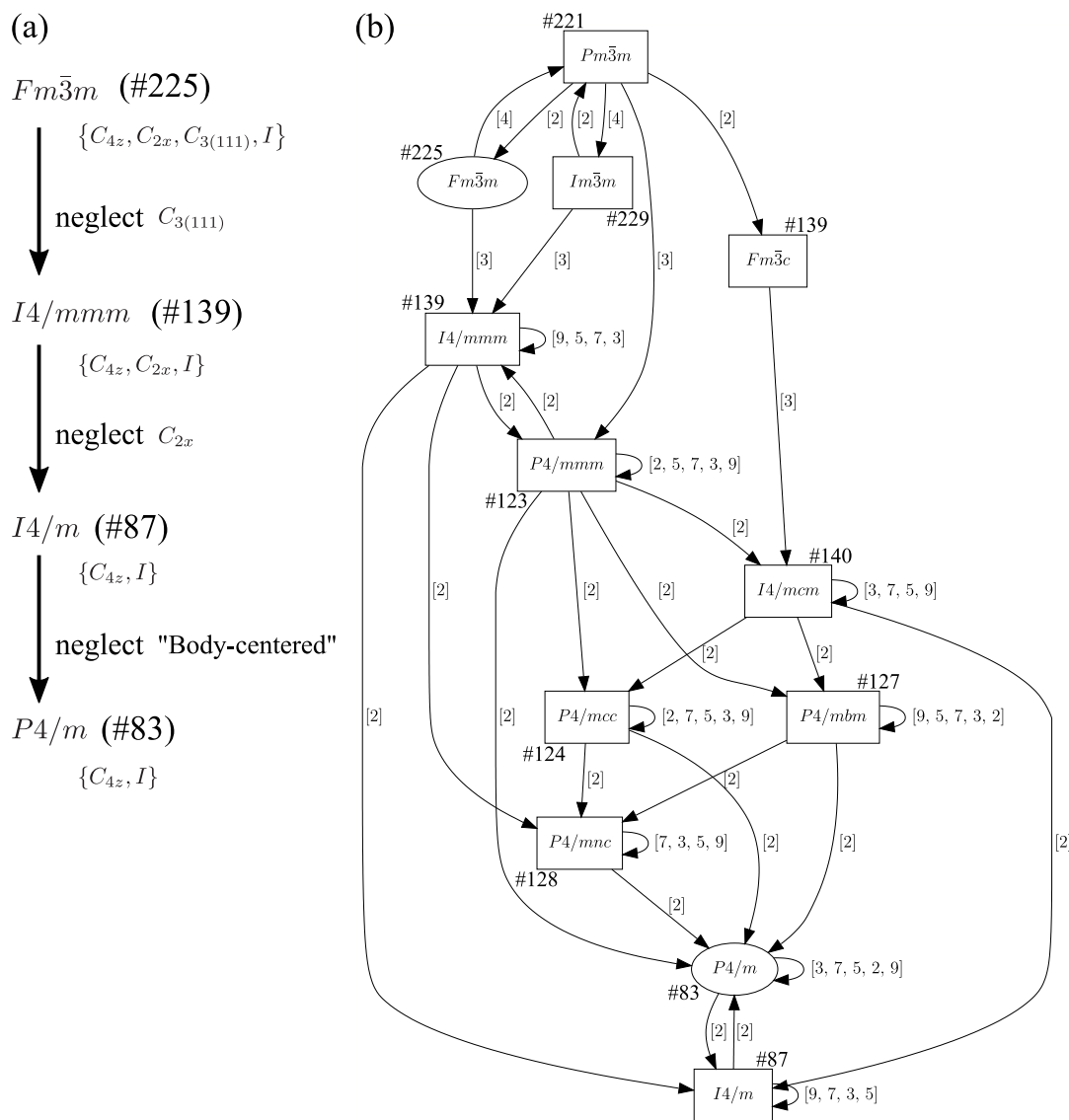
Figure 3.1. Subgroup lattice from the space group 255 to 83 adopted from Bilbao Crystallographic Server [57]. The space group at the end of an arrow is a subgroup of the starting space group. The number [n] labeled on arrows is "the index of the subgroup". Here "index" is a technical term in the group theory. [n] roughly means that the original group is "n times larger" than the subgroup.
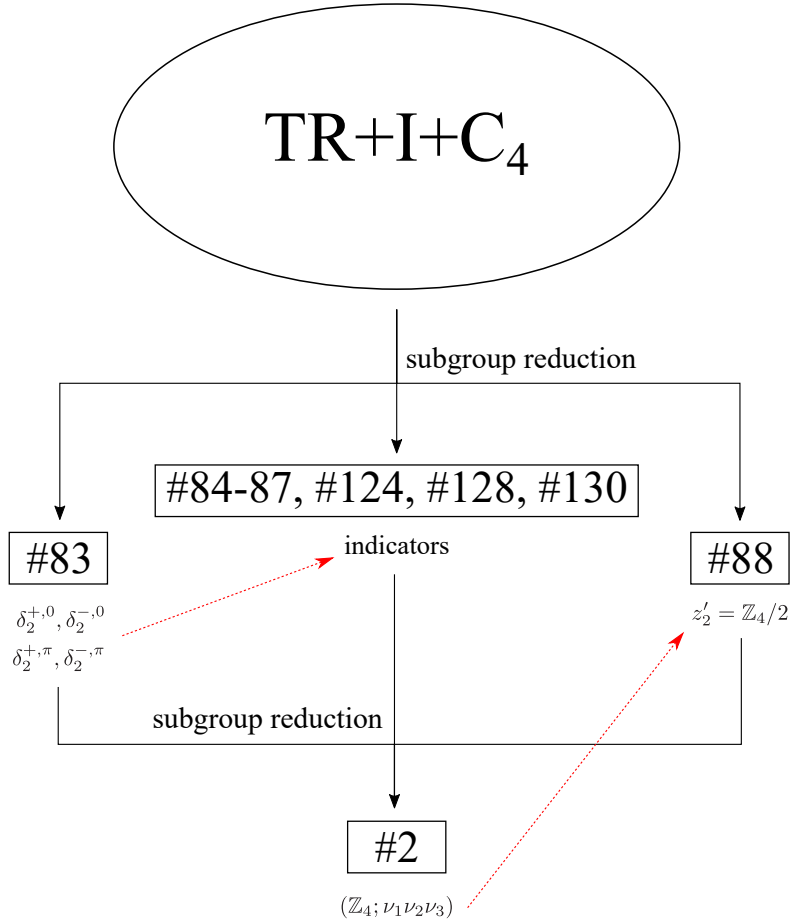
Figure 3.2. Flow of the subgroup reduction. If the C_4 and inversion (I) symmetries are kept, the space groups with nontrivial indicators are 88-88, 124, 128, and 130. However, their indicators are written by that of the space group 83 and 2. Therefore, the indicators of 83 and 2 give a sufficient diagnostic method.

space group	indicators in Ref. [50]	
83	$\delta_2^{+,0}, \delta_2^{-,0}, \delta_2^{+,\pi}, \delta_2^{-,\pi}$	
84	$\delta_2^{+,0}, \delta_2^{-,0}$	
85-86	δ	$\delta = \delta_2^{+,0} + \delta_2^{-,0}$
87	$\delta_2^{+,0}, \phi_2$	$\phi_2 \equiv \delta_2^{+,\pi}$
124,128	$\delta_2^{+,\pi}$	
130	θ	$\theta \equiv \delta_2^{+,0} - \delta_2^{-,0}$

Table 3.2: Indicators of the space groups with TR, inversion, and C_4 symmetries. Indicators of the space groups other than 83 are either some of that of 83 or can be written by using that of 83.

3.3 Calculation formula of the δ indices

As shown in section 3.2, new nodal line semimetals are diagnosed by the δ indices, $(\delta_2^{+,0}, \delta_2^{-,0}, \delta_2^{+,\pi}, \delta_2^{-,\pi})$. In this section, we rewrite $(\delta_2^{+,0}, \delta_2^{-,0}, \delta_2^{+,\pi}, \delta_2^{-,\pi})$ in the original symmetry to give their calculation formula.

It would be too complicated to give formulas for each space groups individually, so we give for the five Bravais lattices listed in the Table 3.1. The given formula is valid in any space group in the same Bravais lattice, although some indices can be fixed to 0 by the space group symmetry.

At first, we give the calculation formula in the primitive tetragonal lattice. It is almost a review of the definition of the indicators of the space group 83 given in Ref. [50]. Next, we move on to the other Bravais lattices, where a nontrivial rewrite is required. For all Bravais lattices, we first give the obtained diagnostic method and the calculation formulas, and then the derivation and Berry phase interpretation are discussed.

In the following, we will consistently use the definitions in Table 3.3 for the eigenvalues of crystalline symmetry operations[1].

Operation	Eigenvalue	(Other)
C_4	ξ	
inversion (I)	χ	
mirror ($m = IC_4^2$)	σ	superscripts $\pm$
$S_4 = IC_4$	ξ'	
$C_2 = Im$	ζ	

Table 3.3: Symmetry operation and their eigenvalues.

3.3.1 Primitive Tetragonal

In the primitive tetragonal lattice, the indices in Eq. (1.14) can be directly used. Let us repeat the definition of $(\delta_2^{+,0}, \delta_2^{-,0}, \delta_2^{+,\pi}, \delta_2^{-,\pi})$,

$$\begin{aligned}
\delta_2^{\pm,0} &= n_{\xi=-1}^{\pm}(\Gamma) + n_{\xi=-1}^{\pm}(M) + n_{\zeta=-1}^{\pm}(X), \\
\delta_2^{\pm,\pi} &= n_{\xi=-1}^{\pm}(Z) + n_{\xi=-1}^{\pm}(A) + n_{\zeta=-1}^{\pm}(R).
\end{aligned} \tag{3.1}$$

Here, $n_{\xi=-1}^{+}(\Gamma)$ is the number of occupied bands with the C_4 eigenvalue $\xi = -1$ and the mirror eigenvalue $\sigma = +1$ in the Γ point, $n_{\zeta=-1}^{+}(X)$ is the number of occupied bands with the C_2 eigenvalue $\zeta = -1$ and the mirror eigenvalue $\sigma = +1$ in the X point, and so on [Fig. 3.3]. Note that the C_2 rotation is a rotation around the XR line, and the mirror is about the ΓMX plane or the ZAR plane.

---

[1]The C_2 eigenvalues is considered in a high symmetry point that is not C_4-invariant. Therefore defining $C_2 = C_4^2$ can be misleading in some cases. Since the mirror-invariant plane of $m = IC_4^2$ touches the C_2-invariant line, defining as $C_2 = Im$ is safer.
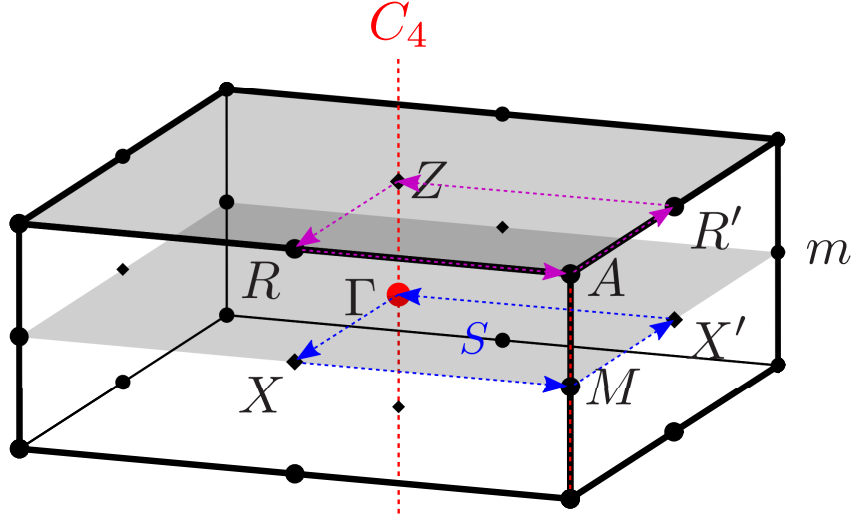
Figure 3.3. Brillouin Zone of the primitive tetragonal lattice.

Due to the C_4 symmetry, $\nu_1 = \nu_2$ is always satisfied. The diagnostic method is given as seven indices,

$$\mathbb{Z}_4, \nu_1, \nu_3, \delta_2^{+,0}, \delta_2^{-,0}, \delta_2^{+,\pi}, \delta_2^{-,\pi} \tag{3.2}$$

Derivation and Berry phase interpretation

The derivation is the same as the symmetry based indicator in the space group 83 [Section 1.3.1]. However, now $(\delta_2^{+,0}, \delta_2^{-,0}, \delta_2^{+,\pi}, \delta_2^{-,\pi})$ are independent because the compatibility condition is not necessarily satisfied.

Even if there is a nodal line that touches a high symmetry line or plane, the Berry phase interpretation basically works[2]. The $\delta_2^{\pm,0}$ corresponds to the parity on the number of the nodal lines that penetrate the loop ΓXMX'Γ [Fig. 3.3, blue loop] in the ± 1 mirror sector. The $\delta_2^{\pm,\pi}$ corresponds to the parity on the number of the nodal lines that penetrate the loop ZRAR'Z [Fig. 3.3, violet loop] in the ± 1 mirror sector. Nodal lines between two bands with different mirror eigenvalues are not found by the δ indices but they are found by using $(\mathbb{Z}_4; \nu_1 \nu_2 \nu_3)$. When the loop ΓXMX'Γ (ZRAR'Z) is touching a nodal line, the loop can be deformed not to touch the nodal line so that ΓX and ΓX' (ZR and ZR') are a C_4 symmetric pair.

3.3.2 Body centered tetragonal

In the body centered tetragonal lattice, three independent indices $\delta_2^{+,0}, \delta_2^{-,0}, \delta_2^{\pi}$ are given. The definitions of them are

$$\delta_2^{\pm,0} = n_{\xi=-1}^{\pm}(\Gamma) + n_{\xi=-1}^{\pm}(M) + n_{\zeta=1}^{\pm}(X) + n^{\pm}(\Gamma) \pmod 2,$$
$$\delta_2^{\pi} = n_{\xi=-1}(\Gamma) + n_{\xi'=-1}(P) + n_{\chi=-1}(N) \pmod 2. \tag{3.3}$$

---

[2]Only if a nodal line is a m_z-protected nodal line, the Berry phase interpretation is invalid. However, the δ indices work as a diagnostic method of nodal line semimetals in that case.
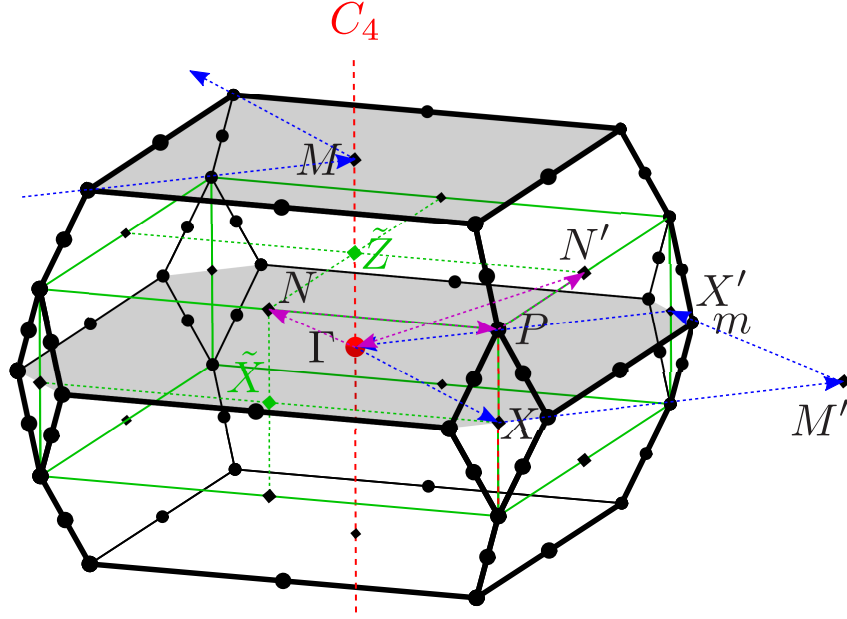
Figure 3.4. Brillouin Zone of the body centered tetragonal lattice ($c > a$).

Here, $n_{\xi'=-1}(P)$ is the number of the occupied bands with the S_4 eigenvalue $\xi' = -1$ in the P point. There are two types of BZ in the body centered tetragonal lattice depending on the ratio of lattice constants [Fig. 3.4 and Fig. 3.5]. Equivalent high symmetry points are given the same name and thus the definition Eq. (3.3) is valid in the both cases. Note that the C_2 rotation is a rotation around the XP line, and the mirror is about the plane perpendicular to the XP line.

Due to the symmetry of the body centered tetragonal lattice, $\nu_1 = \nu_2 = \nu_3$ is always satisfied. The diagnostic method is given as five indices,

$$\mathbb{Z}_4, \nu_1, \delta_2^{+,0}, \delta_2^{-,0}, \delta_2^{\pi} \tag{3.4}$$

Derivation and Berry phase interpretation

By a subgroup reduction that neglects the body centered symmetry, we introduce the four indices in the space group 83. We rewrite them in the symmetry and BZ of the body centered lattice and obtain new indices. However, when the body centered symmetry is neglected, the unit cell is doubled and the BZ is folded in half. As a result, the indices need to be rewritten to take into account the effect of the BZ folding.

Since a tetragonal space group is obtained by the subgroup reduction, the BZ after folding is also tetragonal as shown in Fig. 3.4 and Fig. 3.5 (green cuboids). Here, letters with a tilde ($\tilde{X}$ and $\tilde{Z}$) are the high symmetry points in the folded BZ. The four δ indices are defined in the top face ($\tilde{Z}$PN) and the middle horizontal plane (ΓXX'). However, in the original BZ, some points do not have the symmetry that is needed in the calculation of the δ indices. For example, the X point is not a C_4-invariant point in the original BZ, although it is the corner of the folded BZ and the C_4 eigenvalues should be checked there.

When the BZ is folded, degenerated states appear on the boundary of the folded BZ. If a momentum point gets a new symmetry, a unitary transformation within the
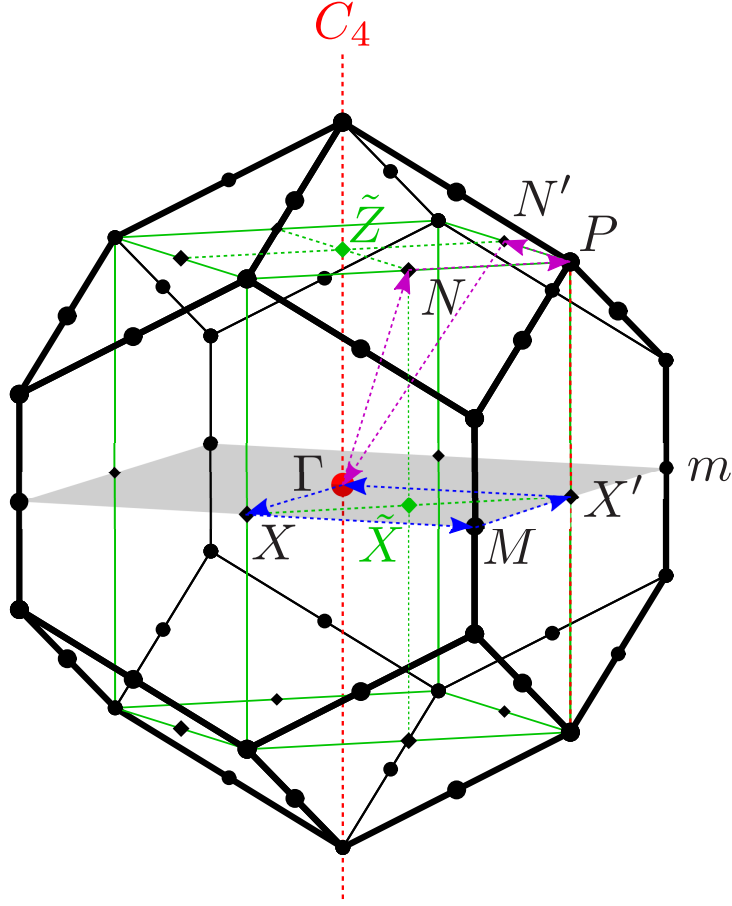
Figure 3.5. Brillouin Zone of the body centered tetragonal lattice ($c < a$).

degenerated states can give a new set of states that diagonalize the C_4 operator. The eigenvalues of the states are restricted by the following two rules. First, it is proved that the sum of the eigenvalues must be 0 (See Appendix C.1). Second, the eigenvalues must be consistent with the symmetry eigenvalues before BZ folding. Using these rules, we can rewrite the δ indices in the original symmetry and BZ.

Let us see the concrete derivations. First, we rewrite $\delta_2^{\pm,0}$. The definition in the folded BZ is

$$\delta_2^{\pm,0} = \tilde{n}_{\xi=-1}^{\pm}(\Gamma) + \tilde{n}_{\xi=-1}^{\pm}(X) + \tilde{n}_{\zeta=-1}^{\pm}(\tilde{X}), \tag{3.5}$$

where $\tilde{n}$ is the number of bands counted in the folded BZ.

Since the the Γ point is a C_4 and mirror-invariant point and thus $n_{\xi=-1}^{\pm}(\Gamma)$ has no ambiguity. However, the M point overlaps with the Γ point as a result of the BZ folding. Therefore, $\tilde{n}_{\xi=-1}^{\pm}(\Gamma)$ is rewritten as

$$\tilde{n}_{\xi=-1}^{\pm}(\Gamma) = n_{\xi=-1}^{\pm}(\Gamma) + n_{\xi=-1}^{\pm}(M) \tag{3.6}$$

The X point is not a C_4-invariant point in the original BZ. Due to the BZ folding, the X point overlaps with the X' point and becomes a C_4-invariant point. As a result, all bands are doubly degenerated with states originated from the X and X' points at the X point in the filded BZ. By making a linear combination of them, they are transformed

into two C_4 eigenstates. It is easily proved that their eigenvalues, $\xi_{\tilde{X},1}$ and $\xi_{\tilde{X},2}$, satisfy $\xi_{\tilde{X},1} + \xi_{\tilde{X},2} = 0$. (the proof is given in Appendix C.1.) Since a C_4 eigenvalue is generally ± 1 or $\pm i$, the possible combination is $(\xi_{\tilde{X},1}, \xi_{\tilde{X},2}) = (+1, -1)$ or $(\xi_{\tilde{X},1}, \xi_{\tilde{X},2}) = (+i, -i)$. Considering that the X point is a C_2-invariant point in the original BZ and $\xi^2 = \zeta$, the C_4 eigenvalues in the folded BZ are determined form the C_2 eigenvalues in the original BZ. The symmetry eigenvalues in the original BZ and the folded BZ are related as[3]

$$
\begin{array}{ccc|c|cccc}
\multicolumn{3}{c}{\text{BZ folding}} & \longrightarrow & \multicolumn{4}{c}{\substack{\text{Dobuly}\\\text{degenerated}}} \\
\chi & \sigma & \zeta & & \chi & \sigma & \zeta & \xi \\
\hline
+1 & +1 & +1 & & +1 & +1 & +1 & +1 \\
& & & & +1 & +1 & +1 & -1 \circ \\
\hline
-1 & +1 & -1 & & -1 & +1 & -1 & +i \\
& & & & -1 & +1 & -1 & -i \\
\hline
-1 & -1 & +1 & & -1 & -1 & +1 & +1 \\
& & & & -1 & -1 & +1 & -1 \bullet \\
\hline
+1 & -1 & -1 & & +1 & -1 & -1 & +i \\
& & & & +1 & -1 & -1 & -i
\end{array}
\tag{3.7}
$$

To calculate the $\delta_2^{+,0}$, the number of occupied bands with $\sigma = +1$ and $\xi = -1$ should be counted at the X point ($\tilde{n}_{\xi=-1}^{+}(X)$) in the folded BZ ($\circ$ in Eq. (3.7)). As shown in Eq. (3.7), those bands are always degenerated with bands with $\sigma = +1$ and $\xi = +1$. The doubly degenerated pairs are originated from bands with $\sigma = +1$ and $\zeta = +1$ in the original BZ. Therefore, the $\tilde{n}_{\xi=-1}^{+}(X)$ is rewritten in the original BZ as

$$
\tilde{n}_{\xi=-1}^{+}(X) = n_{\zeta=1}^{+}(X).
\tag{3.8}
$$

The $\tilde{n}_{\xi=-1}^{-}(X)$ is rewritten in the same way (see $\bullet$ in Eq. 3.7) as

$$
\tilde{n}_{\xi=-1}^{-}(X) = n_{\zeta=1}^{-}(X).
\tag{3.9}
$$

The $\tilde{X}$ point is not a C_2-invariant point in the original BZ but the C_2 eigenvalues of doubly degenerated bands in the folded BZ are determined in the same way. The eigenvalues are determined as

$$
\begin{array}{c|c|cc}
\sigma & \longrightarrow & \multicolumn{2}{c}{\substack{\text{Dobuly}\\\text{degenerated}}} \\
\sigma & & \sigma & \zeta \\
\hline
+1 & & +1 & +1 \\
& & +1 & -1 \circ \\
\hline
-1 & & -1 & +1 \\
& & -1 & -1 \bullet
\end{array}
\tag{3.10}
$$

The reference point can be moved on the mirror-invariant plane[4] and thus

$$
\tilde{n}_{\zeta=-1}^{\pm}(\tilde{X}) = n^{\pm}(\Gamma).
\tag{3.11}
$$

---

[3]Note that $\chi\sigma = \zeta$

[4]If the reference point cross a nodal line, the nodal line can cross the original reference point by a trivial parameter tuning.

In summary, $\delta_2^{\pm,0}$ are rewritten as Eq. (3.3).

Next, we rewrite $\delta_2^{\pm,\pi}$. The definition in the folded BZ is

$$\delta_2^{\pm,\pi} = \tilde{n}_{\xi=-1}^{\pm}(\tilde{Z}) + \tilde{n}_{\xi=-1}^{\pm}(P) + \tilde{n}_{\zeta=-1}^{\pm}(N), \tag{3.12}$$

The $\tilde{Z}$ point is a C_4-invariant point but not a mirror-invariant point in the original BZ. The mirror eigenvalues are defined only after the BZ folding and they are determined as

BZ folding		Dobuly degenerated		
ξ	$\longrightarrow$	ξ	σ	
$+1$		$+1$	$+1$	
		$+1$	-1	
-1		-1	$+1$	$\circ$
		-1	-1	$\bullet$
$+i$		$+i$	$+1$	
		$+i$	-1	
$-i$		$-i$	$+1$	
		$-i$	-1	

$$\tag{3.13}$$

The reference point can be moved along the C_4-invariant line (ΓM line) to the Γ point and thus $\tilde{n}_{\xi=-1}^{\pm}$ is rewritten as

$$\tilde{n}_{\xi=-1}^{\pm}(\tilde{Z}) = n_{\xi=-1}(\Gamma). \tag{3.14}$$

The P point is a S_4 and C_2-invariant point in the original BZ. Using the relations of eigenvalues $\xi'^2 = \zeta$ and $\xi'\xi = \sigma$, the C_4 and mirror eigenvalues in the folded BZ are determined as

BZ folding			Dobuly degenerated			
ξ'	ζ	$\longrightarrow$	ξ'	ζ	σ	ξ
$+1$	$+1$		$+1$	$+1$	$+1$	$+1$
			$+1$	$+1$	-1	-1 $\bullet$
-1	$+1$		-1	$+1$	$+1$	$+1$
			-1	$+1$	$+1$	-1 $\circ$
$+i$	-1		$+i$	-1	-1	$+i$
			$+i$	-1	$+1$	$-i$
$-i$	-1		$-i$	-1	$+1$	$+i$
			$-i$	-1	-1	$-i$

$$\tag{3.15}$$

Therefore, $\tilde{n}_{\xi=-1}^{\pm}(P)$ is rewritten in the original BZ as

$$\tilde{n}_{\xi=-1}^{\pm}(P) = n_{\xi'=\mp}(P) \tag{3.16}$$

The N point is one of the TRIM but not a C_2 and mirror-invariant point. Using the relation of eigenvalues $\chi = \zeta\sigma$, the C_2 and mirror eigenvalues in the folded BZ are

determined as

BZ folding		Dobuly degenerated		
χ	$\longrightarrow$	χ	ζ	σ
$+1$		$+1$ $+1$ $+1$		
		$+1$ -1 -1 $\bullet$		
-1		-1 $+1$ -1		
		-1 -1 $+1$ $\circ$		

$$\text{(3.17)}$$

Therefore, $\tilde{n}^{\pm}_{\zeta=-1}$ is rewritten in the original BZ as

$$\tilde{n}^{\pm}_{\zeta=-1} = n_{\chi=\mp}(N). \tag{3.18}$$

In summary, $\delta^{\pm,\pi}_2$ is rewritten as

$$\delta^{\pm,\pi}_2 = n_{\xi=-1}(\Gamma) + n_{\xi'=\mp}(P) + n_{\chi=\mp}(N). \tag{3.19}$$

However $\delta^{+,\pi}_2$ and $\delta^{-,\pi}_2$ are not independent. $\delta^{+,\pi}_2 + \delta^{-,\pi}_2$ is calculated as

$$\begin{aligned}
\delta^{+,\pi}_2 + \delta^{-,\pi}_2 &= 2n_{\xi=-1}(\Gamma) + n_{\xi'=1}(P) + n_{\xi'=-1}(P) + n_{\chi=1}(N) + n_{\chi=-1}(N) \\
&= n_{\xi'=1}(P) + n_{\xi'=-1}(P) + n_{\chi=1}(N) + n_{\chi=-1}(N) \pmod 2.
\end{aligned} \tag{3.20}$$

The latter two terms are written with the number of occupied bands j as $n_{\chi=1}(N) + n_{\chi=-1}(N) = j$. Additionally, $\xi' = \pm i$ are always appear as a pair in TR symmetric systems and thus the former two terms are written with the number of the $\xi' = \pm i$ pair l as $n_{\xi'=1}(P) + n_{\xi'=-1}(P) = j - 2l$. As a result,

$$\delta^{+,\pi}_2 + \delta^{-,\pi}_2 = j - 2l + j = 0 \pmod 2. \tag{3.21}$$

Therefore, we need to use only $\delta^{+,\pi}_2 = \delta^{\pi}_2$ as given in Eq. (3.3).

These indices are also interpreted as Berry phases. The $\delta^{\pm,0}_2$ corresponds to the parity on the number of the nodal lines that penetrate the loop ΓXM'X'Γ [Fig. 3.4, blue loop] (or ΓXMX'Γ [Fig. 3.5, blue loop]) in the ± 1 mirror sector. The δ^{π}_2 corresponds to the parity on the number of the nodal lines that penetrate the loop ΓNPN'Γ [Fig. 3.4 and Fig. 3.5, violet loop][5].

3.3.3 Primitive cubic

In the primitive cubic lattice, the indices of the primitive tetragonal lattice can be simply applied. The definition of the indices are rewritten with the name of high symmetry points in the cubic lattice [Fig. 3.6] as

$$\begin{aligned}
\delta^{\pm,0}_2 &= n^{\pm}_{\xi=-1}(\Gamma) + n^{\pm}_{\xi=-1}(M) + n^{\pm}_{\zeta=-1}(X), \\
\delta^{\pm,\pi}_2 &= n^{\pm}_{\xi=-1}(X) + n^{\pm}_{\xi=-1}(R) + n^{\pm}_{\zeta=-1}(M).
\end{aligned} \tag{3.22}$$
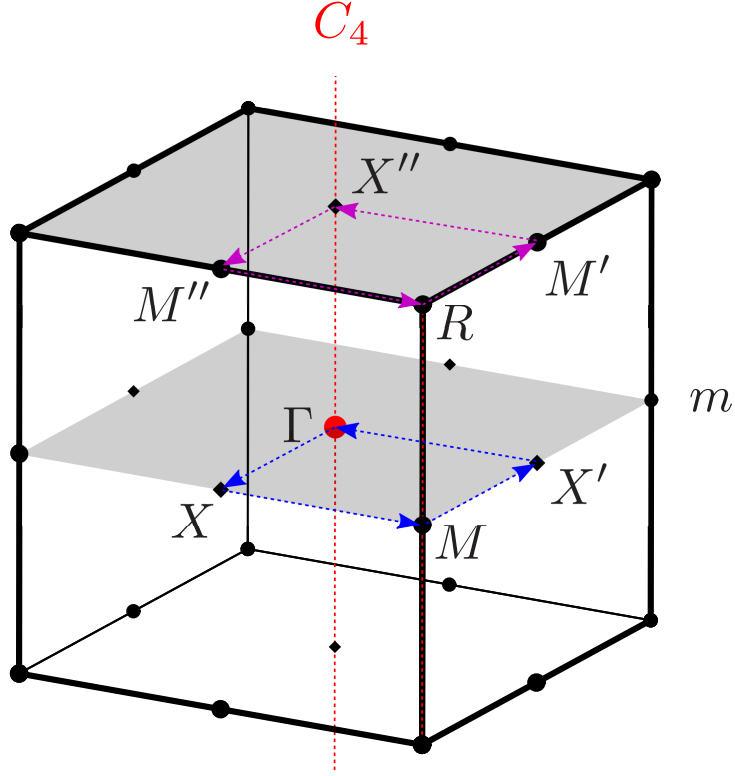
Figure 3.6. Brillouin Zone of the primitive cubic lattice

Note that the C_2 rotation in the X point and M point is a rotation around the XM line, the mirror is always about the plane that perpendicular to the C_4 or C_2 axis.

Due to the cubic symmetry, $\nu_1 = \nu_2 = \nu_3$ is always satisfied. The diagnostic method si given as six indices,

$$\mathbb{Z}_4, \nu_1, \delta_2^{+,0}, \delta_2^{-,0}, \delta_2^{+,\pi}, \delta_2^{-,\pi}. \tag{3.23}$$

Derivation and Berry phase interpretation

The derivation and Berry phase interpretation is equivalent to that of the primitive tetragonal lattice.

3.3.4 Face centered cubic

In the face centered cubic lattice, the indices of body centered tetragonal lattice can be applied. The definitions of the indices are rewritten with the name of high symmetry points in the face centered cubic lattice [Fig. 3.7] as

$$\begin{aligned}
\delta_2^{\pm,0} &= n_{\xi=-1}^{\pm}(\Gamma) + n_{\xi=-1}^{\pm}(X) + n_{\zeta=1}^{\pm}(X) + n^{\pm}(\Gamma) \pmod 2, \\
\delta_2^{\pi} &= n_{\xi=-1}(\Gamma) + n_{\xi'=-1}(W) + n_{\chi=-1}(L) \pmod 2.
\end{aligned} \tag{3.24}$$

Note that the C_2 rotation in the X point is a rotation around the XW line, the mirror is always about the plane perpendicular to the C_4 or C_2 axis.

---

[5]Since the reference point is moved from $\tilde{Z}$ to Γ, the loop is also deformed from $\tilde{Z}$NPN'$\tilde{Z}$ to ΓNPN'Γ
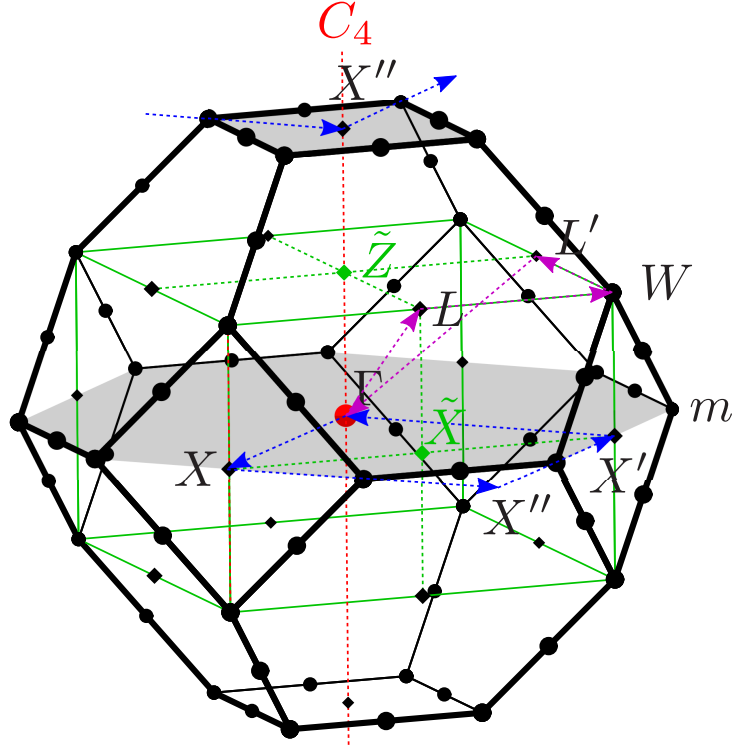
Figure 3.7. Brillouin Zone of the face centered cubic lattice

Due to the face centered cubic symmetry, $\nu_1 = \nu_2 = \nu_3 = 0$ is always satisfied. The diagnostic method is given as four indices,

$$\mathbb{Z}_4, \delta_2^{+,0}, \delta_2^{-,0}, \delta_2^{\pi} \tag{3.25}$$

Derivation and Berry phase interpretation

The derivation is almost the same as that of the body centered tetragonal case, just replacing the point M with X, P with W, and N with L. The $\delta_2^{\pm,0}$ and δ_2^{π} correspond to the blue loop and the violet loop in Fig. 3.7, respectively.

3.3.5 Body centered cubic

In the body centered cubic lattice, the indices of body centered tetragonal lattice can be applied. The definitions of the indices are rewritten with the name of high symmetry points in the body centered cubic lattice [Fig. 3.8] as

$$\delta_2^{\pm,0} = n_{\xi=-1}^{\pm}(\Gamma) + n_{\xi=-1}^{\pm}(H) + n_{\zeta=1}^{\pm}(N) + n^{\pm}(\Gamma) \pmod 2$$
$$\delta_2^{\pi} = n_{\xi=-1}(\Gamma) + n_{\xi'=-1}(P) + n_{\chi=-1}(N) \pmod 2 \tag{3.26}$$

Note that the C_2 rotation in the N point is a rotation around the NP line, the mirror is always about the plane perpendicular to the C_4 or C_2 axis.
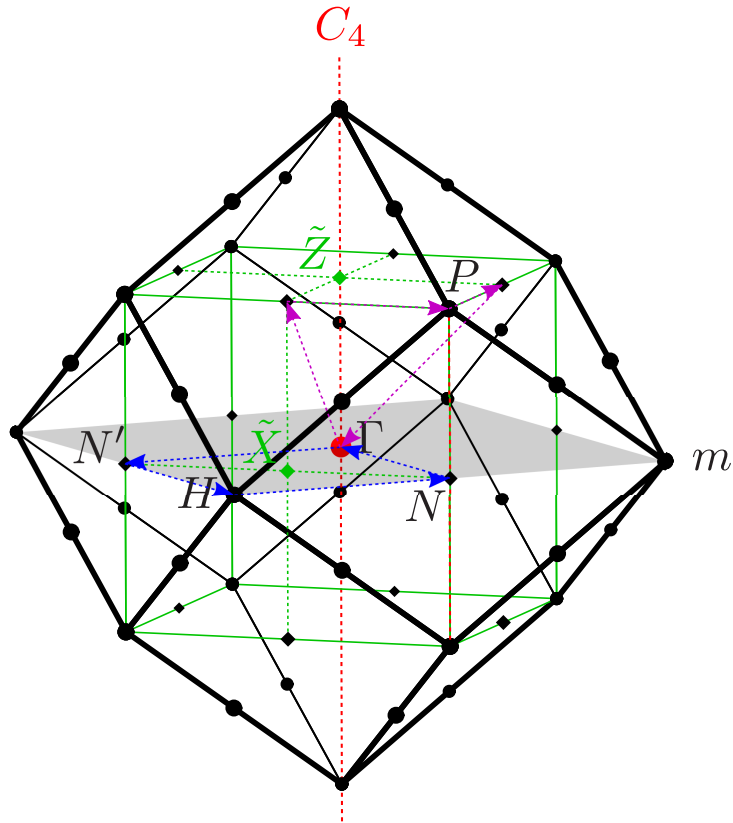
Figure 3.8. Brillouin Zone of the body centered cubic lattice

Due to the body centered cubic symmetry, $\nu_1 = \nu_2 = \nu_3$ is always satisfied. The diagnostic method is given as five indices,

$$\mathbb{Z}_4, \nu_1, \delta_2^{+,0}, \delta_2^{-,0}, \delta_2^\pi \tag{3.27}$$

Derivation and Berry phase interpretation

The derivation is almost the same as that of the body centered tetragonal case, just replacing the point M with H. The $\delta_2^{\pm,0}$ and δ_2^π correspond to the blue loop and the violet loop in Fig. 3.8, respectively.

3.4 Material Examples

In this section, we calculate the δ indices for some materials. These examples are "nodal line semimetals" that have $(\mathbb{Z}_4; \nu_1\nu_2\nu_3) = (0; 000)$ but nontrivial δ indices. Note that here the word "nodal line semimetals" just refers to the existence of band crossings between the j-th band and the $(j+1)$-th band, and materials given in this section can have metallic Fermi surfaces.

3.4.1 Ca, Ba

In Ca and Ba [78], the indices are calculated by focusing on an occupied band. The irreps of their occupied bands are the same and the irreps in each high symmetry point are listed in Table 3.4. The indices are

$$(\mathbb{Z}_4, \delta_2^{+,0}, \delta_2^{-,0}, \delta_2^{\pi}) = (0, 0, 0, 1) \tag{3.28}$$

	Ca (space group 225)			
Band	Γ point	X point	W point	L point
index	irrep : (χ, σ, ξ)	irrep : $\chi, (\sigma_{\perp C_4}, \xi), (\sigma_{\perp C_2}, \zeta)$	irrep : ξ'	irrep : χ
1	$\Gamma_1^+ : (+1, +1, +1)$	$\Gamma_1^+ : +1, (+1, +1), (+1, +1)$	$\Gamma_4 : -1$	$\Gamma_1^+ : +1$

Table 3.4: Irreps and symmetry eigenvalues of the occupied band in high symmetry points in Ca (space group 225)

3.4.2 Face centered cubic SnSe

In FCC SnSe [79], the indices are calculated by focusing on five occupied bands. The irreps in each high symmetry point are listed in Table 3.5. The indices are

$$(\mathbb{Z}_4, \delta_2^{+,0}, \delta_2^{-,0}, \delta_2^{\pi}) = (0, 0, 0, 1) \tag{3.29}$$

3.4.3 Ca$_2$As

In Ca$_2$As [81], the indices are calculated by focusing on seven occupied bands. The irreps in each high symmetry point are listed in Table 3.6. The indices are

$$(\mathbb{Z}_4, \nu_1, \delta_2^{+,0}, \delta_2^{-,0}, \delta_2^{\pi}) = (0, 0, 0, 0, 1) \tag{3.30}$$

	SnSe (space group 225)			
Band	Γ point	X point	W point	L point
index	irrep : (χ,σ,ξ)	irrep : $\chi,(\sigma_{\perp C_4},\xi),(\sigma_{\perp C_2},\zeta)$	irrep : ξ'	irrep : χ
1	Γ_1^+ : $(+1,+1,+1)$	Γ_1^+ : $+1,(+1,+1),(+1,+1)$	Γ_1 : $+1$	Γ_1^+ : $+1$
2	Γ_1^+ : $(+1,+1,+1)$	Γ_1^+ : $+1,(+1,+1),(+1,+1)$	Γ_4 : -1	Γ_2^- : -1
3	$(-1,+1,+i)$	Γ_2^- : $-1,(-1,+1),(+1,-1)$	Γ_5 : $+i$	Γ_3^- : -1
4	Γ_4^- : $(-1,+1,-i)$	Γ_5^- : $-1,(+1,+i),(+1,-1)$	Γ_5 : $-i$	Γ_3^- : -1
5	$(-1,-1,+1)$	$-1,(+1,-i),(-1,+1)$	Γ_4 : -1	Γ_1^+ : $+1$

Table 3.5: Irreps and symmetry eigenvalues of the occupied bands in high symmetry points in FCC SnSe.

	Ca_2As (space group 139)			
Band	Γ point	X point	P point	N point
index	irrep : (χ,σ,ξ)	irrep : $\chi,(\sigma_{\perp C_2},\zeta)$	irrep : ξ'	irrep : χ
1	Γ_1^+ : $(+1,+1,+1)$	Γ_3^- : $-1,(+1,-1)$	Γ_5 : $+i$	Γ_2^- : -1
2	Γ_5^+ : $(+1,-1,+i)$	Γ_4^- : $-1,(+1,-1)$	Γ_5 : $-i$	Γ_1^+ : $+1$
3	$(+1,-1,-i)$	Γ_3^+ : $+1,(-1,-1)$	Γ_5 : $+i$	Γ_1^+ : $+1$
4	Γ_1^+ : $(+1,+1,+1)$	Γ_1^+ : $+1,(+1,+1)$	Γ_5 : $-i$	Γ_2^+ : $+1$
5	Γ_2^- : $(-1,-1,+1)$	Γ_4^+ : $+1,(-1,-1)$	Γ_1 : $+1$	Γ_2^- : -1
6	Γ_5^- : $(-1,+1,+i)$	Γ_2^- : $-1,(-1,+1)$	Γ_4 : -1	Γ_1^- : -1
7	$(-1,+1,-i)$	Γ_1^+ : $+1,(+1,+1)$	Γ_1 : $+1$	Γ_2^- : -1

Table 3.6: Irreps and symmetry eigenvalues of the occupied bands in high symmetry points in Ca_2As (space group 139).

3.5 Summary of this chapter

In this chapter, a diagnostic method for nodal line semimetals that violate the compatibility condition has been obtained by subgroup reduction in C_4 symmetric space groups. The obtained method is based on the four δ indices and they have been rewritten by using the symmetry and BZ of each Bravais lattice before the subgroup reduction. The obtained method has been shown with specific examples to be able to diagnose nodal line semimetals that had not been diagnosed by previous methods.

Chapter 4

Intrinsic link between nodal line semimetals and topological crystalline insulators

In chapter 3, we have defined the δ indices as a new diagnostic method of nodal line semimetals and have confirmed that some materials are diagnosed as nodal line semimetals by the indices. In this chapter, we move on to the other question presented in chapter 2 : to what kind of topological insulator class are these nodal line semimetals linked when SOC is introduced? However, unlike in the case of the $\mathbb{Z}_4$ index, the link is not obvious from the calculation formula of δ. Therefore, although we make some generalizations, we perform some case studies based on the obtained material examples.

We construct effective models that describe the nodal lines in these materials and prove they are linked to topological crystalline insulators by explicitly calculating topological invariants. Furthermore, we show that their nodal line configurations correspond to what kind of topological invariants are nontrivial in the obtained topological crystalline insulators. This result shows that turning off SOC and examining the nodal line configuration can distinguish the two topological crystalline insulator classes that have not been distinguished by previous methods.

4.1 Nodal line semimetals in face centered cubic lattice

First, we focus on the nodal line semimetals in the FCC lattice (Space group 225) system. Based on the proposed material examples [78, 79] (section 3.4), we construct a generalized two-bands effective model, which keeps the same nodal line structure as the material examples. By using the model, we show that the nodal line in the system is intrinsically linked to a mirror Chern number when SOC is introduced. Furthermore, we show that the difference in the configuration of the nodal line corresponds to the difference between the topological crystalline insulator classes. After the calculation and discussion on the model, we show that the intrinsic line is confirmed by first-principles calculations in some materials examples.

4.1.1 Target system

We assume a nodal line semimetal in the FCC system without SOC (Fig. 4.1). To focus on a more concrete system, we construct a half-filled two-bands simple effective model based on some realistic materials such as FCC Ca, Sr, Yb, and SnSe, which are proposed as nodal line semimetals [78, 79]. It is reported that the nodal lines in the FCC systems show two different configurations (Fig. 4.1(b) and (d)) and they are connected by a parameter tuning [78]. To describe the realistic systems well and obtain a generalized model, the two-bands model should satisfy the following assumptions.

(i) The nodal lines are given as a result of band inversion at the L point and they are protected by TR+inversion symmetry [41, 65] [Fig. 4.1(b)].

(ii) The band inversion at the L point does not make a mirror protected nodal line on the (110) plane, i.e., the inverted two bands have the same mirror eigenvalues.

(iii) By tuning a parameter, nodal lines touch each other and reconnection occurs on the Σ line [Fig. 4.1(c)].

(iv) After the reconnection, the nodal lines are located around the W point and there is no nodal line on the (001) plane [Fig. 4.1(d)].

To satisfy the assumption (i), the band structure of the two-bands model must have a crossing point on the C_2-invariant line (L-W line or Q line), and the two bands must have different C_2 rotational eigenvalues. Considering these assumptions, we can determine the irreps of bands in the two-bands model as following. The irreps on each high symmetry point and line and their labeling are given in Tables 4.1, 4.2, 4.3.

L point

The two bands must satisfy the following conditions.

- The two bands have the same mirror eigenvalue for m_v (no nodal line on the mirror plane).

- The two bands have different C_2 rotation eigenvalues.

- The two bands are nondegenerate bands.

The pair of two bands that satisfy these conditions is $\{\Gamma_1^+, \Gamma_2^-\}$ or $\{\Gamma_2^+, \Gamma_1^-\}$.

W point

The two bands must satisfy the following conditions.

- The two bands have the same mirror eigenvalue for m_d (no nodal line on the mirror plane).

- The two bands have different C_2 rotation eigenvalues.

- The two bands are nondegenerate bands.

The pair of two bands that satisfy these conditions is $\{\Gamma_1, \Gamma_4\}$ or $\{\Gamma_2, \Gamma_3\}$.
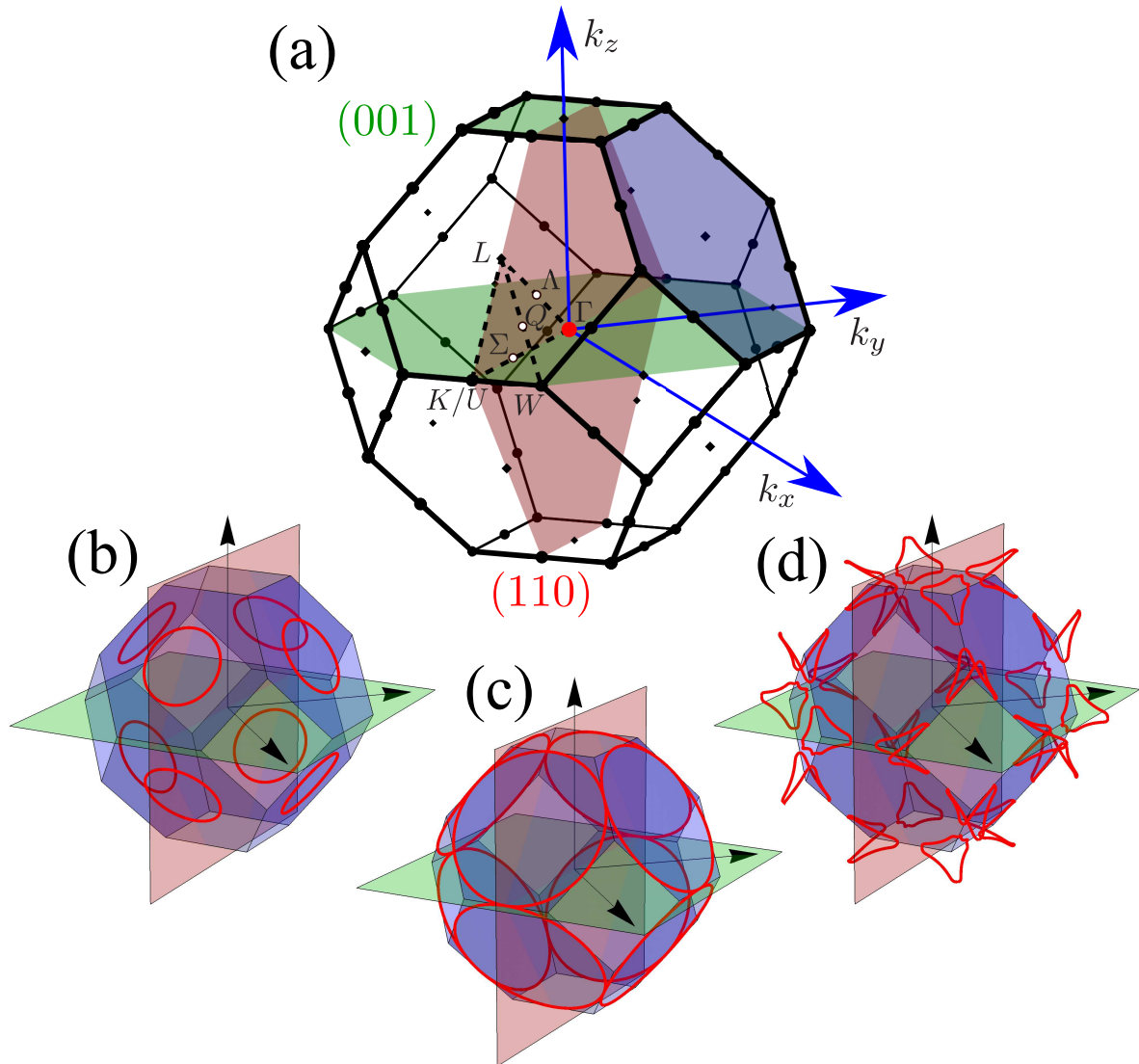
Figure 4.1. (a) Brillouin zone of face centered cubic lattice (Space group #225, $Fm\bar{3}m$). (b)(d) Nodal lines (red lines) in the system we assume. The configuration of nodal lines depends on a parameter. The (001) mirror plane and the (110) mirror plane is shown as green and red planes, respectively. The hexagonal surface of the BZ is shown as a blue plane for convenience, though it is not a high-symmetry plane.

Σ line

The two bands must satisfy the following conditions.

- The two bands have the same mirror eigenvalue for m_x (no nodal line on the mirror plane).

- The two bands have the same mirror eigenvalue for m_y (no nodal line on the mirror plane).

- The two bands are nondegenerate bands.

The pair of two bands which satisfy these conditions is $\{\Gamma_1, \Gamma_1\}$ or $\{\Gamma_2, \Gamma_2\}$ or $\{\Gamma_3, \Gamma_3\}$ or $\{\Gamma_4, \Gamma_4\}$.

Table 4.1: Point group D_{3d} and its irreps. This point group is a little group of the L-point. The m_v is the (110) mirror, and the C_2' is the rotation around the Q-line.

	L point					
D_{3d}	E	$2C_3$	$3C_2'$	I	$2IC_3$	$3m_v$
Γ_1^+	1	1	1	1	1	1
Γ_2^+	1	1	−1	1	1	−1
Γ_3^+	2	−1	0	2	−1	0
Γ_1^-	1	1	1	−1	−1	−1
Γ_2^-	1	1	−1	−1	−1	1
Γ_3^-	2	−1	0	−2	1	0

Table 4.2: Point group D_{2d} and its irreps. This point group is a little group of the W-point. The m_d is the (001) mirror, and the C_2' is the Q-line.

	W-point				
D_{2d}	E	$2IC_4$	C_2	$2C_2'$	$2m_d$
Γ_1	1	1	1	1	1
Γ_2	1	1	1	−1	−1
Γ_3	1	−1	1	1	−1
Γ_4	1	−1	1	−1	1
Γ_5	2	0	−2	0	0

Table 4.3: Point group C_{2v} and its irreps. This point group is a little group of the Σ-line. The m_y is the (110) mirror, and the m_x is the (001) mirror.

	Σ-line			
C_{2v}	E	C_2	m_y	m_x
Γ_1	1	1	1	1
Γ_2	1	1	−1	−1
Γ_3	1	−1	1	−1
Γ_4	1	−1	−1	1

Band connection

By considering the compatibility condition [82, 56], we can decide how the bands in each high-symmetry point (line) are connected. When the system has nodal lines, the irreps of the occupied band on the L point and the W point must violate the compatibility condition along the L-W line, i.e., the eigenvalues of the C_2 rotation along the L-W are different in both ends. The possible combinations are given in Table 4.4. A schematic picture of the band dispersion of the case Table 4.4(1) is shown in Fig. 4.2.

Table 4.4: Possible set of irreps of bands on each high-symmetry points.

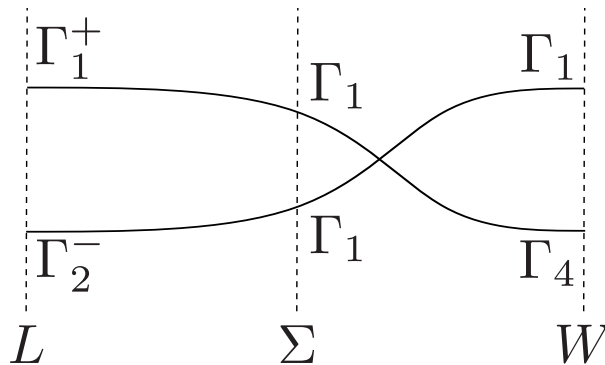|	L-point	Σ-line	W-point
(1)	$\{\Gamma_1^+, \Gamma_2^-\}$	$\{\Gamma_1, \Gamma_1\}$	$\{\Gamma_4, \Gamma_1\}$
(2)	$\{\Gamma_1^+, \Gamma_2^-\}$	$\{\Gamma_3, \Gamma_3\}$	$\{\Gamma_3, \Gamma_2\}$
(3)	$\{\Gamma_2^+, \Gamma_1^-\}$	$\{\Gamma_2, \Gamma_2\}$	$\{\Gamma_3, \Gamma_2\}$
(4)	$\{\Gamma_2^+, \Gamma_1^-\}$	$\{\Gamma_4, \Gamma_4\}$	$\{\Gamma_4, \Gamma_1\}$

Figure 4.2. Schematic picture of the band dispersion of the case (1) in Table 4.4. The band crossing is placed on the right side of the Σ line for convenience. However, the band crossing emerges in a generic point, and thus it is not generally determined on which side it should be.

4.1.2 $\boldsymbol{k} \cdot \boldsymbol{p}$ model calculations

Since the irreps of bases have been obtained, we construct two-by-two models with nodal line by using the $\boldsymbol{k} \cdot \boldsymbol{p}$ perturbation within the second-order of $|\boldsymbol{k}|$ for each high symmetry point (line). Here we call the constructed model "local models" at the L point, the W point, and the Σ line. Although we have obtained four possible combinations of irreps, the following discussion is the same for all of them and thus the case (1) in Table 4.4.

When SOC term with an amplitude $\lambda(> 0)$ is introduced into the local models, they get gapped and the Berry curvature and the mirror Chern numbers can be calculated. By considering a small SOC (small λ) case, we discuss an intrinsic link from nodal lines to the mirror Chern numbers. Especially on Σ line, we discuss how the reconnection of nodal lines affects the Berry curvature and the mirror Chern numbers. The results of calculations in each local models are summarized in Fig. 4.8.

Before going to each local model, we clarify the definition of the mirror Chern number. The mirror Chern number is defined in systems with significant SOC. When a system has a mirror symmetry, the Hamiltonian on the mirror-invariant plane is block diagonalized into two sectors with mirror eigenvalues[1] $\pm i$. Then, we can calculate the Chern number in each sector, $\mathcal{C}_+$ and $\mathcal{C}_-$, and the mirror Chern number $n_\mathcal{M}$ is given as

$$n_\mathcal{M} = \frac{\mathcal{C}_+ - \mathcal{C}_-}{2}. \tag{4.1}$$

Note that $\mathcal{C}_+ = -\mathcal{C}_-$ is always satisfied and thus we need to calculate only $\mathcal{C}_+$.

L point

The coordinate system of the local model around the L point is shown in Fig. 4.3. The origin is placed at the L point and the k_z axis is parallel to the Λ line, which is the C_3 rotation axis. The k_z axis is perpendicular to the hexagonal face of the BZ (the blue plane in Fig. 4.1(a)). The k_x axis is parallel to the Q line, which is the C_2' rotation axis. The m_v mirror-invariant plane, which is the (110) plane, is the $k_x = 0$ plane.

By taking two bases that belong to Γ_1^+ and Γ_2^-, the symmetry operators are written as

$$\begin{aligned} C_2' &\to \sigma_z, \\ I &\to \sigma_z, \\ m_v &\to \sigma_0, \\ \mathcal{T} &\to \mathcal{K}, \end{aligned} \tag{4.2}$$

where the $\sigma_{x,y,z}$ are the Pauli matrices for orbitals and σ_0 is the two-by-two identity matrix. $\mathcal{T}$ is the TR operator and $\mathcal{K}$ is the complex conjugate operator. The local model

---

[1] Since spinful systems are transformed with a representation of $SU(2)$, $m^2(= 2\pi$ rotation) gives -1.
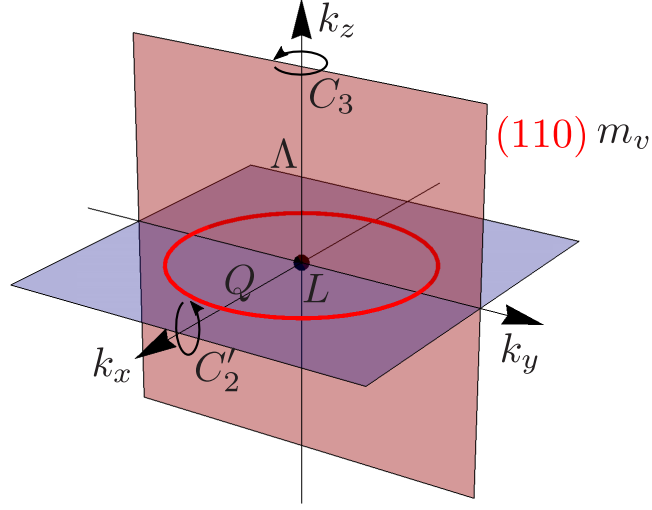
Figure 4.3. Coordinate system of the local model around the L point.

without SOC $H_L(k_x, k_y, k_z)$ must satisfy

$$
\begin{aligned}
C_2'^{-1} H_L(k_x, k_y, k_z) C_2' &= H_L(k_x, -k_y, -k_z), \\
I^{-1} H_L(k_x, k_y, k_z) I &= H_L(-k_x, -k_y, -k_z), \\
m_v^{-1} H_L(k_x, k_y, k_z) m_v &= H_L(k_x, k_y, -k_z), \\
\mathcal{T}^{-1} H_L(k_x, k_y, k_z) \mathcal{T} &= H_L(-k_x, -k_y, -k_z).
\end{aligned}
\tag{4.3}
$$

From these restrictions, $H_L(k_x, k_y, k_z)$ is determined as

$$
H_L(\boldsymbol{k}) = k_z \sigma_y + (k_x^2 + k_y^2 + k_z^2 - \Delta^2)\sigma_z,
\tag{4.4}
$$

where Δ is a real positive constant. We neglect some degree of freedom to make the model simple, e.g., a constant energy shift by σ_0, and the coefficient of the k_z term. It is because they are negligible in our calculation of the topological invariants. The gapless points of this model are given as a solution of

$$
\begin{cases}
k_z = 0 \\
k_x^2 + k_y^2 + k_z^2 - \Delta^2 = 0
\end{cases}.
\tag{4.5}
$$

The solution of these equations is a ring with a radius Δ on the k_x-k_y plane [Fig. 4.3].

When SOC is introduced, operations of the spin part are added to the symmetry operators as

$$
\begin{aligned}
C_2' &\rightarrow i\sigma_z s_x, \\
I &\rightarrow \sigma_z s_0, \\
m_v &\rightarrow -i\sigma_0 s_x, \\
\mathcal{T} &\rightarrow i s_y \mathcal{K},
\end{aligned}
\tag{4.6}
$$

where $s_{x,y,z}$ are the Pauli matrices the spin degree of freedom (see Appendix D.2 for the way to decide the spin parts). Within these restrictions, a Rashba-type SOC term [83, 84] is allowed as the leading order of k. By introducing SOC terms with an amplitude $\lambda(> 0)$, the four-by-four local model with SOC is written as

$$H_{L,\mathrm{soc}} = H_L s_0 + \lambda \sigma_x (-k_y s_x + k_x s_y). \tag{4.7}$$

As a result of introducing the SOC term, the nodal line vanishes and the model becomes gapped.

On the (110) plane [the $k_x = 0$ plane], the model is rewritten as

$$H_{L,\mathrm{soc}} = k_z \sigma_y s_0 + (k_y^2 + k_z^2 - \Delta^2)\sigma_z s_0 - \lambda \sigma_x k_y s_x. \tag{4.8}$$

By using a unitary transformation $U = \sigma_0 \frac{1}{\sqrt{2}}(s_x + s_z)$, the model is block diagonalized as

$$U^\dagger H_{L,\mathrm{soc}} U = k_z \sigma_y s_0 + (k_y^2 + k_z^2 - \Delta^2)\sigma_z s_0 - \lambda \sigma_x k_y s_z. \tag{4.9}$$

The (110) mirror operator is also transformed as $U^\dagger(-i\sigma_0 s_x)U = -i\sigma_0 s_z$. Now the two blocks are corresponding to the blocks with $+i$ and $-i$ mirror eigenvalues, respectively. They are explicitly given as

$$H_{L,+} = X_L \sigma_x + Y_L \sigma_y + Z_L \sigma_z, \tag{4.10}$$

$$H_{L,-} = -X_L \sigma_x + Y_L \sigma_y + Z_L \sigma_z, \tag{4.11}$$

$$X_L = \lambda k_y \quad , \quad Y_L = k_z \quad , \quad Z_L = k_y^2 + k_z^2 - \Delta^2. \tag{4.12}$$

The Berry connection of the occupied band of $H_{L,+}$ is calculated as

$$
\begin{aligned}
A_{L,+,y} &= \frac{-\lambda k_z}{2R_L(R_L - Z_L)}, \\
A_{L,+,z} &= \frac{\lambda k_y}{2R_L(R_L - Z_L)},
\end{aligned}
\tag{4.13}
$$

where R_L is defined as

$$R_L = \sqrt{X_L^2 + Y_L^2 + Z_L^2}. \tag{4.14}$$

The x component of the Berry curvature is given as

$$
\begin{aligned}
B_{L,+,x} &= \frac{\partial A_{L,+,z}}{\partial k_y} - \frac{\partial A_{L,+,y}}{\partial k_z} \\
&= \frac{\lambda}{2R_L^3}(Z_L + 2\Delta^2).
\end{aligned}
\tag{4.15}
$$

The λ dependence of $B_{L,+,x}$ is shown in Fig. 4.4. When λ is large, for example $\lambda = 1.00$, $B_{L,+,x}$ is spread widely. As λ getting smaller, sharper peaks appear on the points where the nodal line penetrates when SOC is neglected. Since the mirror Chern number is topological invariant, it must be independent with λ. Therefore, the nodal line is considered as a source of the mirror Chern number. The Chern number of the occupied

$\Delta = 1$

$\lambda = 1.00$

$B_{+,x}$

$\Delta = 1$

$\lambda = 0.50$

$B_{+,x}$

$\Delta = 1$

$\lambda = 0.01$

$B_{+,x}$
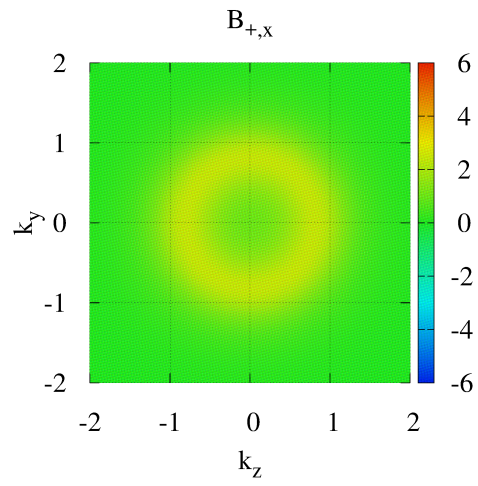
Figure 4.4. λ dependence of $B_{L,+,x}$.

band of the $+i$ block, $\mathcal{C}_{L,+}$, is calculated by integrating the Berry connection on a circle path $(k_y, k_z) = (k\cos\theta, k\sin\theta)$,

$$
\begin{aligned}
\mathcal{C}_{L,+} &= \frac{1}{2\pi}\oint d\boldsymbol{k}\cdot\boldsymbol{A} \\
&= \frac{1}{2\pi}\int_0^{2\pi} d\theta \frac{\lambda k^2}{k^2(\cos^2\theta + \lambda^2\sin^2\theta)} \\
&= \frac{\lambda}{|\lambda|}.
\end{aligned}
\tag{4.16}
$$

Here we assume $k \gg 1$, and then $R_L \sim |Z_L|$ and $R_L - Z_L \sim \frac{X_L^2 + Y_L^2}{2|Z_L|}$. Using the relation $\mathcal{C}_{L,-} = -\mathcal{C}_{L,+}$, the mirror Chern number $n_{L,\mathcal{M}_{(110)}}$ of this local model is given as

$$
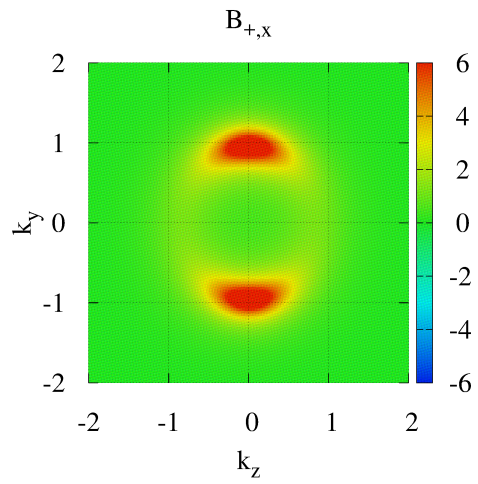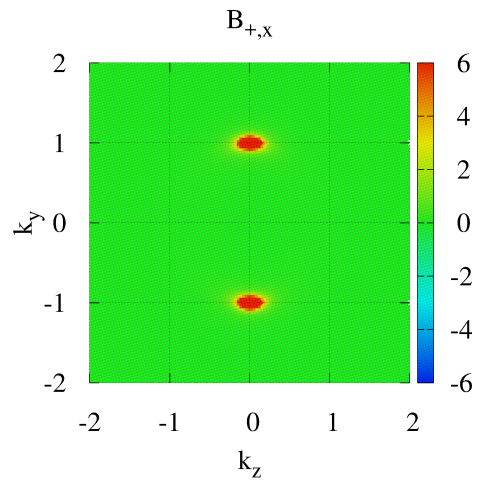n_{L,\mathcal{M}_{(110)}} = \frac{\mathcal{C}_{L,+} - \mathcal{C}_{L,-}}{2} = \frac{\lambda}{|\lambda|} = 1.
\tag{4.17}
$$

It is proved that the mirror Chern number of this local model is $n_{L,\mathcal{M}_{(110)}} = 1$ [Fig. 4.8(d-1)]. Since there are two nonequivalent L point on the (110) plane, the mirror Chern number of the whole BZ is $n_{\mathcal{M}_{(110)}} = 2$ [Fig. 4.8(f-1)]. Here nonequivalent means that the two L points are not connected by the reciprocal lattice vectors.

W point

The coordinate system of the local model around the W point is shown in Fig. 4.5. The origin is placed at the W point and the k_z axis is parallel to the Z line, which is the C_2 rotation axis. The m_d mirror-invariant plane, which is the (001) plane, is the $k_x = 0$ plane. The Q line, which is C_2' rotation axis, is a line represented as $\{k_x + k_y = 0$ and $k_z = 0\}$.

By taking two bases the belong to Γ_1 and Γ_4, the symmetry operators are written as

$$
\begin{aligned}
C_2' &\rightarrow \sigma_z, \\
m_d &\rightarrow \sigma_0, \\
\mathcal{T} &\rightarrow \mathcal{K}.
\end{aligned}
\tag{4.18}
$$

The local model without SOC $H_W(k_x, k_y, k_z)$ must satisfy

$$
\begin{aligned}
C_2'^{-1} H_W(k_x, k_y, k_z) C_2' &= H_W(-k_y, -k_x, -k_z) \\
m_d^{-1} H_W(k_x, k_y, k_z) m_d &= H_W(-k_x, k_y, k_z) \\
\mathcal{T}^{-1} H_W(k_x, k_y, k_z)\mathcal{T} &= H_W(-k_x, -k_y, -k_z)
\end{aligned}
\tag{4.19}
$$

From these restrictions, $H_W(k_x, k_y, k_z)$ is determined as

$$
H_W(\boldsymbol{k}) = (k_z + ak_x^2 - ak_y^2)\sigma_y + (k_x^2 + k_y^2 + k_z^2 - \Delta^2)\sigma_z,
\tag{4.20}
$$

where $\Delta(>0)$ and a are real constants. Here, irrelevant terms are neglected again. In this model, a nodal line emerges around the W point and it is oscillating in the k_z direction, keeping C_2 rotation symmetry around the k_z axis [Fig. 4.5].
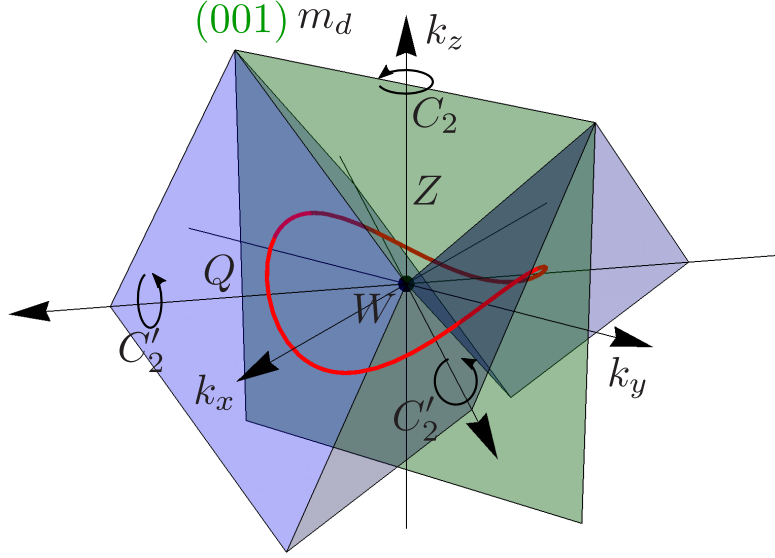
Figure 4.5. Coordinate system of the local model around the W point.

When SOC is introduced, the symmetry operators with spin parts are written as

$$
\begin{aligned}
C_2' &\rightarrow i\frac{1}{\sqrt{2}}\sigma_z(s_x + s_y), \\
m_d &\rightarrow -i\sigma_0 s_x, \\
\mathcal{T} &\rightarrow i s_y \mathcal{K}.
\end{aligned}
\tag{4.21}
$$

The four-by-four local model with SOC (amplitude λ) is written as

$$
H_{W,\text{soc}}(\boldsymbol{k}) = H_W s_0 + \lambda\sigma_x(-k_y s_x + k_x s_y).
\tag{4.22}
$$

On the (001) plane [the $k_x = 0$ plane], the model is rewritten as

$$
H_{W,\text{soc}} = (k_z - ak_y^2)\sigma_y s_0 + (k_y^2 + k_z^2 - \Delta^2)\sigma_z s_0 - \lambda\sigma_x k_y s_x.
\tag{4.23}
$$

By using a unitary transformation $U = \sigma_0 \frac{1}{\sqrt{2}}(s_x + s_z)$, the model is block diagonalized as

$$
U^\dagger H_{W,\text{soc}} U = (k_z - ak_y^2)\sigma_y s_0 + (k_y^2 + k_z^2 - \Delta^2)\sigma_z s_0 - \lambda\sigma_x k_y s_z.
\tag{4.24}
$$

The (001) mirror operator is also transformed as $U^\dagger(-i\sigma_0 s_x)U = -i\sigma_0 s_z$. The two block with $+i$ and $-i$ mirror eigenvalues are explicitly given as

$$
H_{W,+} = X_W\sigma_x + Y_W\sigma_y + Z_W\sigma_z,
\tag{4.25}
$$

$$
H_{W,-} = -X_W\sigma_x + Y_W\sigma_y + Z_W\sigma_z,
\tag{4.26}
$$

$$
X_W = \lambda k_y \quad, \quad Y_W = k_z - ak_y^2 \quad, \quad Z_W = k_y^2 + k_z^2 - \Delta^2.
\tag{4.27}
$$

The Berry connection of the occupied band of $H_{W,+}$ is calculated as

$$
\begin{aligned}
A_{W,+,y} &= \frac{-\lambda(k_z + ak_y^2)}{2R_W(R_W - Z_W)}, \\
A_{W,+,z} &= \frac{\lambda k_y}{2R_W(R_W - Z_W)},
\end{aligned}
\tag{4.28}
$$

where R_W is defined as

$$
R_W = \sqrt{X_W^2 + Y_W^2 + Z_W^2}.
\tag{4.29}
$$

The x component of the Berry curvature is given as

$$
\begin{aligned}
B_{W,+,x} &= \frac{\partial A_{W,+,z}}{\partial k_y} - \frac{\partial A_{W,+,y}}{\partial k_z} \\
&= \frac{\lambda}{2R_W^3}(Z_W + 2\Delta^2 + 2ak_y^2 k_z).
\end{aligned}
\tag{4.30}
$$

The λ dependence of $B_{W,+,x}$ is shown in Fig. 4.6. Similarly to the case of the L point, the sharp peak feature in a small λ region is seen. Therefore, the nodal line is considered as a source of the mirror Chern number also in this case. The Chern number of the occupied band of the $+i$ block is calculated by integrating the Berry connection on a closed path $(k_y, k_z) = (k\cos\theta, k\sin\theta + ak^2\cos^2\theta)$,

$$
\begin{aligned}
\mathcal{C}_{W,+} &= \frac{1}{2\pi}\oint d\boldsymbol{k}\cdot\boldsymbol{A} \\
&= \frac{1}{2\pi}\int_0^{2\pi} d\theta \frac{\lambda k^2}{k^2(\cos^2\theta + \lambda^2\sin^2\theta)} \\
&= \frac{\lambda}{|\lambda|}.
\end{aligned}
\tag{4.31}
$$

Note that the closed path always involves the points where sharp peaks appear. The mirror Chern number $n_{W,\mathcal{M}_{(001)}}$ is given as

$$
n_{W,\mathcal{M}_{(001)}} = \frac{\mathcal{C}_{W,+} - \mathcal{C}_{W,-}}{2} = \frac{\lambda}{|\lambda|} = 1
\tag{4.32}
$$

It is proved that the mirror Chern number of this local model is calculated as $n_{W,\mathcal{M}_{(001)}} = 1$ [Fig. 4.8(d-3)]. There are four nonequivalent X points on the (001) plane and the mirror Chern number of the whole BZ is calculated as $n_{\mathcal{M}_{(001)}} = 4$ [Fig. 4.8(f-2)].

Σ line

The coordinate system of the local model around the Σ line is shown in Fig. 4.7. Now the local model should be constructed to represent the reconnection of nodal lines by tuning a parameter. The symmetry of the FCC lattice requires that the reconnection of the nodal lines should occur on the Σ line. The origin is placed at the point where the

$\Delta = 1$

$a = 0.5$

$\lambda = 1.00$

$\Delta = 1$

$a = 0.5$

$\lambda = 0.50$

$\Delta = 1$

$a = 0.5$

$\lambda = 0.01$
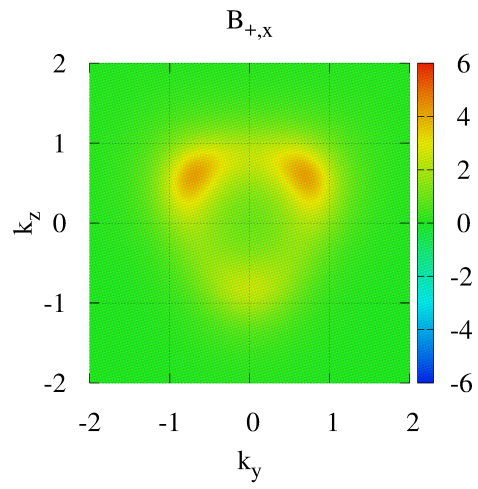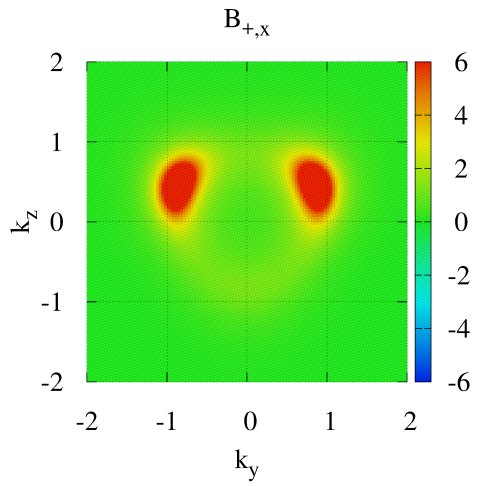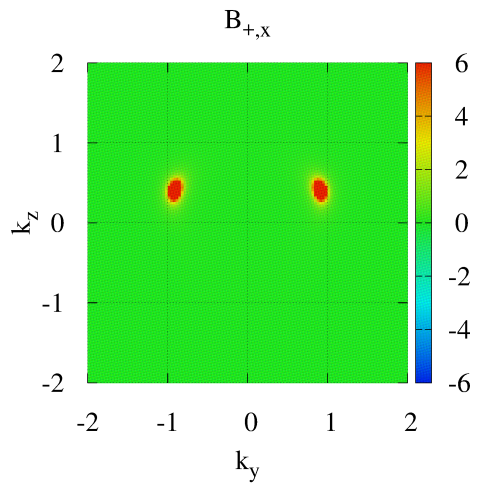
Figure 4.6. λ dependence of $B_{W,+,x}$.
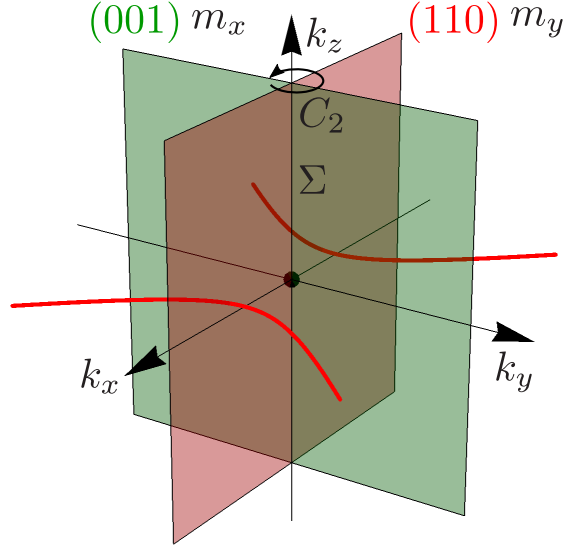
Figure 4.7. Coordinate system of the local model around the Σ line.

reconnection of nodal lines occurs. The k_z axis is parallel to the Σ line. The (001) mirror plane and the (110) mirror plane are the $k_x = 0$ plane and the $k_y = 0$ plane, respectively.

By taking two bases that belong to the same irrep Γ_1, the symmetry operators are written as

$$
\begin{aligned}
m_x &\rightarrow \sigma_0, \\
m_y &\rightarrow \sigma_0, \\
\mathcal{T} &\rightarrow \mathcal{K}.
\end{aligned}
\tag{4.33}
$$

The local model without SOC $H_\Sigma(k_x, k_y, k_z)$ must satisfy

$$
\begin{aligned}
m_x^{-1} H_\Sigma(k_x, k_y, k_z) m_x &= H_\Sigma(-k_x, k_y, k_z), \\
m_y^{-1} H_\Sigma(k_x, k_y, k_z) m_y &= H_\Sigma(k_x, -k_y, k_z), \\
\mathcal{T}^{-1} H_\Sigma(k_x, k_y, k_z) \mathcal{T} &= H_\Sigma(-k_x, -k_y, -k_z).
\end{aligned}
\tag{4.34}
$$

To satisfy these restrictions and represent the nodal line reconnection, $H_\Sigma(k_x, k_y, k_z)$ is determined as

$$
H_\Sigma(\boldsymbol{k}) = k_z \sigma_y + (k_x^2 - k_y^2 + k_z^2 + b)\sigma_z,
\tag{4.35}
$$

where b is a real tuning parameter. In this model, hyperbolic nodal lines emerge on the k_x-k_y plane and a reconnection of them occurs at the origin when $b = 0$ [Fig. 4.7].

When SOC is introduced, the symmetry operators are written as

$$
\begin{aligned}
m_x &\rightarrow -i\sigma_0 s_x, \\
m_y &\rightarrow i\sigma_0 s_y, \\
\mathcal{T} &\rightarrow i s_y \mathcal{K}.
\end{aligned}
\tag{4.36}
$$

71

The four-by-four local model with SOC (amplitude λ) is written as

$$H_{\Sigma,\text{soc}}(\boldsymbol{k}) = H_\Sigma s_0 + \lambda \sigma_x(-k_y s_x + k_x s_y), \tag{4.37}$$

On the $k_x = 0$ plane [the (001) mirror plane], the model is block diagonalized with a unitary transformation $U_1 = \sigma_0 i \frac{1}{\sqrt{2}}(s_x + s_z)$ as

$$H_{\Sigma,+}^{(k_x=0)} = X_{\Sigma,x}\sigma_x + Y_{\Sigma,x}\sigma_y + Z_{\Sigma,x}\sigma_z, \tag{4.38}$$

$$H_{\Sigma,-}^{(k_x=0)} = -X_{\Sigma,x}\sigma_x + Y_{\Sigma,x}\sigma_y + Z_{\Sigma,x}\sigma_z, \tag{4.39}$$

$$X_{\Sigma,x} = \lambda k_y \quad , \quad Y_{\Sigma,x} = k_z \quad , \quad Z_{\Sigma,x} = -k_y^2 + k_z^2 + b. \tag{4.40}$$

The mirror operator about the $k_x = 0$ plane is also transformed as $U_1^\dagger(-i\sigma_0 s_x)U_1 = -i\sigma_0 s_z$. The Berry connection of the occupied band of $H_{\Sigma,+}^{(k_x=0)}$ is calculated as

$$
\begin{aligned}
A_{\Sigma,+,y}^{(k_x=0)} &= \frac{\lambda k_z}{2R_{\Sigma,(k_x=0)}(R_{\Sigma,(k_x=0)} - Z_{\Sigma,x})}, \\
A_{\Sigma,+,z}^{(k_x=0)} &= \frac{-\lambda k_y}{2R_{\Sigma,(k_x=0)}(R_{\Sigma,(k_x=0)} - Z_{\Sigma,x})}, \\
R_{\Sigma,(k_x=0)} &= \sqrt{X_{\Sigma,x}^2 + Y_{\Sigma,x}^2 + Z_{\Sigma,x}^2}
\end{aligned}
\tag{4.41}
$$

and the x component of the Berry curvature is given as

$$
\begin{aligned}
B_{\Sigma,+,x}^{(k_x=0)} &= \frac{\partial A_{\Sigma,+,x}^{(k_x=0)}}{\partial k_y} - \frac{\partial A_{\Sigma,+,x}^{(k_x=0)}}{\partial k_z} \\
&= \frac{-\lambda}{2R_{\Sigma,(k_x=0)}^3}(Z_{\Sigma,x} - 2b).
\end{aligned}
\tag{4.42}
$$

When $b > 0$, the Berry curvature $B_{\Sigma,+,x}^{(k_x=0)}$ has sharp peaks [Fig. 4.8(c-2), top right] at the points where the nodal lines penetrate when SOC is neglected. As b getting smaller, the two peaks get closer, and they meet each other when $b = 0$ [Fig. 4.8(c-2), top middle] and vanish in $b < 0$ [Fig. 4.8(c-2), top left]. The b dependence of the mirror Chern number of this local model $n_{\Sigma,\mathcal{M}_{(001)}}$ is numerically evaluated as

$$
n_{\Sigma,\mathcal{M}_{(001)}} = \begin{cases} 1 \ (b > 0) \\ 0 \ (b < 0) \end{cases}, \tag{4.43}
$$

and the result is shown in Fig. 4.8(d-2). The mirror Chern number is changed at $b = 0$.

Next, we focus on the $k_y = 0$ plane. On the $k_y = 0$ plane [the (110) mirror plane], the model is block diagonalized with a unitary transformation $U_2 = \sigma_0 i \frac{1}{\sqrt{2}}(s_y + s_z)$ as

$$H_{\Sigma,+}^{(k_y=0)} = X_{\Sigma,y}\sigma_x + Y_{\Sigma,y}\sigma_y + Z_{\Sigma,y}\sigma_z, \tag{4.44}$$

$$H_{\Sigma,-}^{(k_y=0)} = -X_{\Sigma,y}\sigma_x + Y_{\Sigma,y}\sigma_y + Z_{\Sigma,y}\sigma_z, \tag{4.45}$$

$$X_{\Sigma,y} = \lambda k_x \quad , \quad Y_{\Sigma,y} = k_z \quad , \quad Z_{\Sigma,y} = k_x^2 + k_z^2 + b. \tag{4.46}$$

The mirror operator about the $k_y = 0$ plane is also transformed as $U_2^\dagger i\sigma_0 s_y U_2 = i\sigma_0 s_z$. The Berry connection of the occupied band of $H_{\Sigma,+}^{(k_y=0)}$ is calculated as

$$
\begin{aligned}
A_{\Sigma,+,x}^{(k_y=0)} &= \frac{\lambda k_z}{2R_{\Sigma,(k_y=0)}(R_{\Sigma,(k_y=0)} - Z_{\Sigma,y})}, \\
A_{\Sigma,+,z}^{(k_y=0)} &= \frac{-\lambda k_x}{2R_{\Sigma,(k_y=0)}(R_{\Sigma,(k_y=0)} - Z_{\Sigma,y})}, \\
R_{\Sigma,(k_y=0)} &= \sqrt{X_{\Sigma,y}^2 + Y_{\Sigma,y}^2 + Z_{\Sigma,y}^2}
\end{aligned}
\tag{4.47}
$$

and the y component of the Berry curvature is given as

$$
\begin{aligned}
B_{\Sigma,+,y}^{(k_y=0)} &= \frac{\partial A_{\Sigma,+,x}^{(k_y=0)}}{\partial k_z} - \frac{\partial A_{\Sigma,+,z}^{(k_y=0)}}{\partial k_x} \\
&= \frac{\lambda}{2R_{\Sigma,(k_y=0)}^3}(Z_{\Sigma,y} - 2b).
\end{aligned}
\tag{4.48}
$$

Contrary to the $k_x = 0$ plane, the sharp peak feature of the Berry curvature on the $k_y = 0$ plane is seen only when $b < 0$ [Fig. 4.8(c-2), bottom three panels]. The mirror Chern number of this local model $n_{\Sigma,\mathcal{M}_{(110)}}$ is numerically evaluated as

$$n_{\Sigma,\mathcal{M}_{(110)}} = \begin{cases} 0 \ (b > 0) \\ 1 \ (b < 0) \end{cases}, \tag{4.49}$$

and it also shows a contrasting behavior to $n_{\Sigma,\mathcal{M}_{(001)}}$ [Fig. 4.8(d-2)].

In both of the results on the $k_x = 0$ plane and the $k_y = 0$ plane, the nodal lines are considered as sources of the mirror Chern numbers. Furthermore, by comparing the two results, we can see that the $b = 0$ is a phase transition point. Considering that the $b = 0$ is the reconnection point of the nodal lines, the reconnection of nodal lines in the system without SOC corresponds to the topological phase transition in the system with SOC. Actually, when $b = 0$, the model Eq. (4.37) has a gapless point at $\boldsymbol{k} = 0$. It is reasonable because generally a gap closing is required for a topological phase transition [17,35]. Finally, we calculate the mirror Chern numbers of the whole BZ. The mirror numbers are $n_{\mathcal{M}_{(110)}} = 0$ and $n_{\mathcal{M}_{(001)}} = 4$ for $b > 0$, and $n_{\mathcal{M}_{(110)}} = 2$ and $n_{\mathcal{M}_{(001)}} = 0$ for $b < 0$. Although the transition of the mirror Chern numbers is one by one in the local model, the transition in the whole BZ occurs between $n_{\mathcal{M}_{(001)}} = 4$ and $n_{\mathcal{M}_{(110)}} = 2$. It is explained as follows. The reconnections of the nodal lines occur in twelve points in the BZ. In the BZ, there are three symmetric planes for the (001) plane, but on the other hand, there are six symmetric planes for the (110) plane. Due to the difference of the multiplicity, the one by one transitions in the reconnection points result in the two by four transition in the whole BZ.
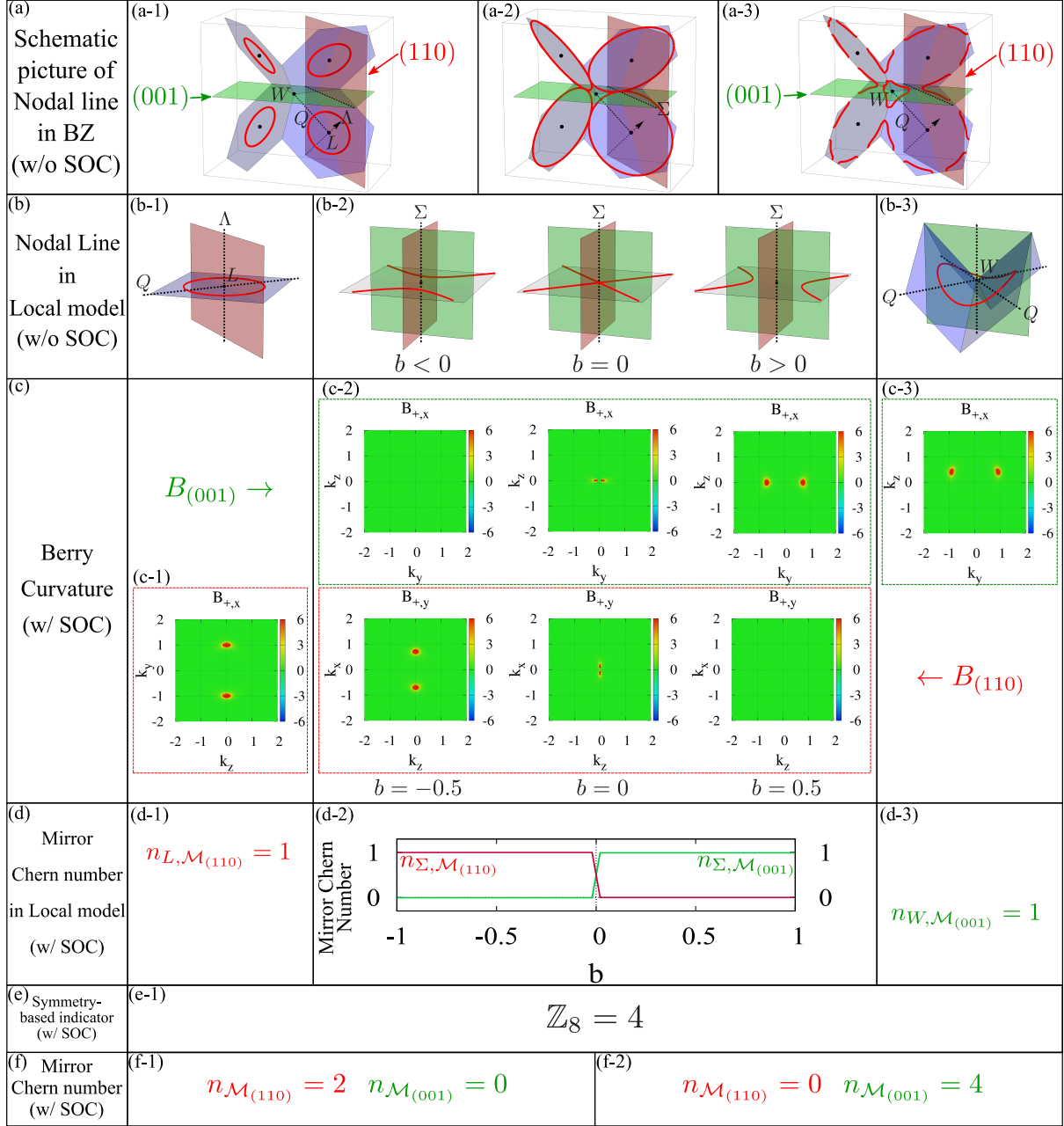
Figure 4.8. (a) Schematic pictures of the two different configurations of nodal lines (red ring) in the target systems (a-1)(a-3) and the reconnection of them on the Σ line (a-2). (b) Schematic pictures of the local models and nodal lines around the L point (b-1), Σ line (b-2), and W point (b-3). For (b-2), the left, middle, and right ones are the $b < 0$, $b = 0$, and $b > 0$ case, respectively. (c) Momentum dependence of the Berry curvature. (c-1) (110) component of Berry curvature in the local model around the L point. (c-2) Top (bottom) three panels are the (001) component ((110) component) of the Berry curvature in the local model around the Σ line. For both rows, the left, middle, and right ones are the $b < 0$, $b = 0$, and $b > 0$ case, respectively. (c-3) (001) component of Berry curvature in the local model around the W point. (d) Mirror Chern number of the local models around the L point (d-1), Σ line (with the b dependence), and W point. (e) Symmetry-based indicator (space group 255). (f) Mirror Chern numbers of the whole BZ. These values are calculated from (d) by counting how many L points (W points) exist on the (110) mirror plane [(001) mirror plane].

4.1.3 Discussion in the whole Brillouin zone

Although the local models are discussed separately, they are originated from a two-bands model in the whole BZ as we assumed first. In the first assumption, there are two nodal line semimetals with different nodal line configurations. One of them has nodal lines roughly located around the L point [Fig. 4.8(a-1)], and the other has nodal lines roughly located around the W point [Fig. 4.8(a-3)]. The former includes the local model around the L point and the local model around the Σ line with $b < 0$. The latter includes the local model around the W point and the local model around the Σ line with $b > 0$. As shown in the local model calculations, when SOC is taken into account, the mirror Chern numbers are calculated by counting how many nodal rings locate on the mirror planes. The former nodal line semimetal is linked to the topological crystalline insulator with $(n_{\mathcal{M}_{(110)}}, n_{\mathcal{M}_{(001)}}) = (2, 0)$ [Fig. 4.8(f-1)], and the latter nodal line semimetal is linked to the topological crystalline insulator with $(n_{\mathcal{M}_{(110)}}, n_{\mathcal{M}_{(001)}}) = (0, 4)$ [Fig. 4.8(f-2)]. Now the obtained topological classes are topological crystalline insulator class when SOC is taken into account, and it has been known that there are eight topological classes (including a trivial class) indicated by the symmetry-based indicator $\mathbb{Z}_8$ in FCC (#225) with SOC [47][2]. It is noteworthy how our obtained classes are classified by the symmetry-based indicator $\mathbb{Z}_8$. Actually, both of the obtained classes have the same indicator $\mathbb{Z}_8 = 4$ [Fig. 4.8(e-1)]. The possible topological invariant combinations for $\mathbb{Z}_8 = 4$ are listed in Table 4.5. It includes our obtained classes, of course. The reason why our obtained classes have the same indicator is that the gap closing on the phase transition point, or the reconnection of nodal lines in the system without SOC, occurs between the two bands with the same irreps. Since the symmetry-based indicator checks the irreps of occupied bands, it must be identical before and after the phase transition. However, our result has shown that when SOC is turned off, there is a clear difference between nodal lines penetrating the (110) mirror plane and nodal lines penetrating the (001) mirror plane. Additionally, considering that the nodal line is crossing the Q line, it must penetrate one of the mirror planes. This means that when SOC is taken into account, the system cannot be topologically trivial and there are only two possible mirror Chern number combinations. This is consistent with the result of the symmetry-based indicator.

In real materials, it is usually difficult to tune the amplitude of SOC. However, in first-principles calculations, we can hypothetically calculate band dispersions without SOC. The result obtained above shows that two different topological crystalline insulators show different nodal line configurations when SOC is neglected, and examining the nodal line configuration leads to a subdividing diagnostic method beyond the symmetry-based indicator.

---

[2]Actually, four of them are prohibited by the compatibility condition in FCC.

Space group #225 : $Fm\bar{3}m$			
$\mathbb{Z}_8$	weak	$n_{\mathcal{M}_{(001)}}$	$n_{\mathcal{M}_{(110)}}$
4	000	0	2
4	000	4	0

Table 4.5: Possible topological invariant combinations for $\mathbb{Z}_8 = 4$ class in the space group 225 with significant SOC excerpted from Supplementary Table 7 in Ref.[49].

4.1.4 Material examples

In this section, we show the link proved in the previous sections is confirmed in material examples, FCC Ca and Ba. We calculate their band dispersions by the first-principles calculation for both cases with and without SOC. These calculations are performed by QUANTUM ESPRESSO [63], which uses the density functional theory [85, 86]. For the exchange-correlation term, generalized gradient approximation with Perdew-Burke-Ernzerhof parametrization [87] is used. The plane wave energy cutoff is set to 50 Ry and the $\boldsymbol{k}$-point grid on the BZ is taken as $8 \times 8 \times 8$ mesh. The lattice constants are 5.601 Å for Ca and 6.0520 Å for Ba [64, 59]. With the output of the first-principles calculations, we calculate the Wannier centers on the mirror-invariant planes by using Z2PACK code [88, 89]. Seeing the Wannier center flows, we calculate the mirror Chern numbers for the cases with SOC (See Appendix D.3 for the details).

The result for Ca is shown in Fig. 4.9. In Fig. 4.9(a), which is a band dispersion without SOC, we can see a band crossing on the W-L line (denoted by a red circle). As explained before, this band crossing is a part of a nodal line. For the (110) and (001) mirror planes, the band gaps between the two bands that make the nodal line are shown in Figs.4.9(e) and 3(f). The rectangle area of Fig. 4.9(e) [the square area of Fig. 4.9(f)] is equivalent to the red rectangle (the green square) in Fig. 4.9(d). In Ca, there are gapless points, which are plotted with red points, only on the (110) mirror plane. Therefore, Ca has Fig. 4.8(a-1) type nodal lines when SOC is neglected. Let us introduce SOC into this system. The system is confirmed to have $\mathbb{Z}_8 = 4$ by using the irreps given by the first-principles calculation [Table 4.6]. The band crossing on the W-L line slightly gaps out by the effect of SOC [Fig. 4.9(c)]. As a result, the band around -4 eV ~ 0 eV has no gapless point. Although Ca is a metal, we focus on the topological properties of a gap above the band and we can calculate the mirror Chern numbers. The mirror Chern numbers are calculated as winding numbers of Wannier centers on the mirror-invariant planes [Figs.4.9(g), 3(h)]. We can see the winding number on the (110) mirror plane is 2, while that on the (001) mirror plane is 0. Therefore, Ca with SOC is a "topological crystalline insulator"[3] with $(n_{\mathcal{M}_{(110)}}, n_{\mathcal{M}_{(001)}}) = (2,0)$ [Fig. 4.8(f-1) phase].

Next, we move to the result for Ba shown in Fig. 4.10. In Fig. 4.10(a), we can see a band crossing on the W-L line also in Ba (denoted by a red circle). This band crossing is also a part of a nodal line and Ba is also confirmed to be indicated with $(\mathbb{Z}_4, \delta_2^{+,0}, \delta_2^{-,0}, \delta_2^{\pi}) = (0,0,0,1)$. The band gaps between the two bands on the (110) and (001) mirror planes are shown in Figs.4.10(e), 4(f). In contrast to the Ca, there are gapless points only on the (001) mirror plane in Ba. Therefore, Ba has Fig. 4.8(a-3) type nodal lines when SOC is neglected. Let us introduce SOC into this system. The system is confirmed to have $\mathbb{Z}_8 = 4$ [Table 4.7]. The band crossing on the W-L line gaps out by the effect of SOC [Fig. 4.10(c)]. As a result, the band around -3 eV ~ 0 eV has no gapless point. Here we also just focus on a gap above the band and consider Ba to be an "insulator". The calculated Wannier centers on the mirror-invariant planes are shown in Fig. 4.10(g), 4(h). We can see the winding number on the (001) mirror plane is 4, while that on the (110) mirror plane is 0. Therefore, Ba with SOC is a "topological crystalline insulator" with $(n_{\mathcal{M}_{(110)}}, n_{\mathcal{M}_{(001)}}) = (0,4)$ [Fig. 4.8(f-2) phase].

---

[3]Note again that we are simply discussing the topological properties of the gap.

Ca

(a) band dispersion (w/o SOC)

(d)

$(1\bar{1}0) \equiv (110)$

(b) w/o SOC

(c) w/ SOC

(e) Ca band gap (110) w/o SOC

(f) Ca band gap (001) w/o SOC

(g) Wannier Center in (110) w/ SOC

(h) Wannier Center in (001) w/ SOC

Figure 4.9. Band dispersion and Wannier centers of FCC Ca. (a) Band dispersion (without SOC). A band crossing exists on the L-W line and it is denoted with a red circle. (b)(c) Enlarged band dispersion (without SOC) around the band crossing. (c) Enlarged band dispersion (with SOC). The two bands are slightly gaped out by the effect of SOC. (d) BZ and mirror-invariant planes. (e) Band gap in the (110) mirror-invariant plane (without SOC). The rectangle area is equivalent to the red rectangle in (d). (f) Band gap in the (001) mirror-invariant plane (without SOC). The square area is equivalent to the green square in (d). (g) Wannier center in (110) mirror-invariant plane (with SOC). The left (right) panel shows the Wannier center of the $+i$ $(-i)$ mirror eigenvalue sector. The Wannier center is winding two times. (h) Wannier center in (001) mirror-invariant plane (with SOC). The left (right) panel shows the Wannier center of the $+i$ $(-i)$ mirror eigenvalue sector.

Ba

(a) band dispersion (w/o SOC)

(d)

(b) w/o SOC

(c) w/ SOC

(e) Ba band gap (110) w/o SOC

(f) Ba band gap (001) w/o SOC

(g) Wannier Center in (110) w/ SOC

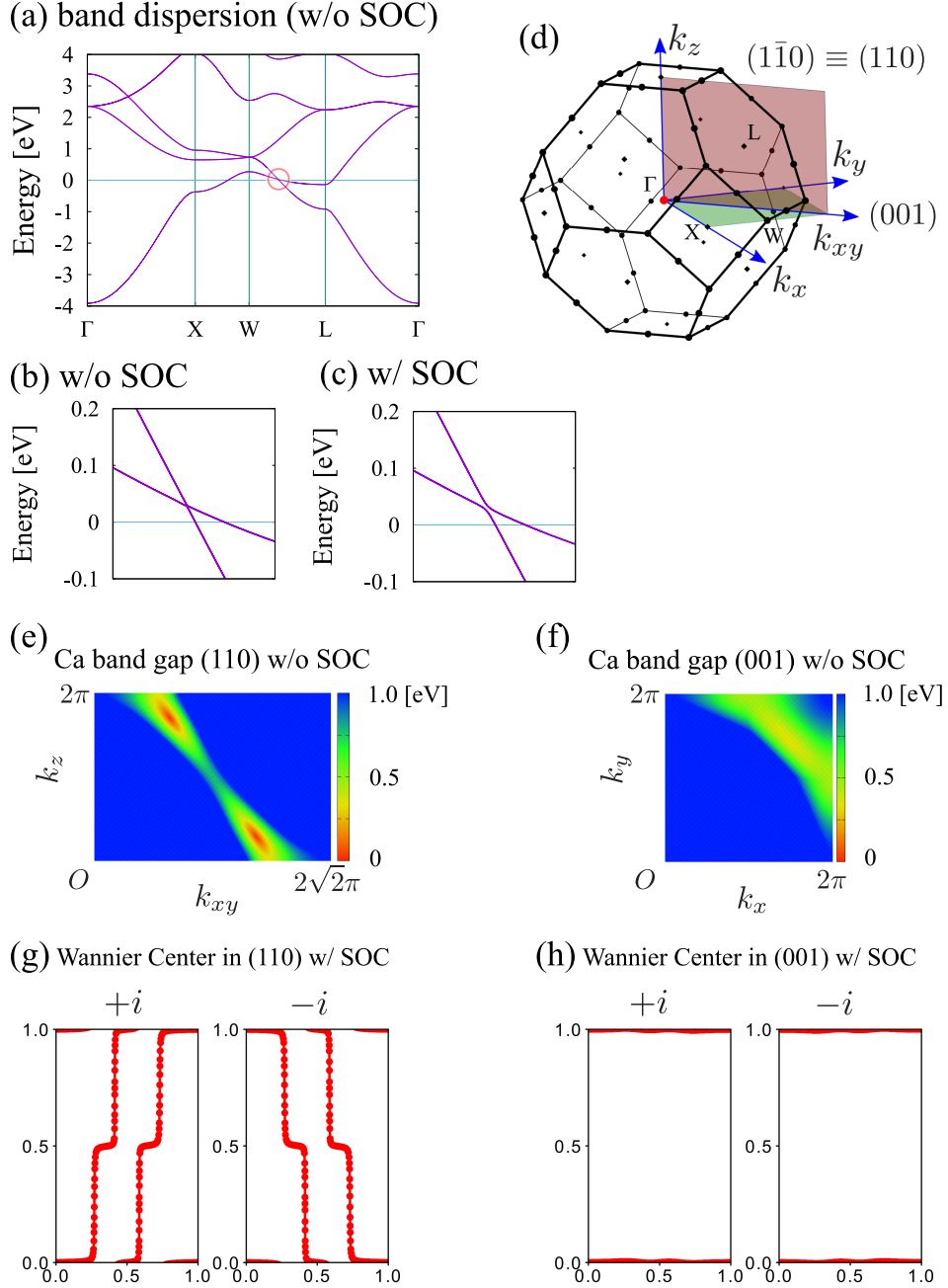## (h) Wannier Center in (001) w/ SOC

Figure 4.10. Band dispersion and Wannier centers of FCC Ba. (a) Band dispersion (without SOC). A band crossing exists on the L-W line and it is denoted with a red circle. (b) Enlarged band dispersion (without SOC) around the band crossing. (c) Enlarged band dispersion (with SOC). The two bands are gaped out by the effect of SOC. (d) BZ and mirror-invariant planes. (e) Band gap in the (110) mirror-invariant plane (without SOC). The rectangle area is equivalent to the red rectangle in (d). (f) Band gap in the (001) mirror-invariant plane (without SOC). The square area is equivalent to the green square in (d). (g) Wannier center in (110) mirror-invariant plane (with SOC). The left (right) panel shows the Wannier center of the $+i$ ($-i$) mirror eigenvalue sector. (h) Wannier center in (001) mirror-invariant plane (with SOC). The left (right) panel shows the Wannier center of the $+i$ ($-i$) mirror eigenvalue sector. The Wannier center is winding four times.
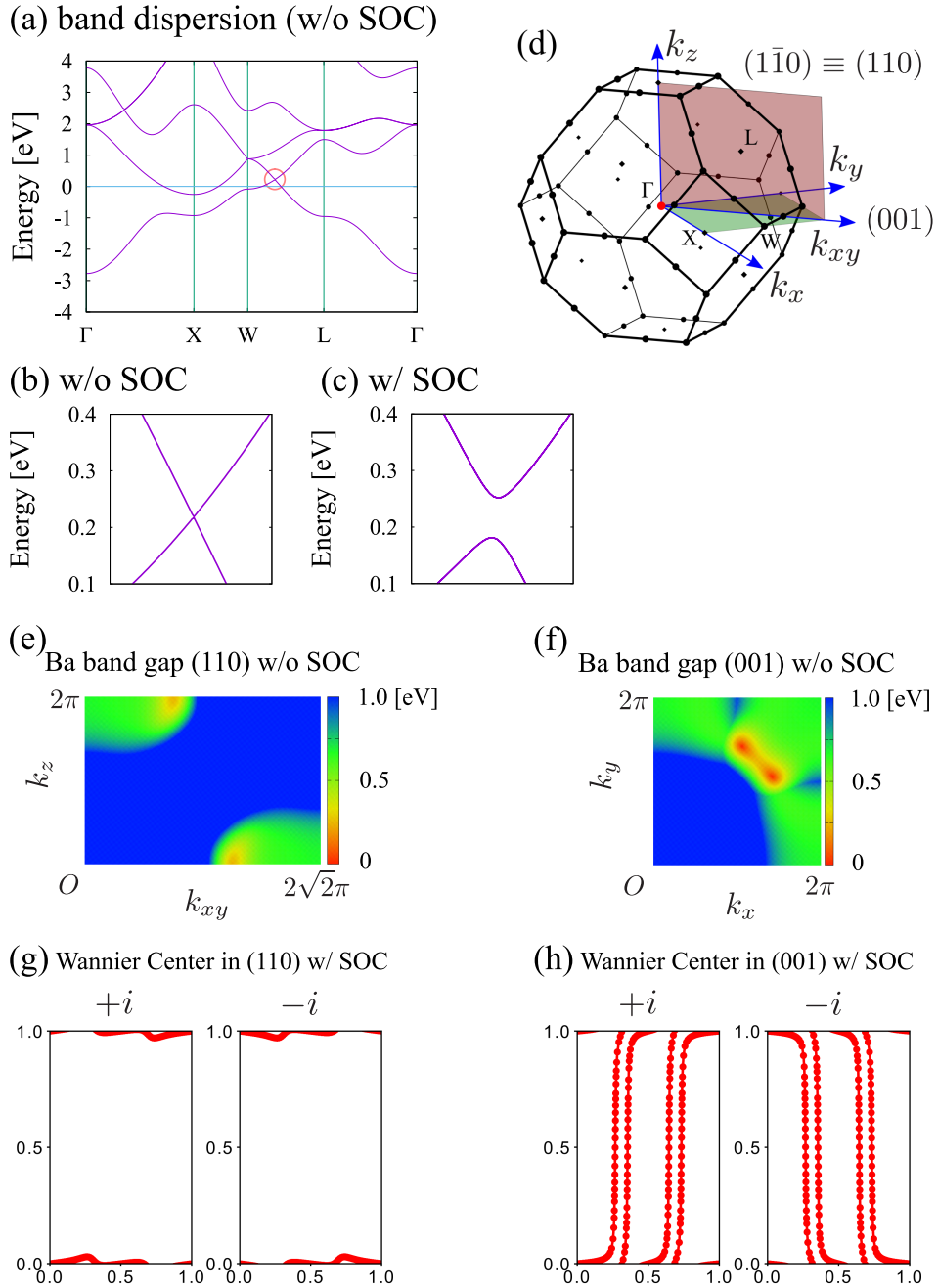
79

Table 4.6: Irreps of the occupied band of FCC Ca.

(Ca)	Γ	X	L	W
w/o SOC	Γ_1^+	Γ_1^+	Γ_1^+	Γ_4
w/ SOC	Γ_6^+	Γ_6^+	Γ_4^+	Γ_7

Table 4.7: Irreps of the occupied band of FCC Ba.

(Ba)	Γ	X	L	W
w/o SOC	Γ_1^+	Γ_1^+	Γ_1^+	Γ_4
w/ SOC	Γ_6^+	Γ_6^+	Γ_4^+	Γ_7

4.1.5   Summary of section 4.1

In this section, we have discussed what kind of topological classes emerge from nodal line semimetals with $(\mathbb{Z}_4, \delta_2^{+,0}, \delta_2^{-,0}, \delta_2^{\pi}) = (0, 0, 0, 1)$ in FCC when SOC is introduced. Our model calculation proved that these nodal line semimetals are linked to topological crystalline insulator classes. Furthermore, the difference in nodal line configurations corresponds to the difference in topological invariants. We also showed that this link is actually found in some material examples by using the first-principles calculations. In this link, two topological crystalline insulator phases, which can not be distinguished by previous diagnostic methods are divided. This result indicates that it is possible to diagnose topological crystalline insulators that are not distinguished in previous methods by hypothetically neglecting SOC and performing first-principles calculations.[4]

---

[4]However, not all nodal line semimetals are linked to topological crystalline insulators. For example, in FCC, a band inversion between Γ_1^+ and Γ_2^+ at the X point produces nodal lines when SOC is neglected, but no nontrivial mirror Chern number emerges from them when SOC is introduced although they penetrate a mirror-invariant plane.
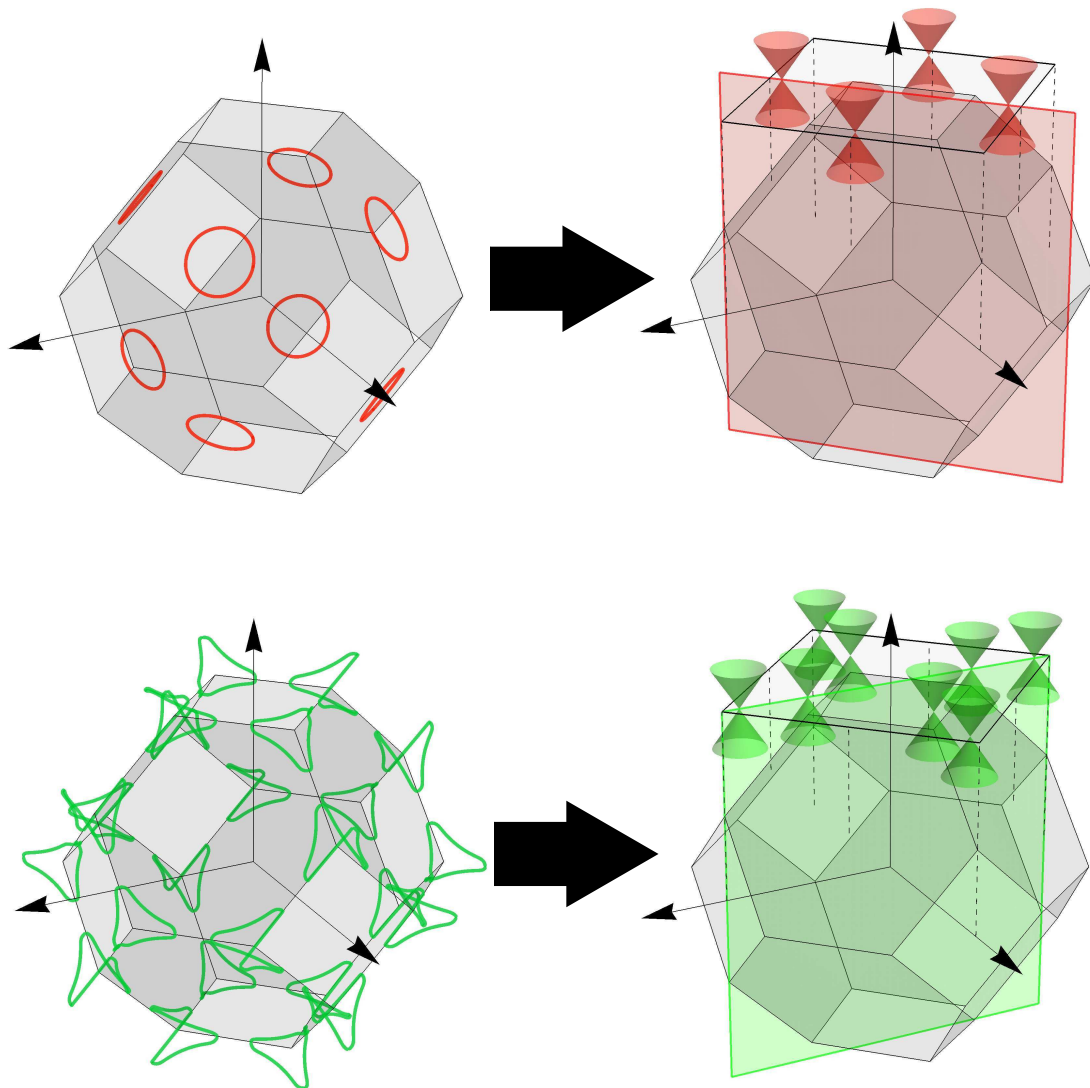
4.2 Nodal line semimetals in body centered tetragonal lattice

We focus on an example of nodal line semimetal in the body centered tetragonal lattice (space group 139). In section 3.4, we have confirmed that Ca_2As is a nodal line semimetal with $(\mathbb{Z}_4, \nu_1, \delta_2^{+,0}, \delta_2^{-,0}, \delta_2^{\pi}) = (0, 0, 0, 0, 1)$. Also for this system, we discuss the link between the nodal lines and the mirror Chern number as in section 4.1.

4.2.1 Target system and nodal lines

The Ca2As is a body centered tetragonal crystal system [Fig. 4.11(a)]. In the (conventional) unit cell, there are 8 Ca atoms and 4 As atoms. The atoms that are connected by symmetry operations are labeled with the same name as Ca(4c), Ca(4e), and As(4e). Here, 4c and 4c is the name of the Wyckoff position.

The results of the first-principles calculation for the electronic band dispersion without SOC is shown in Fig. 4.11(c). We can see that a band inversion occurs at the P point and a gapless node appears on the P-N line, that is a C_2-invariant line. This gapless node is a part of a line node which is indicated by δ_2^{π}. The schematic picture of the configuration of the nodal line is shown in Fig. 4.11(e). The nodal line penetrates the $(1\bar{1}0)$ mirror-invariant plane.

4.2.2 Nodal line and the mirror Chern number

We discuss the intrinsic link between the nodal line and the mirror Chern numbers in Ca_2As. However, the first-principles calculation has given the irreps of the inverted bands at the P point as Γ_1 and Γ_4. The symmetry of the P point and the irreps of the inverted bands are exactly the same as those used in the discussion of the W point in the FCC lattice, and thus the topological properties of the $\boldsymbol{k} \cdot \boldsymbol{p}$ model are calculated in the same way. Therefore, the single nodal ring around the P point is linked to the mirror Chern number $n_{P, \mathcal{M}_{(1\bar{1}0)}} = 1$. Unlike the case of FCC lattice, there are only two nonequivalent P points on the $(1\bar{1}0)$ plane in the BZ of the body centered tetragonal lattice. As a result, it is revealed that the nodal line semimetal Ca_2As is linked to a topological crystalline insulator with $n_{\mathcal{M}_{(1\bar{1}0)}} = 2$ when SOC is introduced.

When SOC is introduced, the symmetry-based indicator of Ca_2As is $(\mathbb{Z}_2, \mathbb{Z}_8) = (0, 4)$, and possible combinations of topological invariants are listed in Table 4.8. Although there are four possible combinations, only two of them have $n_{\mathcal{M}_{(1\bar{1}0)}} = 2$. Furthermore, considering that there is no nodal line other than the ones around the P points, the other mirror Chern numbers are estimated to be 0. Therefore, by combining the symmetry-based indicator and the discussion of nodal line configurations, we can diagnose the topological class of Ca_2As with SOC as $(n_{\mathcal{M}_{(001)}}, n_{\mathcal{M}_{(1\bar{1}0)}}, n_{\mathcal{M}_{(100)}}) = (0, 2, 0)$. This result is consistent with a previous study that numerically calculated the mirror Chern numbers [81]. As in the case of the face centered cubic lattice, a subdividing diagnosis is realized by examining the nodal line configuration.
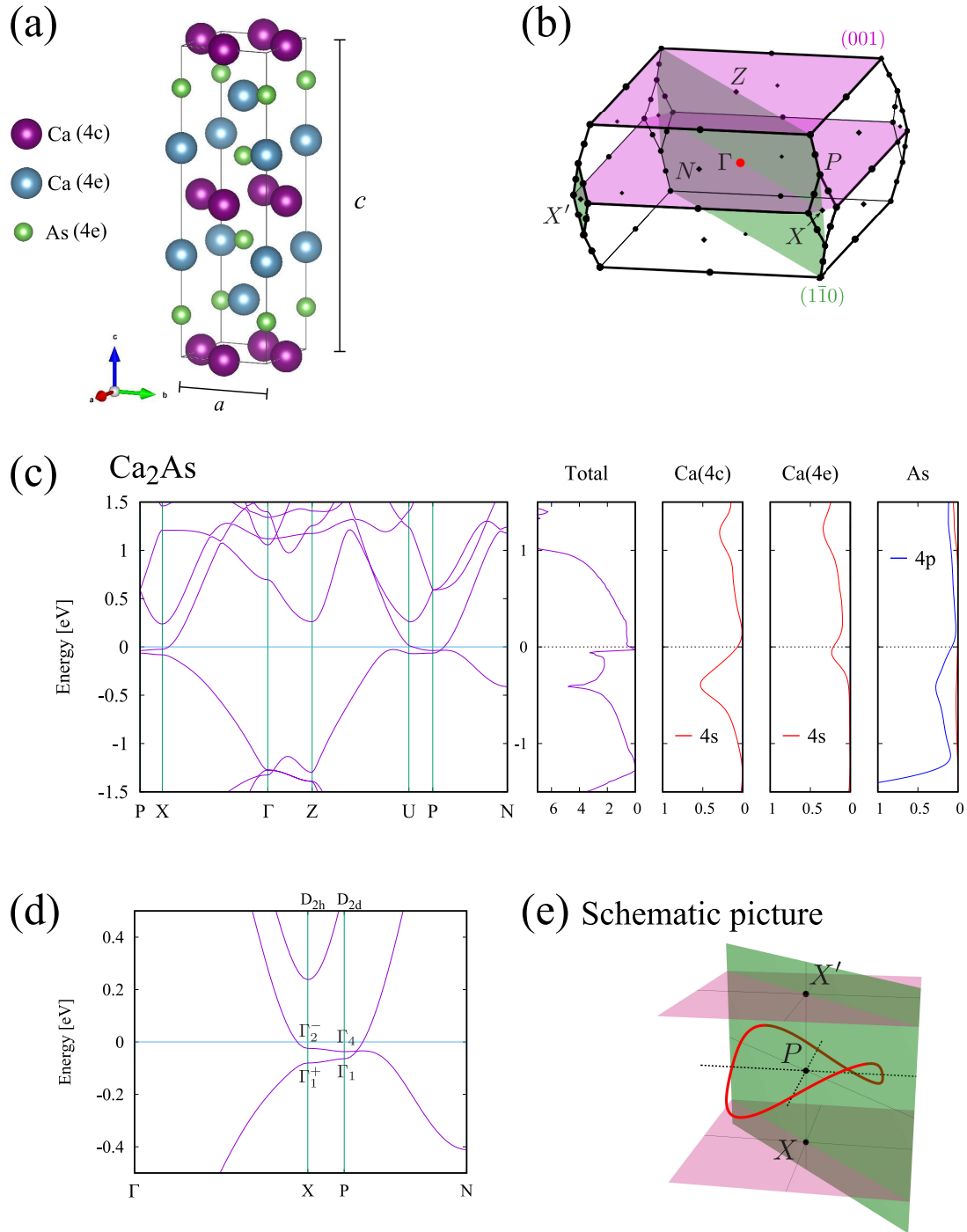
Figure 4.11. (a) Crystal structure of the Ca_2As. (b) BZ of the system. n. The green and purple planes are mirror-invariant planes. (c) Band dispersions and density of states (DOS) pictures without SOC for Ca_2As. In the panel of DOS, projected DOS to each atom and each orbital are also shown. (d) Magnified picture of the band dispersion around X and P points. In the magnified band dispersion, the irreps of each band are also shown. (e) Schematic pictures of the configuration of nodal lines.

Table 4.8: Possible combinations of topological invariants for $(\mathcal{Z}_2, \mathcal{Z}_8) = (0,4)$ excerpted from Supplementary Table 7 in Ref.[49].

$(\mathcal{Z}_2, \mathcal{Z}_8)$	$(\nu_0; \nu_1\nu_2\nu_3)$	$n_{\mathcal{M}_{(001)}}$	$n_{\mathcal{M}_{(1\bar{1}0)}}$	$n_{\mathcal{M}_{(100)}}$
		0	0	2
(0,4)	(0;000)	0	2	0
		4	0	0
		4	2	2

Nodal lines in the related materials

Some materials in related materials (Ca$_2$As family, X_2Y, X =Ca, Sr, Ba, Y =Sb, As, Bi) are nodal line semimetals. All of them have different nodal line configurations than Ca$_2$As, and they are diagnosed by $(\mathbb{Z}_4; \nu_1)$. In contrast to Ca$_2$As, the nodal line in these materials are fixed in a mirror-invariant plane. By thigh-binding model calculation, it is proved that the mirror protected nodal line also works as a source of the mirror Chern number [Fig. 4.12]. However, since a link form $\mathbb{Z}_2$ indicated nodal line semimetals strays from the mainstream of this dissertation, see Appendix E for the details.

4.2.3 Summary of section 4.2

In this section, we have shown that a body centered tetragonal lattice system Ca$_2$As, which has $(\mathbb{Z}_4, \delta_2^{+,0}, \delta_2^{-,0}, \delta_2^{\pi}) = (0,0,0,1)$, is linked to a topological crystalline insulator class with a nontrivial mirror Chern number. This link can be used to determine a topological crystalline insulator class from the candidates given by the symmetry-based indicator, and thus it leads to a subdividing diagnostic method. Since the link confirmed in the body centered tetragonal system is equivalent to that of the FCC lattice case, these links are possibly generalized further.

(a) Schematic picture

(b)

$B_{+,z}$

(c)

$|B_{+,\perp}|$
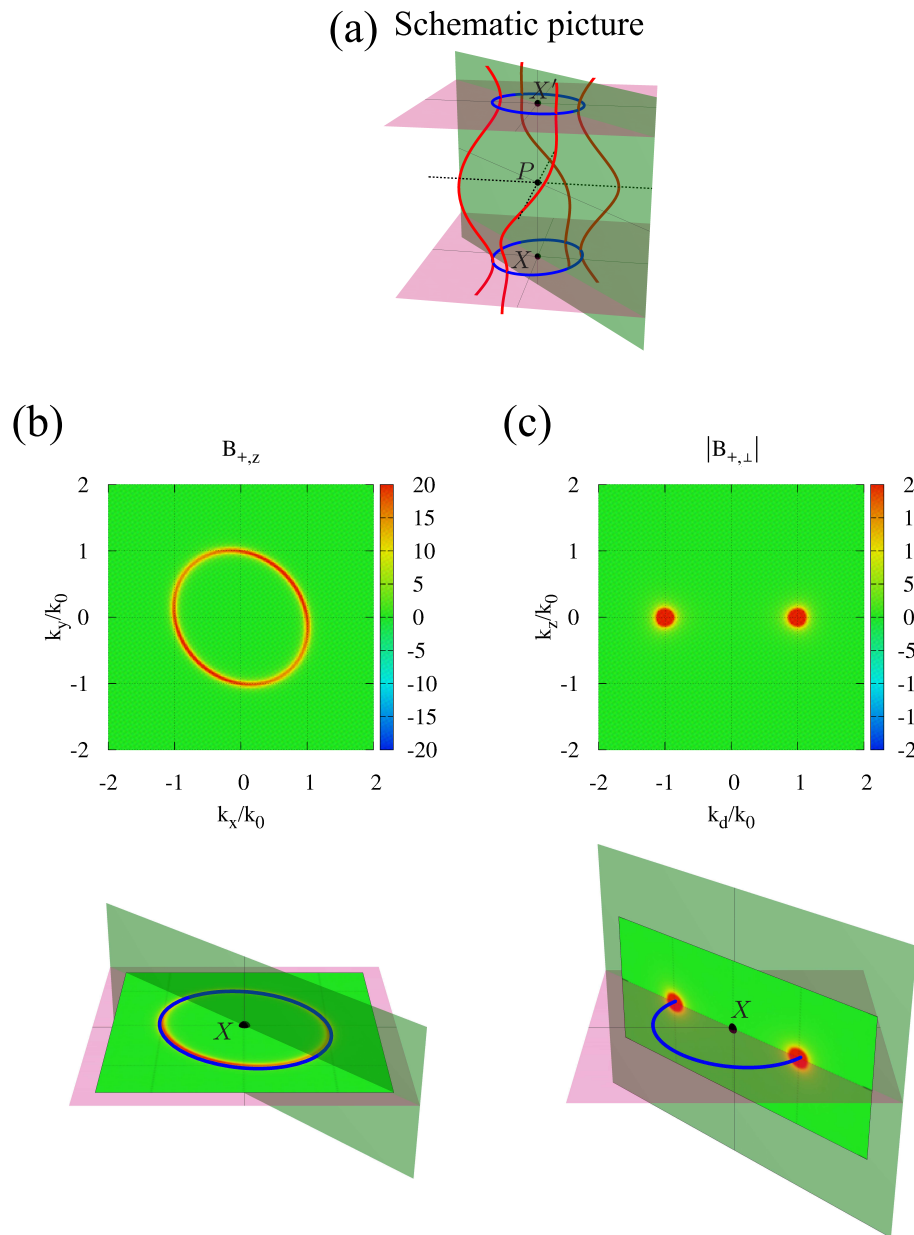
Figure 4.12. (a) Schematic pictures of the configuration of nodal lines in case where mirror-protected nodal lines exist. (b) Berry curvature on the mirror-invariant (001) plane in the case where small SOC is taken into account. There is a sharp ridge on the line where the mirror-protected nodal line exists when SOC is neglected. (c) The absolute value of the Berry curvature on the mirror-invariant $(0\bar{1}1)$ plane in the case where small SOC is taken into account. There are sharp peaks on the points where the nodal lines penetrate the mirror-invariant plane when SOC is neglected. In both cases, the nodal lines can be considered as a source of the Berry curvature.

4.3 Nodal line semimetals in nonsymmorphic tetragonal lattice

Finally, we focus on the space group 127, which is a nonsymmorphic tetragonal space group[5]. It has been proposed in Ref.[90, 91] that due to the nature of the nonsymmorphic operations, a distinctive type of nodal lines can emerge in the space group 127 without SOC. We show that the nodal lines can be (partially) diagnosed by the δ indices, and they are linked to glide-protected topological crystalline insulators.

4.3.1 Target system

The generators of the space group 127 are C_{4z}, g_y (glide), and I (inversion). Here, the glide g_y is defined as

$$g_y = \left\{ m_y \left| \frac{1}{2} \frac{1}{2} 0 \right. \right\} \quad : \quad (x, y, z) \rightarrow (x + \frac{1}{2}, -y + \frac{1}{2}, z). \tag{4.50}$$

Since the generators include the C_{4z} rotation, there is also g_x glide

$$g_x = g_y C_4{}^2 = \left\{ m_x \left| \frac{1}{2} \frac{1}{2} 0 \right. \right\} \quad : \quad (x, y, z) \rightarrow (-x + \frac{1}{2}, y + \frac{1}{2}, z). \tag{4.51}$$

Due to the two glides g_x and g_y, a distinctive type of nodal lines called "concentric intersecting coplanar ellipses (CICE) nodal lines" can emerge around the M point or A point [Fig. 4.13]. The M point and A point have the same symmetry, and thus we focus only on the M point.

First, we consider the case without SOC. Due to the symmetry of the space group 127, all bands in the M point are doubly degenerate. This degeneracy is protected by the glide and TR symmetries, and thus they do not split on the glide-invariant planes. Let us consider a double band inversion at the M point. Note that the degenerate bands have the same m_z eigenvalues ($m_z = IC_4{}^2$) [Table 4.9]. If the inverted bands have different m_z eigenvalues, two mirror-protected nodal lines emerge on the $k_z = 0$ plane [Fig. 4.13(c)(d)]. Since the degeneracy at the M point is kept along the M-X line (M-X' line), the nodal lines intersect each other on the M-X line (M-X' line). As a result, CICE nodal lines emerge around the M point. Double band inversions that produce the CICE nodal lines are $M_1^+ \oplus M_4^+ \leftrightarrow M_1^- \oplus M_4^-$, $M_1^+ \oplus M_4^+ \leftrightarrow M_2^- \oplus M_3^-$, $M_2^+ \oplus M_3^+ \leftrightarrow M_1^- \oplus M_4^-$, $M_2^+ \oplus M_3^+ \leftrightarrow M_2^- \oplus M_3^-$, and $M_5^+ \leftrightarrow M_5^-$. Assuming that $(\mathbb{Z}_4, \nu_1, \nu_3, \delta_2^{+,0}, \delta_2^{-,0}) = (0, 0, 0, 0, 0)$ before the double band inversion[6], we can calculate the indices obtained after the double band inversion as $(2, 0, 0, 1, 1)$ for the $M_5^+ \leftrightarrow M_5^-$ case, and $(2, 0, 0, 0, 0)$ for the other cases. In this dissertation, we focus on the $M_5^+ \leftrightarrow M_5^-$ case, which is newly diagnosed by the δ indices.

Next, we decide a topological invariant that we should calculate when SOC is introduced. In the space group 127 with SOC, Ref.[92] have shown that there are glide-protected topological crystalline insulator classes. These topological crystalline insulators

---

[5] "nonsymmorphic space groups" : space groups that include a glide or screw operation, regardless of the choice of the origin.

[6] $\delta_2^{+,\pi}$ and $\delta_2^{-,\pi}$ have nothing to do with the M point, and thus we neglect them.
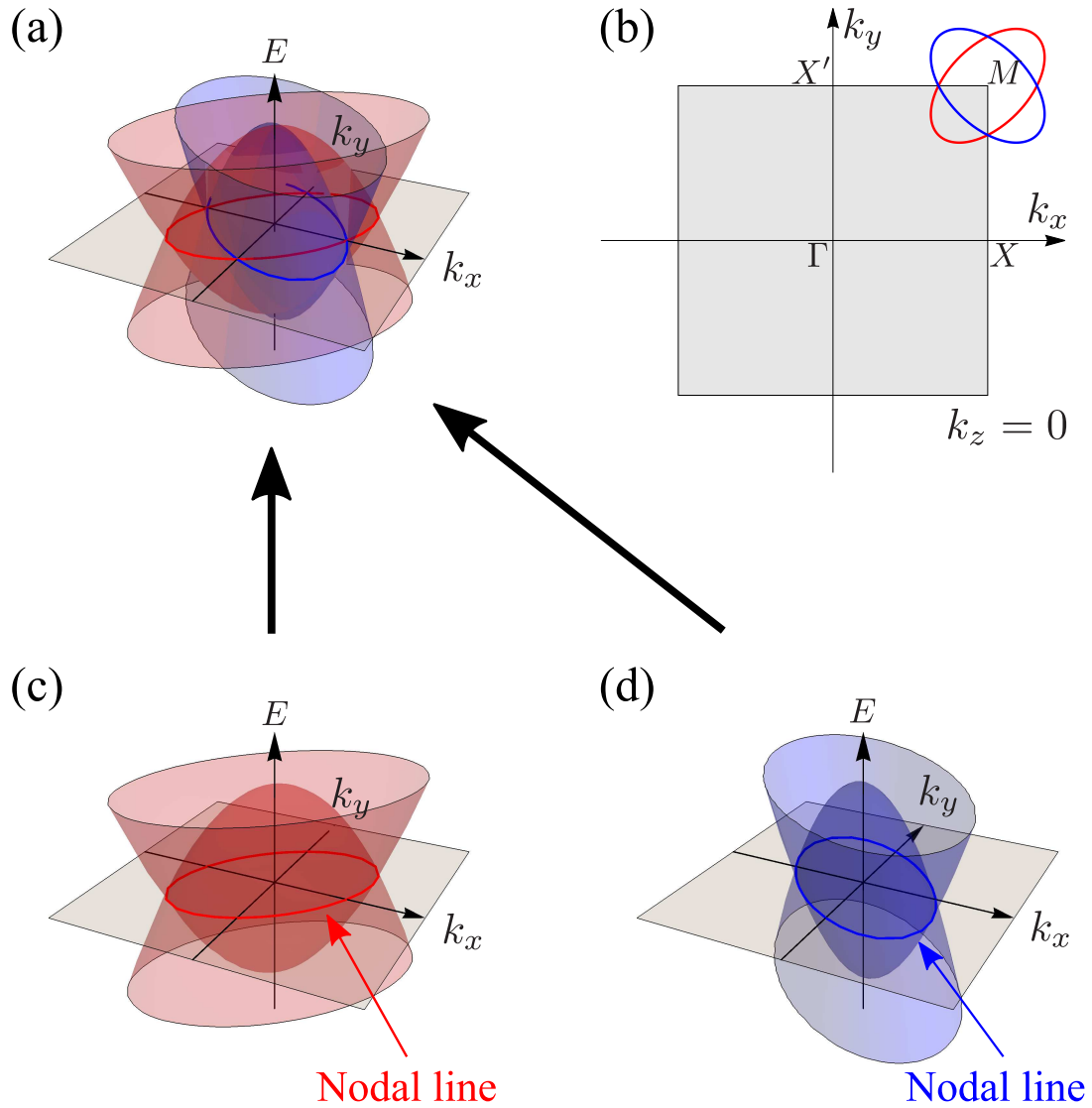
Figure 4.13. (a) Schematic picture of CICE nodal lines. (b) BZ ($k_z = 0$ slice) and CICE nodal lines. They emerge around the M point and are fixed on the $k_z = 0$ plane (mirror-invariant plane). (c)(d) CICE nodal lines decomposed into two ellipses. Both of them are protected by the m_z mirror symmetry.

Table 4.9: Irreps at the M point in the space group 127.

irrep	E	C_4	I	g_y
$M_1^+ \oplus M_4^+$	$\begin{pmatrix} 1 & 0 \\ 0 & 1 \end{pmatrix}$	$\begin{pmatrix} i & 0 \\ 0 & -i \end{pmatrix}$	$\begin{pmatrix} 1 & 0 \\ 0 & 1 \end{pmatrix}$	$\begin{pmatrix} i & 0 \\ 0 & -i \end{pmatrix}$
$M_1^- \oplus M_4^-$	$\begin{pmatrix} 1 & 0 \\ 0 & 1 \end{pmatrix}$	$\begin{pmatrix} i & 0 \\ 0 & -i \end{pmatrix}$	$\begin{pmatrix} -1 & 0 \\ 0 & -1 \end{pmatrix}$	$\begin{pmatrix} -i & 0 \\ 0 & i \end{pmatrix}$
$M_2^+ \oplus M_3^+$	$\begin{pmatrix} 1 & 0 \\ 0 & 1 \end{pmatrix}$	$\begin{pmatrix} -i & 0 \\ 0 & i \end{pmatrix}$	$\begin{pmatrix} 1 & 0 \\ 0 & 1 \end{pmatrix}$	$\begin{pmatrix} i & 0 \\ 0 & -i \end{pmatrix}$
$M_2^- \oplus M_3^-$	$\begin{pmatrix} 1 & 0 \\ 0 & 1 \end{pmatrix}$	$\begin{pmatrix} -i & 0 \\ 0 & i \end{pmatrix}$	$\begin{pmatrix} -1 & 0 \\ 0 & -1 \end{pmatrix}$	$\begin{pmatrix} -i & 0 \\ 0 & i \end{pmatrix}$
M_5^+	$\begin{pmatrix} 1 & 0 \\ 0 & 1 \end{pmatrix}$	$\begin{pmatrix} 0 & 1 \\ 1 & 0 \end{pmatrix}$	$\begin{pmatrix} 1 & 0 \\ 0 & 1 \end{pmatrix}$	$\begin{pmatrix} 0 & 1 \\ -1 & 0 \end{pmatrix}$
M_5^-	$\begin{pmatrix} 1 & 0 \\ 0 & 1 \end{pmatrix}$	$\begin{pmatrix} 0 & 1 \\ 1 & 0 \end{pmatrix}$	$\begin{pmatrix} -1 & 0 \\ 0 & -1 \end{pmatrix}$	$\begin{pmatrix} 0 & -1 \\ 1 & 0 \end{pmatrix}$
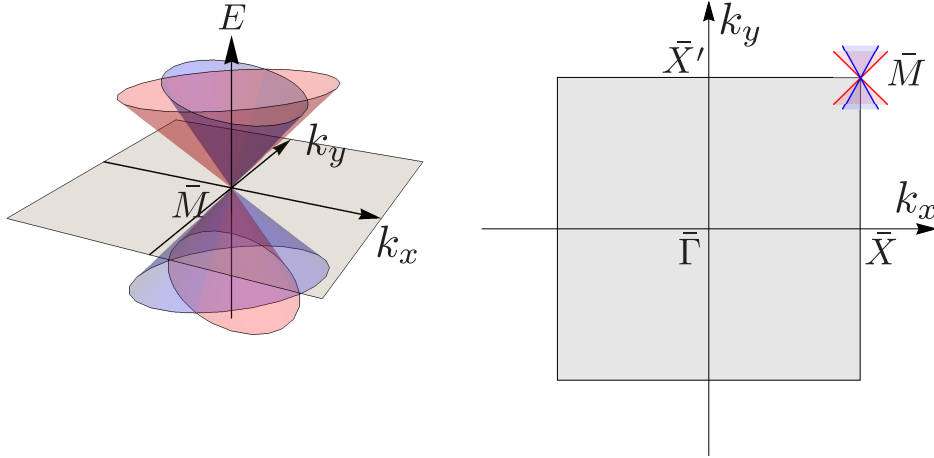
Figure 4.14. Doubly degenarate Dirac-cone-chaped surface states at the $\bar{M}$ point.

have doubly degenerate Dirac-cone-shaped surface states at the $\bar{M}$ point in the (001) surface BZ [Fig. 4.14]. This glide-protected class is characterized by two $\mathbb{Z}_4$-valued glide[7] invariant $(\gamma_x, \gamma_y) = (2, 2)$. Interestingly, these invariants have not been diagnosed by the previous diagnostic methods. Therefore, in the following section, we calculate the (γ_x, γ_y) and discuss the link between the CICE nodal lines semimetals and the glide-protected topological crystalline insulators.

---

[7]Actually, odd numbers are prohibited by the C_4 symmetry. These glide invariants are defined also in orthorhombic lattices and odd numbers are allowed in those cases.

4.3.2 $\boldsymbol{k} \cdot \boldsymbol{p}$ model calculations

We assume a double band inversion between M_5^+ and M_5^- at the M point and no other band inversions at other high symmetry points. First, we neglect SOC and construct a four-by-four model with CICE nodal lines by using $\boldsymbol{k} \cdot \boldsymbol{p}$ perturbation around the M point. Then, we introduce SOC terms and calculate the glide invariants.

When SOC is neglected, by taking four bases that belong to M_5^+ and M_5^-, the symmetry operators are written as block-diagonal matrices[8],

$$
\begin{aligned}
C_{4z} &= \tau_x \sigma_0, \\
g_y &= i\tau_y \sigma_z, \\
I &= \tau_0 \sigma_z, \\
\mathcal{T} &= \mathcal{K}.
\end{aligned}
\tag{4.52}
$$

Here, $\tau_{x,y,z}$ and $\sigma_{x,y,z}$ are Pauli matrices. $\tau_{x,y,z}$ correspond to the representations of $M_5^\pm$ [Table 4.9], and $\sigma_{x,y,z}$ correspond to the "inter-representation" component. The $\boldsymbol{k} \cdot \boldsymbol{p}$ order model (local model) without SOC $H_M(k_x, k_y, k_z)$ must satisfy

$$
\begin{aligned}
C_4^{-1} H_M(k_x, k_y, k_z) C_4 &= H_M(-k_y, k_x, k_z), \\
g_y^{-1} H_M(k_x, k_y, k_z) g_y &= H_M(k_x, -k_y, k_z), \\
I^{-1} H_M(k_x, k_y, k_z) I &= H_M(-k_x, -k_y, -k_z), \\
\mathcal{T}^{-1} H_M(k_x, k_y, k_z) \mathcal{T} &= H_M(-k_x, -k_y, -k_z).
\end{aligned}
\tag{4.53}
$$

From these restrictions, $H_M(k_x, k_y, k_z)$ is determined as

$$
H_M(\boldsymbol{k}) = tk_x k_y \tau_z \sigma_0 + t'k_x k_y \tau_z \sigma_0 + (\Delta^2 - k_x^2 - k_y^2)\tau_0 \sigma_z + k_z \tau_z \sigma_y,
\tag{4.54}
$$

where t, t', and $\Delta > 0$ are real constants. Note that the origin of (k_x, k_y, k_z) is placed at the M point. To obtain CICE nodal lines in the half-filled case, $t > t'$ must be satisfied. Therefore, we assume $t' = 0$ in the following discussions. The eigenvalues of this Hamiltonian are

$$
\begin{aligned}
E_1 &= \sqrt{(tk_x k_y + (\Delta^2 - k_x^2 - k_y^2))^2 + (k_z)^2}, \\
E_2 &= -\sqrt{(tk_x k_y + (\Delta^2 - k_x^2 - k_y^2))^2 + (k_z)^2}, \\
E_3 &= \sqrt{(-tk_x k_y + (\Delta^2 - k_x^2 - k_y^2))^2 + (k_z)^2}, \\
E_4 &= -\sqrt{(-tk_x k_y + (\Delta^2 - k_x^2 - k_y^2))^2 + (k_z)^2}.
\end{aligned}
\tag{4.55}
$$

By solving $E_1 = E_2$ and $E_3 = E_4$, we obtain CICE nodal lines on the $k_z = 0$ plane.

---

[8]Since the glide operation includes a fractional lattice translation, the glide eigenvalue is $\pm i$ in the M point.

Next, we introduce SOC terms. The symmetry operators are written as

$$C_{4z} = \tau_x \sigma_0 \frac{1}{\sqrt{2}}(s_0 - i s_z),$$
$$g_y = \tau_y \sigma_z s_y, \tag{4.56}$$
$$I = \tau_0 \sigma_z s_0,$$
$$\mathcal{T} = i s_y \mathcal{K},$$

where $s_{x,y,z}$ are the Pauli matrices the spin degree of freedom. Within these restrictions, the eight-by-eight local model with SOC is written as

$$
\begin{aligned}
H_{M,\text{soc}} = H_M s_0 &+ v_1 \tau_y \sigma_y (k_x s_x - k_y s_y) \\
&+ v_2 \tau_x \sigma_x (k_x s_y - k_y s_x) + v_3 \tau_0 \sigma_x (k_x s_x + k_y s_y),
\end{aligned} \tag{4.57}
$$

where v_1, v_2, and v_3 are real parameters that represent the amplitude of SOC.

The glide invariants are evaluated by using Wilson loop eigenvalue diagrams ($\simeq$ Wannier cneter)[9]. In the calculation, we calculated a k_z integral [Fig. 4.15(a), green dashed lines] and thus the Wilson loop is expressed as $W(k_x, k_y)$. Originally, to evaluate the glide invariant γ_x (γ_y), we need to plot $W(k_x, k_y)$ along $\bar{X}'\bar{\Gamma}\bar{X}\bar{M}$ $\bar{X}\bar{\Gamma}\bar{X}'\bar{M}$ (see Fig. 4.14 for the definition of $\bar{X}'$ and so on). However, we assumed that band inversions occur only around the M point and we are interested in the topological invariants linked to the CICE nodal lines. Therefore, we focus only on the $\bar{X}\bar{M}$ segment and $\bar{X}'\bar{M}$ segment to evaluate γ_x and γ_y, respectively [Fig. 4.15(a), green solid line].

$\bar{X}\bar{M}$ line

The $\bar{X}\bar{M}$ line corresponds to the g_x-invariant plane $k_x = 0$ in the local model Eq. (4.57). On the g_x-invariant plane, the local model is written as

$$
\begin{aligned}
H_{M,\text{soc}}^{k_x=0} = \left(\Delta^2 - k_y^2\right) \tau_0 \sigma_z s_0 &+ k_z \tau_x \sigma_y s_0 \\
&- v_1 k_y \tau_y \sigma_y s_y - v_2 k_y \tau_x \sigma_x s_x + v_3 k_y \tau_0 \sigma_x s_y.
\end{aligned} \tag{4.58}
$$

This model can be block diagonalized into two sectors with g_x eigenvalues ± 1. By using a unitary transformation $U = \frac{1}{\sqrt{2}}\left(\tau_z \sigma_z s_z + i\tau_x \sigma_0 s_x\right)$, the glide operator $g_x = g_y C_4{}^2 = \tau_y \sigma_z s_y$ is transformed as $U^\dagger \tau_y \sigma_z s_y U = \tau_0 \sigma_0 s_z$ and the sector with glide eigenvalue $+1$ is written as

$$
\begin{aligned}
H_{M,+}^{k_x=0} = \left(\Delta^2 - k_y^2\right) \tau_0 \sigma_z &+ k_z \tau_x \sigma_y \\
&+ v_1 k_y \tau_0 \sigma_x - v_2 k_y \tau_z \sigma_z - v_3 k_y \tau_y \sigma_y.
\end{aligned} \tag{4.59}
$$

We calculate the Wilson loop for the occupied two bands. However, this model is not periodic in the z direction, and thus we need to fix the wavefunctions in the both ends of k_z to avoid gauge issues in the numerical evaluation. When we assume $|k_z| >> 1$, the model is $H_{M,+}^{k_x=0} \simeq k_z \tau_x \sigma_y$ and the occupied states are $\frac{1}{\sqrt{2}}(i\,\text{sgn}(k_z), 0, 0, 1)$ and $\frac{1}{\sqrt{2}}(0, i\,\text{sgn}(k_z), 1, 0)$ for each end. The Wilson loop is effectively calculated like Fig. 4.15(B).

---

[9] Since all bands are degenerate, we need to evaluate the Wilson loop. See Appendix D.3 for details.

The evaluated Wilson loop eigenvalue diagrams is shown in the left half of Fig. 4.15(c) and (d). (c) is for $t = 1.0$, $v_1 = 0.1$, $v_2 = 0.05$, $v_3 = 0$ (relatively large SOC), and (d) is for $t = 1.0$, $v_1 = 0.02$, $v_2 = 0.01$, $v_3 = 0$ (small SOC)[10].

$\bar{M}\bar{X}'$ line

The $\bar{M}\bar{X}'$ line corresponds to the g_y-invariant plane $k_y = 0$ in the local model Eq. (4.57). On the g_y-invariant plane, the local model is written as

$$
\begin{aligned}
H_{M,\mathrm{soc}}^{k_y=0} = {} & \left(\Delta^2 - k_x^2\right)\tau_0\sigma_z s_0 + k_z\tau_x\sigma_y s_0 \\
& + v_1 k_x \tau_y \sigma_y s_x + v_2 k_x \tau_x \sigma_x s_y + v_3 k_x \tau_0 \sigma_x s_x
\end{aligned}
\tag{4.60}
$$

By using a unitary transformation $U = \frac{1}{\sqrt{2}}\left(\tau_0\sigma_0 s_0 + i\tau_y\sigma_z s^x\right)$, the glide operator g_y is transformed as $U^\dagger \tau_y\sigma_z s_y U = \tau_0\sigma_0 s_z$. The model is also block diagonalized and the sector with glide eigenvalue $+1$ is written as

$$
\begin{aligned}
H_{M,+}^{k_y=0} = {} & \left(\Delta^2 - k_x^2\right)\tau_0\sigma_z + k_z\tau_x\sigma_y \\
& - v_1 k_x \tau_0 \sigma_x + v_2 k_x \tau_z \sigma_y - v_3 k_x \tau_y \sigma_y.
\end{aligned}
\tag{4.61}
$$

In the numerical evaluation of the Wilson loop, the wavefunctions in both ends are fixed in the same way as the $\bar{X}\bar{M}$ line.

The evaluated Wilson loop eigenvalue diagrams are shown in the right half of Fig. 4.15(c) and (d).

γ_x and γ_y

The glide invariant γ_x (γ_y) is pictorially calculated [92] from the Wilson loop eigenvalue diagrams [Fig. 4.15(c)(d)] :

1. Draw a horizontal reference line across the diagram.

2. Count the number of times a positively sloped Wilson eigenvalue band crosses the reference line along the $\bar{X}\bar{M}$ segment ($\bar{M}\bar{X}'$ segment) and subtract from it the number of times a negatively sloped band crosses the reference line along the same segment. Multiply the total by 2.

3. Take mod 4, it is γ_x (γ_y)

We can see the glide invariants are $(\gamma_x, \gamma_y) = (2, 2)$. Furthermore, the small SOC case [Fig. 4.15(d)] shows that the Wilson eigenvalue bands quickly winds at the point where the CICE nodal lines penetrate the glide-invariant plane. From this perspective, we can say that the CICE nodal lines are a source of nontrivial glide invariants $(2, 2)$.

---

[10]As long as $v_3 \simeq v_1, v_2$, or smaller, the topological nature of the diagrams is not changed.
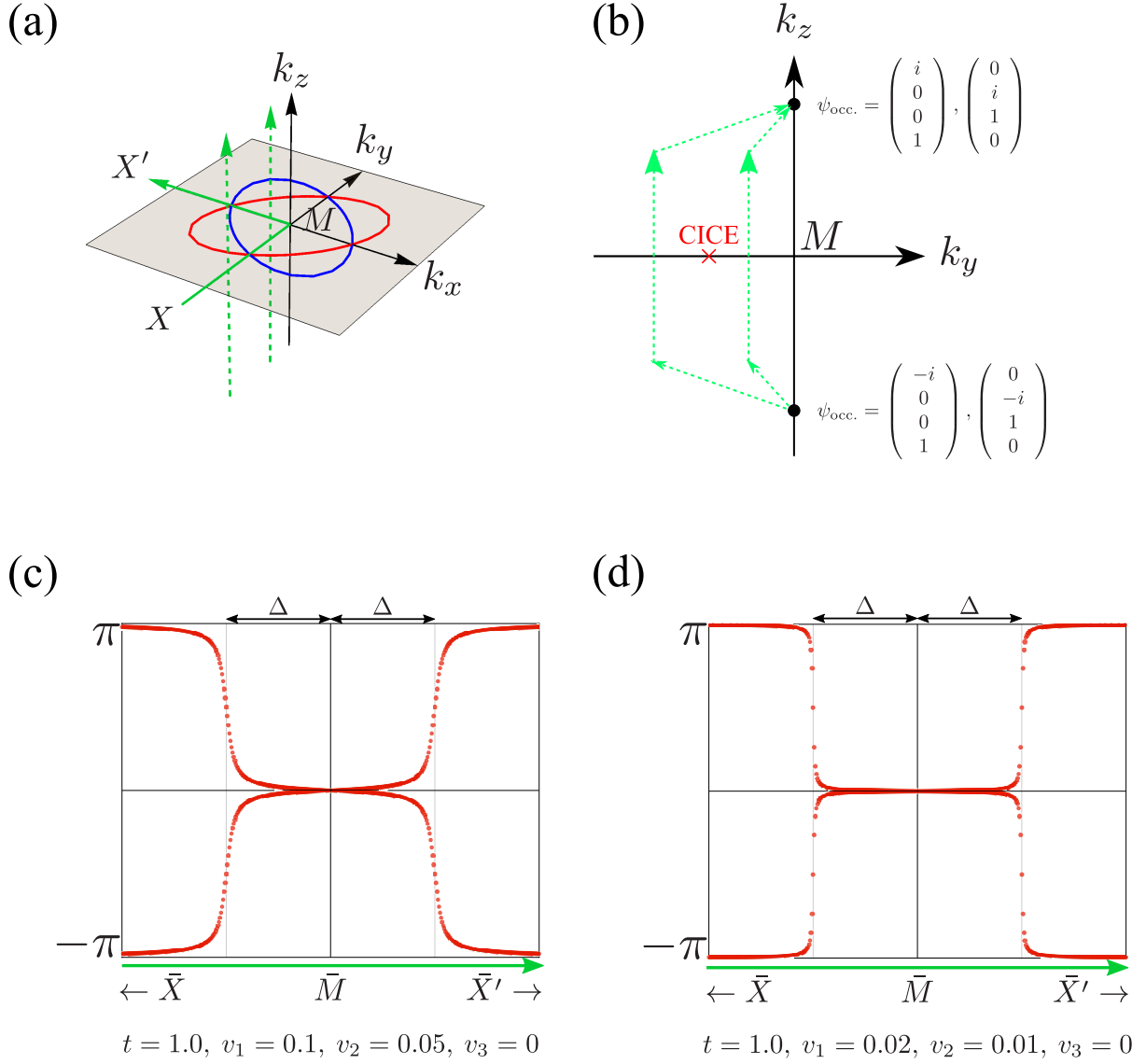
Figure 4.15. (a) CICE nodal lines and the path to evaluate the Wilson loop. The Wilson loops are evaluated in the z direction (green dashed line), and the Wilson loop eigenvalue diagrams are plotted along the $\bar{X}\bar{M}\bar{X}'$ line (green solid line). (b) Schematic picture of the gauge fixing in the numerical evaluation of the Wilson loop. (c) Obtained Wilson loop eigenvalue diagram for $t = 1.0$, $v_1 = 0.1$, $v_2 = 0.05$, $v_3 = 0$ (relatively large SOC) (d) Obtained Wilson loop eigenvalue diagram for $t = 1.0$, $v_1 = 0.02$, $v_2 = 0.01$, $v_3 = 0$ (small SOC).

4.3.3 Summary of section 4.3

In this section, we have focused on a CICE nodal lines semimetal that is given by a double band inversion between M_5^+ and M_5^- at the M point. We have shown that the CICE nodal lines semimetal has nontrivial indices $(\mathbb{Z}_4, \nu_1, \nu_3, \delta_2^{+,0}, \delta_2^{-,0}) = (2, 0, 0, 1, 1)$, and it is linked to glide-protected topological crystalline insulator with $(\gamma_x, \gamma_y) = (2, 2)$ when SOC is introduced. This result suggests that by finding the CICE nodal lines semimetals with nontrivial δ indices, we can indirectly find a glide-protected topological insulator class, which has not been diagnosed by previous diagnostic methods.

4.4 Summary of this chapter

In this chapter, we have looked at three examples of nodal line semimetals that are newly diagnosed with the δ indices. In the case of the FCC lattice, we have shown that the nodal line semimetals are linked to topological crystalline insulators with a nontrivial mirror Chern number. We have also shown that the nodal lines are considered as a source of the mirror Chern numbers, and thus the difference in the configurations of the nodal lines correspond to the difference in the classes of topological crystalline insulators. In the case of the body centered tetragonal lattice, we have seen the same link as for the case of FCC. In the case of nonsymmorphic tetragonal lattice, we have shown that a CICE nodal lines semimetal is linked to a glide-protected topological crystalline insulator. Also, in this case, the CICE nodal lines are considered as a source of nontrivial glide invariants. In these examples, it has been shown that by hypothetically turning off SOC in first-principles calculations and examining the configuration of the nodal lines, we can diagnose the topological crystalline insulators that have not been diagnosed by previous methods.

Although these results are still case studies, the intrinsic link between nodal line semimetals and topological crystalline insulators is confirmed in many cases, and this link is possibly generalized and can lead to more detailed diagnostic methods.

Chapter 5

Summary

In this dissertation, we studied diagnostic methods for nodal line semimetals and intrinsic links between nodal line semimetals and topological crystalline insulators.

In chapter 3, we derived the δ indices as a new diagnostic method for nodal line semimetals that violate the compatibility condition. The δ indices were defined in space groups that have the time-reversal, inversion, and four-fold rotation (or screw) symmetries, by using subgroup reductions of space groups. We derived explicit calculation formulas of the δ indices for each of five Bravais lattices that have the above symmetries : (i) primitive tetragonal lattice, (ii) body centered tetragonal lattice, (iii) primitive cubic lattice, (iv) face centered cubic lattice, and (v) body centered cubic lattice. The calculation formulas were written with symmetry eigenvalues of wavefunctions in high symmetry points of BZ in each Bravais lattice. In the derivation of the calculation formulas, we needed to translate the symmetry eigenvalues of the subgroup to that of the original space group. By combining the δ indices and the previous methods ($\mathbb{Z}_4$ and $\mathbb{Z}_2$ indices), we obtained sufficient diagnostic methods for nodal line semimetals protected by time-reversal and inversion symmetries. We also confirmed that the δ indices diagnose nodal line semimetals that had not been diagnosed by the previous methods with material examples.

In chapter 4, we studied intrinsic links between nodal line semimetals that were diagnosed by the δ indices and topological crystalline insulators, by introducing spin-orbit coupling into the nodal line semimetals. We studied three cases : (a) nodal line semimetals in the face centered cubic lattice and mirror-protected topological crystalline insulators, (b) nodal line semimetals in the body centered tetragonal lattice and mirror-protected topological crystalline insulators, and (c) concentric intersecting coplanar ellipses (CICE) nodal lines semimetals in a nonsymmorphic tetragonal lattice and glide-protected topological crystalline insulators. The former two cases (a) and (b) were discussed based on the material examples obtained in chapter 3, and the latter case (c) were discussed based on theoretical proposals of previous studies. In the case (a) and (b), we showed that non-trivial mirror Chern numbers emerge on the mirror-invariant plane that was penetrated by the nodal lines when spin-orbit coupling was neglected. We also showed that the value of the mirror Chern number corresponded to how many times the nodal lines penetrated the plane. From these results, we concluded that the nodal line semimetals in the case (a) and (b) were intrinsically linked to mirror-protected topological crystalline insulators.

This intrinsic link was confirmed in real materials (Ca and Ba) by using first-principles calculations. In the case of (c) we showed that nontrivial glide invariants emerged from CICE nodal lines. Therefore, we concluded that the CICE nodal lines semimetals in the case (c) were intrinsically linked to glide-protected topological crystalline insulators. In all cases, the intrinsic links were able to use to diagnose topological crystalline insulators the had not been diagnosed by the previous methods.

In the case (a) and (b), we could distinguish topological crystalline insulators by hypothetically turning off spin-orbit coupling and examining the configuration of nodal lines. In the case (c), it is indicated that the glide-protected topological crystalline insulators, which were not diagnosed by previous methods, are found by neglecting SOC and searching CICE nodal line semimetals. These results indicated that by using the intrinsic link and hypothetical SOC-neglecting first-principles calculations, we can enhance the diagnostic methods of topological insulators with SOC. Furthermore, the intrinsic link can be used in the topological materials design. As reviewed in chapter 1, graphene decorated by heavy atom nanoparticles is a topological insulator. If SOC is introduced in a δ-indicated nodal line semimetals similarly, the material should become a topological crystalline insulator. Since the link is expected to be generally extended, the perspective of performing SOC-neglected calculations and considering the intrinsic link should be a useful perspective from now on in many aspects including diagnostic methods and materials design.

Finally, we describe future works. The confirmed intrinsic links between nodal line semimetals and topological crystalline insulators are now just case studies. Although we used generalized models within some assumptions, we need more careful discussion to obtain a more general theory. Also, the diagnosis based on the confirmed links is not necessarily a dramatic advance although it cut calculation costs somewhat. For example, in the case of nodal line semimetals in the face centered cubic lattice, we need to check the configuration of nodal lines to distinguish two topological crystalline insulators. However, at least in our current understandings, we need to numerically evaluate Berry phases to check the configuration, and it is not necessarily a "cheap" calculation. Therefore, we can say that the main future works are a generalization of the intrinsic link and improvement of the evaluation method of nodal line configurations.

Appendix A

Derivations and notes of diagnostic methods

A.1   Symmetry operators

In this section, we define the symbols of symmetric operations [Table.A.1].

E	:	The identical operation.
C_n	:	A $2\pi/n$ rotation. A rotation axis with the largest n is called "main axis".
C_{nz}	:	A C_n rotation around the z axis.
C_2'	:	A π rotation whose axis is perpendicular to the main axis.
I	:	The space inversion.
m_h	:	A mirror about the plane that is perpendicular to the main axis. $(m_h = IC_2)$
m_v	:	A mirror about the plane that is parallel with the main axis and the C_2' axis.
m_d	:	A mirror about the plane that is parallel with the main axis but not with the C_2 axis.
m_z	:	A mirror about the xy plane (perpendicular to the z axis).
S_n	:	A combination of a C_n rotation and the inversion ($n = 3, 4, 6$). $(S_n = IC_n)$

Table A.1: Symbols of symmetry operators.

A.2   Irreducible representation

The Irreducible representations (irreps) are understood as a generalized conception of the symmetry eigenvalues. The irreps for all space groups are listed in Ref.[56] or a website [57] [93, 94, 95].

For example, let us assume a little group of a high symmetry point that is invariant in a C_2 rotation, the inversion I, and a mirror $m = IC_2$. For each occupied band, a C_2 eigenvalue $(\pm i)$, inversion eigenvalue (± 1), and mirror eigenvalue $(\pm i)$ are defined.[1] However, the mirror eigenvalue is decided by the other two eigenvalues because $m = IC_2$. Therefore, there are four possible combinations of eigenvalues. Let us name them Γ_3^+, Γ_4^+, Γ_3^-, and Γ_4^-. They are equivalent to the irreps of the point group C_{2h} [Table A.2].

Table A.2: Character table of the point group C_{2h} for double valued irreducible representations (representations that appear in spinful systems). Since the all irreps are one dimention irreps, the character equals to the symmetry eigenvalue.

C_{2h}	E	C_2	I	m
Γ_3^+	1	i	1	i
Γ_4^+	1	$-i$	1	-1
Γ_3^-	1	i	-1	$-i$
Γ_4^-	1	$-i$	-1	1

A.3   Inversion-based diagnostic methods

In this section, we review the derivations of the inversion-based diagnostic methods. We also mention some points to keep in mind.

A.3.1   SSH model

The Hamiltonian of the SSH model [Section 1.2.1][Fig.1.4] is

$$
\begin{aligned}
H &= \sum_i \left(t_1 a_i^\dagger b_i + t_2 a_i^\dagger b_{i-1} + \text{h.c.} \right) \\
&= \sum_k \begin{pmatrix} a_k^\dagger & b_k^\dagger \end{pmatrix} \begin{pmatrix} 0 & t_1 + t_2 e^{-ik} \\ t_1 + t_2 e^{ik} & 0 \end{pmatrix} \begin{pmatrix} a_k \\ b_k \end{pmatrix},
\end{aligned}
\tag{A.1}
$$

where $a^\dagger$ and a ($b^\dagger$ and b) are the creation and annihilation operators on the A (B) sites. Its energy eigenvalues $E_\pm$ are

$$
E_\pm = \pm \sqrt{t_1^2 + t_2^2 + t_1 t_2 \cos k} \quad (\equiv \pm \epsilon).
\tag{A.2}
$$

We consider the half-filled case and the eigenstate of the occupied band (the lower energy band) is

$$
|u_k\rangle = \frac{1}{\sqrt{2}} \begin{pmatrix} 1 \\ -\frac{t_1 + t_2 e^{ik}}{\epsilon} \end{pmatrix}.
\tag{A.3}
$$

---

[1]We are considering a spinful system and thus we use irreps of the double space group.

The topological property of this system is characterized by the Berry phase θ, which is calculated as

$$A_k = i \langle u_k | \frac{\partial}{\partial k} | u_k \rangle, \tag{A.4}$$

$$
\begin{aligned}
\theta &= \int_{-\pi}^{\pi} dk A_k \\
&= \frac{1}{2} \int_{-\pi}^{\pi} dk \frac{1 + (t_1/t_2) \cos k}{1 + (t_1/t_2)^2 + 2(t_1/t_2) \cos k} \\
&= \begin{cases} 0 & (t_1/t_2 > 1) \\ \pi & (t_1/t_2 < 1) \end{cases}.
\end{aligned}
\tag{A.5}
$$

A_k is the Berry connection. Only when $\theta = \pi$, middle-gap states appear in the energy spectrum of a finite length chain. These middle-gap states are localized on the ends of the chain, and thus we can say they are "end states". Therefore, we can say that this model is topologically nontrivial when $\theta = \pi$.

Next, we add the inversion symmetry into this model. Let us assume the inversion center is locating on the t_1 bond [Fig.1.4]. Since the Hamiltonian is inversion symmetric, the inversion operator I projects an eigenstate $|u_k\rangle$ into another eigenstate that belongs to $-k$. Now $|u_k\rangle$ is defined as a continuous function of k in a fixed gauge, and thus the projection by I generally gives a phase factor as,

$$I |u_k\rangle = e^{-i\beta(k)} |u_{-k}\rangle. \tag{A.6}$$

With this relation, A_{-k} is calculated as

$$
\begin{aligned}
A_{-k} &= i \langle u_{-k} | \frac{\partial}{\partial k} | u_{-k} \rangle \\
&= -\frac{\partial}{\partial k} \beta(k) - A_k.
\end{aligned}
\tag{A.7}
$$

Now θ is 0 or π and thus we can know the value by calculating $e^{i\theta}$. $e^{i\theta}$ is

$$
\begin{aligned}
e^{i\theta} &= \exp \left[i \int_{-\pi}^{\pi} dk A_k \right] \\
&= \exp \left[i \int_{0}^{\pi} dk (A_k + A_{-k}) \right] \\
&= e^{-i\beta(\pi)} e^{i\beta(0)}.
\end{aligned}
\tag{A.8}
$$

$k = 0$ and $k = \pi$ are inversion-invariant momenta. We can see from Eq.(A.6) that in these momenta $e^{-i\beta(k)}$ is inversion eigenvalue of the eigenstate of the occupied band. Using the fact that the inversion eigenvalue is ± 1, the topological property of this model can be diagnosed by checking the inversion eigenvalues χ in $k = 0, \pi$. The diagnosing method is summarised in Table 1.1.

The inversion operator is written as

$$Ia_i = b_{-i} \;,\;\; Ia_k = \sum_i e^{-ikr_i} b_{-i} = b_{-k},$$
$$Ib_i = a_{-i} \;,\;\; Ib_k = \sum_i e^{-ikr_i} a_{-i} = a_{-k}, \tag{A.9}$$
$$I = \begin{pmatrix} 0 & 1 \\ 1 & 0 \end{pmatrix},$$

and the eigenstates of the occupied bands satisfy

$$I\,|u_0\rangle = |u_0\rangle \,,$$
$$I\,|u_\pi\rangle = \mathrm{sgn}(t_1 - t_2)\,|u_\pi\rangle \,. \tag{A.10}$$

Arbitrariness of the inversion center So far we have assumed that the inversion center is locating on the t_1 bond. However, we can take it on the t_2 bond instead. It is worth checking how the diagnostic method works in this case. The inversion operator I' is written as

$$I'a_i = b_{-i-1} \;,\;\; I'a_k = \sum_i e^{-ikr_i} b_{-i-1} = e^{-ik} b_{-k},$$
$$I'b_i = a_{-i-1} \;,\;\; I'b_k = \sum_i e^{-ikr_i} a_{-i-1} = e^{-ik} a_{-k}, \tag{A.11}$$
$$I' = e^{-ik} \begin{pmatrix} 0 & 1 \\ 1 & 0 \end{pmatrix}.$$

Only the inversion eigenvalue in $k = \pi$ is changed and as a result $\chi_{k=0}\chi_{k=\pi}$ flips its sign. It sounds that by changing the inversion center the model can be changed from trivial to nontrivial. This may seem that the artificial change in interpretation affects the physical properties of the model, but in fact, the end of the chain is specifically affected. Once the inversion center is fixed, the unit cell must be taken in such a way that its center of mass overlaps the inversion canter, and the end of the chain must coincide with the end of the unit cell [Fig.A.1]. In other words, the broken bond is changed when the inversion center is changed. When $t_2 > t_1$, there is a bonding state on the t_2 bond, and thus the nontrivial end states appear only when t_2 bond is broken. On the other hand, When $t_1 > t_2$, the nontrivial end states appear only when the t_1 bond is broken. In both cases, the diagnostic method "When $\chi_{k=0}\chi_{k=\pi} = -1$, nontrivial end states appear" works well.

The change of the inversion center is also understood as a change of the origin to measure a position. The Berry phase is the Wannier center (charge center) of the occupied band. The Wannier function $|0\rangle$ is defined as

$$|0\rangle = \int dk\, e^{ikr}\,|u_k\rangle \,, \tag{A.12}$$

where $|u_k\rangle$ is the periodic part of the Bloch wavefunction $|\psi_k\rangle = e^{ikr}\,|u_k\rangle$. Using the Wannier function, we can see that the expectation value of the position r is the same as

(a)

Unit cell

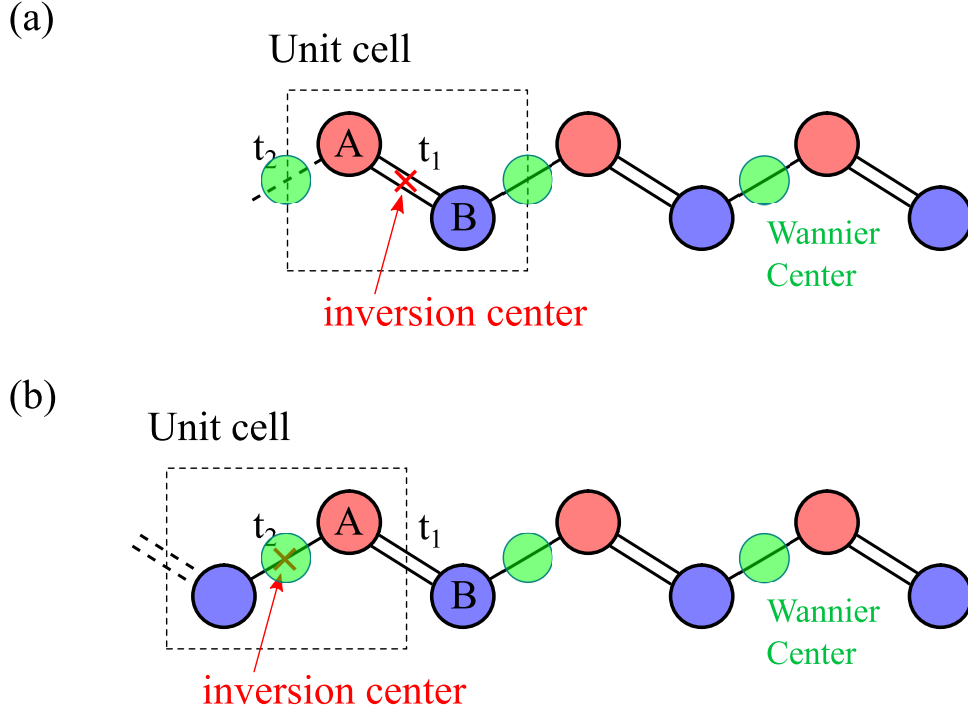inversion center

(b)

Unit cell

inversion center

Figure A.1. Unit cell configuration and the end of the chain. (a) When the inversion center is taken on the t_1 bond. The t_2 bond is broken in the chain end. When Wannier center is locating on the t_2 bond, nontrivial end states appear. (b) When the inversion center is taken on the t_2 bond. The t_1 bond is broken in the chain end. In this case, the Wannier center is inside the unit cell, and thus no end state appears.

the Berry phase,

$$
\begin{aligned}
\langle 0 | \, r \, | 0 \rangle &= \int dk dk' \, \langle u_k | \, e^{-ikr} r e^{ik'r} \, | u_k \rangle \\
&= \int dk i \, \langle u_k | \, \frac{\partial}{\partial k} \, | u_k \rangle \\
&= \theta
\end{aligned}
\tag{A.13}
$$

When the Wannier center is shifted by half of the unit cell from the origin, the Berry phase is π. The inversion center is taken on the origin, and thus the position of the Wannier center is (relatively) changed when the inversion center is changed.

Because of this inversion center dependence, we must carefully check the unit cell configuration and the surface we want to see when we use the diagnostic method.

A.3.2 Chern insulator

Since the Chern insulator is a quantum Hall system, it is required to break the TR symmetry and thus there is no spin degeneracy in generic point in the momentum space. For the simple explanation, we assume a single occupied band case. The Chern number
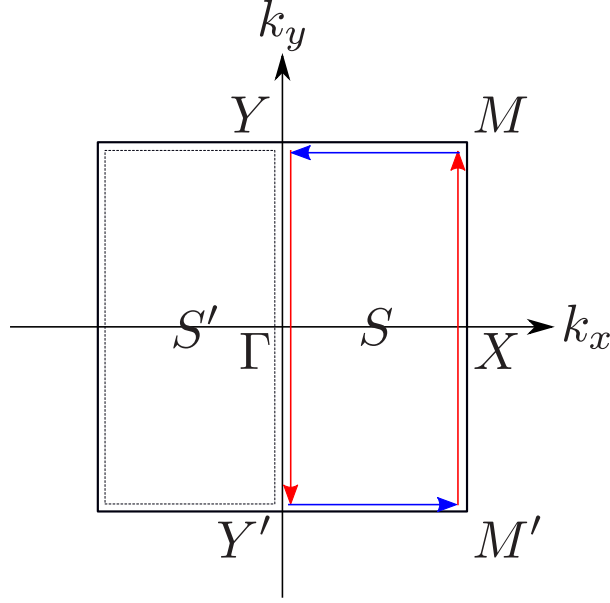
Figure A.2. Brillouin Zone and path used in the calculation of the Chern number. Due to the inversion symmetry, the integral on S' equals that on S.

$\mathcal{C}$ is calculated as

$$
\begin{aligned}
A_x =&\, i \langle u_{\boldsymbol{k}} | \frac{\partial}{\partial k_x} | u_{\boldsymbol{k}} \rangle, \\
A_y =&\, i \langle u_{\boldsymbol{k}} | \frac{\partial}{\partial k_y} | u_{\boldsymbol{k}} \rangle, \\
\mathcal{C} =&\, \frac{1}{2\pi} \int_{\mathrm{BZ}} dk_x dk_y \left(\frac{\partial A_y}{\partial k_x} - \frac{\partial A_x}{\partial k_y} \right).
\end{aligned}
\tag{A.14}
$$

The Hall current corresponds to the chiral edge state. The Chern number $\mathcal{C}$ is the number of clockwise chiral edge stats [4]. Therefore, when the C is nonzero, the system has a nonzero Hall conductivity and those cases are "topologically nontrivial" cases.

Let us introduce the inversion symmetry into the Chern insulator. Since the Berry curvature $B_z(\boldsymbol{k}) = \frac{\partial A_y}{\partial k_x} - \frac{\partial A_x}{\partial k_y}$ is a pseudovector, $B_z(\boldsymbol{k}) = B_z(-\boldsymbol{k})$ is satisfied. Due to this relation, we can divide the BZ into two inversion symmetric parts [Fig.A.2], for example S ($k_x > 0$) and S' ($k_x < 0$), and the Chern number can be calculated on one of them. Using the Stokes' theorem,

$$
\mathcal{C} = \frac{1}{\pi} \int_S dk_x dk_y \left(\frac{\partial A_y}{\partial k_x} - \frac{\partial A_x}{\partial k_y} \right) = \frac{1}{\pi} \int_{\partial S} d\boldsymbol{k} \cdot \boldsymbol{A}.
\tag{A.15}
$$

Now the path ∂S is $M \to Y \to Y' \to M' \to M$.

To calculate Eq.(A.15), let us fix the gauge so that the wave functions $|u_k\rangle$ in YM and $Y'M'$ match without any phase factor. By this gauge fixing, the integrals along MY and $Y'M'$ cancel each other. The Chern number can be evaluated by calculating $e^{i\pi\mathcal{C}}$,
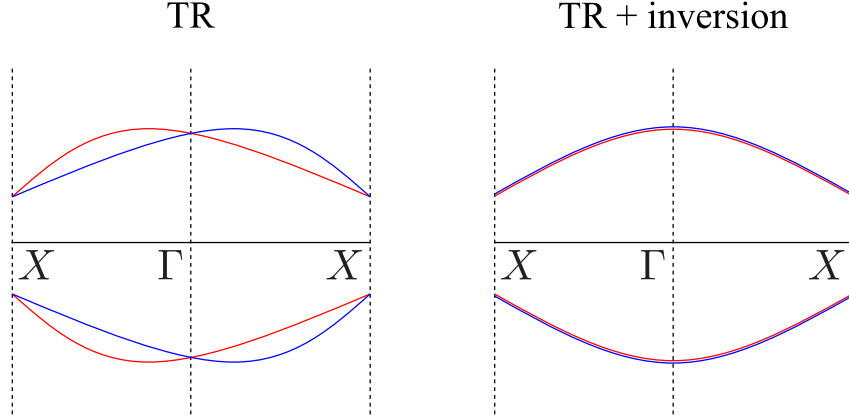
Figure A.3. Schematic picture of the band dispersion in TR symmetric system. With only TR symmetry, bands are required to degenerate with a spin only on TRIM (now Γ and X). If inversion symmetry is added, bands are required to degenerate everywhere in the momentum space.

and it is given by using Eq.(A.8) as

$$
\begin{aligned}
e^{i\pi\mathcal{C}} &= \exp\left[i\int_{M'XM} d\boldsymbol{k}\cdot\boldsymbol{A}\right]\exp\left[i\int_{Y\Gamma Y'} d\boldsymbol{k}\cdot\boldsymbol{A}\right] \\
&= \chi_\Gamma\chi_X\chi_Y\chi_M,
\end{aligned}
\tag{A.16}
$$

where χs are the inversion eigenvalues of the occupied band in the four inversion-invariant points.

For multi occupied bands systems, this diagnostic method is extended as

$$
e^{i\pi\mathcal{C}} = \prod_{n:\text{occupied}}\prod_{\boldsymbol{k}:4\text{TRIM}} \chi_n(\boldsymbol{k}),
\tag{A.17}
$$

where n is the band index and $\chi_n(\boldsymbol{k})$ is the inversion eigenvalue of the n-th band in $\boldsymbol{k}$.

Although this diagnostic method subduces the $\mathbb{Z}$ valued Chern number into a $\mathbb{Z}_2$ value, we can say the Chern number is nonzero when $\chi_\Gamma\chi_X\chi_Y\chi_M = -1$.

A.3.3 2D TR protected topological insulator

To get a nontrivial insulator in TR symmetric system, significant (unignorable) SOC is required. In a TR symmetric spinful system, a single chiral edge state is prohibited. The edge state that appears in these systems is a pair of states called helical edge state, one of which goes forwards and the other backward, but with opposite spins. Therefore, the 2D TR protected topological insulator is also referred to as a quantum spin Hall system.

First, we review the definition of the topological invariant ν in systems with only the TR symmetry. When a spinful system has TR symmetry, the eigenstates in TRIM are always doubly degenerated with spin (or pseudospin) [FigA.3] [56]. The TR operator $\mathcal{T}$ projects an eigenstate $|u_{1,\boldsymbol{k}}\rangle$ into an eigenstate of the opposite spin $|u_{2,-\boldsymbol{k}}\rangle$, and thus

"the TR eigenvalue" is not well-defined in TRIM. However, when $|u_{1,\mathbf{k}}\rangle$ and $|u_{2,\mathbf{k}}\rangle$ are continuously defined and the gauge is fixed, the phase factor given by $\mathcal{T}$ can be defined like Eq.(A.6) as

$$
\begin{aligned}
\mathcal{T}|u_{2,\mathbf{k}}\rangle &= e^{-i\beta(\mathbf{k})}|u_{1,-\mathbf{k}}\rangle, \\
\mathcal{T}|u_{1,\mathbf{k}}\rangle &= -e^{-i\beta(-\mathbf{k})}|u_{2,-\mathbf{k}}\rangle.
\end{aligned}
\tag{A.18}
$$

Using this relation, we define the w matrix as

$$
\begin{aligned}
w &= \begin{pmatrix} \langle u_{1,-\mathbf{k}}|\mathcal{T}|u_{1,\mathbf{k}}\rangle & \langle u_{1,-\mathbf{k}}|\mathcal{T}|u_{2,\mathbf{k}}\rangle \\ \langle u_{2,-\mathbf{k}}|\mathcal{T}|u_{1,\mathbf{k}}\rangle & \langle u_{2,-\mathbf{k}}|\mathcal{T}|u_{2,\mathbf{k}}\rangle \end{pmatrix} \\
&= \begin{pmatrix} 0 & e^{-i\beta(\mathbf{k})} \\ -e^{-i\beta(-\mathbf{k})} & 0 \end{pmatrix}.
\end{aligned}
\tag{A.19}
$$

This w matrix plays an essential role to describe the topological properties of the system.

To calculate the topological invariant of the spin quantum Hall system, we define the spin-polarized Berry connection,

$$
\mathbf{A}^s(\mathbf{k}) = i\langle u_{1,\mathbf{k}}|\frac{\partial}{\partial\mathbf{k}}|u_{1,\mathbf{k}}\rangle - i\langle u_{2,\mathbf{k}}|\frac{\partial}{\partial\mathbf{k}}|u_{2,\mathbf{k}}\rangle.
\tag{A.20}
$$

From Eq.(A.18), $A^s(-\mathbf{k})$ is related with $A^s(\mathbf{k})$ as

$$
\mathbf{A}^s(-\mathbf{k}) = -\mathbf{A}^s(\mathbf{k}) + \frac{\partial}{\partial\mathbf{k}}[\beta(\mathbf{k}) - \beta(-\mathbf{k})].
\tag{A.21}
$$

Fixing the gauge in the same way as Eq.(A.16), the topological invariant ν is given as

$$
\nu = \frac{1}{2\pi}\int_{Y\Gamma Y'} d\mathbf{k}\cdot\mathbf{A}^s(\mathbf{k}) + \frac{1}{2\pi}\int_{M'XM} d\mathbf{k}\cdot\mathbf{A}^s(\mathbf{k}).
\tag{A.22}
$$

Now considering a spinful system and thus there is a factor 2 compared to Eq.(A.16). We first evaluate the first term. It is calculated as

$$
\begin{aligned}
\frac{1}{2\pi}\int_{Y\Gamma Y'} d\mathbf{k}\cdot\mathbf{A}^s(\mathbf{k}) &= \frac{1}{2\pi}\int_{-\pi}^{\pi} dk_y A_y^s(0,k_y) \\
&= \frac{1}{2\pi}\int_0^{\pi} dk_y\left[A_y^s(0,k_y) + A_y^s(0,-k_y)\right] \\
&= \frac{1}{2\pi}\int_0^{\pi} dk_y\frac{\partial}{\partial k_y}[\beta(0,k_y) - \beta(0,-k_y)]
\end{aligned}
\tag{A.23}
$$

From Eq.(A.19), $\beta(\mathbf{k}) = i\log(w_{12})$ and $\beta(-\mathbf{k}) = i\log(-w_{21})$ hold,

$$
\begin{aligned}
\frac{1}{2\pi}\int_{Y\Gamma Y'} d\mathbf{k}\cdot\mathbf{A}^s(\mathbf{k}) &= \frac{1}{2\pi}\int_0^{\pi} dk_y\frac{\partial}{\partial k_y}[i\log(w_{12}) - i\log(-w_{21})] \\
&= -\frac{1}{2\pi i}\left[\log\frac{w_{12}(\pi)}{w_{12}(0)} - \log\frac{w_{21}(\pi)}{w_{21}(0)}\right]
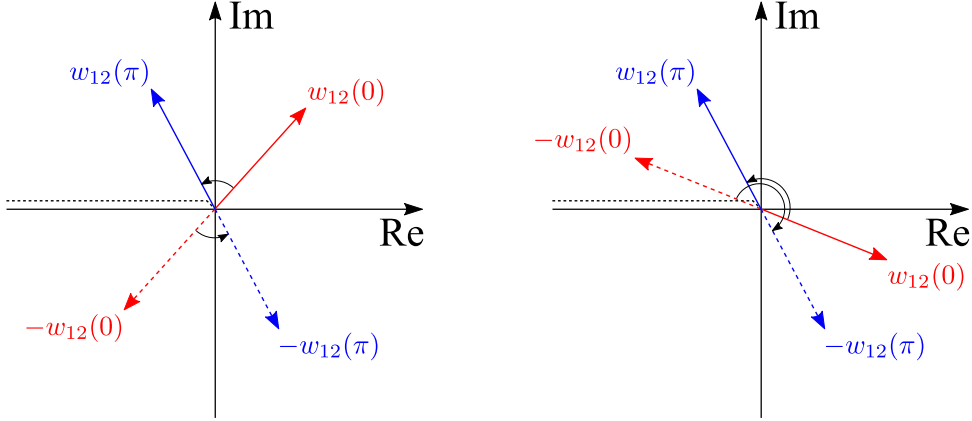\end{aligned}
\tag{A.24}
$$

Figure A.4. $w_{12}(0)$ and $w_{12}(\pi)$ for trivial (left) and nontrivial (right) cases. The branch cut is taken on the negative real axis. The arguments should be measured without crossing the branch cut.

In TRIM, due to the anti-unitarity of $\mathcal{T}$, the w matrix is antisymmetric matrix and thus $w_{21} = -w_{12}$. To evaluate this value, we must be careful that the argument must be measured in the same branch cut of log. Here we define the image of log is $[-\pi, \pi)$, and note that $\log(-1) = -i\pi$. We also define the upper (lower) half of the complex plane as $\{z \in \mathbb{C} \,|\, \text{Im}\log z \in [0, \pi)\}$ ($\{z \in \mathbb{C} \,|\, \text{Im}\log z \in [-\pi, 0)\}$). Fig.A.4 shows that when both of $w_{12}(0)$ and $w_{12}(\pi)$ are in the upper (or lower) half Eq.(A.24) is 0. On the other hand, when $w_{12}(0)$ and $w_{12}(\pi)$ are in the opposite half, it is -1. Summarising these result, we can rewrite as

$$\frac{1}{2\pi} \int_{Y\Gamma Y'} d\boldsymbol{k} \cdot \boldsymbol{A}^s(\boldsymbol{k}) = \frac{1}{\pi i} \log \left[\frac{w_{12}(\pi)}{\sqrt{w_{12}(\pi)^2}} \frac{w_{12}(0)}{\sqrt{w_{12}(0)^2}} \right], \tag{A.25}$$

where $\sqrt{z}$ is the square root of z that is in the upper half of the complex plane.

The integral along $M'XM$ can be calculated in the same way. As a result, the topological invariant ν is given as

$$(-1)^\nu = \prod_{4\ \text{TRIM}} \frac{w_{12}(\boldsymbol{k})}{\sqrt{w_{12}(\boldsymbol{k})^2}} \tag{A.26}$$

When $\nu = 1$ (nontrivial), there are helical edge states and Dirac cone surface bands appear in the band dispersion around the Fermi energy.

When the system is also inversion symmetric, the Eq.(A.26) is described as a simpler formula. The inversion I changes the momentum $\boldsymbol{k}$ to $-\boldsymbol{k}$, but does not change the spin part. Combining with $\mathcal{T}$, $I\mathcal{T}$ works as an operator that flips the spin in the same $\boldsymbol{k}$. As a result, when the system is TR and inversion symmetric, all bands are doubly degenerated with spin everywhere in the momentum space [Fig.A.3]. TRIM is also inversion invariant points and therefore inversion eigenvalue $\chi(\boldsymbol{k})$ is defined in TRIM. Since $[I, \mathcal{T}] = 0$, the two degenerated bands always have the same inversion eigenvalue. Using these fact, the

105

w matrix in TRIM ($\boldsymbol{k} \equiv -\boldsymbol{k}$) is rewritten with the inversion eigenvalue,

$$
\begin{aligned}
w_{mn}(\boldsymbol{k}) &= \langle u_{m,-\boldsymbol{k}} | \, \mathcal{T} \, | u_{n,\boldsymbol{k}} \rangle \\
&= \langle u_{m,\boldsymbol{k}} | \, II\mathcal{T} \, | u_{n,\boldsymbol{k}} \rangle \\
&= \chi_m(\boldsymbol{k}) \langle u_{m,\boldsymbol{k}} | \, I\mathcal{T} \, | u_{n,\boldsymbol{k}} \rangle \\
&= \chi_n(\boldsymbol{k}) \langle u_{m,\boldsymbol{k}} | \, I\mathcal{T} \, | u_{n,\boldsymbol{k}} \rangle .
\end{aligned}
\tag{A.27}
$$

It is possible to choose the gauge of $|u_1(\boldsymbol{k})\rangle$ such as

$$
\forall \boldsymbol{k}, \quad \langle u_{2,-\boldsymbol{k}} | \, I\mathcal{T} \, | u_{1,\boldsymbol{k}} 1 \rangle = 1.
\tag{A.28}
$$

In this gauge, the w matrix in TRIM is

$$
w = \chi_1(\boldsymbol{k}) \begin{pmatrix} 0 & 1 \\ -1 & 0 \end{pmatrix}.
\tag{A.29}
$$

Therefore, the topological invariant ν (Eq.(A.26)) is diagnosed by a product of the inversion eigenvalues in TRIM,

$$
(-1)^\nu = \prod_{\boldsymbol{k}:\mathrm{4TRIM}} \chi_1(\boldsymbol{k}).
\tag{A.30}
$$

Note that the inversion eigenvalue is taken only once for a degenerated pair.

For multi occupied (paired) bands systems, this diagnostic method is extended as

$$
(-1)^\nu = \prod_{n:\mathrm{occupied}} \prod_{\boldsymbol{k}:\mathrm{4TRIM}} \chi_{2n}(\boldsymbol{k}),
\tag{A.31}
$$

where n is the band index. Because we need to see one band of a paired bands, only $\chi_{2n}(\boldsymbol{k})$ is taken into account and $\chi_{2n-1}(\boldsymbol{k})$ is not.

Now $\chi = \pm 1$, and thus it can also be written by counting the -1 inversion eigenvalues as

$$
\nu = \sum_{\boldsymbol{k}:\mathrm{4TRIM}} n^-(\boldsymbol{k}) \pmod 2,
\tag{A.32}
$$

where $n^-(\boldsymbol{k})$ is the number of occupied band pair with -1 inversion eigenvalues.

A.3.4   3D TR protected topological insulator

In the discussion of 3D TR protected topological insulator, spin-orbit coupled systems are assumed for the same reason as the 2D case.

In 3D momentum space, there are eight TRIM. By choosing four of them, it is attributed to the 2D case. For easy explanation, let us see a primitive orthorhombic case and see the four TRIM on the $k_z = 0$ plane and the four on the $k_z = \pi$ plane [Fig.A.5]. Each of them is understood as a 2D topological insulator. When the (001) surface is considered, the two 2D topological insulators overlap on the surface BZ. When only one of them, for example, $k_z = 0$, has nontrivial invariant $\nu_{2\mathrm{D}} = 1$, a 2D topological insulator is given on the surface BZ. Projecting into the (001) surface BZ is understood in the real space as making a slab with a finite thickness along the (001) direction. In this case, the
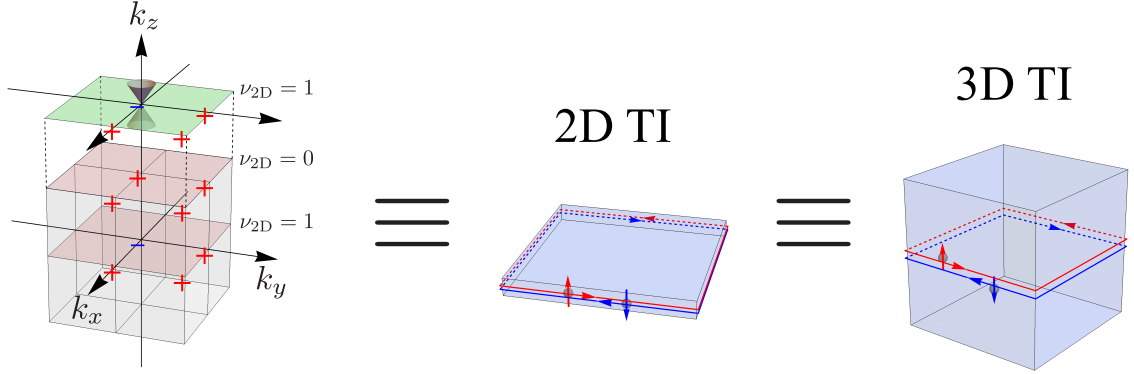
Figure A.5. 3D topological insulator and its attribution to the 2D topological insulator. The 3D bulk is understood as two 2D systems when a slab is assumed. The 3D crystal has helical edge states on the surface that corresponds to the "edge of slab".

slab, which is a 2D system, posses helical edge states on its edge. If we move back to a more 3D-like picture, the helical edge states are on the surface that is NOT perpendicular to the (001) direction.

If both of the $k_z = 0$ and $k_z = \pi$ plane have $\nu_{2D} = 1$, the surface is $\nu_{2D} = 0$. In naive extrapolation, the band dispersion on the surface BZ can have two Dirac cone surface bands but those surface states are not necessarily robust against a perturbation [Fig.1.8]. For example, let us assume a super-cell periodic perturbation. The perturbation folds the BZ and as a result, the two Dirac cones may overlap each other and get gapped.

As explained above, we get two kinds of 3D topological insulators as an extension of the 2D case. One of them is given as a combination of two nontrivial 2D topological insulators, and the other is given as a combination of trivial and nontrivial 2D topological insulators. The former one is not necessarily robust against perturbation and thus it is called a "weak topological insulator". On the other hand, the latter is robust against perturbation. It is because the condition to realize the latter one is written as

$$\sum_{\boldsymbol{k}:8\mathrm{TRIM}} n^-(\boldsymbol{k}) = 1 \pmod 2, \tag{A.33}$$

and this relation is never violated by a BZ folding. Due to this robustness, the latter one is called a "strong topological insulator". Furthermore, Eq.(A.33) has nothing to do with the surface direction. Therefore, the strong topological insulator has helical edge stets on all surfaces. In the surface BZ, the surface states appear as an odd number of Dirac cones.

Using the relation between surface Dirac cones and inversion eigenvalues, the shape of the surface Fermi arc can be qualitatively known [Fig.1.7].

Summarising and generalising the discussion above, the 3D TR protected topological insulator with the inversion symmetry is diagnosed by four invariants, ν_0 (strong invariant) and $\nu_1\nu_2\nu_3$ (weak invariants). The definition of them are

$$(-1)^{\nu_0} = \prod_{n:\text{occupied}} \prod_{\boldsymbol{k}:8\text{TRIM}} \chi_{2n}(\boldsymbol{k}),$$

$$(-1)^{\nu_1} = \prod_{n:\text{occupied}} \prod_{\substack{\boldsymbol{k}:4\text{TRIM}\\m_1=1}} \chi_{2n}(\boldsymbol{k}),$$

$$(-1)^{\nu_2} = \prod_{n:\text{occupied}} \prod_{\substack{\boldsymbol{k}:4\text{TRIM}\\m_2=1}} \chi_{2n}(\boldsymbol{k}), \tag{A.34}$$

$$(-1)^{\nu_3} = \prod_{n:\text{occupied}} \prod_{\substack{\boldsymbol{k}:4\text{TRIM}\\m_3=1}} \chi_{2n}(\boldsymbol{k}),$$

where the TRIM are represented by $m_1, m_2, m_3 = 0, 1$ and reciprocal lattice vestors $\boldsymbol{b}_1, \boldsymbol{b}_2, \boldsymbol{b}_3$ as $\boldsymbol{k} = \frac{1}{2}(m_1\boldsymbol{b}_1 + m_2\boldsymbol{b}_2 + m_3\boldsymbol{b}_3)$. For example, in a primitive orthorhombic case, the ν_1 is calculated with the four TRIM on $k_x = \pi$. These invariants are also written with the number of occupied band pair with -1 inversion eigenvalues,

$$\nu_0 = \sum_{\boldsymbol{k}:8\text{TRIM}} n^-(\boldsymbol{k}) \pmod 2,$$

$$\nu_1 = \sum_{\substack{\boldsymbol{k}:4\text{TRIM}\\m_1=1}} n^-(\boldsymbol{k}) \pmod 2,$$

$$\nu_2 = \sum_{\substack{\boldsymbol{k}:4\text{TRIM}\\m_2=1}} n^-(\boldsymbol{k}) \pmod 2, \tag{A.35}$$

$$\nu_3 = \sum_{\substack{\boldsymbol{k}:4\text{TRIM}\\m_3=1}} n^-(\boldsymbol{k}) \pmod 2.$$

To attribute to the 2D topological insulator, we considered two 2D systems and topological invariants on them. Although there are only three invariants ν_1, ν_2, ν_3 that is calculated with four TRIM, the invariants of "the other four" are calculated as $\nu_0 - \nu_1$ and so on. In other words, the independent invariants are only four that are given in Eq.(A.35). For any surface configurations, the corresponding weak invariants are given by adding or subtracting the four invariants.

A.4 Symmetry-based indicator

In this section, we discuss detailed notes on the symmetry-based indicator.

A.4.1 "Trivial" in the symmetry-based indicator

The symmetry-based indicator essentially judges whether a given system can be continuously deformed into an insulator originate from isolated orbitals. This definition

is based on the assumption that systems that can be represented by isolated orbitals are "trivial". Although in most cases this assumption is appropriate to the topological classification, the word "topologically trivial" and "topologically nontrivial" are not necessarily used in the same definition as given in section 1.1. The typical exception is the SSH model. The nontrivial phase in the SSH model is diagnosed as "trivial" in the definition of the symmetry-based indicator, in spite of the existence of the end states. It is because the case with end states is represented by an atomic insulator, in which an orbital is placed on the boundary of the unit cell.

Therefore, in some exceptional cases, we need to be careful.

A.4.2 Note on the symmetry label

Uniqueness of the symmetry label

Due to the compatibility condition, the set of the irreps of the occupied bands is constant on a high symmetry line and thus the symmetry label is unique. If the compatibility condition is violated, the label can depend on the reference point (where we check the irreps).

The symmetry label as a linear space

In the original definition of the symmetry label, the component is prohibited to be negative and thus the spaces {BS} and {AI} are not linear spaces. However, to make it easy to handle them mathematically, we extend {BS} and {AI} to linear spaces. This extension involves some complicated problems.

Since the addition and subtraction are defined in the linear space {BS}, the elements of the linear space {BS} satisfies

$$\forall b_1, b_2 \in \{BS\}, \quad b_1 + b_2 \in \{BS\} \text{ and } b_1 - b_2 \in \{BS\}. \tag{A.36}$$

The addition is easily understood. The addition means that giving a new set of occupied bands from two sets of occupied bands by overlapping them. On the other hand, the subtraction can give a set of occupied bands with "negative number of bands". Therefore, the linear space {BS} includes unrealistic elements.

The elements of the linear space {AI} also satisfy

$$\forall a_1, a_2 \in \{AI\}, \quad a_1 + a_2 \in \{AI\} \text{ and } a_1 - a_2 \in \{AI\}. \tag{A.37}$$

The subtraction involves more complicated and interesting problems. Even if $a_1 - a_2$ consists of non-negative integers, it is not clear whether there really is an insulator originate from isolated orbitals that corresponds to $a_1 - a_2$.

Actually, by discussing these this problem, a new topological class called "fragile topological insulator" has been proposed [96, 97, 98]. The fragile topological insulator class is diagnosed as "trivial" by the symmetry-based indicator, but cannot be continuously connected to an insulator originate from isolated orbitals.

Although the there are some problem with the linear space {BS} and {AI}, they are defined as linear spaces in the symmetry-based indicator.

Enumeration of {AI}

Enumeration of {AI} is done in the following process. Once the space group of the system is fixed, a list of the Wyckoff position is given. The Wyckoff position is a classification of real space points in the unit cell according to their symmetry [56, 57]. Points with the same symmetry are classified in the same Wyckoff position. Placing an orbital in each Wyckoff position, we can obtain the set {AI}. When we place an orbital, we choose one from several orbitals with different symmetry depending on the symmetry of the Wyckoff position. When the Wyckoff position has multiplicity, i.e. we need to place more than one orbitals to satisfy the space group symmetry, we enumerate all possible combinations of the phase factor. Since both of the Wyckoff position and possible orbitals are finite, enumerating all possible isolated orbitals in each Wyckoff position gives {AI} with a finite trial.

Let us see an explicit example of the space group 2. Now there is only inversion symmetry, so we need to check only two orbitals, an inversion symmetric one and an inversion antisymmetric one. In the space group 2, there are nine Wyckoff positions. Eight of them are inversion symmetric points, and the other one is a generic point. In Fig.A.6, four examples of s and p_x orbitals in the Wyckoff position $(0, 0, 0)$ and $(1/2, 0, 0)$ (fractional coordinate). Fig.A.6 shows only the $z = 0$ plane since there is no oscillation in the z direction in these cases. By deciding the momentum we focus on, we can determine a phase factor given by a lattice translation. In the space group 2, we need to check eight TRIM to obtain the symmetry label. In Fig.A.6, only the case of X point $((\pi, 0, 0)$ in fractional coordinate) is shown. With the inversion center in $(0, 0, 0)$, the inversion eigenvalue of each case is calculated. For example, when we place a s orbital in $(0, 0, 0)$, the inversion eigenvalue is 1 in both of Γ and X. On the other hand, when we place a s orbital in $(1/2, 0, 0)$, the inversion eigenvalue is 1 in Γ, while -1 in X. By checking all combinations of an orbital and Wyckoff position, we can enumerate the {AI} of the space group 2.

Although the elements of {AI} obtained by this process are finite, they include the all bases of the linear space {AI}.

$$\boldsymbol{k}_\Gamma = (0, 0, 0) \qquad \boldsymbol{k}_X = (\pi, 0, 0)$$

s, $(0, 0, 0)$ — $\chi_\Gamma = 1$, $\chi_X = 1$

s, $(1/2, 0, 0)$ — $\chi_\Gamma = 1$, $\chi_X = -1$

p$_x$, $(0, 0, 0)$ — $\chi_\Gamma = -1$, $\chi_X = -1$

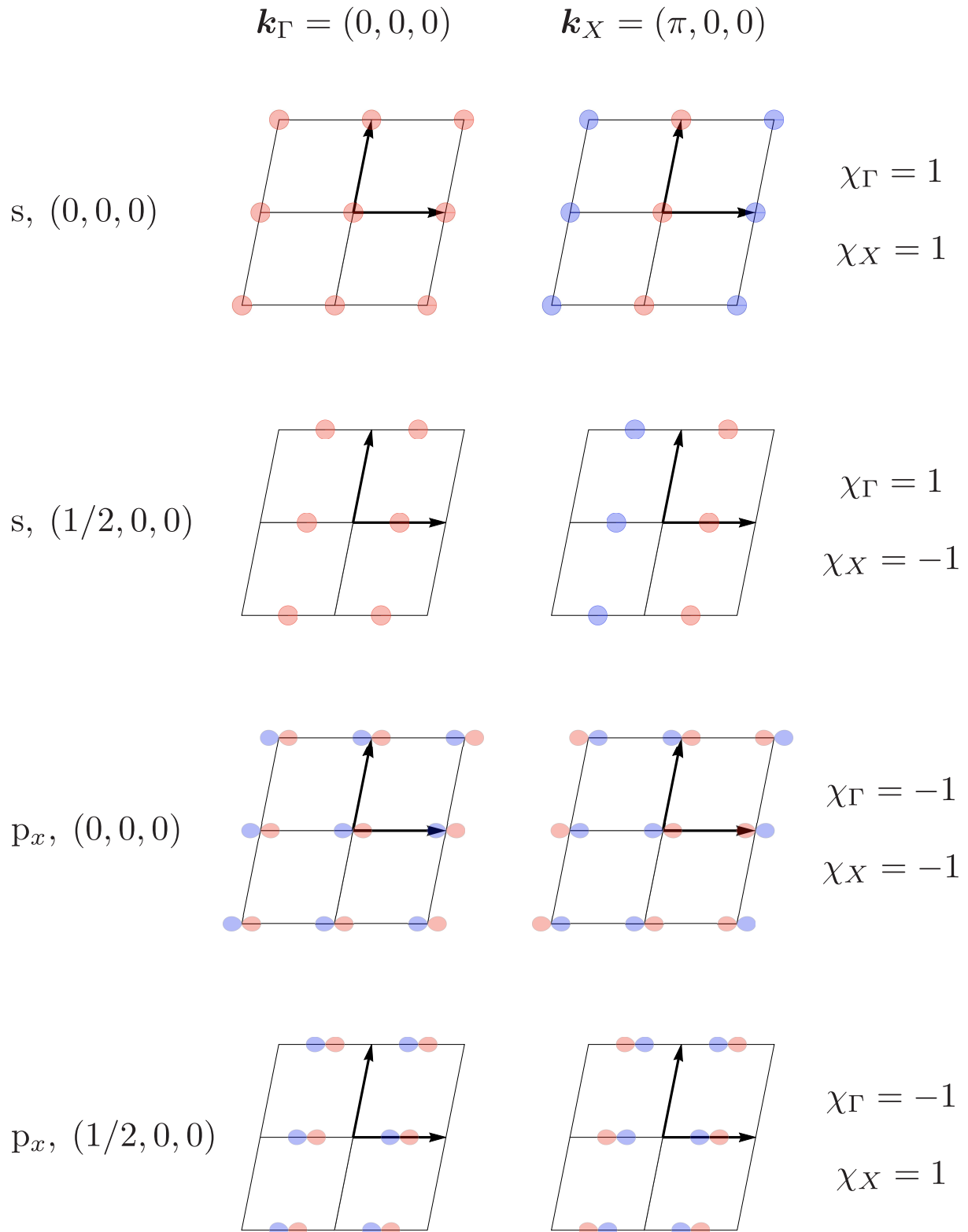p$_x$, $(1/2, 0, 0)$ — $\chi_\Gamma = -1$, $\chi_X = 1$

Figure A.6. Examples of atomic insulators. The left (right) columns show the wavefunction in the Γ point (X point). The top two rows are the case where a s orbital (inversion symmetric) is placed and the bottom two rows are the case where a p$_x$ (inversion antisymmetric) is placed. The inversion eigenvalues about $(0, 0, 0)$ are visually obtained.

111

A.4.3   The symmetry-based indicator and calculation formulas

The calculation formulas of the symmetry based indicator in systems with significant SOC are given in table A.3, A.4, and A.5.

SI set	SI group	SGs
$z_{2w,1}$ $z_{2w,2}$ $z_{2w,3}$ z_4	$\mathbb{Z}_2 \times \mathbb{Z}_2 \times \mathbb{Z}_2 \times \mathbb{Z}_4$	2, 10, 47
	$\mathbb{Z}_2 \times \mathbb{Z}_2 \times \mathbb{Z}_4$	11, 12, 13, 49, 51, 65, 67, 69
	$\mathbb{Z}_2 \times \mathbb{Z}_4$	14, 15, 48, 50, 53, 54, 55, 57, 59, 63, 64, 66 68, 71, 72, 73, 74, 84, 85, 86, 125, 129, 131, 132 134, 147, 148, 162, 164, 166, 200, 201, 204, 206, 224
	$\mathbb{Z}_4$	52, 56, 58, 60, 61, 62, 70, 88, 126, 130 133, 135, 136, 137, 138, 141, 142, 163, 165 167, 202, 203, 205, 222, 223, 227, 228, 230
z_2	$\mathbb{Z}_2$	81, 82, 111, 112, 113, 114, 115, 116, 117, 118 119, 120, 121, 122, 215, 216, 217, 218, 219, 220
$z_{2w,1}$ $z_{4m,\pi}$ z_8	$\mathbb{Z}_2 \times \mathbb{Z}_4 \times \mathbb{Z}_8$	83, 123
$z_{2w,1}$ z_8	$\mathbb{Z}_2 \times \mathbb{Z}_8$	87, 124, 139, 140, 229
$z_{4m,\pi}$ z_8	$\mathbb{Z}_4 \times \mathbb{Z}_8$	127, 221
z_8	$\mathbb{Z}_8$	128, 225, 226
$z_{3m,0}$ $z_{3m,\pi}$	$\mathbb{Z}_3 \times \mathbb{Z}_3$	174, 187, 189
$z_{3m,0}$	$\mathbb{Z}_3$	188, 190
$z_{6m,\pi}$ z_{12}	$\mathbb{Z}_6 \times \mathbb{Z}_{12}$	175, 191
z_{12}	$\mathbb{Z}_{12}$	192
z'_{12}	$\mathbb{Z}_{12}$	176, 193, 194

Table A.3: SI in all SGs adopted from Z. Song, *et. al.*, Physical Review X, **8**, 031069, (2018). The indicators whose odd values correspond to strong TI are printed in red.

Indicator	SGs	Formula
$z_{2\mathrm{w},j=1,2,3}$	All SGs with inversion	$\sum_{\mathbf{K}}' n_{\mathbf{K}}^- \mod 2$ [1]
z_4	All SGs with inversion	$\sum_{\mathbf{K}\in\mathrm{TRIM}} \frac{1}{2}n_{\mathbf{K}}^- - \frac{1}{2}n_{\mathbf{K}}^+ \mod 4$
z_2	All SGs with S_4	$\sum_{\mathbf{K}} \frac{1}{2}n_{\mathbf{K}}^{\frac{3}{2}} - \frac{1}{2}n_{\mathbf{K}}^{\frac{1}{2}} \mod 2$ [2]
$z_{4\mathrm{m},\pi}$	83 (123, 127)[3]	$\frac{3}{2}n(E^{\mathrm{Z}}_{\frac{3}{2}\mathrm{g}}) - \frac{3}{2}n(E^{\mathrm{Z}}_{\frac{3}{2}\mathrm{u}}) - \frac{1}{2}n(E^{\mathrm{Z}}_{\frac{1}{2}\mathrm{g}}) + \frac{1}{2}n(E^{\mathrm{Z}}_{\frac{1}{2}\mathrm{u}}) + \frac{3}{2}n(E^{\mathrm{A}}_{\frac{3}{2}\mathrm{g}}) - \frac{3}{2}n(E^{\mathrm{A}}_{\frac{3}{2}\mathrm{u}})$ $- \frac{1}{2}n(E^{\mathrm{A}}_{\frac{1}{2}\mathrm{g}}) + \frac{1}{2}n(E^{\mathrm{A}}_{\frac{1}{2}\mathrm{u}}) + n(E^{\mathrm{R}}_{\frac{1}{2}\mathrm{g}}) - n(E^{\mathrm{R}}_{\frac{1}{2}\mathrm{u}}) \mod 4$
	221	$\frac{3}{2}n(E^{\mathrm{X}}_{\frac{3}{2}\mathrm{g}}) - \frac{3}{2}n(E^{\mathrm{X}}_{\frac{3}{2}\mathrm{u}}) - \frac{1}{2}n(E^{\mathrm{X}}_{\frac{1}{2}\mathrm{g}}) + \frac{1}{2}n(E^{\mathrm{X}}_{\frac{1}{2}\mathrm{u}})$ $+ \frac{3}{2}n(E^{\mathrm{R}}_{\frac{5}{2}\mathrm{g}}) - \frac{3}{2}n(E^{\mathrm{R}}_{\frac{5}{2}\mathrm{u}}) + n(F^{\mathrm{R}}_{\frac{3}{2}\mathrm{g}}) - n(F^{\mathrm{R}}_{\frac{3}{2}\mathrm{u}}) - \frac{1}{2}n(E^{\mathrm{R}}_{\frac{1}{2}\mathrm{g}}) + \frac{1}{2}n(E^{\mathrm{R}}_{\frac{1}{2}\mathrm{u}})$ $+ n(E^{\mathrm{M}}_{\frac{1}{2}\mathrm{g}}) + n(E^{\mathrm{M}}_{\frac{3}{2}\mathrm{g}}) - n(E^{\mathrm{M}}_{\frac{1}{2}\mathrm{u}}) - n(E^{\mathrm{M}}_{\frac{3}{2}\mathrm{u}}) \mod 4$
z_8	83, 87, 123, 124, 127, 128, 139, 140, 221, 225, 226, 229	$\frac{3}{2}n^+_{\frac{3}{2}} - \frac{3}{2}n^-_{\frac{3}{2}} - \frac{1}{2}n^+_{\frac{1}{2}} + \frac{1}{2}n^-_{\frac{1}{2}} \mod 8$ [4]
$z_{3\mathrm{m},0}$	174 (187, 188, 189, 190)[3]	$-\frac{1}{2}n(^1E^K_{\frac{1}{2}}) + \frac{3}{2}n(^1E^K_{\frac{3}{2}}) + \frac{1}{2}n(^1E^K_{\frac{5}{2}}) - \frac{1}{2}n(^2E^K_{\frac{1}{2}}) + \frac{3}{2}n(^2E^K_{\frac{3}{2}}) + \frac{1}{2}n(^2E^K_{\frac{5}{2}})$ $+ n(E^\Gamma_{\frac{1}{2}}) - n(E^\Gamma_{\frac{5}{2}}) \mod 3$
$z_{3\mathrm{m},\pi}$	174 (187, 189)[3]	$-\frac{1}{2}n(^1E^H_{\frac{1}{2}}) + \frac{3}{2}n(^1E^H_{\frac{3}{2}}) + \frac{1}{2}n(^1E^H_{\frac{5}{2}}) - \frac{1}{2}n(^2E^H_{\frac{1}{2}}) + \frac{3}{2}n(^2E^H_{\frac{3}{2}}) + \frac{1}{2}n(^2E^H_{\frac{5}{2}})$ $+ n(E^A_{\frac{1}{2}}) - n(E^A_{\frac{5}{2}}) \mod 3$
$z_{6\mathrm{m},0}$	175 (191, 192), 176 (193, 194)[3]	$\frac{3}{2}n(E^\Gamma_{\frac{3}{2}\mathrm{g}}) - \frac{5}{2}n(E^\Gamma_{\frac{5}{2}\mathrm{g}}) - \frac{1}{2}n(E^\Gamma_{\frac{1}{2}\mathrm{g}}) - \frac{3}{2}n(E^\Gamma_{\frac{3}{2}\mathrm{u}}) + \frac{5}{2}n(E^\Gamma_{\frac{5}{2}\mathrm{u}}) + \frac{1}{2}n(E^\Gamma_{\frac{1}{2}\mathrm{u}})$ $+ 3n(E^K_{\frac{3}{2}}) - 5n(E^K_{\frac{5}{2}}) - n(E^K_{\frac{1}{2}}) + \frac{3}{2}n(E^M_{\frac{1}{2}\mathrm{g}}) - \frac{3}{2}n(E^M_{\frac{1}{2}\mathrm{u}}) \mod 6$
$z_{6\mathrm{m},\pi}$	175 (191, 192)[3]	$\frac{3}{2}n(E^A_{\frac{3}{2}\mathrm{g}}) - \frac{5}{2}n(E^A_{\frac{5}{2}\mathrm{g}}) - \frac{1}{2}n(E^A_{\frac{1}{2}\mathrm{g}}) - \frac{3}{2}n(E^A_{\frac{3}{2}\mathrm{u}}) + \frac{5}{2}n(E^A_{\frac{5}{2}\mathrm{u}}) + \frac{1}{2}n(E^A_{\frac{1}{2}\mathrm{u}})$ $+ 3n(E^H_{\frac{3}{2}}) - 5n(E^H_{\frac{5}{2}}) - n(E^H_{\frac{1}{2}}) + \frac{3}{2}n(E^L_{\frac{1}{2}\mathrm{g}}) - \frac{3}{2}n(E^L_{\frac{1}{2}\mathrm{u}}) \mod 6$
z_{12}	175, 191, 192	$\{\bar{z}_{6\mathrm{m}} + 3[(\bar{z}_{6\mathrm{m}} - z_4) \mod 4]\} \mod 12$ [5]
z'_{12}	176, 193, 194	$\{z_{6\mathrm{m},0} + 3[(z_{6\mathrm{m},0} - z_4) \mod 4]\} \mod 12$

Table A.4: Fu-Kane-like formulae for all SI adopted from Z. Song, *et. al.*, Physical Review X, **8**, 031069, (2018). The indicators whose odd values correspond to strong TI are printed in red. The notations of high symmetry momenta follow the standard convention [99], and the notations of point group irreps follow [100]

---

[1]$\mathbf{K}$ is summed over the four TRIMs with $k_j = \pi$.

[2]$\mathbf{K}$ is summed over the four S_4 invariant TRIMs, $n_{\mathbf{K}}^{\frac{1}{2}}$ is the number of Kramer pairs at $\mathbf{K}$ with $\mathrm{tr}[D(S_4)] = \sqrt{2}$, $n_{\mathbf{K}}^{\frac{3}{2}}$ is the number of Kramer pairs at $\mathbf{K}$ with $\mathrm{tr}[D(S_4)] = -\sqrt{2}$, and $D(S_4)$ is the representation matrix on the corresponding Kramer pair.

[3]The equation is derived for the SG in front of the bracket but also applicable to the SGs in the bracket, which are supergroups of the SG in front of the bracket. To apply the equation for these supergroups, one should omit the additional symmetries and count them as the corresponding subgroup.

[4]The concrete definitions for $n^+_{\frac{3}{2}}$, $n^-_{\frac{3}{2}}$, $n^+_{\frac{1}{2}}$, and $n^-_{\frac{1}{2}}$ is given in Table A.5

[5]Here $\bar{z}_{6\mathrm{m}} = z_{6\mathrm{m},0} + z_{6\mathrm{m},\pi} \mod 6$

Lattice	SGs	n	Definitions for $n_{\frac{3}{2}}^+, n_{\frac{3}{2}}^-, n_{\frac{1}{2}}^+, n_{\frac{1}{2}}^-$
Tetragonal primitive	83 (123, 124, 127, 128)[1]	$n_{\frac{1}{2}}^+$	$n(E_{\frac{1}{2}g}^\Gamma) + n(E_{\frac{1}{2}g}^M) + n(E_{\frac{1}{2}g}^Z) + n(E_{\frac{1}{2}g}^A) + n(E_{\frac{1}{2}g}^X) + n(E_{\frac{1}{2}g}^R)$
		$n_{\frac{1}{2}}^-$	$n(E_{\frac{1}{2}u}^\Gamma) + n(E_{\frac{1}{2}u}^M) + n(E_{\frac{1}{2}u}^Z) + n(E_{\frac{1}{2}u}^A) + n(E_{\frac{1}{2}u}^X) + n(E_{\frac{1}{2}u}^R)$
		$n_{\frac{3}{2}}^+$	$n(E_{\frac{3}{2}g}^\Gamma) + n(E_{\frac{3}{2}g}^M) + n(E_{\frac{3}{2}g}^Z) + n(E_{\frac{3}{2}g}^A) + n(E_{\frac{1}{2}g}^X) + n(E_{\frac{1}{2}g}^R)$
		$n_{\frac{3}{2}}^-$	$n(E_{\frac{3}{2}u}^\Gamma) + n(E_{\frac{3}{2}u}^M) + n(E_{\frac{3}{2}u}^Z) + n(E_{\frac{3}{2}u}^A) + n(E_{\frac{1}{2}u}^X) + n(E_{\frac{1}{2}u}^R)$
Tetragonal body-centred	87 (139, 140)[1]	$n_{\frac{1}{2}}^+$	$n(E_{\frac{1}{2}g}^\Gamma) + n(E_{\frac{1}{2}g}^M) + n(E_{\frac{1}{2}g}^X) + 2n(E_{\frac{1}{2}g}^N) + n(E_{\frac{1}{2}}^P)^2$
		$n_{\frac{1}{2}}^-$	$n(E_{\frac{1}{2}u}^\Gamma) + n(E_{\frac{1}{2}u}^M) + n(E_{\frac{1}{2}u}^X) + 2n(E_{\frac{1}{2}u}^N) + n(E_{\frac{3}{2}}^P)$
		$n_{\frac{3}{2}}^+$	$n(E_{\frac{3}{2}g}^\Gamma) + n(E_{\frac{3}{2}g}^M) + n(E_{\frac{1}{2}g}^X) + 2n(E_{\frac{1}{2}g}^N) + n(E_{\frac{3}{2}}^P)$
		$n_{\frac{3}{2}}^-$	$n(E_{\frac{3}{2}u}^\Gamma) + n(E_{\frac{3}{2}u}^M) + n(E_{\frac{1}{2}u}^X) + 2n(E_{\frac{1}{2}u}^N) + n(E_{\frac{1}{2}}^P)$
Cubic primitive	221	$n_{\frac{1}{2}}^+$	$n(E_{\frac{1}{2}g}^\Gamma) + n(F_{\frac{3}{2}g}^\Gamma) + n(E_{\frac{1}{2}g}^R) + n(F_{\frac{3}{2}g}^R) + 2n(E_{\frac{1}{2}g}^M) + n(E_{\frac{3}{2}g}^M) + 2n(E_{\frac{1}{2}g}^X) + n(E_{\frac{3}{2}g}^X)$
		$n_{\frac{1}{2}}^-$	$n(E_{\frac{1}{2}u}^\Gamma) + n(F_{\frac{3}{2}u}^\Gamma) + n(E_{\frac{1}{2}u}^R) + n(F_{\frac{3}{2}u}^R) + 2n(E_{\frac{1}{2}u}^M) + n(E_{\frac{3}{2}u}^M) + 2n(E_{\frac{1}{2}u}^X) + n(E_{\frac{3}{2}u}^X)$
		$n_{\frac{3}{2}}^+$	$n(F_{\frac{3}{2}g}^\Gamma) + n(E_{\frac{5}{2}g}^\Gamma) + n(F_{\frac{3}{2}g}^R) + n(E_{\frac{5}{2}g}^R) + 2n(E_{\frac{3}{2}g}^M) + n(E_{\frac{1}{2}g}^M) + 2n(E_{\frac{3}{2}g}^X) + n(E_{\frac{1}{2}g}^X)$
		$n_{\frac{3}{2}}^-$	$n(F_{\frac{3}{2}u}^\Gamma) + n(E_{\frac{5}{2}u}^\Gamma) + n(F_{\frac{3}{2}u}^R) + n(E_{\frac{5}{2}u}^R) + 2n(E_{\frac{3}{2}u}^M) + n(E_{\frac{1}{2}u}^M) + 2n(E_{\frac{3}{2}u}^X) + n(E_{\frac{1}{2}u}^X)$
Cubic face-centred	225	$n_{\frac{1}{2}}^+$	$n(E_{\frac{1}{2}g}^\Gamma) + n(F_{\frac{3}{2}g}^\Gamma) + 2n(E_{\frac{1}{2}g}^X) + n(E_{\frac{3}{2}g}^X) + 2n(E_{\frac{1}{2}g}^L) + 2n(E_{\frac{3}{2}g}^L) + n(E_{\frac{1}{2}}^W)$
		$n_{\frac{1}{2}}^-$	$n(E_{\frac{1}{2}u}^\Gamma) + n(F_{\frac{3}{2}u}^\Gamma) + 2n(E_{\frac{1}{2}u}^X) + n(E_{\frac{3}{2}u}^X) + 2n(E_{\frac{1}{2}u}^L) + 2n(E_{\frac{3}{2}u}^L) + n(E_{\frac{3}{2}}^W)$
		$n_{\frac{3}{2}}^+$	$n(F_{\frac{3}{2}g}^\Gamma) + n(E_{\frac{5}{2}g}^\Gamma) + 2n(E_{\frac{3}{2}g}^X) + n(E_{\frac{1}{2}g}^X) + 2n(E_{\frac{1}{2}g}^L) + 2n(E_{\frac{3}{2}g}^L) + n(E_{\frac{3}{2}}^W)$
		$n_{\frac{3}{2}}^-$	$n(F_{\frac{3}{2}u}^\Gamma) + n(E_{\frac{5}{2}u}^\Gamma) + 2n(E_{\frac{3}{2}u}^X) + n(E_{\frac{1}{2}u}^X) + 2n(E_{\frac{1}{2}u}^L) + 2n(E_{\frac{3}{2}u}^L) + n(E_{\frac{1}{2}}^W)$
	226	$n_{\frac{1}{2}}^+$	$n(E_{\frac{1}{2}g}^\Gamma) + n(F_{\frac{3}{2}g}^\Gamma) + n(E_{\frac{3}{2}g}^X) + n(E_{\frac{1}{2}u}^X) + n(E_{\frac{3}{2}u}^X)$
		$n_{\frac{1}{2}}^-$	$n(E_{\frac{1}{2}u}^\Gamma) + n(F_{\frac{3}{2}u}^\Gamma) + n(E_{\frac{3}{2}u}^X) + n(E_{\frac{1}{2}g}^X) + n(E_{\frac{3}{2}g}^X)$
		$n_{\frac{3}{2}}^+$	$n(F_{\frac{3}{2}g}^\Gamma) + n(E_{\frac{5}{2}g}^\Gamma) + n(E_{\frac{1}{2}g}^X) + n(E_{\frac{1}{2}u}^X) + n(E_{\frac{3}{2}u}^X)$
		$n_{\frac{3}{2}}^-$	$n(F_{\frac{3}{2}u}^\Gamma) + n(E_{\frac{5}{2}u}^\Gamma) + n(E_{\frac{1}{2}u}^X) + n(E_{\frac{1}{2}g}^X) + n(E_{\frac{3}{2}g}^X)$
Cubic body-centred	229	$n_{\frac{1}{2}}^+$	$n(E_{\frac{1}{2}g}^\Gamma) + n(F_{\frac{3}{2}g}^\Gamma) + n(E_{\frac{1}{2}g}^H) + n(F_{\frac{3}{2}g}^H) + 3n(E_{\frac{1}{2}g}^N) + n(E_{\frac{1}{2}}^P) + n(F_{\frac{3}{2}}^P)$
		$n_{\frac{1}{2}}^-$	$n(E_{\frac{1}{2}u}^\Gamma) + n(F_{\frac{3}{2}u}^\Gamma) + n(E_{\frac{1}{2}u}^H) + n(F_{\frac{3}{2}u}^H) + 3n(E_{\frac{1}{2}u}^N) + n(F_{\frac{3}{2}}^P) + n(E_{\frac{5}{2}}^P)$
		$n_{\frac{3}{2}}^+$	$n(F_{\frac{3}{2}g}^\Gamma) + n(E_{\frac{5}{2}g}^\Gamma) + n(F_{\frac{3}{2}g}^H) + n(E_{\frac{5}{2}g}^H) + 3n(E_{\frac{1}{2}g}^N) + n(F_{\frac{3}{2}}^P) + n(E_{\frac{5}{2}}^P)$
		$n_{\frac{3}{2}}^-$	$n(F_{\frac{3}{2}u}^\Gamma) + n(E_{\frac{5}{2}u}^\Gamma) + n(F_{\frac{3}{2}u}^H) + n(E_{\frac{5}{2}u}^H) + 3n(E_{\frac{1}{2}u}^N) + n(E_{\frac{1}{2}}^P) + n(F_{\frac{3}{2}}^P)$

Table A.5: The concrete expressions for $n_{\frac{3}{2}}^+$, $n_{\frac{3}{2}}^-$, $n_{\frac{1}{2}}^+$, $n_{\frac{1}{2}}^-$ in the z_8 Fu-Kane-like formulae in all applicable SGs adopted from Z. Song, *et. al.*, Physical Review X, **8**, 031069, (2018). The notations of high symmetry momenta follow the standard convention [99], and the notations of point group irreps follow [100].

---

[1] The equations here are derived for SG #83 (#87) but also applicable to the SGs in the bracket, which are supergroups of SG #83 (#87). To apply these equations for these supergroups, one should omit the additional symmetries and count them as SG #83 (#87).

[2] In SG #87, the little group at N is C_i and the irrep notations in [100] is $A_{\frac{1}{2}g}$ and $A_{\frac{1}{2}u}$, both of which are one dimensional. However, due to the Kramer's theorem, the irreps at N should be double degenerate, thus we adopt the two dimensional notations $E_{\frac{1}{2}g}$ and $E_{\frac{1}{2}u}$.

A.5 Difference between the classes $\mathbb{Z}_4 = 1$ and $\mathbb{Z}_4 = 3$

The Fu-Kane's strong $\mathbb{Z}_2$ index ν_0 for nodal line semimetals is extended to $\mathbb{Z}_4$. In the four classes indicated by $\mathbb{Z}_4$, $\mathbb{Z}_4 = 1$ and $\mathbb{Z}_4 = 3$ correspond to the nodal line semimetal class without the monopole charge ($\nu_0 = 1$). Then, what is the difference between them?

The difference is called "relative difference", which means

- They are topologically distinct classes in the definition of section 1.1.

- They can be exchanged when the unit cell configuration is changed.

- Their nodal line configurations are the same.

The first statement means that $\mathbb{Z}_4 = 1$ and $\mathbb{Z}_4 = 3$ cannot be continuously connected without closing the gap (at high symmetry points) or breaking the symmetry of the system. However, the second statement insists that if we change the unit cell configuration, $\mathbb{Z}_4 = 1$ can be changed to $\mathbb{Z}_4 = 3$. For example, in the space group 2, it is known that a change of inversion center can change the indices as

$$(\mathbb{Z}_4; \nu_1, \nu_2, \nu_3) \to (\mathbb{Z}_4 + 2\nu_j; \nu_1, \nu_2, \nu_3), \quad (j = 1, 2, 3), \tag{A.38}$$

where j is determined by in which direction the inversion center is shifted [50]. The $(1; 001)$ class can be changed to $(3; 001)$ by changing the inversion center. However, this statement does not contradict the first statement because they cannot be connected in a fixed unit cell configuration. The change of the inversion center keeps all physical observables invariant, and thus the third statement is obtained. Note that $(2; 000)$ cannot be changed to $(0; 000)$ even if we change the inversion center. There is "absolute difference" between them.

For the topological insulator classes, more detailed discussions are needed. If we focus only on the presence or absence of the surface states, we can say that $\mathbb{Z}_4 = 1$ and $\mathbb{Z}_4 = 3$ have the same properties. However, since the difference between them is interpreted as the particle-hole flip, the chirality of the helical surface states should not be the same. From that point of view, we cannot necessarily say that they are the same.

A.6 Useful tools for diagnosis of topological materials

Useful tools are summarized in Table.A.6 [101].

Table A.6: Some useful tools for diagnosis of topological materials. * indicates that the author have used and can recommend.

Types of tools	Resources
Topological materials databases	*Materiae [59, 102], *Topological Materials Database [48, 58], Topological Materials Arsenal [60]...
Wannier function methods and tools	*Wannier90 [103, 104], WannierTools [105], *Z2Pack [88], WannierBerri [106], ...
Band representations tools	*Bilbao Crystallographic Server [57], SymTopo [102], Irvsp [107], IrRep [108], qeirreps [109] ...
Materials databases	ICSD [110], Springer Materials, Materials Project [111], ...
Visualization tools	*VESTA [62], *PyProcar [112] Xcrysden [113], ...

A.7 Nodal line and Berry phase

In this section, we explain the Berry phase interpretation of indices in diagnostic methods for nodal line semimetals.

A.7.1 Symmetry-based indicator in the space group 83

In particular in the space group 83, the system has the inversion and C_4 symmetries and thus there must be a mirror symmetry $m = IC_4^2$. On the mirror-invariant planes, the Hamiltonian can be block diagonalized into two sectors with mirror eigenvalues $\sigma = \pm 1$. When the Berry phase is calculated along a loop on the mirror-invariant planes, it can be separately calculated in each sector. Consequently, there are four sectors to evaluate the Berry phase, $\sigma = \pm$ sectors on the ΓMX plane ($k_z = 0$) and $\sigma = \pm$ sectors on the ZAR plane ($k_z = \pi$).

The Berry phase on each sector is given by using the symmetry eigenvalues [114]. Let us see an example of the sector on ΓMX plane with $\sigma = +1$. Due to the C_4 symmetry, the area where the Berry phase is calculated can be reduced to a quarter (S in Fig.1.13). The Berry phase $\omega_{\partial S}^{+,0}$ along the loop ΓXMX'Γ [Fig.1.13,blue loop] is

$$
\begin{aligned}
\omega_{\partial S}^{+,0} &= \int_{\partial S} d\boldsymbol{k} \cdot \boldsymbol{A}(\boldsymbol{k}) \\
&= \int_{\Gamma}^{X} d\boldsymbol{k} \cdot \boldsymbol{A}(\boldsymbol{k}) - \int_{\Gamma}^{X'} d\boldsymbol{k} \cdot \boldsymbol{A}(\boldsymbol{k}) + \int_{X}^{M} d\boldsymbol{k} \cdot \boldsymbol{A}(\boldsymbol{k}) - \int_{X'}^{M} d\boldsymbol{k} \cdot \boldsymbol{A}(\boldsymbol{k}).
\end{aligned}
\tag{A.39}
$$

When the C_4 operation acts on $|u(\boldsymbol{k})\rangle$ as $C_4 |u(\boldsymbol{k})\rangle = e^{-i\beta(\boldsymbol{k})} |u(C_4\boldsymbol{k})\rangle$, the Berry connection satisfies

$$
\boldsymbol{A}(C_4\boldsymbol{k}) = -C_4\nabla_{\boldsymbol{k}}\beta(\boldsymbol{k}) + C_4\boldsymbol{A}(\boldsymbol{k}).
\tag{A.40}
$$

Using the fact that the ΓX and ΓX' (XM and X'M) are connected by the C_4 operation, the Berry phase is

$$
\begin{aligned}
\omega_{\partial S}^{+,0} &= \int_{\Gamma}^{X} d\boldsymbol{k} \cdot \left(\boldsymbol{A}(\boldsymbol{k}) - C_4^{-1}\boldsymbol{A}(C_4\boldsymbol{k}) \right) + \int_{X'}^{M} d\boldsymbol{k} \cdot \left(-\boldsymbol{A}(\boldsymbol{k}) + C_4^{-1}\boldsymbol{A}(C_4\boldsymbol{k}) \right) \\
&= \int_{\Gamma}^{X} d\boldsymbol{k} \cdot \nabla_{\boldsymbol{k}}\beta(\boldsymbol{k}) - \int_{X'}^{M} d\boldsymbol{k} \cdot \nabla_{\boldsymbol{k}}\beta(\boldsymbol{k}) \\
&= \beta(\boldsymbol{k}_X) + \beta(\boldsymbol{k}_{X'}) - \beta(\boldsymbol{k}_\Gamma) - \beta(\boldsymbol{k}_M).
\end{aligned}
\tag{A.41}
$$

The Berry phase modulo 2π is evaluated with $e^{i\omega_{\partial S}}$ as

$$
e^{i\omega_{\partial S}^{+,0}} = e^{i\beta(\boldsymbol{k}_X)}e^{i\beta(\boldsymbol{k}_{X'})}e^{-i\beta(\boldsymbol{k}_\Gamma)}e^{-i\beta(\boldsymbol{k}_M)} = \xi_\Gamma\xi_M\zeta_X.
\tag{A.42}
$$

Here, we used the fact that $e^{-i\beta(\boldsymbol{k}_\Gamma)}$ $\left(e^{-i\beta(\boldsymbol{k}_M)}\right)$ is the C_4 eigenvalue at the Γ (M) point ξ_Γ (ξ_M), and $e^{-i\beta(\boldsymbol{k}_X)}e^{-i\beta(\boldsymbol{k}_{X'})}$ is the C_2 eigenvalue at the X point ζ_X, which can be easily obtained from the definition of $\beta(\boldsymbol{k})$[3]. In multi occupied bands case, the Berry phase is given as

$$
e^{i\omega_{\partial S}^{+,0}} = \prod_{j:\text{occupied}} \xi_{\Gamma,j}\xi_{M,j}\zeta_{X,j},
\tag{A.43}
$$

---

[3]Since $\zeta = \pm 1$, $\zeta^{-1} = \zeta$

where $\xi_{\Gamma,j}$ is the C_4 eigenvalue of the j-th band at the Γ point. Although the C_4 eigenvalue is generally ± 1 or $\pm i$, it is known that $+i$ and $-i$ always appear as a degenerated pair in systems with TR and inversion symmetries. Therefore, we need to see only the -1 eigenvalue, and the $\delta_2^{+,0} = 0,1$ is defined as

$$
\begin{aligned}
e^{i\pi\delta_2^{+,0}} &= e^{i\omega_{\partial S}^{+,0}}, \\
\delta_2^{+,0} &= n_{\xi=-1}(\Gamma) + n_{\xi=-1}(M) + n_{\zeta=-1}(X) \quad (\mathrm{mod}\ 2).
\end{aligned}
\tag{A.44}
$$

The other three $\delta_2^{-,0}, \delta_2^{+,\pi}, \delta_2^{-,\pi}$ are given in the same way. When $\delta_2^{+,0} = 1$, an odd number of nodal line penetrates the ΓXMX'Γ loop in the $\sigma = +1$ sector[4] Similarly, $\delta_2^{+,\pi}$ is related to the number of nodal lines of the mirror $+1$ sector in the loop ZRAR' [Fig.1.13].

A.7.2 $\mathbb{Z}_2$ index for nodal line semimetals

Let us assume a nodal line around the V point in the space group 10 [Fig.A.7]. The nodal line (the red ring in Fig.A.7) is protected by a mirror m_z and fixed on the $k_z = 0$ plane. A Berry phase along a loop through X, U, R, and V (the blue and green lines in Fig.A.7) is calculated as ν_1 in mod 2π. In this case the nodal line penetrates the loop $XURV$ once and thus $\nu_1 = -1$. Note that the blue solid lines and blue dashed lines are inversion symmetric pairs (reciprocal lattice transformations are allowed). On the other hand, the green lines are not inversion-invariant but they have nothing to do with the Berry phase within a properly fixed gauge. If we want to know whether a nodal line exist in a loop ΓZTY, it is diagnosed by $\nu_0 - \nu_1$. Considering these facts, a system with a nodal line like Fig.A.7 has $(\nu_0; \nu_1\nu_2\nu_3) = (1; 110)$.

The $XURV$ loop is has been easily interpreted because it does not touch the nodal line. On the other hand, the ΓYVX loop touches the nodal line, so the Berry phase along the ΓYVX is not well defined as it is. To overcome this problem, the loop can be transformed while keeping the inversion symmetry. The path between Y and V does not have to be a line segment YV. It can curve to avoid touching the nodal line [Fig.A.8, solid blue line]. However, the other part of the path (dashed blue line) is fixed without arbitrariness to keep the inversion symmetry of the path. By this transformation, the number of nodal lines that penetrate the loop is well defined.

---

[4]Nodal lines between two bands with different mirror eigenvalues violates the compatibility condition.
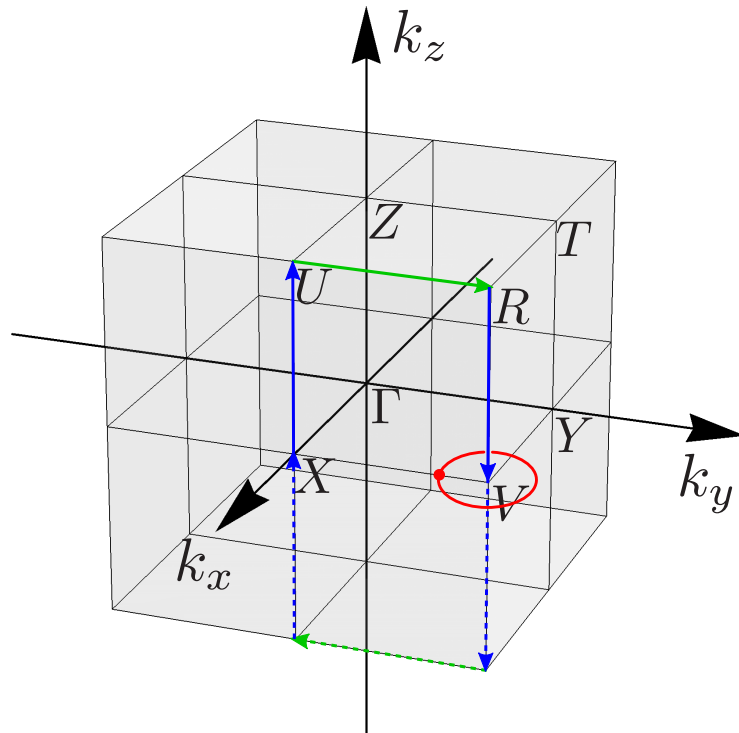
Figure A.7. BZ and TRIM of the space group 10. A TR-invariant path through $XURV$ is shown as blue and green lines. When a nodal line exists around the V point, the Berry phase along the $XURV$ loop is $\pi \pmod{2\pi}$
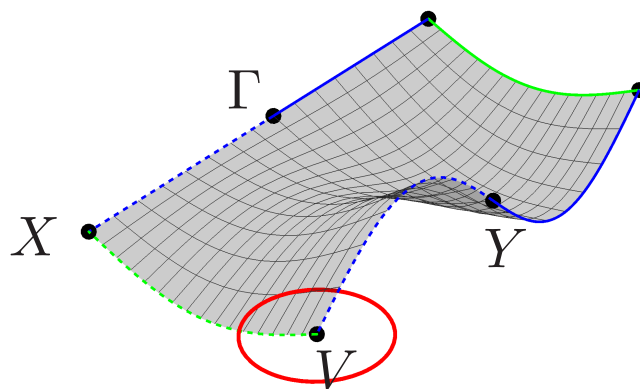

Figure A.8. Nodal line and TR-invariant path that is transformed to avoid touching the nodal line. The solid blue line and the dashed blue line are a inversion symmetric pair. The green lines are equivalent lines, which have no contribution to the Berry phase.

Appendix B

Classification theories and diagnostic methods

In this section, we review the classification theories of topological materials and discuss the relationship between them and the diagnostic methods. We review three classification theories, classifications in the Altland-Zirnbauer symmetry classes, a classification based on the Clifford algebra, and a classification based on the K-theory.

B.1 Altland-Zirnbauer symmetry class

The Altland-Zirnbauer (AZ) symmetry classes [51] consist of ten classes based on three symmetries, TR symmetry ($\mathcal{T}$), particle-hole symmetry ($\mathcal{C}$), and chiral symmetry ($\mathcal{S}$) [Table B.1]. $\mathcal{S}$ is defined as $\mathcal{S} = \mathcal{T}\mathcal{C}$, and therefore the presence/absence of $\mathcal{S}$ is determined by the presence/absence of $\mathcal{T}$ and $\mathcal{C}$ in most case. The exception is the case where both of them are absent (A and AIII classes). For a integer factor δ, a "periodic table" of topological invariants is given as Table B.1. The δ is defined as $\delta = d - D$, where d is the (insulating) space dimension and $D + 1$ is the codimension of defects. The word "codimension" means that the surface/hinge state emerges in a $d - (D + 1)$ dimension space. For example, in a 3D topological insulator, $d = 3$ and $D + 1 = 1$ since the surface state emerges in a 2D space on a surface. The 3D TR-protected topological insulators belong to the AII class ($\delta = 3$), and we can see the classification is $\mathbb{Z}_2$. Although the periodic table tells us just the framework of classifications, we know this $\mathbb{Z}_2$ is the Fu-Kane's $\mathbb{Z}_2$ index.

This periodic table is correct when only $\mathcal{T}$, $\mathcal{C}$, and $\mathcal{S}$ are considered. However, in general, the topological classes are divided further if crystalline symmetries are additionally considered. The symmetry-based indicator with TR symmetry and significant SOC classifies the subdivided topological classed in the AII class with crystalline symmetries. The symmetry-based indicator with TR and negligible SOC is related to the classification in the AI class with crystalline symmetries[1].

---

[1]Note that d is a dimension of an insulating Hamiltonian. Therefore, $d = 1$ in the case of nodal line semimetals characterized by a Berry phase (1D topological invariant).

class\δ	$\mathcal{T}$	$\mathcal{C}$	$\mathcal{S}$	0	1	2	3	4	5	6	7
A	0	0	0	$\mathbb{Z}$	0	$\mathbb{Z}$	0	$\mathbb{Z}$	0	$\mathbb{Z}$	0
AIII	0	0	1	0	$\mathbb{Z}$	0	$\mathbb{Z}$	0	$\mathbb{Z}$	0	$\mathbb{Z}$
AI	$+$	0	0	$\mathbb{Z}$	0	0	0	$2\mathbb{Z}$	0	$\mathbb{Z}_2$	$\mathbb{Z}_2$
BDI	$+$	$+$	1	$\mathbb{Z}_2$	$\mathbb{Z}$	0	0	0	$2\mathbb{Z}$	0	$\mathbb{Z}_2$
D	0	$+$	0	$\mathbb{Z}_2$	$\mathbb{Z}_2$	$\mathbb{Z}$	0	0	0	$2\mathbb{Z}$	0
DIII	$-$	$+$	1	0	$\mathbb{Z}_2$	$\mathbb{Z}_2$	$\mathbb{Z}$	0	0	0	$2\mathbb{Z}$
AII	$-$	0	0	$2\mathbb{Z}$	0	$\mathbb{Z}_2$	$\mathbb{Z}_2$	$\mathbb{Z}$	0	0	0
CII	$-$	$-$	1	0	$2\mathbb{Z}$	0	$\mathbb{Z}_2$	$\mathbb{Z}_2$	$\mathbb{Z}$	0	0
C	0	$-$	0	0	0	$2\mathbb{Z}$	0	$\mathbb{Z}_2$	$\mathbb{Z}_2$	$\mathbb{Z}$	0
CI	$+$	$-$	1	0	0	0	$2\mathbb{Z}$	0	$\mathbb{Z}_2$	$\mathbb{Z}_2$	$\mathbb{Z}$

Table B.1: Periodic table of topological insulators and superconductors adopted from C.-K. Chiu *et. al.*, Reviews of Modern Physics, **88**, 035005 (2016); $\delta := d - D$, where d is the space dimension and $D + 1$ is the codimension of defects; the left-most column (A, AIII, ..., CI) denotes the ten symmetry classes of fermionic Hamiltonians, which are characterized by the presence/absence of time-reversal ($\mathcal{T}$), particle-hole ($\mathcal{C}$), and chiral ($\mathcal{S}$) symmetry of different types denoted by ± 1. The entries "$\mathbb{Z}$", "$\mathbb{Z}_2$", "$2\mathbb{Z}$", and "0" represent the presence/absence of non-trivial topological insulators/superconductors or topological defects, and when they exist, types of these states. The case of $D = 0$ (i.e., $\delta = d$) corresponds to the tenfold classification of gapped bulk topological insulators and superconductors.

B.2   Classification based on the Clifford algebra

A classification based on the Clifford algebra derives a framework of topological classes by considering an algebra of symmetry operations in AZ class with some crystalline symmetries [115]. For example, in the AII class with a mirror symmetry, the classification is given as $\mathbb{Z}$. This $\mathbb{Z}$ corresponds to a mirror Chern number.

B.3   Classification based on the K-theory

In principle, a classification based on the K-theory gives a complete classification for all AZ class with space group symmetry. Recently, the procedure to obtain the classification has been also proposed [52]. However, at the moment, it is not necessarily easy to complete the procedure in an exact way for the systems with crystalline symmetries. Therefore, comprehensive understanding has not been achieved. In some cases, classifications are obtained and the result is consistent with the other classification theories and diagnostic methods.

Appendix C

Notes of the δ indices

C.1 BZ folding and symmetry eigenvalues

In this dissertation, only double BZ folding is considered. When the BZ is doubly folded, doubly degenerated states appear on the boundary of the folded BZ. Let us assume the doubly degenerated states $\psi_{\boldsymbol{k}_1}$ and $\psi_{\boldsymbol{k}_2}$ are originated from two momentum, $\boldsymbol{k}_1$ and $\boldsymbol{k}_2$. We can construct new bases by making linear combinations of $\psi_{\boldsymbol{k}_1}$ and $\psi_{\boldsymbol{k}_2}$, and get eigenstates of symmetry operators such as mirror, C_2, or C_4).

Let us consider a symmetry operator $R(= C_4, C_2, m)$. If k_1 and k_2 are R-invariant point in the folded BZ, they are connected by R in the original BZ ($R\boldsymbol{k}_1 = \boldsymbol{k}_2$). The representation of R is written as

$$R = \begin{pmatrix} 0 & * \\ * & 0 \end{pmatrix} : \text{bases} = \begin{pmatrix} \psi_{\boldsymbol{k}_1} \\ \psi_{\boldsymbol{k}_2} \end{pmatrix}. \tag{C.1}$$

The reconstruction of the bases is a Unitary transformation by U,

$$URU^\dagger = \begin{pmatrix} \rho_1 & 0 \\ 0 & \rho_2 \end{pmatrix} : \text{bases} = U \begin{pmatrix} \psi_{k_1} \\ \psi_{k_2} \end{pmatrix}. \tag{C.2}$$

Here, ρ_1 and ρ_2 are R eigenvalues.

By taking the trace,

$$0 = \text{Tr}(R) = \text{Tr}(URU^\dagger) = \rho_1 + \rho_2. \tag{C.3}$$

It is proved that the BZ folding gives a doubly degenerated pair with opposite eigenvalues.

Appendix D

Note about the intrinsic link between nodal line semimetals and topological crystalline insulators

D.1 Sign of the mirror Chern number

The sign of the mirror Chern number has no physical meaning. The sign depends on the definition of the mirror operator, which has uncertainty.

Let us assume a mirror operator m in a spinful system. The Chern number of the sectors with $\pm i$ mirror eigenvalues are $\mathcal{C}_+$ and $\mathcal{C}_-$ and the mirror Chern number $n_{\mathcal{M}}$ is

$$n_{\mathcal{M}} = \frac{\mathcal{C}_+ - \mathcal{C}_-}{2}. \tag{D.1}$$

Let us consider a symmetry operation $m' = m^3$. In the real space (as an element of $SO(3)$), m' is the same mirror operation as m. On the other hand, in the spin space (as an element of $SU(2)$), $m' = -m$. Therefore, if we use m' as the mirror operation instead of m, the mirror eigenvalues are flipped and the mirror Chern number for m' is $-n_{\mathcal{M}}$. The choice of the mirror operation corresponds to the choice of gauge. This uncertainty has nothing to do with physical observables, and thus the sign of the mirror Chern number has no physical meaning.

D.2 Spin part of symmetry operators

Since spin is a pseudovector, only rotations are considered. For a rotation which is described by Euler angles (α, β, γ), the representation for the spin part is

$$
\begin{aligned}
\mathcal{D}^{1/2}(\alpha, \beta, \gamma) &= e^{-i\frac{1}{2}\alpha\sigma_z} e^{-i\frac{1}{2}\beta\sigma_y} e^{-i\frac{1}{2}\gamma\sigma_z} \\
&= \begin{pmatrix} e^{-i\frac{1}{2}\alpha} \cos\frac{1}{2}\beta \, e^{-i\frac{1}{2}\gamma} & -e^{-i\frac{1}{2}\alpha} \sin\frac{1}{2}\beta \, e^{i\frac{1}{2}\gamma} \\ e^{i\frac{1}{2}\alpha} \sin\frac{1}{2}\beta \, e^{-i\frac{1}{2}\gamma} & e^{i\frac{1}{2}\alpha} \cos\frac{1}{2}\beta \, e^{i\frac{1}{2}\gamma} \end{pmatrix}.
\end{aligned} \tag{D.2}
$$

We have two possible representation for a rotation since (α, β, γ) and $(\alpha+\pi, 2\pi-\beta, \gamma+\pi)$ describe the same rotation as an element of $SO(3)$. The two representations satisfy

$$\mathcal{D}^{1/2}(\alpha, \beta, \gamma) = -\mathcal{D}^{1/2}(\alpha + \pi, 2\pi - \beta, \gamma + \pi). \tag{D.3}$$

This is exactly the sign degree of freedom of the mirror Chern number.

D.3 Wilson loop evaluation of Chern number

D.3.1 The Chern number and Wannier center

The Chern number $\mathcal{C}$ is calculated as

$$
\begin{aligned}
2\pi\mathcal{C} &= \int_{-\pi}^{\pi} dk_x \int_{-\pi}^{\pi} dk_y \left(\frac{\partial}{\partial k_x} A_y - \frac{\partial}{\partial k_y} A_x \right) \\
&= \int_{-\pi}^{\pi} dk_x \int_{-\pi}^{\pi} dk_y \frac{\partial}{\partial k_x} A_y - \int_{-\pi}^{\pi} dk_x \int_{-\pi}^{\pi} dk_y \frac{\partial}{\partial k_y} A_x \\
&= \int_{-\pi}^{\pi} dk_y A_y(k_x, k_y) \Big|_{k_x=-\pi}^{k_x=\pi} - \int_{-\pi}^{\pi} dk_y \frac{\partial}{\partial k_y} \left(\int_{-\pi}^{\pi} dk_x A_x(k_x, k_y) \right).
\end{aligned}
\tag{D.4}
$$

The gauge can be fixed to satisfy $\psi(\pi, k_y) = \psi(-\pi, k_y)$ ($\Rightarrow A_y(\pi, k_y) = A_y(-\pi, k_y)$), and in that gauge the first term vanishes.

$$
\begin{aligned}
2\pi\mathcal{C} &= -\int_{-\pi}^{\pi} dk_y \frac{\partial}{\partial k_y} \theta_x(k_y) \\
&= -\int_{-\pi}^{\pi} d\theta_x(k_y).
\end{aligned}
\tag{D.5}
$$

Here, $\theta_x(k_y)$ is the 1D Wannier center along a fixed k_x line,

$$\theta_x(k_y) = \int_{-\pi}^{\pi} dk_x A_x(k_x, k_y). \tag{D.6}$$

Since the system is periodic, $\theta_x(k_y) = \theta_x(k_y + 2\pi)$ (mod 2π) is satisfied and thus the Chern number is calcualted as "how many times the θ_x winds" form $k_y = -\pi$ to $k_y = \pi$.

D.3.2 Numerical evaluation of the Wannier center

To evaluate the θ_x, the gauge of wavefunctions needs to be carefully treated. When a wavefunction $\psi(\boldsymbol{k})$ is given by numerical diagonalization of a Hamiltonian $H(\boldsymbol{k})$, generally different gauges are taken in each $\boldsymbol{k}$ point. Therefore, the numerical differential does not suit the calculation of θ_x. Instead of the numerical differential, the following gauge independent method is used.

Given wavefunctions $\psi(\boldsymbol{k}_i)$ in a $\boldsymbol{k}$ points line (loop) $\boldsymbol{k}_i = \{\boldsymbol{k}_1, \boldsymbol{k}_2, \boldsymbol{k}_3, \cdots \boldsymbol{k}_{n-1}, \boldsymbol{k}_n \equiv \boldsymbol{k}_1\}$, the Berry phase between $\boldsymbol{k}_i$ and $\boldsymbol{k}_{i+1}$ can be calculated in the $n \to \infty$ limit as

$$|\psi(\boldsymbol{k}_{i+1})\rangle \simeq \left(1 + \Delta\boldsymbol{k}_i \cdot \frac{\partial}{\partial\boldsymbol{k}}\right)|\psi(\boldsymbol{k}_i)\rangle \quad (\Delta\boldsymbol{k}_i = \boldsymbol{k}_{i+1} - \boldsymbol{k}_i)$$
$$\langle\psi(\boldsymbol{k}_i)\,|\,\psi(\boldsymbol{k}_{i+1})\rangle \simeq 1 - i\Delta\boldsymbol{k}_i \cdot \boldsymbol{A}(\boldsymbol{k}_i)$$
$$\simeq e^{-i\Delta\boldsymbol{k}_i \cdot \boldsymbol{A}(\boldsymbol{k}_i)}. \tag{D.7}$$

Here $\boldsymbol{A}(\boldsymbol{k}) = i\langle\psi(\boldsymbol{k})|\frac{\partial}{\partial\boldsymbol{k}}|\psi(\boldsymbol{k})\rangle$ is the Berry connection. Using this relation, the θ is calculated within mod 2π as

$$e^{-i\theta} = e^{-i\int d\boldsymbol{k}\cdot\boldsymbol{A}(\boldsymbol{k})} \simeq e^{-i\sum_{i=1}^{n-1}\Delta\boldsymbol{k}_i\cdot\boldsymbol{A}(\boldsymbol{k}_i)} = \prod_{i=1}^{n-1}e^{-i\Delta\boldsymbol{k}_i\cdot\boldsymbol{A}(\boldsymbol{k}_i)} \simeq \prod_{i=1}^{n-1}\langle\psi(\boldsymbol{k}_i)\,|\,\psi(\boldsymbol{k}_{i+1})\rangle. \tag{D.8}$$

Since $\boldsymbol{k}_1 \equiv \boldsymbol{k}_n$ (genarally 2π difference is allowed), the gauge fixing condition $\psi(\boldsymbol{k}_1) = \psi(\boldsymbol{k}_n)$ is easily satisfied by using $\psi(\boldsymbol{k}_1)$ as $\psi(\boldsymbol{k}_n)$. For a gauge transformation

$$|\psi(\boldsymbol{k}_i)\rangle \Rightarrow e^{i\lambda_i}\left|\tilde{\psi}(\boldsymbol{k}_i)\right\rangle, \tag{D.9}$$

the right hand side of Eq.(D.8) is transformed as

$$\prod_{i=1}^{n-1}\langle\psi(\boldsymbol{k}_i)\,|\,\psi(\boldsymbol{k}_{i+1})\rangle = \prod_{i=1}^{n-1}\left\langle\tilde{\psi}(\boldsymbol{k}_i)\,\middle|\,\tilde{\psi}(\boldsymbol{k}_{i+1})\right\rangle e^{-i\lambda_i}e^{i\lambda_{i+1}}$$
$$= e^{-i\lambda_1}e^{i\lambda_n}\prod_{i=1}^{n-1}\left\langle\tilde{\psi}(\boldsymbol{k}_i)\,\middle|\,\tilde{\psi}(\boldsymbol{k}_{i+1})\right\rangle \tag{D.10}$$
$$= \prod_{i=1}^{n-1}\left\langle\tilde{\psi}(\boldsymbol{k}_i)\,\middle|\,\tilde{\psi}(\boldsymbol{k}_{i+1})\right\rangle.$$

It is proved that this method is gauge independent.

However, in numerical evaluation of $\theta_x(k_y)$, we cannot see how $\theta_x(k_y)$ and $\theta_x(k_y+\Delta k_y)$ are connected. Therefore, if the θ_x quickly winds compared to the k_y step size, we can miss the nontrivial structure. Generally, when the band gap is small, the Wannier center moves quickly and we need to evaluate with a fine k_y mesh.

D.3.3 The Multi band Wannier centers and the Wilson matrix

For a multi occupied bands case, the Wilson loop approach is used as an extended method to calculate the "Berry phase".

Given m occupied band in $\boldsymbol{k}$, $\{\psi_1(\boldsymbol{k}), \psi_2(\boldsymbol{k})\cdots\psi_m(\boldsymbol{k})\}$, in each point in a $\boldsymbol{k}$ points line (loop), the $m \times m$ Berry connection matrix is given as

$$W_{\alpha\beta}(\boldsymbol{k}_i) = \langle\psi_\alpha(\boldsymbol{k}_i)\,|\,\psi_\beta(\boldsymbol{k}_{i+1})\rangle. \tag{D.11}$$

As an analogy of the single band case, the topological invariant along the $\boldsymbol{k}$ loop is obtained by calculating the product of each step,

$$W = \prod_{i=1}^{n-1} W(\boldsymbol{k}_i). \tag{D.12}$$

The absolute value of the eigenvalues of W is always 1 because that of each step $W(\boldsymbol{k}_i)$ is 1. Let us write the eigenvalues as $\left\{ e^{i\theta_1}, e^{i\theta_2}, \cdots e^{i\theta_m} \right\}$, the arguments of then, $\{\theta_1, \theta_2, \cdots \theta_m\}$ represents the topological properties of the system. For example, the Chern number is calculated by following $\theta = \sum_{i=1}^{m} \theta_i$ as is in the single band case. In the calculation of W, we need not to care the energy sequence in the occupied bands. Additionally, a degenerate point between occupied bands also does not matter, even if the degeneracy is held on the whole line.

D.3.4   Example : Ca

The example of the numerical evaluation of the Chern number is shown in Fig.D.1 (the mirror Chern number in Ca). The bottom left (bottom right) of the Fig.D.1 is the Wannier center diagram of the $+i$ mirror sector of on the (110) mirror-invariant plane (the (001) mirror-invariant plane).

The "first BZ" on the (110) mirror-invariant plane is written as

$$\left\{ \boldsymbol{k}(t_1, t_2) = t_1 \begin{pmatrix} 2\pi \\ -2\pi \\ 2\pi \end{pmatrix} + t_2 \begin{pmatrix} -2\pi \\ 2\pi \\ 2\pi \end{pmatrix} \middle| t_1, t_2 \in [0, 1) \right\}. \tag{D.13}$$

In the Wannier center diagram, the horizontal axis is t_1 and the vertial axis is $\theta_2/(2\pi)$. Here, θ_2 is defined as

$$\begin{aligned} \theta_2(t_1) &= \int_0^{2\sqrt{3}\pi} dk_{\bar{1}11} A_{\bar{1}11}(\boldsymbol{k}) \\ &= \int_0^1 dt_2 \frac{\partial \boldsymbol{k}(t_1, t_2)}{\partial t_2} \cdot \boldsymbol{A}(\boldsymbol{k}(t_1, t_2)). \end{aligned} \tag{D.14}$$

The Wannier canter in the $+i$ mirror sector winds two times, and thus the Chern number in the sector is $+2$.

The "first BZ" on the (001) mirror-invariant plane is written as

$$\left\{ \boldsymbol{k}(t_1, t_2) = t_1 \begin{pmatrix} 4\pi \\ 0 \\ 0 \end{pmatrix} + t_2 \begin{pmatrix} 0 \\ 4\pi \\ 0 \end{pmatrix} \middle| t_1, t_2 \in [0, 1) \right\}. \tag{D.15}$$

The horizontal and vertical axes in the Wannier center diagram are t_1 and $\theta_2/(2\pi)$, respectively. The θ_2 is defined in the same way as Eq.(D.14). The Wannier canter in the $+i$ mirror sector does not wind, and thus the Chern number in the sector is 0.
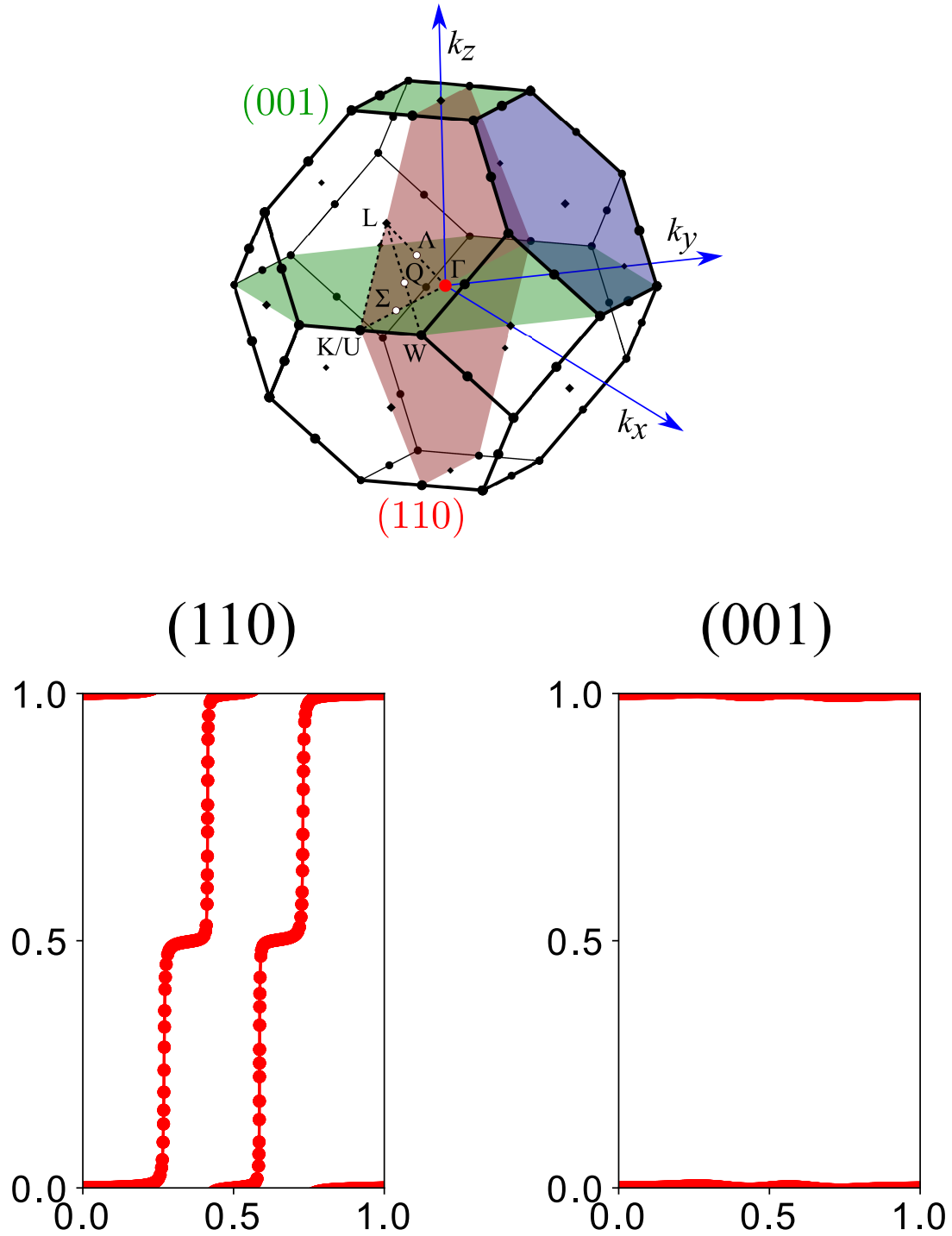
Figure D.1. BZ and Wannier center diagrams on mirror-invariant planes

Appendix E

Nodal lines in Ca$_2$As family

By the first-principles calculation, it is revealed the the mirror-protected nodal line is a pert of intersecting nodal lines (see Fig.4.12(a)). Therefore, we start from a tight-binding model and consider the $\boldsymbol{k} \cdot \boldsymbol{p}$ perturbation around $(k_x, k_y) = (\pi, \pi)$, in which we keep the z direction periodic.

We fit the values of hopping parameters to reproduce the band dispersion by using WANNIER90 [103]. From the result given by WANNIER90, the 11 largest hopping parameters are taken into account and others are neglected. To represent the transition of nodal line configurations between Ca$_2$As and other materials, we use a tunable parameter η. To make the calculation easier, we derive a 2×2 model for the system without SOC by the $\boldsymbol{k} \cdot \boldsymbol{p}$ perturbation around $(k_x, k_y) = (\pi, \pi)$. For the bases, we take two wavefunctions whose energies are close to the Fermi energy. As a result, The 2×2 model is given as

$$H_{2\times2}(\boldsymbol{k}) = Z\sigma_z + Y\sigma_y, \tag{E.1}$$

$$Z = J + K(k_x^2 + k_y^2) + L \cos ck_z + Mk_xk_y \cos \frac{ck_z}{2}, \tag{E.2}$$

$$Y = S \sin ck_z + Tk_xk_y \sin \frac{ck_z}{2}, \tag{E.3}$$

$$
\begin{aligned}
J &\simeq 0.7483 - 3.9229 \times \eta, \\
K &\simeq 0.1962, \\
L &\simeq 0.009357, \\
M &\simeq 0.04060, \\
S &\simeq 0.008565, \\
T &\simeq 0.04047,
\end{aligned}
\tag{E.4}
$$

where σ_y and σ_z are the Pauli matrices and σ_0 is a two-dimension identity matrix, (k_x, k_y) is redefined as a relative coordinate from (π, π). The presence of nodal lines and it configuration depend on *eta* [Fig.E.1]. When $\eta \lesssim 0.1884$, there is no nodal line. When $0.1884 \lesssim \eta \lesssim 0.1931$, the nodal line configuration is the same as that of Ca$_2$As. When $0.1931 \lesssim \eta \lesssim 0.2311$, mirror-protected nodal lines additionally appear, but they are separated. When $0.2311 \lesssim \eta$, they intersect with each other.

$$0.1931 \lesssim \eta \lesssim 0.2311 \qquad\qquad 0.2311 \lesssim \eta$$

$$(\mathbb{Z}_2, \mathbb{Z}_8) = (1, 2)$$

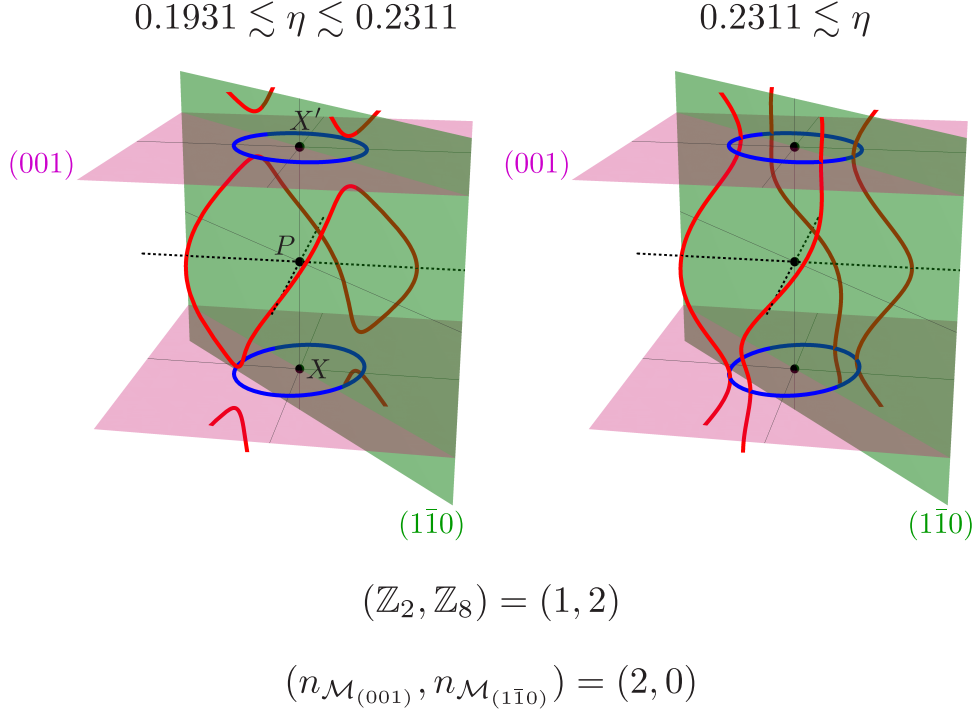$$\left(n_{\mathcal{M}_{(001)}}, n_{\mathcal{M}_{(1\bar{1}0)}}\right) = (2, 0)$$

Figure E.1. Schematic picture of the configuration of nodal lines. Both of the two nodal line semimetals are linked to the same topological crystalline insulator.

We introduce a Rashba-type SOC term with amplitude λ, and then the tight-binding model is 4 written as

$$H_{4\times4}(\boldsymbol{k}) = H_{2\times2}(\boldsymbol{k})s_0 + \lambda\sigma_x(-k_y s_x + k_x s_y). \tag{E.5}$$

The (001) mirror operator (m_z) and the $(1\bar{1}0)$ mirror operator $(m_\perp)$ are written as

$$\begin{aligned} m_z &\rightarrow -i\sigma_z s_z, \\ m_\perp &\rightarrow -i\frac{1}{\sqrt{2}}\sigma_0(s_x - s_y). \end{aligned} \tag{E.6}$$

For the (001) plane, the z component of the Berry curvature in the $+i$ mirror sector is written as

$$B_{z,+} = \frac{\lambda^2}{2R_+^3}\left((J + L) + K(k_x^2 + k_y^2) + Mk_x k_y - 2Mk_x k_y\frac{Z_+^2}{(R_+ + Z_+)^2}\right), \tag{E.7}$$

where

$$\begin{aligned} X_+ &= -\lambda k_y, \\ Y_+ &= \lambda k_x, \\ Z_+ &= -Z_{(k_z=0)}, \\ R_+ &= \sqrt{X_+^2 + Y_+^2 + Z_+^2}. \end{aligned} \tag{E.8}$$

The mirror Chern number evaluated in this model is $n_{X,\mathcal{M}_{(001)}} = 1$. There are two X points in the BZ and it is easy to see that only the sign of the term with coefficient M is different in the other X point. Therefore, both nodal lines around the X points have the same contribution to the mirror Chern number and thus the mirror Chern number is $n_{\mathcal{M}_{(001)}} = 2$ when there are nodal lines on the $k_z = 0$ plane [Fig.E.1]. It should be noted that in this calculation it did not matter whether some other nodal lines are touching the nodal line on the mirror plane.

For the $(1\bar{1}0)$ plane $(k_x, k_y, k_z) = (k_d, k_d, k_z)$, the perpendicular component of the Berry curvature in the $+i$ mirror sector is written as and

$$B_{\perp,+} = -\frac{\lambda V}{2R_+^3}\left(|J + L| + (K + \frac{M}{2})k_d^2\right), \tag{E.9}$$

$$\begin{aligned} X_+ &= \chi k_d, \\ Y_+ &= Y \simeq V k_z, \\ Z_+ &= Z \simeq (J + L) + (K + \frac{M}{2})k_d^2, \end{aligned} \tag{E.10}$$

where V is defined as

$$V = \begin{cases} (S + \frac{T}{4}k_d^2) & (k_z = 0) \\ (S - \frac{T}{4}k_d^2) & (k_z = \pi) \end{cases}. \tag{E.11}$$

$k_z = 0, \pi$ correspond to the two nonequivalent P points. Since the Berry curvature shows sharp peaks around $k_z = 0, \pi$ in case of $\lambda \ll 1$, we assumed $k_z \ll 1$ or $k_z - \pi \ll 1$ for each case. For $k_z = 0$, V is always positive. On the other hand, $V_{k_z = \pi}$ is positive before the nodal lines are separeted ($\eta \lesssim 0.2311$) but negative after they touch ($\eta \lesssim 0.2311$). Due to the difference of the sign of V, the mirror Chern numbers from the two X points cancel each other when $\eta \lesssim 0.2311$. When $\eta \lesssim 0.2311$, on the other hand, mirror Chern numbers from the two separeted nodal lines cancel each other. Consequently, in the whole BZ $n_{\mathcal{M}_{(1\bar{1}0)}} = 0$ in the both cases [Fig.E.1].

To know the sign of the mirror Chern number that evaluated in the local models, detailed discussions are generally needed. Therefore, as long as we just see the configuration of nodal lines, we cannot uniquely specify the class of topological crystalline insulator that is obtained by introducing SOC. However, the number of candidates can be decreased by using the intrinsic link between nodal lines and the mirror Chern numbers.

Acknowledgements

Bibliography

[1] K. v. Klitzing, G. Dorda, and M. Pepper: Phys. Rev. Lett. **45**, 494 (1980).

[2] D. J. Thouless, M. Kohmoto, M. P. Nightingale, and M. den Nijs: Phys. Rev. Lett. **49**, 405 (1982).

[3] Y. Hatsugai: Phys. Rev. Lett. **71**, 3697 (1993).

[4] Y. Hatsugai: Phys. Rev. B **48**, 11851 (1993).

[5] T. Thonhauser and D. Vanderbilt: Phys. Rev. B **74**, 235111 (2006).

[6] M. Z. Hasan and C. L. Kane: Rev. Mod. Phys. **82**, 3045 (2010).

[7] X.-L. Qi and S.-C. Zhang: Rev. Mod. Phys. **83**, 1057 (2011).

[8] C. L. Kane and E. J. Mele: Phys. Rev. Lett. **95**, 146802 (2005).

[9] B. A. Bernevig and S.-C. Zhang: Phys. Rev. Lett. **96**, 106802 (2006).

[10] L. Fu and C. L. Kane: Phys. Rev. B **74**, 195312 (2006).

[11] L. Fu, C. L. Kane, and E. J. Mele: Phys. Rev. Lett. **98**, 106803 (2007).

[12] J. E. Moore and L. Balents: Phys. Rev. B **75**, 121306 (2007).

[13] R. Roy: Phys. Rev. B **79**, 195322 (2009).

[14] J. C. Y. Teo, L. Fu, and C. L. Kane: Phys. Rev. B **78**, 045426 (2008).

[15] D. Hsieh, D. Qian, L. Wray, Y. Xia, Y. S. Hor, R. J. Cava, and M. Z. Hasan: Nature **452**, 970 (2008).

[16] C.-X. Liu, X.-L. Qi, H. Zhang, X. Dai, Z. Fang, and S.-C. Zhang: Phys. Rev. B **82**, 045122 (2010).

[17] Y. Xia, D. Qian, D. Hsieh, L. Wray, A. Pal, H. Lin, A. Bansil, D. Grauer, Y. S. Hor, R. J. Cava, et al.: Nature physics **5**, 398 (2009).

[18] Y. Chen, J. G. Analytis, J.-H. Chu, Z. Liu, S.-K. Mo, X.-L. Qi, H. Zhang, D. Lu, X. Dai, Z. Fang, et al.: science **325**, 178 (2009).

[19] Y. Ando: Journal of the Physical Society of Japan **82**, 102001 (2013).

[20] L. Fu: Phys. Rev. Lett. **106**, 106802 (2011).

[21] Y. Tanaka, Z. Ren, T. Sato, K. Nakayama, S. Souma, T. Takahashi, K. Segawa, and Y. Ando: Nature Physics **8**, 800 (2012).

[22] P. Dziawa, B. Kowalski, K. Dybko, R. Buczko, A. Szczerbakow, M. Szot, E. Łusakowska, T. Balasubramanian, B. M. Wojek, M. Berntsen, et al.: Nature materials **11**, 1023 (2012).

[23] F. Schindler, A. M. Cook, M. G. Vergniory, Z. Wang, S. S. Parkin, B. A. Bernevig, and T. Neupert: Science advances **4**, eaat0346 (2018).

[24] E. Khalaf: Phys. Rev. B **97**, 205136 (2018).

[25] A. Matsugatani and H. Watanabe: Phys. Rev. B **98**, 205129 (2018).

[26] G. van Miert and C. Ortix: Phys. Rev. B **98**, 081110 (2018).

[27] F. Schindler, Z. Wang, M. G. Vergniory, A. M. Cook, A. Murani, S. Sengupta, A. Y. Kasumov, R. Deblock, S. Jeon, I. Drozdov, et al.: Nature physics **14**, 918 (2018).

[28] S. Wang, B.-C. Lin, A.-Q. Wang, D.-P. Yu, and Z.-M. Liao: Advances in Physics: X **2**, 518 (2017).

[29] B. Yan and C. Felser: Annual Review of Condensed Matter Physics **8**, 337 (2017).

[30] C. Fang, Y. Chen, H.-Y. Kee, and L. Fu: Physical Review B **92**, 081201 (2015).

[31] M. J. Allen, V. C. Tung, and R. B. Kaner: Chemical reviews **110**, 132 (2010).

[32] T. Kariyado and M. Ogata: Journal of the Physical Society of Japan **80**, 083704 (2011).

[33] S. M. Young, S. Zaheer, J. C. Teo, C. L. Kane, E. J. Mele, and A. M. Rappe: Physical review letters **108**, 140405 (2012).

[34] Z. Wang, Y. Sun, X.-Q. Chen, C. Franchini, G. Xu, H. Weng, X. Dai, and Z. Fang: Physical Review B **85**, 195320 (2012).

[35] Z. Wang, H. Weng, Q. Wu, X. Dai, and Z. Fang: Physical Review B **88**, 125427 (2013).

[36] A. Burkov and L. Balents: Physical review letters **107**, 127205 (2011).

[37] G. B. Halász and L. Balents: Physical Review B **85**, 035103 (2012).

[38] O. Vafek and A. Vishwanath: Annual Review of Condensed Matter Physics **5**, 83 (2014).

[39] S.-M. Huang, S.-Y. Xu, I. Belopolski, C.-C. Lee, G. Chang, B. Wang, N. Alidoust, G. Bian, M. Neupane, C. Zhang, et al.: Nature communications **6**, 7373 (2015).

[40] S. Jia, S.-Y. Xu, and M. Z. Hasan: Nature materials **15**, 1140 (2016).

[41] A. Burkov, M. Hook, and L. Balents: Physical Review B **84**, 235126 (2011).

[42] R. Yu, H. Weng, Z. Fang, X. Dai, and X. Hu: Physical review letters **115**, 036807 (2015).

[43] Y. Kim, B. J. Wieder, C. Kane, and A. M. Rappe: Physical review letters **115**, 036806 (2015).

[44] L. Fu and C. L. Kane: Phys. Rev. B **76**, 045302 (2007).

[45] R.-J. Slager, A. Mesaros, V. Juričić, and J. Zaanen: Nature Physics **9**, 98 (2013).

[46] J. Kruthoff, J. de Boer, J. van Wezel, C. L. Kane, and R.-J. Slager: Phys. Rev. X **7**, 041069 (2017).

[47] H. C. Po, A. Vishwanath, and H. Watanabe: Nature communications **8**, 50 (2017).

[48] B. Bradlyn, L. Elcoro, J. Cano, M. Vergniory, Z. Wang, C. Felser, M. Aroyo, and B. A. Bernevig: Nature **547**, 298 (2017).

[49] Z. Song, T. Zhang, Z. Fang, and C. Fang: Nature communications **9**, 3530 (2018).

[50] Z. Song, T. Zhang, and C. Fang: Physical Review X **8**, 031069 (2018).

[51] C.-K. Chiu, J. C. Y. Teo, A. P. Schnyder, and S. Ryu: Rev. Mod. Phys. **88**, 035005 (2016).

[52] K. Shiozaki, M. Sato, and K. Gomi: arXiv preprint arXiv:1802.06694 (2018).

[53] T. L. Hughes, E. Prodan, and B. A. Bernevig: Phys. Rev. B **83**, 245132 (2011).

[54] W. P. Su, J. R. Schrieffer, and A. J. Heeger: Phys. Rev. B **22**, 2099 (1980).

[55] J. K. Asbóth, L. Oroszlány, and A. Pályi: Lecture notes in physics **919**, 997 (2016).

[56] C. Bradley and A. Cracknell: *The mathematical theory of symmetry in solids: representation theory for point groups and space groups* (Oxford University Press, 2009).

[57] *Bilbao Crystallographic Server* (http://webbdcrista1.ehu.es/).

[58] M. Vergniory, L. Elcoro, C. Felser, N. Regnault, B. A. Bernevig, and Z. Wang: Nature **566**, 480 (2019).

[59] T. Zhang, Y. Jiang, Z. Song, H. Huang, Y. He, Z. Fang, H. Weng, and C. Fang: Nature **566**, 475 (2019).

[60] F. Tang, H. C. Po, A. Vishwanath, and X. Wan: Nature **566**, 486 (2019).

[61] Y. Xu, L. Elcoro, Z.-D. Song, B. J. Wieder, M. Vergniory, N. Regnault, Y. Chen, C. Felser, and B. A. Bernevig: Nature **586**, 702 (2020).

[62] K. Momma and F. Izumi: Journal of Applied Crystallography **41**, 653 (2008).

[63] P. Giannozzi, S. Baroni, N. Bonini, M. Calandra, R. Car, C. Cavazzoni, D. Ceresoli, G. L. Chiarotti, M. Cococcioni, I. Dabo, et al.: Journal of physics: Condensed matter **21**, 395502 (2009).

[64] *Topological Materials Databese* (https://www.topologicalquantumchemistry.com/).

[65] H. Huang, J. Liu, D. Vanderbilt, and W. Duan: Phys. Rev. B **93**, 201114 (2016).

[66] Z. Wang, B. J. Wieder, J. Li, B. Yan, and B. A. Bernevig: Physical review letters **123**, 186401 (2019).

[67] J. Hu, Z. Tang, J. Liu, X. Liu, Y. Zhu, D. Graf, K. Myhro, S. Tran, C. N. Lau, J. Wei, and Z. Mao: Phys. Rev. Lett. **117**, 016602 (2016).

[68] M. M. Hosen, K. Dimitri, I. Belopolski, P. Maldonado, R. Sankar, N. Dhakal, G. Dhakal, T. Cole, P. M. Oppeneer, D. Kaczorowski, F. Chou, M. Z. Hasan, T. Durakiewicz, and M. Neupane: Phys. Rev. B **95**, 161101 (2017).

[69] J. Hu, Z. Tang, J. Liu, Y. Zhu, J. Wei, and Z. Mao: Phys. Rev. B **96**, 045127 (2017).

[70] Y. Okamoto, T. Inohara, A. Yamakage, Y. Yamakawa, and K. Takenaka: Journal of the Physical Society of Japan **85**, 123701 (2016).

[71] X.-B. Wang, X.-M. Ma, E. Emmanouilidou, B. Shen, C.-H. Hsu, C.-S. Zhou, Y. Zuo, R.-R. Song, S.-Y. Xu, G. Wang, L. Huang, N. Ni, and C. Liu: Phys. Rev. B **96**, 161112 (2017).

[72] E. Emmanouilidou, B. Shen, X. Deng, T.-R. Chang, A. Shi, G. Kotliar, S.-Y. Xu, and N. Ni: Phys. Rev. B **95**, 245113 (2017).

[73] Q. Xu, R. Yu, Z. Fang, X. Dai, and H. Weng: Phys. Rev. B **95**, 045136 (2017).

[74] S. Li, Z. Guo, D. Fu, X.-C. Pan, J. Wang, K. Ran, S. Bao, Z. Ma, Z. Cai, R. Wang, et al.: Science bulletin **63**, 535 (2018).

[75] C. L. Kane and E. J. Mele: Phys. Rev. Lett. **95**, 226801 (2005).

[76] K. Hatsuda, H. Mine, T. Nakamura, J. Li, R. Wu, S. Katsumoto, and J. Haruyama: Science advances **4**, eaau6915 (2018).

[77] S. Ono and H. Watanabe: Phys. Rev. B **98**, 115150 (2018).

[78] M. Hirayama, R. Okugawa, T. Miyake, and S. Murakami: Nature communications **8**, 14002 (2017).

[79] I. Tateishi and H. Matsuura: Journal of the Physical Society of Japan **87**, 073702 (2018).

[80] T. Zhang, L. Lu, S. Murakami, Z. Fang, H. Weng, and C. Fang: Phys. Rev. Research **2**, 022066 (2020).

[81] X. Zhou, C.-H. Hsu, T.-R. Chang, H.-J. Tien, Q. Ma, P. Jarillo-Herrero, N. Gedik, A. Bansil, V. M. Pereira, S.-Y. Xu, H. Lin, and L. Fu: Phys. Rev. B **98**, 241104 (2018).

[82] C. Herring: Phys. Rev. **52**, 365 (1937).

[83] D. Bercioux and P. Lucignano: Reports on Progress in Physics **78**, 106001 (2015).

[84] J. Schliemann: Rev. Mod. Phys. **89**, 011001 (2017).

[85] P. Hohenberg and W. Kohn: Phys. Rev. **136**, B864 (1964).

[86] W. Kohn and L. J. Sham: Phys. Rev. **140**, A1133 (1965).

[87] J. P. Perdew, K. Burke, and M. Ernzerhof: Phys. Rev. Lett. **77**, 3865 (1996).

[88] D. Gresch, G. Autès, O. V. Yazyev, M. Troyer, D. Vanderbilt, B. A. Bernevig, and A. A. Soluyanov: Phys. Rev. B **95**, 075146 (2017).

[89] A. A. Soluyanov and D. Vanderbilt: Phys. Rev. B **83**, 235401 (2011).

[90] X. Zhou, C.-H. Hsu, C.-Y. Huang, M. Iraola, J. L. Mañes, M. G. Vergniory, H. Lin, and N. Kioussis: arXiv preprint arXiv:2005.06071 (2020).

[91] X. Zhou, C.-H. Hsu, H. Aramberri, M. Iraola, C.-Y. Huang, J. L. Mañes, M. G. Vergniory, H. Lin, and N. Kioussis: arXiv preprint arXiv:2005.04360 (2020).

[92] B. J. Wieder, B. Bradlyn, Z. Wang, J. Cano, Y. Kim, H.-S. D. Kim, A. M. Rappe, C. Kane, and B. A. Bernevig: Science **361**, 246 (2018).

[93] M. I. Aroyo, J. Perez-Mato, D. Orobengoa, E. Tasci, G. de la Flor, and A. Kirov: Bulg. Chem. Commun **43**, 183 (2011).

[94] M. I. Aroyo, J. M. Perez-Mato, C. Capillas, E. Kroumova, S. Ivantchev, G. Madariaga, A. Kirov, and H. Wondratschek: Zeitschrift für Kristallographie-Crystalline Materials **221**, 15 (2006).

[95] M. I. Aroyo, A. Kirov, C. Capillas, J. Perez-Mato, and H. Wondratschek: Acta Crystallographica Section A: Foundations of Crystallography **62**, 115 (2006).

[96] H. C. Po, H. Watanabe, and A. Vishwanath: Phys. Rev. Lett. **121**, 126402 (2018).

[97] B. Bradlyn, Z. Wang, J. Cano, and B. A. Bernevig: Phys. Rev. B **99**, 045140 (2019).

[98] Z.-D. Song, L. Elcoro, Y.-F. Xu, N. Regnault, and B. A. Bernevig: Phys. Rev. X **10**, 031001 (2020).

[99] M. I. Aroyo, D. Orobengoa, G. de la Flor, E. S. Tasci, J. M. Perez-Mato, and H. Wondratschek: Acta Crystallographica Section A: Foundations and Advances **70**, 126 (2014).

[100] S. L. Altmann and P. Herzig: *Point-group theory tables* (Oxford, 1994).

[101] J. Xiao and B. Yan: arXiv preprint arXiv:2010.08371 (2020).

[102] Y. He, Y. Jiang, T. Zhang, H. Huang, C. Fang, and Z. Jin: Chinese Physics B **28**, 087102 (2019).

[103] A. A. Mostofi, J. R. Yates, Y.-S. Lee, I. Souza, D. Vanderbilt, and N. Marzari: Computer physics communications **178**, 685 (2008).

[104] G. Pizzi, V. Vitale, R. Arita, S. Blügel, F. Freimuth, G. Géranton, M. Gibertini, D. Gresch, C. Johnson, T. Koretsune, et al.: Journal of Physics: Condensed Matter **32**, 165902 (2020).

[105] Q. Wu, S. Zhang, H.-F. Song, M. Troyer, and A. A. Soluyanov: Computer Physics Communications **224**, 405 (2018).

[106] S. S. Tsirkin: arXiv preprint arXiv:2008.07992 (2020).

[107] J. Gao, Q. Wu, C. Persson, and Z. Wang: arXiv preprint arXiv:2002.04032 (2020).

[108] M. Iraola, J. L. Mañes, B. Bradlyn, T. Neupert, M. G. Vergniory, and S. S. Tsirkin: arXiv preprint arXiv:2009.01764 (2020).

[109] A. Matsugatani, S. Ono, Y. Nomura, and H. Watanabe: arXiv preprint arXiv:2006.00194 (2020).

[110] M. Hellenbrandt: Crystallography Reviews **10**, 17 (2004).

[111] A. Jain, S. P. Ong, G. Hautier, W. Chen, W. D. Richards, S. Dacek, S. Cholia, D. Gunter, D. Skinner, G. Ceder, et al.: Apl Materials **1**, 011002 (2013).

[112] U. Herath, P. Tavadze, X. He, E. Bousquet, S. Singh, F. Munoz, and A. H. Romero: Computer Physics Communications **251**, 107080 (2020).

[113] A. Kokalj: Journal of Molecular Graphics and Modelling **17**, 176 (1999).

[114] C. Fang, M. J. Gilbert, and B. A. Bernevig: Phys. Rev. B **86**, 115112 (2012).

[115] T. Morimoto and A. Furusaki: Phys. Rev. B **88**, 125129 (2013).